INFLUENCE OF PROCESSING PARAMETERS IN THE MECHANICAL PROPERTIES ENHANCEMENT OF FORSTERITE CERAMIC

TAN YOKE MENG

FACULTY OF ENGINEERING
UNIVERSITY OF MALAYA
KUALA LUMPUR

2017

INFLUENCE OF PROCESSING PARAMETERS IN THE MECHANICAL PROPERTIES ENHANCEMENT OF FORSTERITE CERAMIC

TAN YOKE MENG

THESIS SUBMITTED IN FULFILMENT OF THE REQUIREMENTS FOR THE DEGREE OF DOCTOR OF PHILOSOPHY

FACULTY OF ENGINEERING
UNIVERSITY OF MALAYA
KUALA LUMPUR

2017

UNIVERSITY OF MALAYA

ORIGINAL LITERARY WORK DECLARATION

Name of Candidate: Tan Yoke Meng

Registration/Matric No: KHA120109

Name of Degree: Doctor of Philosophy

Title of Project Paper/Research Report/Dissertation/Thesis ("this Work"): Influence of processing parameters in the mechanical properties enhancement of forsterite ceramic

Field of Study: Manufacturing Processes

I do solemnly and sincerely declare that:

(1) I am the sole author/writer of this Work;
(2) This Work is original;
(3) Any use of any work in which copyright exists was done by way of fair dealing and for permitted purposes and any excerpt or extract from, or reference to or reproduction of any copyright work has been disclosed expressly and sufficiently and the title of the Work and its authorship have been acknowledged in this Work;
(4) I do not have any actual knowledge nor do I ought reasonably to know that the making of this work constitutes an infringement of any copyright work;
(5) I hereby assign all and every rights in the copyright to this Work to the University of Malaya ("UM"), who henceforth shall be owner of the copyright in this Work and that any reproduction or use in any form or by any means whatsoever is prohibited without the written consent of UM having been first had and obtained;
(6) I am fully aware that if in the course of making this Work I have infringed any copyright whether intentionally or otherwise, I may be subject to legal action or any other action as may be determined by UM.

Candidate's Signature Date:

Subscribed and solemnly declared before,

Witness's Signature Date:

Name:

Designation:

ABSTRACT

Phase pure forsterite was synthesized by mechanochemical method owing to its simplicity and low cost process. Different milling methods, i.e. ball milling and attrition milling, were investigated over sintering temperature ranging from 1200 ^{o}C to 1500 ^{o}C. Upon comparison and selection for the best method based on relative density, Vickers hardness and fracture toughness, the effect of ZnO addition ranging from 0.1-3.0 wt% on the sinterability of forsterite when sintered at 1200 ^{o}C to 1500 ^{o}C was evaluated. Subsequently, microwave sintering was conducted on both undoped and doped forsterite bulk at temperature ranging from 1100 ^{o}C to 1250 ^{o}C.

In the present study, phase pure forsterite was successfully synthesized upon sintering at 1200 ^{o}C and 1300 ^{o}C for attrition-milled and ball-milled samples, respectively. It was revealed that attrition milling provides higher grinding energy and particle refinement on the mixtures thus producing powder with significantly smaller particle size as compared to ball-milled powder. The optimum sintering temperature obtained was 1400 ^{o}C for both samples having the highest fracture toughness value of 4.3 MPa $m^{1/2}$ and 3.52 MPa $m^{1/2}$ for attritor-milled and ball-milled samples, respectively. No decomposition of forsterite was observed throughout the sintering regime. This study had also revealed that the incorporation of 1.0 wt% ZnO into forsterite had enhanced the overall mechanical properties of forsterite with a maximum of 4.51 MPa $m^{1/2}$ fracture toughness value obtained upon sintering at 1400 ^{o}C. In general, all doped samples showed better mechanical properties than the undoped sample at all sintering temperatures studied. In addition, microwave sintering was proven to be beneficial towards the mechanical properties enhancement at a lower sintering temperature with very short sintering duration. Fracture toughness of 4.25 MPa $m^{1/2}$ was successfully obtained at sintering temperature of 1250 ^{o}C for 1.0 wt%

ZnO doped sample. The fracture toughness value obtained was 36% higher as compared to the conventional sintered sample under equal sintering temperature. This promising result had shown the potential of microwave sintering in further enhancing forsterite ceramic without sacrificing the phase stability of the material. This research had highlighted the advantageous of using attrition milling in synthesizing phase pure forsterite, the economical production of ZnO doped forsterite having enhanced mechanical properties and the significant reduction in sintering process with acceptable mechanical properties for clinical application via microwave sintering.

ABSTRAK

Fasa forsterite tulen telah disintesis melalui kaedah mechanochemical kerana kesederhanaan dan proses kos rendah. kaedah pengilangan yang berbeza, iaitu bola pengilangan dan pergeseran pengilangan, telah disiasat atas suhu pensinteran dalam julat 1200 ^{o}C sehingga 1500 ^{o}C. Setelah perbandingan dan pemilihan kaedah terbaik berdasarkan ketumpatan relatif, kekerasan Vickers dan keliatan patah, kesan dop ZnO sebanyak 0.1-3.0% berat pada forsterite apabila disinter pada 1200 ^{o}C 1500 ^{o}C disiasat. Selepas itu, pensinteran melalui gelombang mikro telah dijalankan ke atas kedua-dua pukal forsterite tanpa dop dan didopkan pada suhu antara 1100 ^{o}C hingga 1250 ^{o}C.

Dalam kajian ini, fasa forsterite tulen telah berjaya disintesis atas pensinteran pada 1200 ^{o}C dan 1300 ^{o}C untuk pergeseran gilingan dan bola gilingan sampel, masing-masing. Ia telah mendedahkan bahawa pergeseran pengilangan menyediakan lebih tinggi tenaga pengisaran dan kehalusan zarah pada campuran itu menghasilkan serbuk dengan saiz zarah lebih kecil berbanding dengan serbuk bola gilingan. Suhu pensinteran optimum yang diperolehi ialah 1400 ^{o}C untuk kedua-dua sampel yang mempunyai nilai keliatan patah tertinggi sebanyak 4.3 MPa $m^{1/2}$ dan 3.52 MPa $m^{1/2}$ untuk attritor gilingan dan bola gilingan sampel, masing-masing. Tiada penguraian forsterite diperhatikan di seluruh rejim pensinteran. Kajian ini juga telah mendedahkan bahawa penggabungan 1.0% berat ZnO ke forsterite telah meningkatkan sifat-sifat mekanikal keseluruhan forsterite dengan maksimum 4.51 MPa $m^{1/2}$ nilai keliatan apabila disinter pada 1400 ^{o}C. Secara umum, semua sampel yang telah dop menunjukkan sifat-sifat mekanikal yang lebih baik daripada sampel undoped di semua pensinteran suhu dikaji. Di samping itu, pensinteran melalui gelombang mikro telah terbukti memberi manfaat dalam peningkatan sifat mekanikal pada suhu pensinteran yang lebih rendah dengan tempoh pensinteran yang singkat. Patah keliatan 4.25 MPa $m^{1/2}$ telah berjaya diperolehi pada pensinteran suhu 1250 ^{o}C bagi sampel yang didop sebanyak 1.0% berat ZnO. Nilai

keliatan patah yang diperolehi ialah 36% lebih tinggi berbanding dengan sampel yang disinter secara konvensional di bawah suhu pembakaran yang sama. Hasil memberangsangkan ini telah menunjukkan potensi pensinteran ketuhar gelombang mikro di meningkatkan lagi forsterite seramik tanpa mengorbankan kestabilan fasa bahan. Kajian ini telah menekankan berfaedah menggunakan pergeseran pengilangan dalam mensintesis fasa forsterite tulen, pengeluaran ekonomi ZnO forsterite didopkan telah dipertingkatkan ciri-ciri mekanikal dan pengurangan yang ketara dalam proses pensinteran dengan sifat-sifat mekanikal yang boleh diterima untuk aplikasi klinikal melalui gelombang pensinteran mikro.

ACKNOWLEDGEMENTS

First and foremost, I would like to express my sincerest gratitude to my honorific supervisors, Assoc. Prof. Dr. Tan Chou Yong and Prof. Ramesh Singh for their countless advice, guidance, and patience have significantly encouraged my journey in research. I am very grateful to my advisor, Prof Dinesh Agrawal at Pennsylvania State University, University Park, United States for his incredible and valuable advice and important support in the advancement of this research.

I would like to wish and express my warmest and sincere thanks to all lecturers, administrative and technical staffs in the Faculty of Engineering, UM for continuous assistance to achieve the goal of this research. My special thanks to the staffs in Faculty of Geology and Physics for their excellent expertise in guiding me throughout the research.

Special thanks are also given to my lab mates, Teh Yee Ching, Dr. Ali Asghar Niakan and Dr Kelvin Chew Wai Jin for their extensive and helpful guide throughout my graduate study in University of Malaya especially during the early semesters.

Lastly, I would like to show my countless appreciation and endless encouragement from my family and friends in completing my PhD project. It has been a wonderful experience, going through obstalces throughout the study and the satisfaction in unraveling them, together with my family, collegeaus and friends.

TABLE OF CONTENTS

Abstract iii

Abstrak v

Acknowledgements vii

Table of Contents viii

List of Figures xii

List of Tables xix

List of Symbols and Abbreviations xxi

List of Appendices xxiii

CHAPTER 1: INTRODUCTION 1

1.1 Background of the Study 1

1.2 Scope of Research 6

1.3 Research Objectives 6

1.4 Structure of the Thesis 7

CHAPTER 2: POWDER PROCESSING METHOD OF FORSTERITE 9

2.1 Introduction to biomaterials 9

2.1.1 Types of biomaterials 10

2.1.2 Classification and requirement of bioceramics 11

2.1.2.1 Bioactive 12

2.1.2.2 Bioresorbable 12

2.1.2.3 Bioinert 13

2.2 Biocompatibility study of forsterite ceramic 15

2.3 Powder processing method of forsterite ceramic 17

2.3.1 Solid-state reaction via mechanical activation 19

2.3.2 Sol-gel method 25

2.3.3 Other methods 28

CHAPTER 3: SINTERABILITY OF FORSTERITE CERAMIC 31

3.1 Introduction 31

3.2 Conventional method 32

3.2.1 Heat treatment temperature and Mg/Si ratio 32

3.2.2 Sintering temperature and dwell time 39

3.3 Non-conventional method 44

3.3.1 Two-step sintering 44

3.3.2 Microwave sintering 48

3.3.2.1 Introduction 48

3.3.2.2 Microwave sintering on bioceramics 50

3.4 Sintering additives on bioceramics 57

3.4.1 Introduction 57

3.4.2 Types of sintering additives 58

3.4.3 Amount of sintering additives 60

3.4.4 Zinc oxide as sintering additive 63

3.4.5 Application of sintering additives on forsterite 68

CHAPTER 4: METHODOLOGY 69

4.1 Introduction 69

4.2 Powder synthesis 69

4.2.1 Starting powder preparation 69

4.2.2 Forsterite preparation with different milling durations 70

4.2.3 Forsterite preparation with attrition milling 71

4.2.4 Zinc oxide (ZnO) – doped forsterite powder preparation 71

4.3 Consolidation of green body 72
4.3.1 Conventional sintering 72
4.3.2 Microwave sintering 73
4.4 Sample characterization 74
4.4.1 Phase composition analysis 74
4.4.2 Brunaeur-Emmett-Teller (BET) surface area 75
4.4.3 Differential thermal (DT) and thermogravimetric (TG) analysis 76
4.4.4 Bulk density measurement 76
4.4.5 Vickers hardness and fracture toughness 77
4.4.6 Grain size measurement 80
4.4.7 Morphology and Elemental Examination 81
4.4.7.1 Scanning Electron Microscope (SEM) 81
4.4.7.2 Field-emission Scanning Electron Microscope (FESEM) 82
4.4.7.3 Transmission Electron Microscopy (TEM) 82
4.4.7.4 Cell morphology 82

CHAPTER 5: RESULTS AND DISCUSSION 85

5.1 Part 1: Comparison between types of milling and milling duration in synthesizing forsterite ceramic 85
5.1.1 Phase analysis of starting powder 86
5.1.2 Phase and particle size analysis of forsterite powder and bulk 87
5.1.3 Mechanical properties and cell morphology of forsterite 95
5.2 Part 2: Comparison between ZnO doped forsterite and pure forsterite 106
5.2.1 Phase and elemental analysis of forsterite bulk 108
5.2.2 Sinterability of forsterite bulk 111
5.3 Part 3: Effect of microwave sintering on the sinterability of forsterite 119
5.3.1 Phase analysis of forsterite bulk 119

5.3.2 Mechanical properties evaluation of forsterite bulk 120

5.3.3 Comparison between conventional sintering (CS) and microwave sintering (MS) 130

5.3.3.1 Pure (undoped) forsterite 130

5.3.3.2 ZnO doped forsterite 132

CHAPTER 6: CONCLUSIONS 135

6.1 Conclusions 135

6.2 Future directions 141

REFERENCES 143

List of Publications and Papers Presented 154

Appendix A 156

Appendix B 158

Appendix C 174

LIST OF FIGURES

Figure 2.1: Phase-contrast microscopic images of rat calvaria osteoblasts cultured on forsterite discs for 4 h (a) and 24 h (b) after seeding (Ni et al., 2007). 16

Figure 2.2: Proliferation of osteoblast cultivated on forsterite ceramics for 1, 3 and 7 days in comparison with the control (Ni et al., 2007). 16

Figure 2.3: Phase purity of analysis of forsterite prepared using MgO and talc upon milling at various duration and heat treated at 1000 ^{o}C for 1 hour (Tavangarian & Emadi, 2010b). 21

Figure 2.4: Phase purity of MgO-SiO_2 mixtures milled at various duration and heated at 850 ^{o}C for 3 hours (Cheng et al., 2012). 23

Figure 2.5: Average particle size as a function of milling duration (Cheng et al., 2012). 23

Figure 2.6: Types of motion in a ball mill: (A) cascading, (B) falling or cataracting, (C) centrifugal. (Bernotat & Schonert, 1998). 24

Figure 2.7: Phase purity result of forsterite powder heated at various temperatures for 3 hours in air (Hassanzadeh-Tabrizi et al., 2016). 27

Figure 2.8: Phase purity of S1, S2, S3 and S4 samples. Weak peak represented by the asterisk defined the peak for MgO phase (45-0946) (Sun et al., 2009). 28

Figure 2.9: Phase stability results of the spray-dried precursors heated at various temperatures to form forsterite powder (Douy, 2002). 30

Figure 2.10: Phase stability results of the evaporated precursors heated at various temperatures to form forsterite powder (Douy, 2002). 30

Figure 3.1: Phase purity result of forsterite powder milled at various durations and subsequently heated at 1000 ^{o}C for 1 hour (Tavangarian & Emadi, 2009). 33

Figure 3.2: Phase purity result of forsterite powder milled at various durations and subsequently heated at 1200 ^{o}C for 1 hour (Tavangarian & Emadi, 2009). 34

Figure 3.3: Phase purity of powder milled for 5 hours and annealed for 10 minutes at corresponding temperatures (Tavangarian et al., 2010). 35

Figure 3.4: Phase purity of powder milled for 10 hours and annealed for 10 minutes at corresponding temperatures (Tavangarian et al., 2010). 36

Figure 3.5: Phase purity of MgO-SiO_2 mixtures milled for 30 hours and heated at various temperatures for 3 hours (Cheng, et al., 2012). 37

Figure 3.6: Phase purity of forsterite powders heated at various temperatures for 3 hours in air with Mg/Si ratio of 2 (Shi et al., 2012). 38

Figure 3.7: Phase purity result of forsterite powders heated at 1350 ^{o}C for 3 hours in air with various ratio of Mg/Si (Shi et al., 2012). 38

Figure 3.8: Phase purity result of forsterite bulk sintered at 1450 ^{o}C and 1550 ^{o}C for 8 hours (Ni et al., 2007). 39

Figure 3.9: SEM micrograph of forsterite bulk sintered at 1450 ^{o}C for 8 hours (Ni et al., 2007). 40

Figure 3.10: SEM of the fracture surface of forsterite upon sintering at a) 1450 ^{o}C and b) 1550 ^{o}C (Ni et al., 2007). 41

Figure 3.11: Mechanical properties evaluation of heat treated (solid lines) and non-heat treated (dash lines) forsterite bulked sintered at different temperatures for 2 hours (Ramesh, et al., 2013). 43

Figure 3.12: Phase stability result heat treated forsterite sintered in bulk form at different temperatures for 2 hours (Ramesh et al., 2013). 44

Figure 3.13: Example of a typical two-step sintering profile. 45

Figure 3.14: Relative density of forsterite bulk in a function of the first stage (T1) of two-step sintering temperature (Fathi & Kharaziha, 2009). 46

Figure 3.15: Average grain size versus relative density of forsterite bulk under TSS1 (T1 = 1300 ^{o}C and T2 = 750 ^{o}C) and TSS2 (T1 = 1300 ^{o}C and T2 = 850 ^{o}C) profiles with 15 hours holding for second step sintering (Fathi & Kharaziha, 2009). 46

Figure 3.16: (a) Vickers hardness and (b) fracture toughness of forsterite as a function of relative density sintered at 1300 ^{o}C for first step sintering (Fathi & Kharaziha, 2009). 47

Figure 3.17: Phase purity of mixtures of initial precursors milled for 40 hours and heated at different temperatures via microwave heating (Bafrooei et al., 2014). 51

Figure 3.18: Relative density of forsterite ceramic sintered using conventional and microwave sintering (Bafrooei et al., 2014)..... 52

Figure 3.19: XRD traces of pure HA microwave sintered at 900, 1000, 1100 and 1200 ^{o}C (Veljovic et al., 2010)..... 53

Figure 3.20: XRD traces of pure HA microwave sintered at 900, 1000, 1100 and 1200 ^{o}C (Veljovic et al., 2010)..... 53

Figure 3.21: The relationship between grain size and sintering temperature of HA and HA/TCP 54

Figure 3.22: Effect of conventional and microwave sintering temperature on the relative density of zirconia (Borrell et al., 2012). 56

Figure 3.23: Effect of conventional and microwave sintering temperature on the grain size of zirconia (Borrell et al., 2012)..... 56

Figure 3.24: Effect of conventional and microwave sintering temperature on the fracture toughness of zirconia (Borrell et al., 2012). 57

Figure 3.25: SEM micrograph of the grain size of (a) undoped TCP, (b) TCP-MgO/SrO, (c) TCP-SrO/SiO_2 and (d) TCP-MgO/SrO/SiO_2 sintered at 1250 ^{o}C for 2 hours (Bose et al., 2011). 59

Figure 3.26: Relative density variation sintered at different sintering temperature (Ramesh et al., 2007). 61

Figure 3.27: SEM micrograph of HA sintered at 1300 ^{o}C (Ramesh et al., 2007)..... 61

Figure 3.28: Effect of sintering temperature and Mn addition on the Vickers hardness of HA (Ramesh et al., 2007)..... 61

Figure 3.29: Effect of Nb_2O_5 content on the Vickers hardness of alumina composites sintered at 1650 ^{o}C (Hassan et al., 2014). 63

Figure 3.30: Effect of Nb_2O_5 content on the fracture toughness of alumina composites sintered at 1650 ^{o}C (Hassan et al., 2014). 63

Figure 3.31: Densification of TCP and HA sintered at 1250 ^{o}C under different composition of ZnO addition (Bandhopadhyay et al., 2007). 65

Figure 3.32: Density for green and sintered of pure and doped nano-HAp sintered at 1250 ^{o}C for 6 hours (Kalita & Bhatt, 2007) 66

Figure 3.33: Vickers hardness and fracture toughness of PMNT/ZnO ceramics (Promsawat et al., 2012)..... 67

Figure 4.1: Sintering profile for the firing of green bulk samples via conventional sintering. 73

Figure 4.2: Schematic diagram of a pyramidal indenter used in Vickers hardness test (D1, D2 = diagonal length of indentation; L1, L2, L3, L4 = length of fracture). 78

Figure 4.3: Flow chart of project research 84

Figure 5.1: XRD traces of magnesium carbonate powder. 86

Figure 5.2: XRD traces of talc powder. 86

Figure 5.3: XRD traces of proto forsterite powder upon attrition milling for 5 hours. .. 87

Figure 5.4: XRD of conventional milled forsterite bulk for 3 hours and sintered at 1200 ^{o}C for 2 hours at ramp rate of 10 ^{o}C/min. 88

Figure 5.5: XRD of conventional milled forsterite bulk for 5 hours and sintered at 1200 ^{o}C for 2 hours at ramp rate of 10 ^{o}C/min. 88

Figure 5.6: XRD of conventional milled forsterite bulk for 3 hours and sintered at 1300 ^{o}C for 2 hours at ramp rate of 10 ^{o}C/min. 89

Figure 5.7: XRD of conventional milled forsterite bulk for 5 hours and sintered at 1300 ^{o}C for 2 hours at ramp rate of 10 ^{o}C/min. 90

Figure 5.8: XRD of conventional ball milled forsterite bulk for 3 hours and sintered at 1400 and 1500 ^{o}C for 2 hours at ramp rate of 10 ^{o}C/min..... 91

Figure 5.9: XRD of conventional ball milled forsterite bulk for 5 hours and sintered at 1400 and 1500 ^{o}C for 2 hours at ramp rate of 10 ^{o}C/min..... 92

Figure 5.10: XRD of attritor milled forsterite bulk for 5 hours and sintered at 1200, 1300, 1400 and 1500 ^{o}C for 2 hours at ramp rate of 10 ^{o}C/min..... 93

Figure 5.11: SEM image of forsterite powder upon attrition milling revealing the presence of loosely packed powders with both small and large size particles. 94

Figure 5.12: TEM images of powders upon (a) ball milled for 3 hours, (b) ball milled for 5 hours and (c) attritor milled for 5 hours. 95

Figure 5.13: Relative density comparison between conventional ball mill (BM) and attritor mill (AM) for 5 hours of forsterite bulk as a function of sintering temperature. 96

Figure 5.14: Morphology of AM sample sintered at (a) 1200 ^{o}C, (b) 1300 ^{o}C, (c) 1400 ^{o}C and (d) 1500 ^{o}C for 2 hours at 10 ^{o}C/min. Large pores were entrapped between small and large grains when sintered at 1500 ^{o}C. 97

Figure 5.15: Vickers hardness of ball and attritor milled forsterite as a function of sintering temperature..... 98

Figure 5.16: Variation of hardness with density of sintered BM samples 99

Figure 5.17: Morphology of BM sample sintered at a) 1200 ^{o}C and b) 1300 ^{o}C for 2 hours at 10 ^{o}C/min..... 100

Figure 5.18: Fracture toughness of ball and attritor milled of forsterite as a function of sintering temperature. 102

Figure 5.19: Morphology of BM sample sintered at 1400 ^{o}C. Arrows showed the formation of elongated grain structure in forsterite. 103

Figure 5.20: Morphology of BM sample sintered at 1500 ^{o}C. High ratio of large to small grain was observed and pores were still detected. 103

Figure 5.21: Cell morphology upon culturing for 4 hours on AM sample (sintered at 1400 ^{o}C). The white arrows indicate the adhered cell with filopodial extensions. 104

Figure 5.22: SEM image of cells proliferation of MC3T3-E1 on AM sample: (a) 1 day culture and (b) 3 days culture. 105

Figure 5.23: TG and DTA curves of attritor-milled powder heat treated up to 1000 ^{o}C. 107

Figure 5.24: XRD of heat treated forsterite powder at 1000 ^{o}C for 2 hours with ramping rate of 10 ^{o}C/min. 108

Figure 5.25: XRD traces of pure (undoped) forsterite sintered at (a) 1200 ^{o}C, (b) 1250 ^{o}C and (c) 1500 ^{o}C 109

Figure 5.26: XRD traces of 0.5 wt% ZnO doped forsterite sintered at (a) 1200 ^{o}C, (b) 1250 ^{o}C and (c) 1500 ^{o}C. 109

Figure 5.27: XRD traces of 1.0 wt% ZnO doped forsterite sintered at (a) 1200 ^{o}C, (b) 1250 ^{o}C and (c) 1500 ^{o}C. 110

Figure 5.28: XRD traces of 3.0 wt% ZnO doped forsterite sintered at (a) 1200 ^{o}C, (b) 1250 ^{o}C and (c) 1500 ^{o}C. 110

Figure 5.29: Elemental analysis of (a) 3.0 wt% and (b) 1.0 wt% of ZnO content sintered at 1500 ^{o}C 111

Figure 5.30: Relative density variation as a function of sintering temperatures for forsterite. 112

Figure 5.31: Vickers hardness variation as a function of sintering temperature for forsterite. 113

Figure 5.32: Morphology of (a) undoped, (b) 0.5 wt%, (c) 1.0 wt% and (d) 3.0 wt% ZnO-doped forsterite sintered at 1200 ^{o}C. 114

Figure 5.33: Fracture toughness variation as a function of sintering temperature for forsterite. 115

Figure 5.34: Fracture toughness variation in terms of Vickers hardness for pure forsterite samples. 115

Figure 5.35: Grain size of pure and doped forsterite bulk under various sintering temperatures. 116

Figure 5.36: Morphology of (a) undoped, (b) 0.5 wt% and (c) 1.0 wt% ZnO doped forsterite bulk sintered at 1400 ^{o}C..... 117

Figure 5.37: Fracture toughness dependence on the grain size of forsterite. 117

Figure 5.38: XRD traces of (a) undoped, (b) 0.5 wt%, (c) 1.0 wt% and (d) 3.0 wt% doped ZnO forsterite microwave sintered at 1100 ^{o}C. 119

Figure 5.39: XRD traces of (a) undoped, (b) 0.5 wt%, (c) 1.0 wt% and (d) 3.0 wt% doped ZnO forsterite microwave sintered at 1250 ^{o}C. 120

Figure 5.40: Relative density variation of forsterite with different ZnO composition as a function of sintering temperature. 121

Figure 5.41: SEM morphology of 3.0 wt% ZnO sample sintered at 1200 ^{o}C. 121

Figure 5.42: Morphology of (a) pure (undoped) and (b) 0.5 wt% ZnO doped forsterite samples microwave-sintered at 1100 ^{o}C. 122

Figure 5.43: Vickers hardness variation as a function of sintering temperature of forsterite bulk. 122

Figure 5.44: Vickers hardness variation in terms of relative density. 123

Figure 5.45: Fracture toughness variation as a function of sintering temperature of forsterite bulk. 124

Figure 5.46: SEM morphology of a) undoped and b) 1.0 wt% ZnO doped samples microwave sintered at 1250 ^{o}C. Red circles indicating the clustering of ZnO particles. 125

Figure 5.47: Fracture toughness variation as a function of Vickers hardness. 126

Figure 5.48: Morphology of 1.0 wt% ZnO doped sample microwave sintered at 1250 ^{o}C. 128

Figure 5.49: Morphology of 3.0 wt% ZnO doped forsterite sample microwave sintered at 1150 ^{o}C. White circle signify the spot for EDX. 128

Figure 5.50: Morphology of 3.0 wt% ZnO doped forsterite sample microwave sintered at 1250 ^{o}C 129

Figure 5.51: SEM image of pure forsterite sintered at 1250 ^{o}C via a) microwave sintering and b) conventional sintering 131

Figure 5.52: SEM images of 1.0 wt% ZnO doped forsterite sintered at 1250 ^{o}C via a) microwave sintering and b) conventional sintering 133

LIST OF TABLES

Table 2.1: Types and Uses of Current Biomaterials (Llyod & Cross, 2002; Dorozhkin, 2010; Straley et al., 2010; Sionkowska, 2011).....10

Table 2.2: Classification of bioceramic and its response (Cao & Hench, 1996; Wang, 2003; Jayaswal et al., 2010; Geetha et al., 2009; Dee et al., 2003).....14

Table 2.3: Mechanical properties of hard tissues and forsterite (Legros, 1993; Fathi & Kharaziha, 2009; Ni et al., 2007; Ghomi et al., 2011). 17

Table 2.4: Formation of forsterite powder via sol-gel route with different starting precursors. All profiles successfully produced pure phase forsterite unless stated. 27

Table 2.5: Reactant ratios and annealing temperature (Sun et al., 2009).....28

Table 3.1: Mechanical properties of sintered forsterite bulk at different temperature for 6 hours (Ni et al., 2007). 41

Table 3.2: Mechanical properties of sintered forsterite bulk at 1450 ^{o}C at different holding time (Ni et al., 2007). 41

Table 3.3: Surface area and particle size of forsterite nanopowder at different temperature upon milled for 40 hours (Bafrooei et al., 2014). 51

Table 3.4: Processing conditions and mechanical properties of HA sintered via conventional and microwave sintering (Veljovic et al., 2010). 54

Table 3.5: Mechanical properties of HA with different sintering cycles (Bose et al., 2010). 55

Table 3.6: Relative density and grain size of doped and undoped TCP sintered at 1250 ^{o}C for 2 hours (Bose et al., 2011).....59

Table 3.7: Relative density, and grain size of PMNT/ZnO ceramics (Promsawat et al., 2012). 67

Table 4.1: Weight of precursors for a 50 g batch of forsterite.....69

Table 4.2: Table of ZnO weight percentage in forsterite and mass needed for a 50 g batch.....72

Table 4.3: JCPDS reference cards to analyze the phases in forsterite powder 75

Table 5.1: Particle size and specific surface area of proto forsterite powder milled using conventional ball mill.....91

Table 5.2: Particle size and specific surface area of proto forsterite powder milled using conventional ball mill and attritor mill.....93

Table 5.3: EDX result on 3.0 wt% ZnO doped forsterite sample microwave sintered at 1150 ^{o}C.....129

Table 5.4: Mechanical properties of pure forsterite sintered via conventional and microwave sintering.....132

Table 5.5: Mechanical properties of 1.0 wt% ZnO doped forsterite sintered via conventional and microwave sintering.....134

LIST OF SYMBOLS AND ABBREVIATIONS

AM	:	Attritor mill
ASTM	:	American Society of Testing and Materials
BET	:	Brunaeur-Emmett-Teller
BM	:	Ball mill
CTAB	:	Cetyltrimethylammonium bromide
EDX	:	Emission Dispersive X-Ray
FESEM	:	Field-emission scanning electron microscope
HA	:	Hydroxyapatite
HDMS	:	Hexamethyldisilazane
HEBM	:	High energy ball milling
JCPDS	:	Joint Committee on Powder Diffraction Standard
MCP	:	Mechanochemical process
MgO	:	Periclase / Magnesium oxide
$MgSiO_3$	:	Enstatite
MHC	:	Magnesium Carbonate Basic
MW	:	Microwave
NaCl	:	Sodium chloride
NH_4Cl	:	Ammonium Chloride
NIH	:	National institute of health
SBF	:	Simulated bodily fluid
SEM	:	Scanning electron microscope
SiC	:	Silicon Carbide
TCP	:	Tri-calcium phosphate/ calcium deficient HA
TEM	:	Transmission emission microscope

TEOS	:	Tetra ethyl ortho-silicate
XRD	:	X-ray diffraction
ZnO	:	Zinc Oxide

LIST OF APPENDICES

Appendix A: Calculation of raw materials preparation …… 156

Appendix B: X-ray diffraction reference cards……. 158

Appendix C: Materials and Equipments…… 174

CHAPTER 1: INTRODUCTION

1.1 Background of the Study

Researchers had undergone a huge revolution in bone treatment that shifted from painkilling treatment of contagious diseases of bone to an interventional treatment of continuous age-related issues (Hench, 2000). The discovery of antibiotics to control infections has brought about to a new anesthetic for safer surgeries that involved a stable fixation devices and development of joint prostheses (artificial joint). However at present, the reconstruction of bone defects is still a challenge to many researchers in the field of medic and dental. Bone graft has been used extensively in treating bone diseases that affects the daily quality life of victim especially aged patients (Kokubo et al., 2003). These implants were defined as "manufactured devices that have been designed and developed to fulfill particular functions when implanted into the living body, and usually for specific indications" (Wang et al., 2011). It was well established by Hench (2000) and Kloss and Glassner (2006) that bone strength deteriorates significantly faster as the age of victims reaches about 50-60 years (Hench, 2000; Kloss & Glassner, 2006). Disease and injury from accidents also cause damage and degeneration of tissues and bones in human body, which emphasize more on the need for bone grafting. Bone grafting can be divided into three main categories. Autograft tissue involved the transplantation of bones from one site to another from the same host. The applicability of autograft has been restricted by the expensive cost, painful, second site morbidity and limited supply since it involved the same host. Allograft or homograft was introduced to solve the limited supply issue from autograft method. Bones were transplant from a different host to the victim but it may cause the infection or disease to spread from the donor to the patient. Also, the patient's immune system may reject the tissue thus causing complication upon transplantation (Hench, 2000; Brien, 2011; Naderi et al., 2011). The third method is heterograft or xenograft in which the tissue/graft transplant

involved both living and non-living of different species. However, the difference in genetics made this method controversial and hardly being used at present (Hench, 2000). Therefore, artificial bone substitute materials were introduced and have attracted the attention of many researchers for clinical applications.

The most common material used for artificial bone substitution is bioceramic. Bioceramics was first introduced and implemented into surgery for humans in 1980s whereby hydroxyapatite (HA) was used as a coating for implants. HA was chosen due to the excellent biocompatibility, bone bonding ability and chemical similarity to natural bone (Dorozhkin & Epple, 2002; Dorozhkin, 2009; Juhasz & Best, 2012). Then in 1985 to 2001, zirconia was widely used as a hip joint femoral heads implant owing to its good mechanical properties (Jayaswal et al, 2010). Bioceramic materials were also chosen for bone tissue replacement because of the simplicity in fabrication and low production cost (Tomoaia et al., 2013).

Generally, bioceramics are divided into several types depending on its properties and functionality. For example, HA has good biocompatibility which gives rise to its usage as dental fillers and coating of implants whereas zirconia has very good mechanical properties that makes it useful for load-bearing applications (Amir *et al*., 2012). Before zirconia was introduced, alumina was widely used as joint prostheses and wear plates in knees (Jayaswal et al., 2010; Binyamin et al., 2006). Then, an attempt was made to counter the low fracture toughness of alumina by introducing zirconia into the network and producing a biphasic structure. However, due to ageing of zirconia the structure became unstable (Deville et al., 2006). Many other methods and materials were introduced throughout the years to enhance the mechanical properties and biocompatibility of bioceramics with the aim of having both good biocompatibility and optimal mechanical properties for bone implantation.

Forsterite, with a chemical formula Mg_2SiO_4, is a crystalline magnesium orthosilicate that is grouped under the olivine family and being named by Armand Levy after a German scientist Johann Forster (Brindley & Hayami, 1965). Forsterite consists of magnesium (Mg) and silicate (SiO_4) with an ionic ratio of 2:1, respectively, which makes it a good candidate for bone implantation in terms of bioactivity. The silicon and oxygen atom are bonded by a single covalent bonding and due to the repulsive force among the oxygen atoms, the atoms are arranged far from each other and formed a tetragonal shape (Downing et al., 2013).

Aside for clinical application, forsterite was initially used in many other industries. It was discovered by Verdun et al. (1988) that chromium doped forsterite possessed good potential as a tunable laser with a near infrared range of 1.1 – 1.3 μm. Also, forsterite can be an excellent host material for nickel as well for optical telecommunication industry (Petricevic, et al., 1988). Owing to the high melting point, low thermal expansion and chemically stable (1890 ^{o}C) of forsterite, it served as a refractory for many high temperature applications including steel casting and making and metallurgy of ladle (Vallepu et al., 2005; Saberi, 2007; Mustafa, et al., 2002; Jing et al., 2009) and with alumina refractory material, they are used for lining regenerator checkers (Popov et al., 1988). In addition, Douy (2002) claimed that forsterite can be used for solid oxide fuel cell (SOFC) because of the linear thermal expansion coefficient and high stability properties in fuel cell environment. In electronic industries, forsterite can be used as a dielectric material for high frequency circuit due to their low dielectric loss (ε = 6-7) relative to high-frequency electromagnetic waves (Ohsato et al., 2004; Tavangarian & Emadi, 2011a).

The need to find for a high quality bioceramic materials with good biocompatibility and high mechanical properties lead to the introduction of forsterite (Mg_2SiO_4) bioceramic in the field of orthopaedics. In regards with HA, it was reported that the fracture toughness is in the range of 0.6 – 1.0 MPa $m^{1/2}$ which is not within the region of cortical bone (2 – 12 MPa $m^{1/2}$) (Ghomi et al., 2011; Ni et al., 2009). Recently, Khanal et al. (2016) had tried adding carboxyl functionalized single walled carbon nanotubes and nylon by 1 % into HA and obtained 3.6 MPa $m^{1/2}$. Nevertheless, no proper biological evaluation was conducted by the researcher to illustrate the reliability of the additives in human body. Due to the low fracture toughness of HA, the application was restricted only to non-load bearing application. With the growing demand for a suitable material in bone industry, forsterite was reintroduced recently owing to its good biocompatibility and better mechanical properties as compared to HA with fracture toughness of 2.4 MPa $m^{1/2}$ obtained by Ni et al (2007). In order to further increase the mechanical properties of forsterite, the doping with zinc oxide (ZnO) was carried out to improve the mechanical properties. It was reported that ZnO doping could enhance the mechanical properties of HA (Bandyophadhyay et al., 2007) which will be discussed in the next chapter.

Despite the high demand, production of forsterite is a real challenge to many researchers. Appearance of secondary phases, which is enstatite ($MgSiO_3$) and periclase (MgO), is very common during the synthesizing of forsterite due to the similarity in chemical composition and relatively low diffusion rate (Tavangarian & Emadi, 2010; Tavangarian & Emadi, 2011). The low diffusivity of formed compound leads to the sluggish formation of silicate with oxide which then causes the formation of enstatite (Douy, 2002). With the existence of secondary phases, formation of forsterite bioceramic will be slower during the synthesis stage and requires higher firing temperature of up to 1600 ^oC. Additionally, the dissociation of enstatite in forsterite due

to lower melting point (1557 ^{o}C) will cause SiO_2-rich liquid to form and thus negatively affecting the overall mechanical properties of forsterite (Sanosh, 2010). Hence, some researchers suggested for higher sintering temperature (>1300 ^{o}C) to successfully remove the secondary phases. Though, higher temperature could solve the impurities in forsterite, coarser particles were observed which is not favorable in enhancing mechanical properties (Kiss, 2001; Sanosh, 2010). Hence, a balance between the purity and mechanical properties of forsterite needs to be achieved by introducing a new sintering method namely microwave sintering.

One of the common methods used to produce forsterite is the mechanochemical method which involved solid-state reaction due to the simplicity compared to other methods. Milling plays a huge role in ensuring that solid-state reaction occurs between the starting precursors used. Generally, most researchers used the conventional ball mill and planetary mill for their work. Also, prolonged milling was suggested by few researchers to produce pure forsterite powders (Fathi & Kharaziha, 2008; Cheng et al., 2012). However, it was claimed by another researcher that ball milling itself was insufficient to produce pure forsterite powder and heat treatment is necessary (Kosanovic, 2005). A study was done by Ramesh et al. (2013), on the effect of both milling and heat treatment on the formation of pure forsterite. It was found that heat treatment up to 1400 ^{o}C with 3 hours of ball mill still showed the presence of secondary phase. The prolonged mill from 1 h to 3 h showed drastic reduction in the secondary phases peak via x-ray diffraction (XRD) result but unable to eliminate the peak entirely (Ramesh et al., 2013). Hence, in this study, a new milling method will be introduced with higher grinding energy to reduce the required sintering temperature to obtain pure forsterite while maintaining and/or improving the mechanical properties.

1.2 Scope of Research

The research can be divided into three parts; first part involved the preparation of forsterite powder using mechanochemical method involving two different milling methods i.e. ball and attrition milling. The phase and mechanical behavior was studied and optimization based on sintering temperature was conducted.

The second part was to study on the effect of sintering additives, particularly zinc oxide (ZnO), towards the phase stability and mechanical properties enhancement. For the doping step, forsterite powder was first prepared via heat treatment and according to the thermal analysis; a suitable heat treatment temperature was selected.

The final part was to investigate on the effect of microwave sintering and a comparative study was conducted between both conventional and microwave sintering on the phase stability and mechanical behavior under varying sintering profile.

All in all, the main goal for this research is to produce pure forsterite with improved mechanical properties that can be used for clinical application.

1.3 Research Objectives

This study focuses on the synthesizing of pure forsterite powder via mechanochemical method utilizing attritor mill instead of the conventional ball or planetary mill, doping of ZnO and applying microwave sintering on forsterite bulk to further enhance the mechanical properties of forsterite bulk. The main objectives are:

a) To synthesize pure forsterite powder via mechanochemical method by introducing attritor mill instead of conventional ball mill. The idea of using attritor mill is to provide higher grinding energy than conventional milling and investigation will be conducted mainly on the phase purity as well as the particle size of forsterite. Above

that, mechanical properties and morphology of the synthesized forsterite bulk will be evaluated as well.

b) To investigate the effect of doping ZnO into forsterite powder on the mechanical properties that includes densification, microhardness and fracture toughness as well as the morphology of forsterite bioceramic. Sintering will be conducted on the bulk samples ranging from 1200 – 1500 ^{o}C with a ramping rate of 10 ^{o}C/min for 2 h.

c) To compare the phase stability, mechanical properties and morphology of conventional and microwave sintered bulk forsterite samples. A short and preliminary study will be conducted on the effect of microwave sintering on the forsterite samples with sintering temperature of 1100 – 1250 ^{o}C and a ramping rate of 50 ^{o}C/min for 30 min. The as-compared results will be used as the benchmark of the upcoming future work in the application of microwave sintering on forsterite.

1.4 Structure of the Thesis

In Chapter 2, a brief overview on the effects of different powder processing methods on the properties of forsterite powder is presented. Parameters including types of starting precursors, duration of milling and heat treatment profiles are discussed and compared based on the phase stability and powder particle size.

Chapter 3 will discuss on the sinterability of forsterite ceramic under various sintering methods such as conventional sintering, two step sintering and microwave sintering. These discussions will involve a comparative study between different sintering methods with regards to the mechanical properties of forsterite as well as particle size. Also, the effect of sintering additives on bioceramics was presented to highlight the important parameters that require attention with regards to doping on forsterite.

The description on the synthesis method used in manufacturing the forsterite powders as well as the sintering methods are presented in Chapter 4. The characterization methods are also discussed in this chapter.

Results and discussions are presented in Chapter 5. A thorough discussion on the effects of different milling methods and duration are laid out in this chapter, i.e. forsterite powder prepared via ball and attrition milling are compared in terms of phase stability, particle size and specific surface area. Based on the results obtained, further work is carried out by selecting for the best milling methods employed based on the sintering behavior and mechanical properties upon sintering. The effect of ZnO as sintering additives on the properties of forsterite upon sintering at 1200 ^{o}C to 1500 ^{o}C are presented and based on the results, microwave sintering is employed as well on the undoped and doped samples to do a comparative study between these two sintering methods.

Lastly, Chapter 6 will conclude the entire work based on the findings obtained and provide suggestions for future work. The appendices contain various experimental details and machinery specifications as well as research publications.

CHAPTER 2: POWDER PROCESSING METHOD OF FORSTERITE

2.1 Introduction to biomaterials

Since half a century ago, biomaterial was extensively studied under medicine, biology, tissue engineering, materials science and chemistry field (Amogh et al., 2010). A biomaterial is essentially a material that is used and adapted for medical applications such as surgery and drug delivery and generally, biomaterial can be defined as (Cao & Hench, 1996):

i. Performance of implant material that is equivalent with the host tissue.
ii. The tissue at the interface should be equivalent to the normal host tissue and the response of the material to physical stimuli should be like that of the tissue it replaces.

Also, according to United States National Institute of Health (NIH), a biomaterial is defined as:

> "any substance (other than a drug) or a combination or substances, synthetic or natural in origin, which can be used for any period of time, as a whole or a part of a system which treats, augments, or replaces any tissue, organ, or function of the body" (National Institute of Health, 1982, p. 1).

Another researcher defined biomaterials as "a non-drug substance suitable for inclusion in system which augment or replace the function of bodily tissue or organ" (Jayaswal et al., 2010). Recently, a more sophisticated definition of biomaterial was defined by William, 2009. The researcher defined it as:

> "a substance that has been engineered to take a form which, alone or as part of a complex system, is used to direct, by control of interactions with components of

living system, the course of any therapeutic or diagnostic procedure, in human or veterinary medicine" (William, 2009, p. 5908).

Based on the definitions given by various researchers, biomaterials can be considered as synthetic or natural materials, used in the making of implants to replace the lost or diseased biological structure and restoring the form and functionality without causing negative side effect. Example of parts of the human body that uses biomaterials for implantation are artificial valves for heart, stents in blood vessels, replacement for shoulders, hips, knees, ears, elbows, cardiovascular and orodental structures (Ramakrishna et al., 2001; Wise, 2000; Park & Bronzino, 2003; Chevalier & Gremillard, 2009; Schopka, 2010).

2.1.1 Types of biomaterials

Owing to the various applications contributed by biomaterials, the selection and design of biomaterials depend highly on the intention of the application. There are five types of biomaterial which are composites, metals and alloys, polymers, biological materials and ceramics. With unique abilities for each of these biomaterials, various applications were discovered owing to their unique capabilities, thus, improving our everyday life (Llyod & Cross, 2002). Table 2.1 shows the usage of different types of biomaterials

Table 2.1: Types and Uses of Current Biomaterials (Llyod & Cross, 2002; Dorozhkin, 2010; Straley et al., 2010; Sionkowska, 2011).

Biomaterials	Typical uses	Advantages
Polymers	Catheters, sutures, heart valves, lenses, spinal cord	Tailorable properties, cheap
Composites	Dental and orthopaedic components	Strength and weight
Metals/alloys	Joint replacements	Strength and ductility
Ceramics	Structural implants, alleviates pain	Wear resistant
Biologic materials	Soft tissue augmentation, vascular grafts, collagen replacement	Complex function

2.1.2 Classification and requirement of bioceramics

Two of the most important requirements of a bioceramic for bone reconstruction are the mechanical properties and biocompatibility (Geetha, et al., 2009; O'Brien, 2011).

Depending on the application such as hip transplant and dental implant, the type of material used will be different and it is determined based on the mechanical properties. Hardness, fracture toughness, elongation, tensile strength and modulus are few of the important properties of the material that will determine the reliability of the implants (Geetha et al., 2009). For example, owing to a very high hardness and density, zirconia was chosen for hip joint femoral heads implant instead of other bioceramics (Jayaswal et al, 2010). However, if zirconia bioceramic was implanted on a bone that requires minimal stiffness, the stress will be diverted from the adjacent bone causing bone resorption surrounding the implant and led to implant loosening. On the other hand, if the fracture toughness of the implant is lower than the requirement, cracking will occur and can be referred as biomechanical incompatibility. The term stress shielding effect was introduced when the biomechanical incompatibility causes fatality on the bone cells (Geetha et al., 2009; Monaco et al., 2013). During the production of scaffolds, the mechanical properties need to be consistent with the implantation site to ensure proper surgical handling during the implantation. However, certain amount of porosity was also needed to allow cell penetration and vascularization (O'Brien, 2011). It was generally known that porosity will cause deterioration in the mechanical properties of the material. Thus, a balance between the mechanical properties and the porosities are required to ensure the successfulness of the implant.

Biocompatibility can be defined as "the ability of a material to perform with an appropriate response in a specific application" (Lemons, 1996). So, the materials are expected to not cause inflammatory or allergic reactions and must be non-toxic to the

human body. Upon implantation, the cells must be able to adhere, operate as usual and move onto the surface of the implant and proliferate on the surface to form new matrix (O'Brien, 2011). The successfulness of an implant is controlled by the reaction of the human body's response. The degradation and host response due to the material in human body are the two main criteria that influence the biocompatibility of a material which give rise to the three major classifications of bioceramics which are bioactive, bioresorbable and bioinert (Geetha et al., 2009; Jayaswal *et al.*, 2010 Best et al., 2008).

2.1.2.1 Bioactive

According to Cao & Hench (1996), bioactive material was defined as "a biological material that elicits a specific biological response at the interface of the material which results in the formation of a bond between the tissues and the material". Mineral layers of biological apatite between the material and bone produced from the dissolution of bioactive material would enhance the natural bonding between the implant and the bone to create an environmentally compatible bonding with osteogenesis (bone growth) and provide good stabilization (Cao & Hench, 1996; Dorozhkin, 2010). Although HA and bioglass are both bioactive material, the bonding mechanism between these materials differ (Cao & Hench, 1996).

2.1.2.2 Bioresorbable

Bioresorbable material has the ability to dissolve in human body environment to allow new tissues to form and grow on any surface abnormalities but may not be interfacing directly with the material (Dorozhkin, 2010). Generally, this type of material degrades over time and will be replaced by endogenous tissue which then becomes a normal, functional bone (Binyamin et al., 2006). Scaffolds will usually use bioresorbable materials as a mean to fill spaces and allowing the tissues to infiltrate and substitute with the scaffold itself thus repairing the irregularities of the body part

(Dorozhkin, 2010). Few examples of bioresorbable bioceramics are hydroxyapatite (when sintered at low temperature), calcium phosphate and calcium sulfate dihydrate (Binyamin et al., 2006; Dee et al., 2003).

Similarly to calcium phosphate, HA is also more stable than calcium phosphate especially when the surrounding pH dropped to 5.5 whereby in the case of calcium phosphate, dissolution will occur and reprecipitate (Jayaswal et al., 2010). Further, Ruys et al. (1995) and Katti (2004) reported that HA has good osteogenesis ability by controlling its stability in terms of chemical composition under *in vivo* condition and also calcium phosphate was undesirable owing to its low mechanical strength, particularly fracture toughness.

2.1.2.3 Bioinert

Best (2009), defined bioinert material as a material with "a minimal level of response from the host tissue in which the implant becomes covered in a thin fibrous layer which is non-adherent". This material possesses biocompatibility while maintaining the mechanical and physical properties upon implantation. Instead of reacting with the host tissue, bioinert material lack biological response but it is nontoxic. Hence, bioinert materials are commonly used for supporting role in orthopaedics field owing to its decent wear properties and useful slithering functions (Binyamin, et al., 2006).

Alumina was categorized as bioinert materials that has good wear properties and was widely used for joint replacement implant (Jayaswal et al., 2010; Katti, 2004). Alumina can be easily produced with high surface finish which is beneficial to its surface properties (Jayaswal et al., 2010; Binyamin et al., 2006). Nevertheless, the application of alumina as hip implant was negated due to the loosening of joint between the implant and the hip joint which eventually leads to irritation to the patient (Suchanek & Yoshimura, 1998). One of the drawback of alumina as an implant falls on its high

rigidity which is not compatible for hip joint replacement as Bizot & Sedel (2001) claimed that the shock absorbance of alumina was reduced especially during a sudden fall by the patient.

Zirconia, another material that has bioinert properties is widely used in ball heads for total hip implantation (Katti, 2004). Comparing with alumina, partially stabilized zirconia has better flexural strength, fracture toughness and low Young's modulus and owing to its high scratch and corrosion resistance compared to metal, zirconia ceramic was commonly used for orthopaedics implant (Clarke et al., 2003; Aboushelib et al., 2008; Jayaswal et al., 2010). Also, zirconia was widely used in dental implant owing to the mechanical properties and the aesthetic color similar to tooth (Piconi & Maccauro, 1999). Table 2.2 shows the classification of bioceramic and the responses it gives to the human body.

Table 2.2: Classification of bioceramic and its response (Cao & Hench, 1996; Wang, 2003; Jayaswal et al., 2010; Geetha et al., 2009; Dee et al., 2003).

Classification of Bioceramic	Response	Example of bioceramic
Bioactive	Bony tissue formation around the implant material and integrating strongly with the surface of implant	Bioglass/glass ceramic, hydroxyapatite (at high sintering temperature)
Bioresorbable	Replaced by the autologous tissue	Calcium phosphate, hydroxyapatite (at low sintering temperature)
Bioinert	Formation of fibrous tissue layer and the layer does not allow adherence to the implant surface.	Alumina, zirconia, carbon

2.2 Biocompatibility study of forsterite ceramic

Silicon plays an important role in bone and osteoblast growth as well as during early bone calcification (Carlisle, 1988). Schwarz (1972) demonstrated that silicon deficient rats experienced skeletal deformations and when the amount of silicon increased, the growth rate of the rats improved. In general, magnesium is important to human metabolism and it can be found in bone tissues (Vorman, 2003; Wolf and Cittadini, 2003). Additionally, magnesium also contributes in bone mineralization and indirectly affecting the mineral metabolism positively (LeGeros, 1991; Althoff et al., 1982; Chou et al., 2014). Magnesium also affects the insulin secretion to regulate the bone growth (Pietak et al., 2007; Liu et al., 1988). Thus, owing to the chemical composition of forsterite, researchers had recently begun investigating on the mechanical capability of forsterite to substitute HA in future.

In the field of biomedical, forsterite was introduced as early as the 1990's as many researchers were still investigating for a new potential biomaterial in orthopaedics. With recent studies done on forsterite for biomedical application, forsterite has gained many interests from researchers i.e. from synthesizing of forsterite to enhancing the mechanical properties and towards the fabrication of scaffolds using forsterite. In the 2000's, Ni et al. (2007) had successfully proven that forsterite possessed good biocompatibility and better mechanical properties than HA which then caught the attention of other researchers on the potential of forsterite as the next candidate for biomedical application. A thorough research was conducted on the viability of forsterite for bone substitution by conducting bioactivity and biocompatibility examination. The experiment was conducted on rat calvarias osteoblast for 24 h and cell attachment was observed and began to spread throughout the surface of forsterite as seen in Figure 2.1. Then, MTT test was conducted and showed good development in cell proliferation relative to the incubation time as shown in Figure 2.2. It was found that the greater cell

viability as compared to glass is due to the rough and irregular surface topography. All in all, forsterite bioceramic is suitable for hard tissue repair owing to its good biocompatibility.

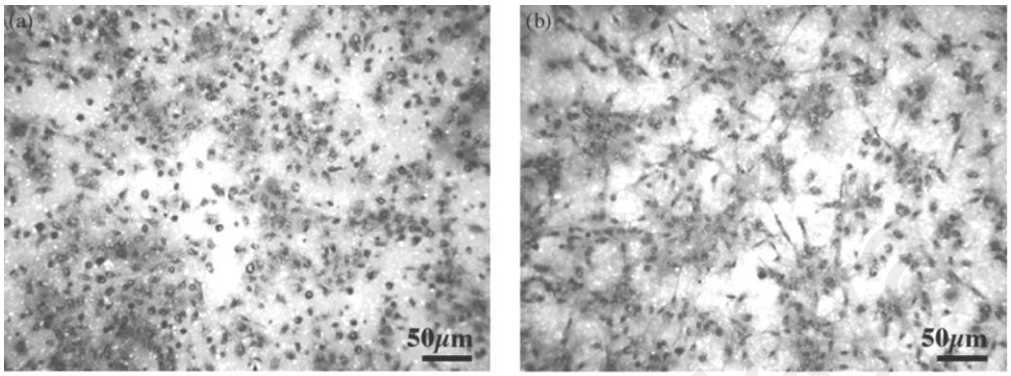

Figure 2.1: Phase-contrast microscopic images of rat calvaria osteoblasts cultured on forsterite discs for 4 h (a) and 24 h (b) after seeding (Ni et al., 2007).

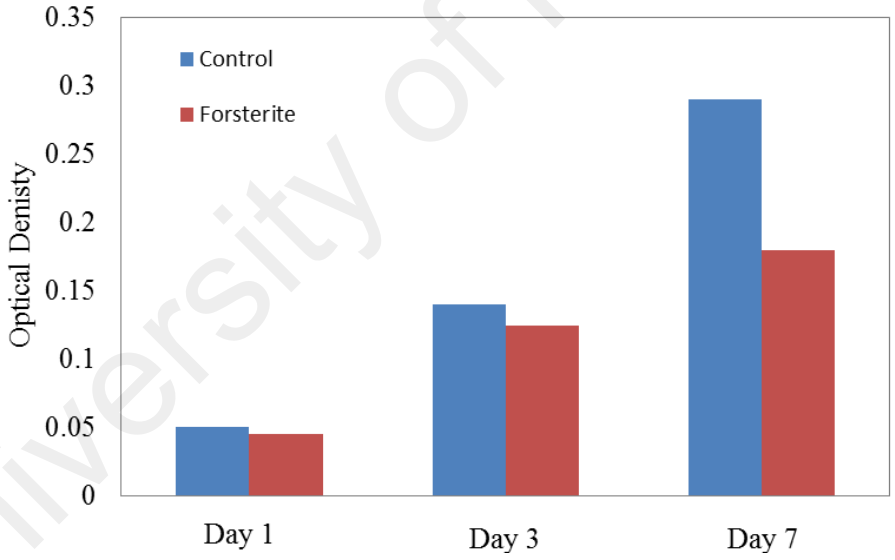

Figure 2.2: Proliferation of osteoblast cultivated on forsterite ceramics for 1, 3 and 7 days in comparison with the control (Ni et al., 2007).

Further, it was found by another researcher that the size of forsterite powder played an important role in enhancing the bioactivity. Micron size forsterite powder did not possessed good bioactivity responses. It possessed low degradation rate with apatite forming ability as reported by Ni et al. (2007). Nano-size forsterite powder increases the degradation rate of forsterite as well as enhancing the apatite forming ability. With high-

volume fraction of grain boundaries owing to the nanostructured forsterite powder, the osteoblast adhesion, proliferation and mineralization of forsterite were significantly improved (Catledge et al., 2002; Webster et al., 2001; Kharaziha & Fathi, 2010). Additionally, with the nanostructured technology of forsterite, researchers have the luxury and flexibility to design the surface and mechanical properties and grain size distribution of forsterite to match it with human bone (Gutwein & Webster, 2002). Hence, enhanced mechanical properties of forsterite were obtainable for nanostructured forsterite instead of micron size (Cottom & Mayo, 1996; Kharaziha & Fathi, 2010). The mechanical properties of forsterite are also comparable to that of human bone. Typical mechanical properties of human hard tissues are tabulated in Table 2.3 to show the comparison between the human hard tissues and forsterite.

Table 2.3: Mechanical properties of hard tissues and forsterite (Legros, 1993; Fathi & Kharaziha, 2009; Ni et al., 2007; Ghomi et al., 2011).

Mechanical Properties	Enamel	Bone	Forsterite
Density (g/cm^3)	2.9 – 3.0	1.5 – 2.2	3.271
Relative density (%)	-	-	82 – 92.5
Mechanical strength (MPa)			
• Compressive	250 – 400	140 – 300	-
• Bending	-	100 – 200	145 – 203
• Tensile	-	20 – 114	-
Young's modulus (GPa)	40 – 84	10 – 22	
Fracture toughness (MPa $m^{1/2}$)		2.2 – 4.6	2.4 – 4.3
Hardness (GPa)	3.4 – 3.7	0.4 – 0.7	9.4 – 11.02

2.3 Powder processing method of forsterite ceramic

There are various techniques introduced throughout the years in synthesizing forsterite powder with each technique possessing its own uniqueness and challenges.

The two most commonly used methods are solid-state reaction via mechanical activation with heat treatment and sol-gel route.

One of the main drawbacks of forsterite ceramic occurred during the synthesis stage in which forming pure forsterite powder is challenging. Secondary phases tend to appear during the synthesis of forsterite when the parameter for heat treatment profile, milling profile and amount of starting precursors are not optimized. Enstatite ($MgSiO_3$) and periclase (MgO) are the two commonly found secondary phases in the phase stability of forsterite upon synthesis (Hiraga, et al., 2010). Owing to its chemical similarities to forsterite, the synthesis stage requires high accuracy and sensitivity to ensure for a proper formation of forsterite which will be discussed further in later section.

Appearance of secondary phases led to many complications in the mechanical properties of forsterite. Due to the appearance of enstatite, it will dissociate in forsterite and formed SiO_2-rich liquid upon heated at 1557 ^oC which causes reduction in the mechanical properties of forsterite (Tavangarian et al., 2010; Tavangarian & Emadi, 2011). In regards with optical industry, huge size of impurities in forsterite cause significant light scattering and loss of visual clarity (Sun et al., 2009). Generally, formation of secondary phases is not preferred by majority of researchers although a few of them claimed that having enstatite in forsterite will enhance the crushing strength and density due to the formation of glassy matrix at 1500 ^oC (Mustafa et al., 2002). However, the formation of glassy phase will be detrimental to the fracture toughness of forsterite. Thus, depending on the types of mechanical properties needed to enhance, the formation of enstatite is subjective.

2.3.1 Solid-state reaction via mechanical activation

This method is also known as mechanochemical process (MCP) and was first demonstrated by McCormick (1995). This process involved the use of mechanical energy such as milling to activate the chemical reactions between the precursors and also causes structural changes such as particle refinement (McCormick, 1995). During milling process, balls will collide with powders thus deforming the particles and introducing fracture and refinement on the grain and particle size. Prolonged milling duration will induce more energy to the mixtures of powder causing dislocation on the structure and forming random nanostructure grains but if not controlled, contamination can occur from the milling ball. Generally, a short milling will only involve homogenizing the mixing between precursors whereas prolonging the duration of milling eventually leads to minor chemical reactions. Aside from the regular type of milling, high energy ball milling (HEBM) or attrition milling was introduced and gain major acceptance in the industrial work owing to its high energy shearing and collision of milling balls and precursors. The ability of HEBM to produce grain size in the order of 10^3-10^4 as well as particle refinement has definitely attracted researchers to implement this type of milling in hope to obtain nano-size particles and grains. Although HEBM could cause contamination on the precursors due to the shearing between milling balls, the high yield and simplistic procedure has gain the acceptance by researchers (Mukhopadhyay, & Basu, 2007).

Few of the parameters that are important during milling are the size, density, hardness and composition of ball mills or also known as milling media. Size of balls used is usually bigger than the pieces of material to be milled to obtain a finer size of the material. A denser ball should be used to ensure that the ball does not float on the top of the material. Also, a more durable ball is required to disallow wear of the tumbler and the ball itself during milling. Lastly, the composition of the ball should be

controlled to safeguard the final product from contamination by the milling media (Suryanarayana, 2009).

There are many combinations of starting precursors used by researchers to obtain pure forsterite. One of the well-known researchers in the field of forsterite bioceramic had tried several combinations of precursors including MgO or $MgCO_3$ mixed with SiO_2 or talc (Tavangarian & Emadi, 2009, 2010 & 2010a). A study was done on prolonged milling on the formation of single phase forsterite ceramic. Based on a study by Tavangarian & Emadi (2009), duration of 5 min until 100 hours were selected with a controlled heat treatment temperature of 1000 ^{o}C and held for 1 h. During the initial stage, milling at 5 min, 1 and 5 hours showed the presence of periclase. Upon milling for 10 hours, single phase forsterite was successfully obtained. No significant changes were observed on the phase purity and structural composition of samples upon milling up to 100 hours. Only the intensity of sample decreased as the milling duration increases with crystallite size ranging from 28-40 nm (Tavangarian & Emadi, 2009). It was also suggested by the researcher that the formation of forsterite via solid-state reaction was governed by the following reactions (Equations 2.1 and 2.2):

$$5MgCO_3 \rightarrow 5MgO + 5CO_2 \quad (2.1)$$

$$Mg_3Si_4O_{10}(OH)_2 + MgO \rightarrow 4MgSiO_3 + H_2O \quad (2.2)$$

Upon reaching 1000 ^{o}C of heat treatment, another reaction occurred between the products of the initial reaction and can be shown in equation 2.3:

$$4MgO + 4MgSiO_3 \rightarrow 4Mg_2SiO_4 \quad (2.3)$$

It was proposed by Brindley & Hayami (1965) that during the initial stage of reaction, MgO reacted with the surface of SiO_2 and form enstatite. With the formation

of enstatite, the excess MgO continued to react with the enstatite at 1000 ^{o}C and formed forsterite. Mechanical activation that was introduced on the starting precursors earlier before heat treatment had provided higher reacting phases thus increasing the kinetic reactions (Tavangarian & Emadi, 2009).

In another study, Tavangarian & Emadi (2010) compared the formation of forsterite between the precursors of MgO and $MgCO_3$ with talc. In general, $MgCO_3$ was used as one of the precursors owing to its ability to break down and liberating CO_2 gas to form micro pores that helped in decreasing grain size and increasing the contact surface of grains to allow quicker diffusion process of forsterite. Nonetheless, this researcher found that MgO, as precursor, was able to form phase pure forsterite at 5 hours of milling with 1000 ^{o}C of heat treatment temperature as shown in Figure 2.4. The mean crystallite size obtained for forsterite sample prepared using MgO and $MgCO_3$ were 60 nm and 40 nm, respectively, as shown in Figure 2.3.

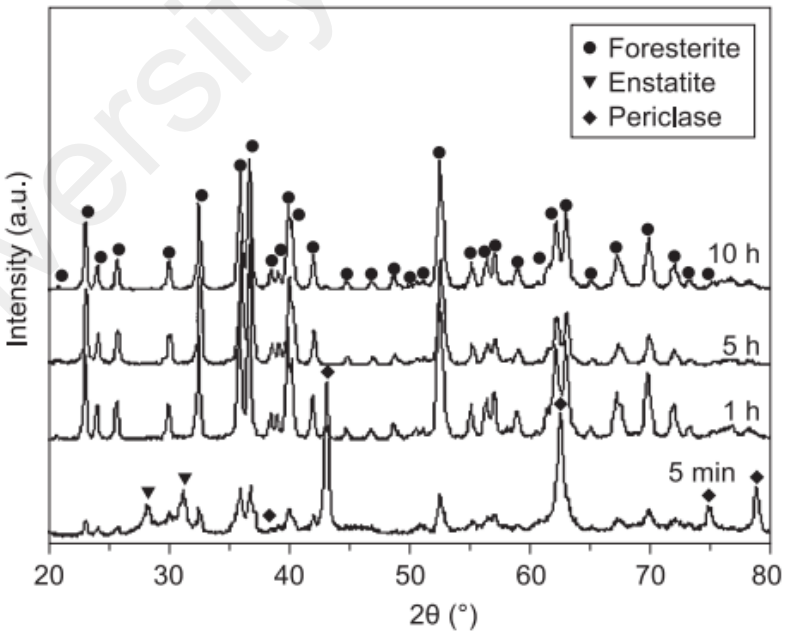

Figure 2.3: Phase purity of analysis of forsterite prepared using MgO and talc upon milling at various duration and heat treated at 1000 ^{o}C for 1 hour (Tavangarian & Emadi, 2010b).

All the works done by Tavangarian & Emadi (2009; 2010; 2010a; 2010b) were based on the use of planetary milling. The name of planetary milling comes from its planet-like movement of the vial. The vial and rotating disc rotates in opposite directions thus causing the milling balls to experience 'friction effect' (Suryanarayana, 2001). It operates under two relative motions which are planetary motion around the vial axis and rotary motion surrounding the mill axis (Balaz, 2008).

Cheng et al. (2012) had introduced another high energy ball milling process to produce forsterite using MgO and silica (SiO_2). Based on the study, 5 to 30 hours of milling was conducted followed by heat treatment at 850 ^oC for 3 hours. The phase purity result was represented in Figure 2.4. Forsterite peak was observed for the entire milling duration. Nonetheless, both SiO_2 and MgO peaks were observed as well for mixtures milled from 5 to 20 hours. The author proved that the milling duration played an important role in ensuring the formation of phase pure forsterite. The result obtained was supported by the particle size results obtained under various milling durations as shown in Figure 2.5. Increasing milling duration had led to the reduction in particle size thus producing phase pure forsterite powder (Cheng et al., 2012).

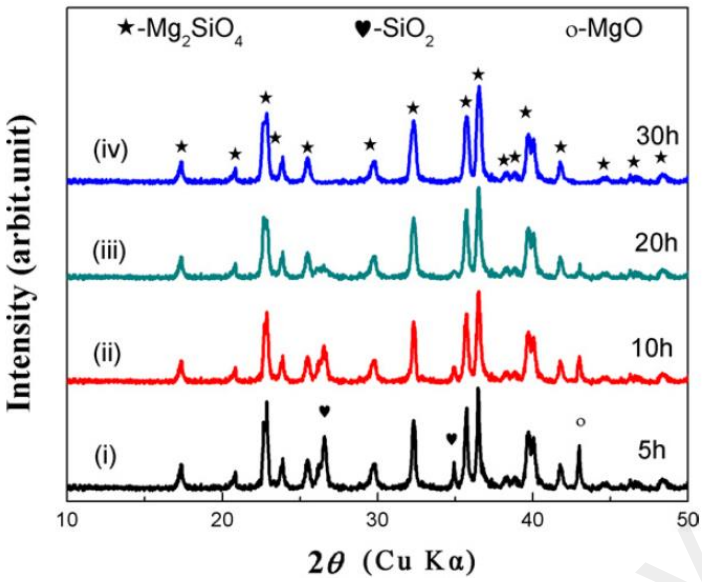

Figure 2.4: Phase purity of MgO-SiO_2 mixtures milled at various duration and heated at 850 ^{o}C for 3 hours (Cheng et al., 2012).

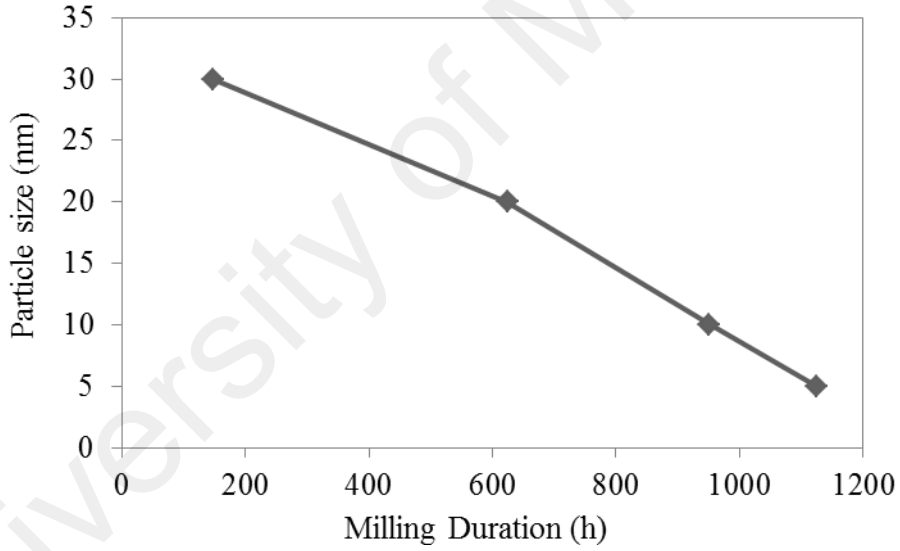

Figure 2.5: Average particle size as a function of milling duration (Cheng et al., 2012).

Aside from planetary milling, conventional ball mill is another milling method used in synthesizing forsterite. Ball mill operates through a simple process of only rotation of milling jar/drum filled with milling balls and precursors (Castro & Mitchell, 2002). During the rotation, there are three types of motions observed depending on the speed of the rotating drum. First type is the cascading motion in which the ball will move along the wall of the drum and rolled over at certain height on to other balls. Second type is

cataracting motion whereby the ball will fall from the top to the base of the drum without rolling over other balls. Lastly is the centrifugal motion that occurs when the centrifugal force is higher than the gravitational force causing the ball to stick on the wall of the drum throughout the milling process (Balaz, 2008). A simple diagram of all three types of motions is shown in Figure 2.6. According to Ramesh et al. (2013), forsterite was synthesized via ball mill between MgO and talc and found that the formation of MgO was unavoidable although sintered at 1500 ^{o}C. Based on the findings, it can be concluded that the types of milling significantly affecting the formation of single phase forsterite.

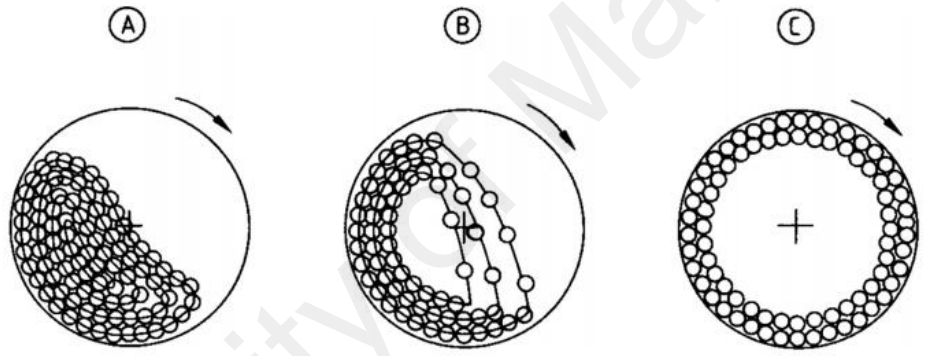

Figure 2.6: Types of motion in a ball mill: (A) cascading, (B) falling or cataracting, (C) centrifugal. (Bernotat & Schonert, 1998).

Another type of milling called attrition milling is similar to conventional ball mill except for the speed and rotating mechanism. It consists of a vertical jar/drum with an impeller inside which is positioned normal to the axis of the drum. During operation, the impeller rotates, energizing the milling balls causing impact between balls; ball and the wall; and the impeller and ball. Attrition milling is highly used in metal industry for the purpose of particle reduction. One of the benefits of attrition milling over ball mill is the capability to mill large amount of powder at the same time while exerting high grinding energy for powder size reduction (Castro & Mitchell, 2002). Hence, attrition milling

should be introduced in the synthesizing of forsterite via solid-state reaction to obtain finer particle and grain refinement.

2.3.2 Sol-gel method

Sol-gel method is another widely used method in synthesizing forsterite. Generally, sol-gel method involved processes such as hydrolysis, condensation, gelation, ageing, drying and densification which produce solid materials from small molecules. Sol is known as a stabilize suspension of colloidal solid particles in liquid surrounding whereas gel is a porous, continuous solid network that surrounds an unceasing liquid phase. The major advantage of using sol-gel method over other methods in producing forsterite is the ability to provide high degree of homogeneity and molecular-level mixing of precursors. This will then reduce the crystallization temperature of forsterite and preventing phase isolation from happening during annealing. However, sol-gel method is a very lengthy, sensitive and complicated method in which a proper control on the amount of silicon is needed because the rate of hydrolysis and condensation varies accordingly. With variation in the rate of hydrolysis and condensation, non-uniform precipitation and inhomogeneous chemical phase of gels will occur resulting in higher crystallization temperature and formation of undesired phases i.e. enstatite and periclase (Kosanovic et al., 2005; Petricevic et al., 1998; Maliavski et al., 1997; Yoldas, 1982; Livage et al., 1997; Hench, 1997; Saberi et al., 2007; Ni et al., 2007).

Forsterite can be synthesized via one phase and two phase sol. Based on Sanosh et al. (2010) research, pure forsterite was obtained by using magnesium nitrate hexahydrate ($Mg(NO_3)_2.6H_2O$) and tetra ethyl ortho-silicate (TEOS) as the precursors and calcined at 800 ^oC for 30 min whereas in another similar work done by Naghiu et al (2013), it was reported that periclase was observed in all samples heated at 800 ^oC to 1000 ^oC for 2 hours. For a two phase sol, $Mg(NO_3)_2.6H_2O$ and colloidal SiO_2 was used to synthesize

forsterite (Afonina et al., 2005). Saberi et al. (2009) has produced forsterite via polymer matrix and citrate nitrate methods by using $Mg(NO_3)_2.6H_2O$, citric acid, ammonia solution and SiO_2. Upon calcination at 860 ^oC for 1 hour, single phase forsterite was obtained. The collective results of some researchers using sol-gel method to produce pure forsterite are tabulated in Table 2.4.

Surfactant-assisted sol-gel route was introduced by Hassanzadeh-Tabrizi et al. (2016) via addition of cetyltrimethylammonium bromide (CTAB) as surfactant into the starting precursors of TEOS and $Mg(NO_3)_2.6H_2O$. The gel was heated at 400 ^oC to 900 ^oC for 3 hours in air with two different amounts of CTAB added (3 and 6 g). From Figure 2.7, phase pure forsterite was obtained upon heating at 700 ^oC with no significant effect by CTAB on forsterite phase formation. Nevertheless, the required temperature to formed phase pure forsterite powder is lower than that of solid-state method. This is due to the finer crystallite size of powder and molecular mixing of starting precursors. Further increasing the heating temperature would only decrease the broadening of the peaks but with higher peak intensities (Hassanzadeh-Tabrizi et al., 2016).

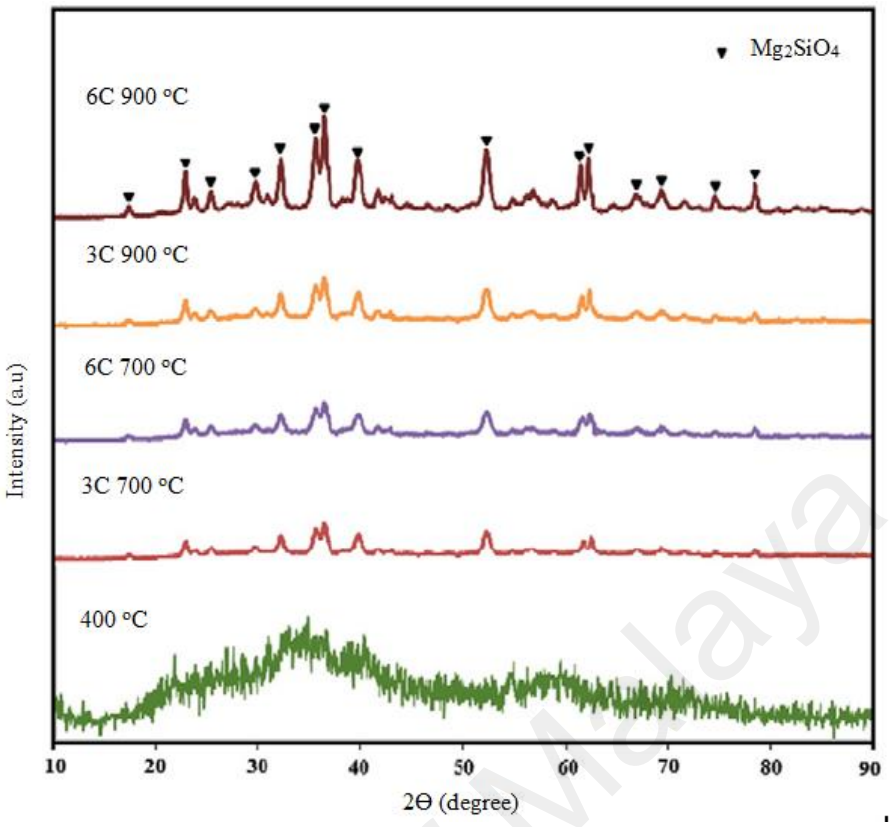

Figure 2.7: Phase purity result of forsterite powder heated at various temperatures for 3 hours in air (Hassanzadeh-Tabrizi et al., 2016).

Table 2.4: Formation of forsterite powder via sol-gel route with different starting precursors. All profiles successfully produced pure phase forsterite unless stated.

Starting Precursors	Heat Treatment Profile	Reference
$Mg(NO_3)_2.6H_2O$ and TEOS	800 ^oC held for 30 minutes	Sanosh et al. 2010
$Mg(NO_3)_2.6H_2O$ and colloidal SiO_2	800 ^oC held for 3 hours	Saberi et al., 2007
$Mg(NO_3)_2.6H_2O$ and colloidal SiO_2	1200 ^oC held for 3 hours	Ni et al., 2007
$Mg(NO_3)_2.6H_2O$, citric acid, ammonia solution and SiO_2	860 ^oC held for 1 hour	Saberi et al., 2009
$Mg(NO_3)_2.6H_2O$ and colloidal SiO_2	800 ^oC held for 2 hours	Kharaziha & Fathi, 2010
$Mg(OEt)_2$, 2-methoxyethanol and TEOS	400 ^oC-1200 ^oC held for 1 hour (not pure)	Mitchell et al., 1998
$Mg(NO_3)_2.6H_2O$ and TEOS	800 ^oC-1000 ^oC held for for 2 hours (not pure)	Naghiu et al., 2013

2.3.3 Other methods

Molten salt approach was introduced by Sun et al. (2009) in synthesizing forsterite. It was claimed by the researcher to be the simplest and most cost-effective method with overall shorter reaction time. By using $Mg(NO_3)_2.5H_2O$, SiO_2, sodium chloride (NaCl), $Ni(NO_3)_2.5H_2O$ and polyoxyethylene nonyt phenyl ether, a range of reactant ratio and annealing temperature were tabulated as shown in Table 2.5 and the phase purity result was obtained in Figure 2.8. According to the results, it was proven that the particle size can be tailored easily by varying the parameter of the annealing temperature and ratio of reactants (Sun et al., 2009).

Table 2.5: Reactant ratios and annealing temperature (Sun et al., 2009).

Sample	$Mg(NO_3)_2.5H_2O$ (mmol)	SiO_2 (mmol)	NaCl (mmol)	Anneal temp. (^oC)
S1	1	0.5	12.5	820
S2	1	0.5	25	820
S3	1	0.5	12.5	850
S4	1	0.5	12.5	900

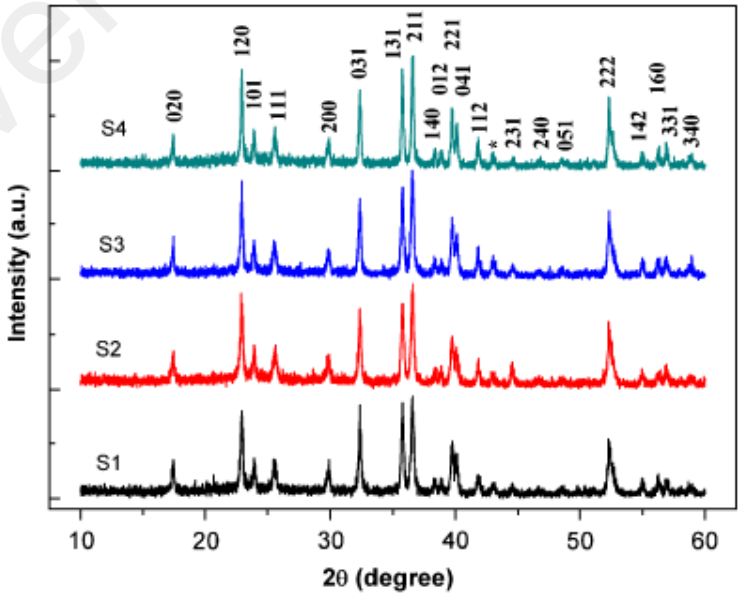

Figure 2.8: Phase purity of S1, S2, S3 and S4 samples. Weak peak represented by the asterisk defined the peak for MgO phase (45-0946) (Sun et al., 2009).

There is another method in synthesizing forsterite which is called aqueous route. This method is similar with sol-gel method. The starting precursors used was $Mg(NO_3)_2.6H_2O$ and TEOS. However, TEOS was directly hydrolyzed into $Mg(NO_3)_2.6H_2O$ and sprayed through a 0.5 mm nozzle with compressed air flowing in a parallel direction while heated to 200 ^oC. The collected powders were heated to 500 ^oC for 1 hour initially to decompose the nitrates completely and further heat treated to 1200 ^oC for an hour to obtain phase pure forsterite powder (Douy, 2002). The phase stability results were shown in Figure 2.9.

In comparison to evaporated precursors, both periclase (MgO) and enstatite ($MgSiO_3$) was observed after heated at 1400 ^oC and at the highest heating temperature, MgO was still observed in the result as shown in Figure 2.10. The incomplete reaction between MgO and $MgSiO_3$ was due to the lack of homogeneity between the precursors. Hence, the author proved the need for homogeneous mixing between the precursors by introducing spray-drying instead of using evaporation technique. The heating of sample stopped at 1540 ^oC was due to the melting point of $MgSiO_3$ (Douy, 2002).

Based on all the methods discussed, synthesizing pure forsterite powder requires high accuracy and optimization owing to the chemical similarities between the secondary phases with forsterite. Even though same precursors are used to synthesize forsterite, the outcome may differ depending on the heat treatment profiles, methods in conducting the experiment, and many others. Hence, extreme care should be taken as well as optimization during the synthesis of pure forsterite powder.

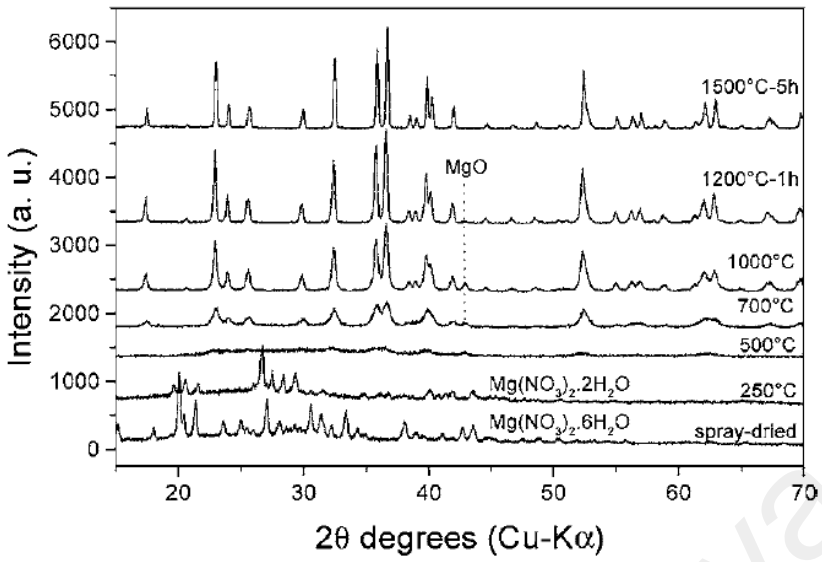

Figure 2.9: Phase stability results of the spray-dried precursors heated at various temperatures to form forsterite powder (Douy, 2002).

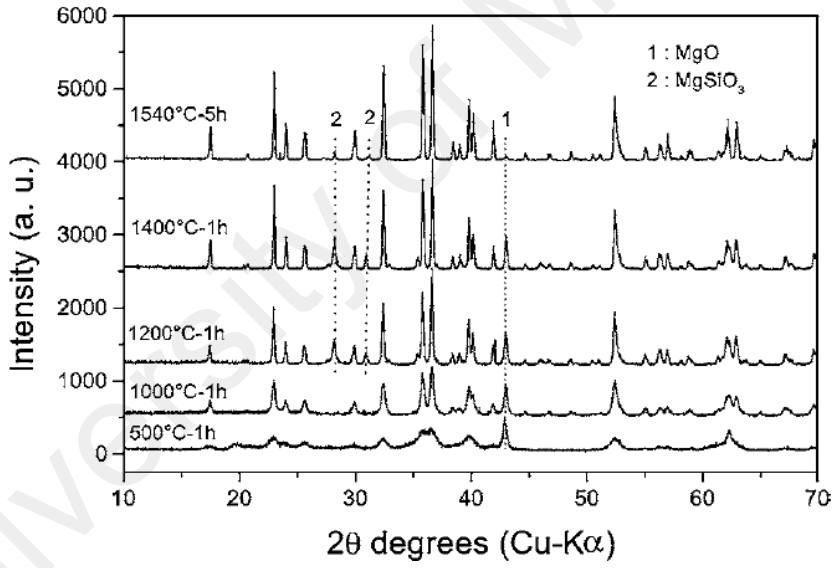

Figure 2.10: Phase stability results of the evaporated precursors heated at various temperatures to form forsterite powder (Douy, 2002).

In summary, forsterite was long proven by researchers for its good biocompatibility and applicability for clinical application. Also, there are various methods that were applied by researchers to produce forsterite powder. The vast choice of precursors, milling durations and heat treatment profiles had led to numerous different results obtained. Nevertheless, the main goal in powder processing is to produce phase pure forsterite powder which is achievable via many different methods.

CHAPTER 3: SINTERABILITY OF FORSTERITE CERAMIC

3.1 Introduction

Sintering is one of the most important processes in enhancing the mechanical properties of ceramics. It involved the densification of the solid via firing process typically to a temperature of 0.5 – 0.9 of the melting point. The driving force for sintering lies on the elimination of internal surface area namely pore and consequently increasing the density of solid. Typically, sintering can be divided into three different stages. Initial stage begins the moment when atomic mobility is obtained and through observation, necking is found between individual particles but with a low densification rate. Then, intermediate stage comes with higher curvatures of the initial stage. Densification rate is the highest at this point and usually only ~5 – 10% porosity is left. At the final stage, grain coarsening begins by breaking the channel-like pores into isolated and closed voids. Many obstacles were faced by researchers in removing the leftover pores from intermediate stage due to the excessive growth of grain entrapping the pores forming transgranular pores (Rahaman, 2003).

In order to obtain phase pure forsterite powder, heat is needed to transform the initial reactant into the final product upon preparation. Energy, in the form of heat, will be transferred to the reactant to react chemically into the required product according to equation 2.1 – 2.3 in subsection 2.3.1. There are many sintering methods introduced for past 20 years in enhancing the mechanical properties of ceramics. In the case of forsterite ceramic, only three types of sintering (conventional sintering, two step sintering and microwave sintering) were implemented for research. Up until now, there are no studies done using pressure-assisted sintering as well as thorough study of microwave sintering on forsterite. Hence, discussion on sinterability of forsterite will be grouped into conventional and non-conventional methods.

3.2 Conventional method

In conventional method, forsterite will be heated and/or sintered under atmospheric pressure with preset heating profile to provide energy either for chemical and/or mechanical purposes.

3.2.1 Heat treatment temperature and Mg/Si ratio

For forsterite, heat treatment was deemed necessary by Kosanovic et al (2005) as it provides energy to complete the reaction between the precursors. This claimed was supported by another researcher that produced forsterite via solid-state reaction method by using $MgCO_3$ and talc as the starting precursors. The researcher milled the mixture using planetary mill from 5 minutes to 100 hours without heat treatment to observe on the possibility for the formation of forsterite. It was found that upon milling up to 5 hours, the mixture transformed into an amorphous state with no sign of formation of forsterite observed (Tavangarian & Emadi, 2009).

Hence, the mixtures were then annealed at 1000 ^oC and 1200 ^oC for 1 hour to investigate on the formation of forsterite phase. The XRD traces are shown in Figure 3.1 and 3.2. Samples milled from 10 hours onward and annealed at 1000 ^oC showed pure forsterite phase. Prolonged milling did not show any significant effect on the structure and phase purity of forsterite. Further, for samples annealed at 1200 ^oC, pure forsterite was successfully obtained upon milling for 5 hours (Tavangarian & Emadi, 2009 & 2010a). The reappearance of $MgSiO_3$ was observed for samples milled at 80 and 100 hours. Since the enstatite phase at 1200 ^oC is meta-stable, forsterite was formed instead owing to its more negative free energy change than enstatite. Nonetheless, as the milling increases, faster kinetic was experienced by the mixture thus reforming the enstatite phase which was known to be stable up to 1600 ^oC (Tavangarian & Emadi, 2009; Kazakos, et al., 1990). It can be deduced that higher heat treatment temperature can

reduced the required milling duration but with a drawback of larger crystallite size which may detriment the mechanical properties of forsterite (Tavangarian & Emadi, 2009).

Figure 3.1: Phase purity result of forsterite powder milled at various durations and subsequently heated at 1000 ^{o}C for 1 hour (Tavangarian & Emadi, 2009).

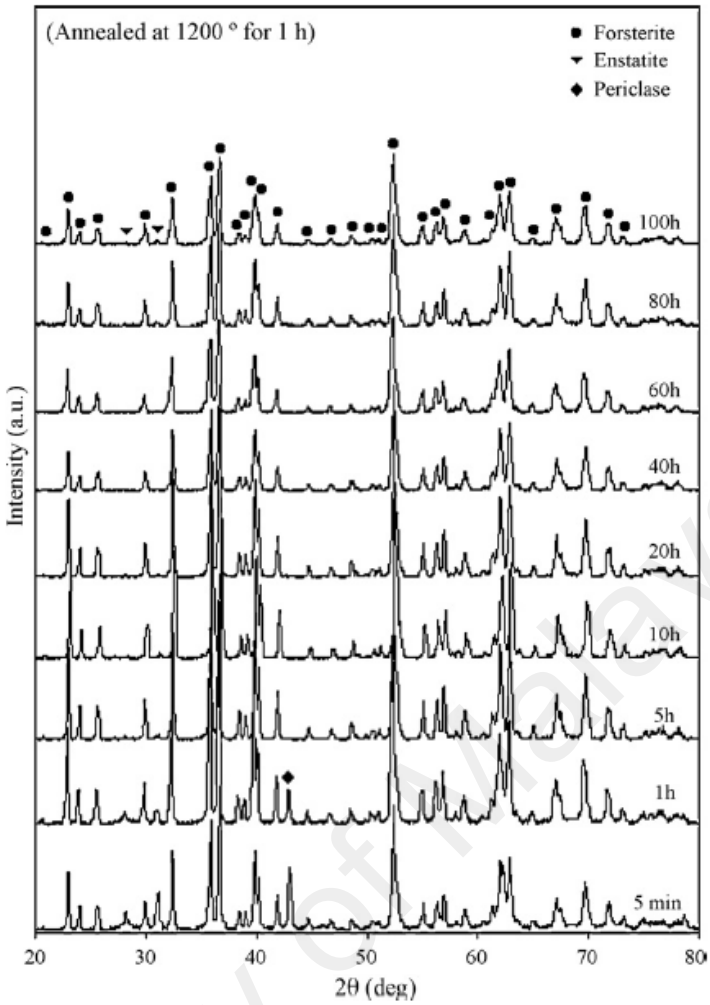

Figure 3.2: Phase purity result of forsterite powder milled at various durations and subsequently heated at 1200 ^{o}C for 1 hour (Tavangarian & Emadi, 2009).

In another work, the effect of heat treatment temperature was investigated by Tavangarian et al. (2010). Figure 3.3 and 3.4 showed the phase purity results of forsterite powder milled for 5 and 10 hours and heated at various temperatures for 10 min, respectively. The forsterite synthesis was based on solid-state reaction using $MgCO_3$ and talc as the starting precursors. As observed from the results, 5 hours of milling still showed the presence of secondary phases although it had been heated to 1400 ^{o}C. It was concluded by the researcher that the MgO and $MgSiO_3$ were unable to react completely in forming Mg_2SiO_4 due to insufficient reaction kinetics. Hence, by increasing the milling duration to 10 hours, upon heating, phase pure forsterite was successfully obtained. Also, prior to heating, an amorphous structure was observed on

the sample. Finer particles and partially decomposed $MgCO_3$ was deduced by the researcher which then led to the formation of amorphous structure. The prolonged milling had increases the reacting phases of sample and ease the formation of forsterite upon heating (Tavangarian et al., 2010). The inability to identify the presence of MgO and $MgSiO_3$ before heating could be attributed by the amorphous state of these phases (Kostic et al., 1997). Further heating was done to investigate for decomposition of forsterite. At 1400 ^oC, no phase changes were observed on the result (Figure 3.4) but there was an increase in the intensity due to the recovery of internal strain and growth of crystallite size from 30 nm to 78 nm. Hence, a lower crystallite size is preferable to produce good mechanical properties forsterite.

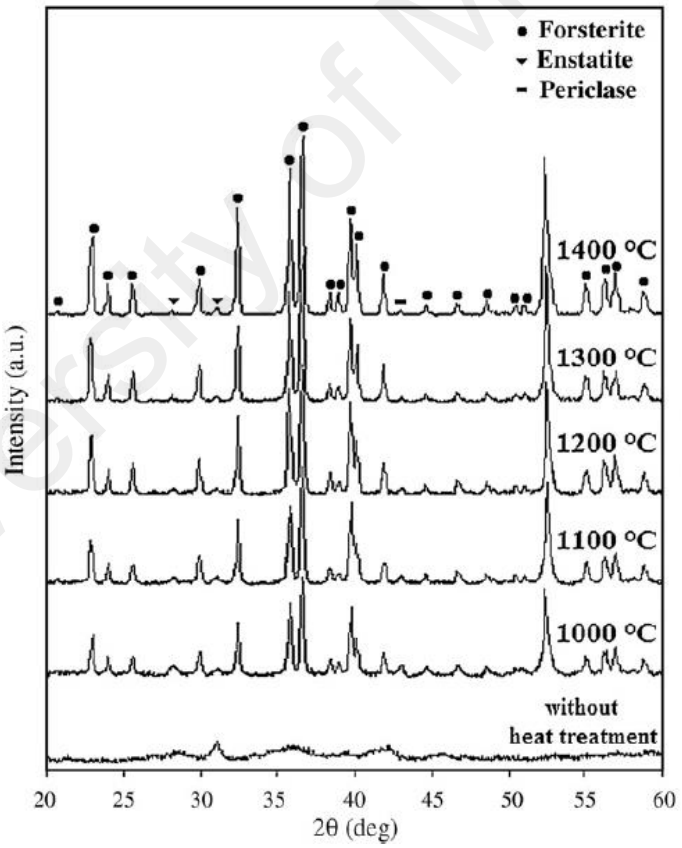

Figure 3.3: Phase purity of powder milled for 5 hours and annealed for 10 minutes at corresponding temperatures (Tavangarian et al., 2010).

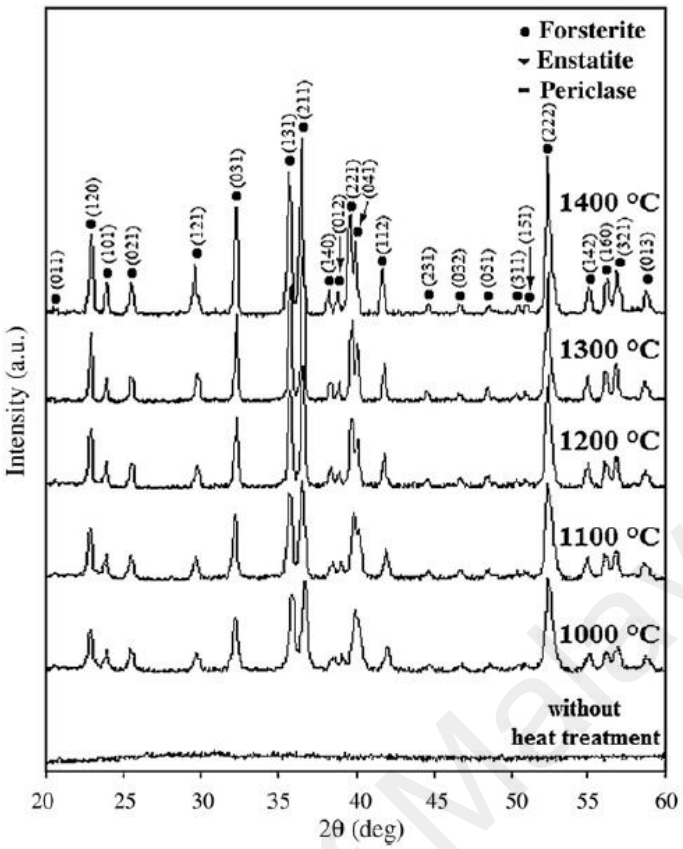

Figure 3.4: Phase purity of powder milled for 10 hours and annealed for 10 minutes at corresponding temperatures (Tavangarian et al., 2010).

Cheng et al. (2012) had also synthesized forsterite via solid-state reaction by using planetary mill. Based on Figure 3.5, the mixture of precursors was milled for 30 hours and heated from 600 ^{o}C to 950 ^{o}C for 3 hours. No sign of forsterite peak was observed for the unheated powder. Heating at 600 ^{o}C had made the forsterite peak to be more prominent but with the presence of secondary phases. As the temperature increases to 850 ^{o}C, the entire secondary phases' peaks were removed and phase pure forsterite was obtained. However, increasing further the heating temperature led to the decomposition of forsterite into MgO and $MgSiO_3$. This could be attributed by the reaction of MgO and $MgSiO_3$ being a reversible process.

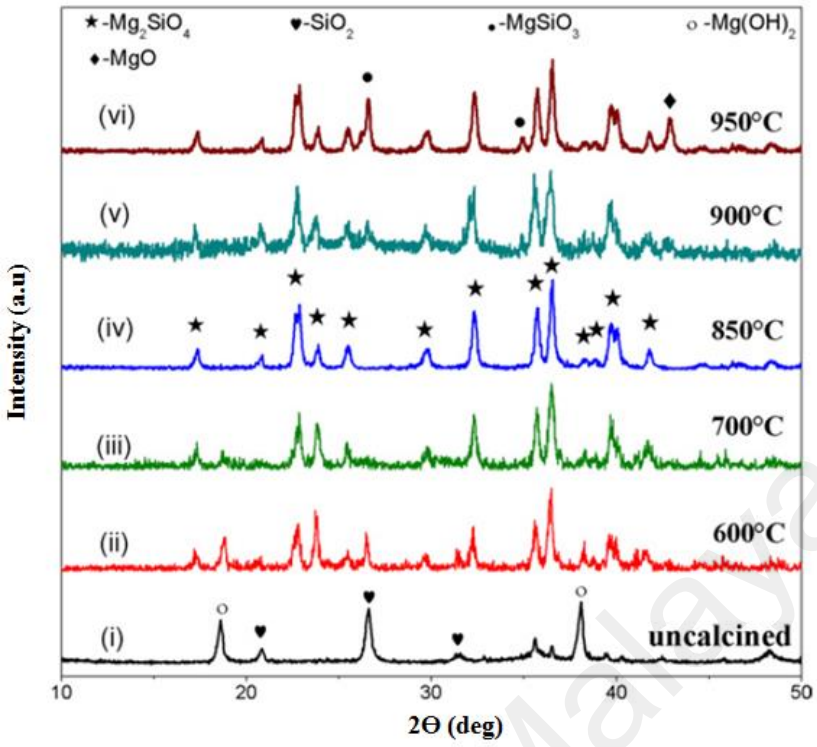

Figure 3.5: Phase purity of MgO-SiO_2 mixtures milled for 30 hours and heated at various temperatures for 3 hours (Cheng, et al., 2012).

In another recent work, heat treatment temperature and Mg/Si ratio were investigated. Initially, Mg/Si ratio was preset to 2 and the sample was heated from 1200 ^oC to 1350 ^oC for 3 hours upon milling for 6 hours. Figure 3.6 showed the phase stability result of the samples. It was observed that all samples contained secondary phases of both $MgSiO_3$ and SiO_2. The author concluded that the starting precursors had reacted with each other but there was still an excess in SiO_2 and insufficient MgO to react completely with both SiO_2 and $MgSiO_3$ to form forsterite. Hence, the work was further investigated by increasing the ratio of Mg/Si up to 2.1 as shown in Figure 3.7. With the increase in the ratio, the peak for SiO_2 and $MgSiO_3$ had significantly decreased owing to the reaction with MgO to form forsterite. The ideal ratio of Mg/Si was found to be 2.075 by the author (Shi et al., 2012).

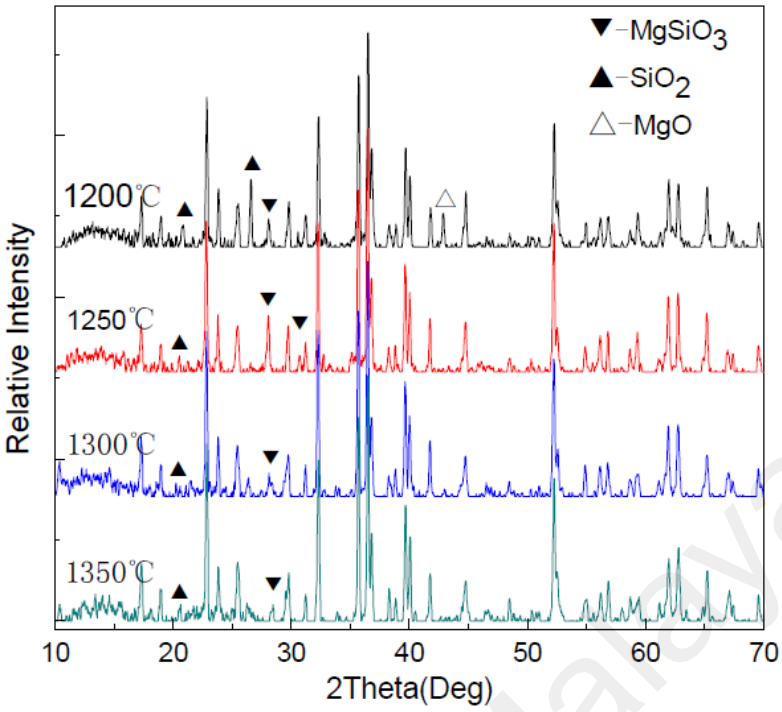

Figure 3.6: Phase purity of forsterite powders heated at various temperatures for 3 hours in air with Mg/Si ratio of 2 (Shi et al., 2012).

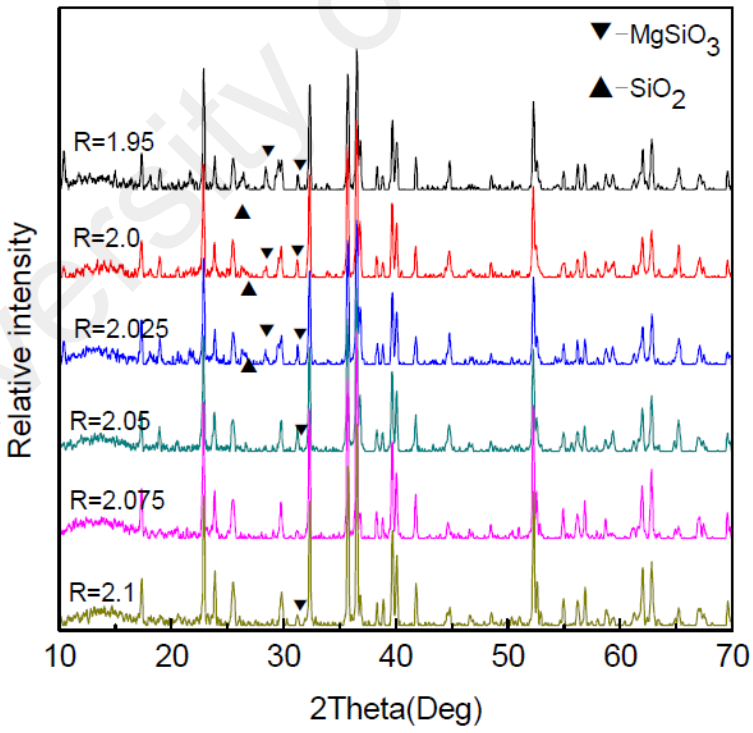

Figure 3.7: Phase purity result of forsterite powders heated at 1350 ^{o}C for 3 hours in air with various ratio of Mg/Si (Shi et al., 2012).

3.2.2 Sintering temperature and dwell time

Sintering process plays an important role in enhancing the mechanical properties of forsterite. At this stage, densification took place followed by the overall increase in mechanical properties. However, without proper control of the sintering profile, it may deter or even weaken the mechanical properties of forsterite. Sintering profile can be divided into three important criteria which are sintering temperature, holding time and heating rate. In general, forsterite was conventionally sintered in a box furnace under atmospheric air by most researchers. For sintering study, Ni et al. (2007) had synthesized forsterite via sol-gel route with TEOS and $Mg(NO_3)_2.6H_2O$ as the starting precursors. Upon obtaining phase pure forsterite, the powders were uniaxially pressed into a disc shape and sintered at 1450 ^oC and 1550 ^oC for 8 hours. Based on the phase purity results, no change on the phase composition was observed as shown in Figure 3.8. From the scanning electron microscope (SEM) image (Figure 3.9), irregular pores and grain size were observed indicating that the sintered forsterite was unable to form a dense body.

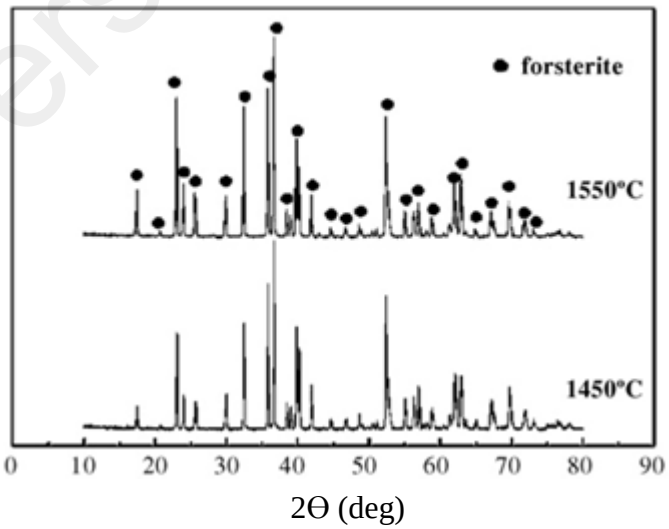

Figure 3.8: Phase purity result of forsterite bulk sintered at 1450 ^oC and 1550 ^oC for 8 hours (Ni et al., 2007).

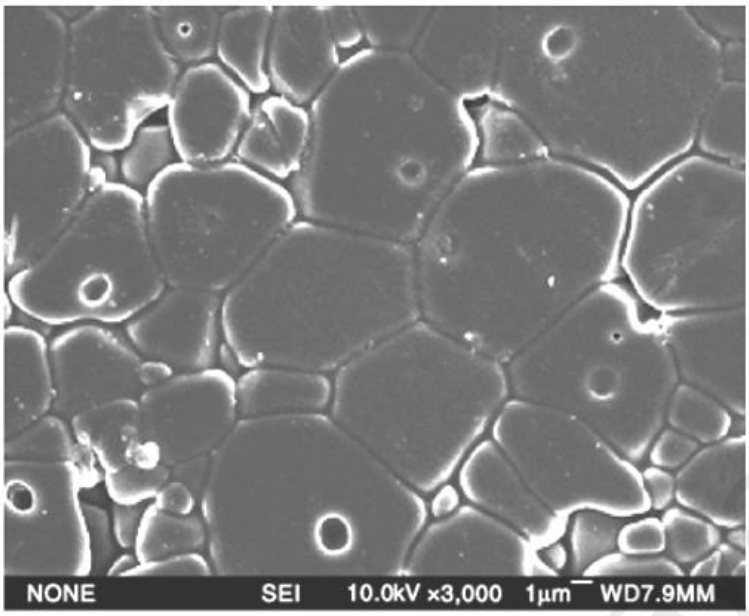

Figure 3.9: SEM micrograph of forsterite bulk sintered at 1450 ^{o}C for 8 hours (Ni et al., 2007).

Hence, the densification and fracture toughness of forsterite was evaluated under various sintering temperature and holding time in Table 3.1 and 3.2, respectively. By varying the sintering temperature, heating at 1450 ^{o}C for 6 hours showed the best mechanical properties out of the other two temperatures (1350 and 1550 ^{o}C) with a value of 2.3 MPa $m^{1/2}$ and 181 MPa for fracture toughness and bending strength, respectively, under equal holding time. However, highest densification was obtained at 1550 ^{o}C with a value of 91.4%. The rapid increase in mechanical properties of forsterite was attributed by the high sintering temperature. However, upon increasing the temperature to 1550 ^{o}C, excessive grain coarsening and flaw structure caused the mechanical properties to deteriorate as shown in the fractography of forsterite (Figure 3.10). It was observed that for forsterite sintered at 1450 ^{o}C, the pores consisted of sharped edges that appeared between grains whereas forsterite sintered at 1550 ^{o}C showed pores that were trapped in grains due to grain growth. Grain growth is an anomaly that usually occurs when the material is heated at a very high temperature and the grain began to grow very fast causing the pores to be entrapped between them

instead of being removed. Upon deciding the best sintering temperature, Ni et al. (2007) proceeded by varying the holding time of the sintering process to 3, 5 and 8 hours while sintering forsterite bulk at 1450 ^{o}C. The best result was obtained when sintered for 8 hours (Ni et al., 2007). All the mechanical properties examined showed an increasing trend up until the highest holding time.

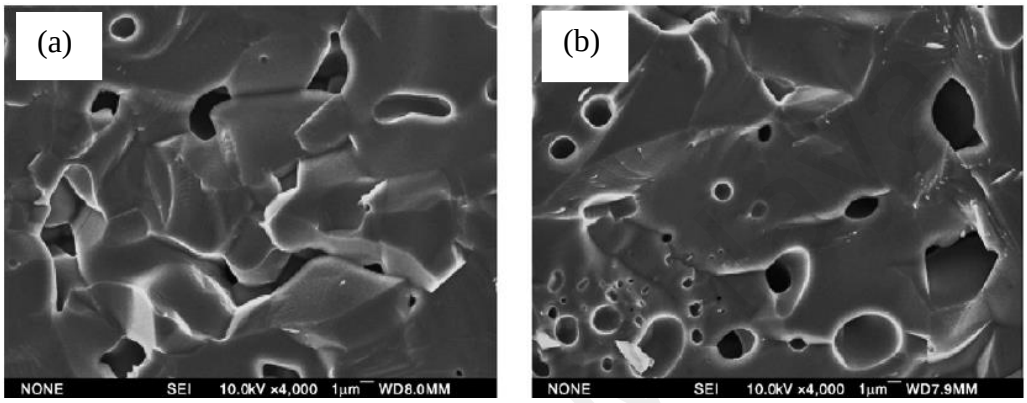

Figure 3.10: SEM of the fracture surface of forsterite upon sintering at a) 1450 ^{o}C and b) 1550 ^{o}C (Ni et al., 2007).

Table 3.1: Mechanical properties of sintered forsterite bulk at different temperature for 6 hours (Ni et al., 2007).

Sintering Temp. (^{o}C)	Relative Density (%)	Shrinkage (%)	Bending Strength (MPa)	Fracture toughness (MPa m$^{1/2}$)
1350	82.6	7.0	150	1.8
1450	87.7	9.0	181	2.3
1550	91.4	10.1	145	1.6

Table 3.2: Mechanical properties of sintered forsterite bulk at 1450 ^{o}C at different holding time (Ni et al., 2007).

Holding Time (hours)	Relative Density (%)	Shrinkage (%)	Bending Strength (MPa)	Fracture toughness (MPa m$^{1/2}$)
3	86.6	8.2	152	2.1
6	87.7	9.0	181	2.3
8	92.5	9.2	203	2.4

In another work, Ramesh et al. (2013) had produced forsterite bulk via solid-state reaction using MgO and talc as the starting precursors. Sintering temperature ranging from 1200 ^{o}C until 1500 ^{o}C, held for 2 hours with ramping rate of 10 ^{o}C/min was investigated and comparisons were done between the heat treated and non-heat treated forsterite powders.

Figure 3.11 and 3.12 showed and the evaluation of mechanical properties of forsterite and the phase stability result of forsterite sintered at various temperatures, respectively. The non-heat treated samples showed superior densification compared to heat treated samples with a maximum value of 74.4% and 90.7%, respectively. In general, all mechanical properties of forsterite samples were enhanced as the sintering temperature increased. However, considering the decomposition of forsterite at high temperature, higher sintering temperature than 1500 ^{o}C was not advisable as enstatite has melting point of 1557 ^{o}C. The author had reported that owing to the migration of MgO to the surface of forsterite from the heat treatment, grain growth was suppressed but densification was thwarted. Thus, non-heat treated samples experienced a drastic increase in grain size upon heated at 1500 ^{o}C with high hardness and fracture toughness due to the high relative density and low concentration of MgO (Ramesh et al., 2013).

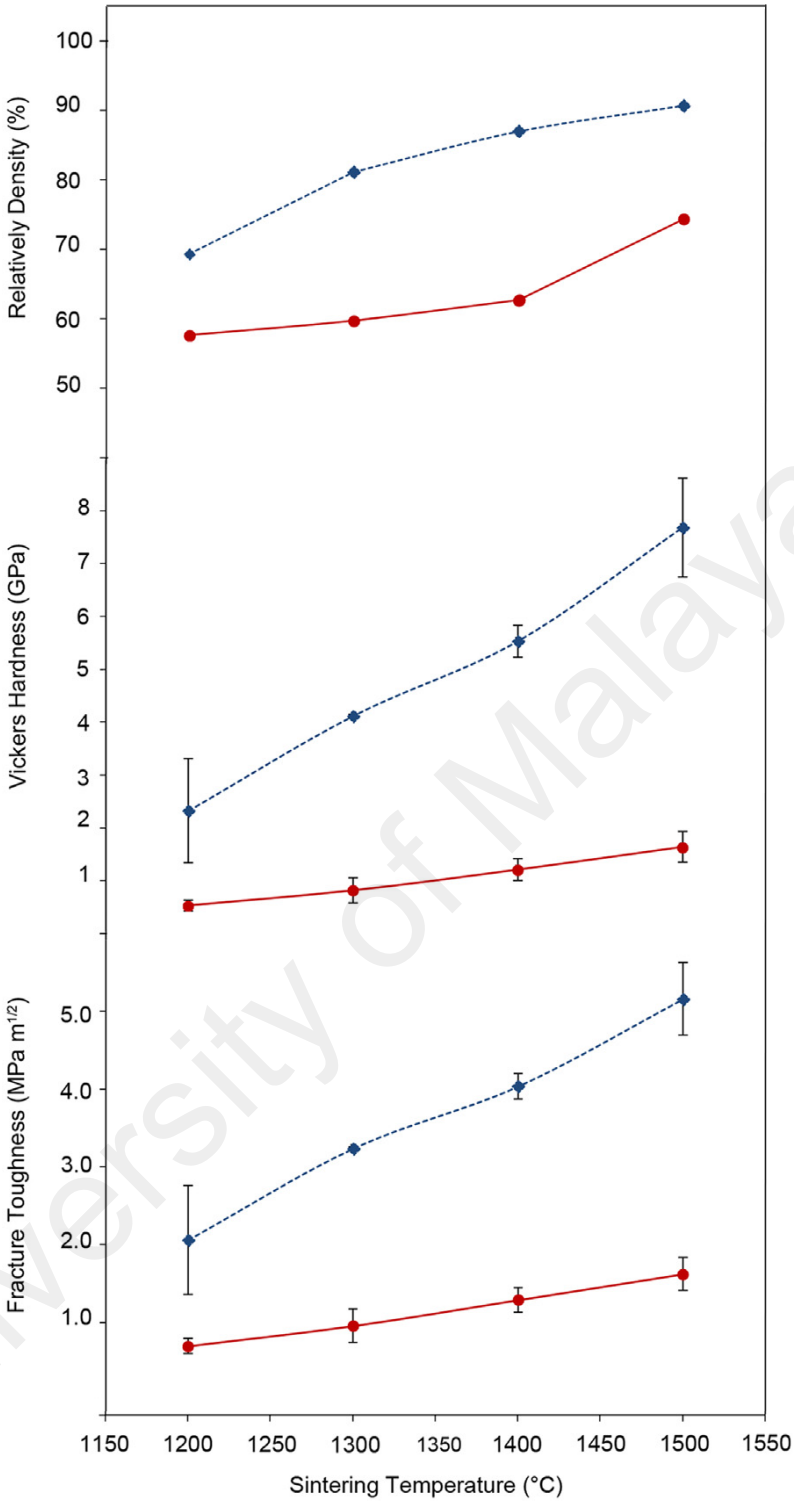

Figure 3.11: Mechanical properties evaluation of heat treated (solid lines) and non-heat treated (dash lines) forsterite bulked sintered at different temperatures for 2 hours (Ramesh, et al., 2013).

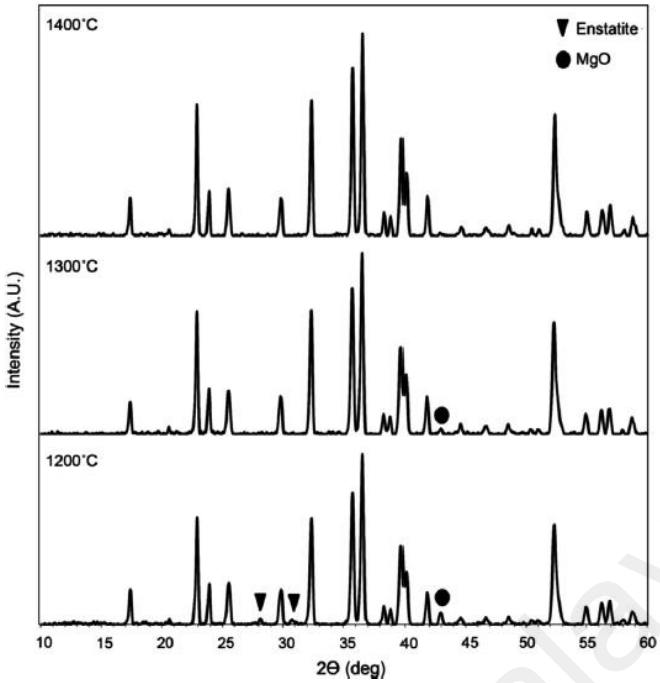

Figure 3.12: Phase stability result heat treated forsterite sintered in bulk form at different temperatures for 2 hours (Ramesh et al., 2013).

3.3 Non-conventional method

Aside from the usual sintering method using a furnace and heating forsterite in air with a simple sintering profile, there are other methods introduced by other researchers to innovate the sintering method in hope to enhance the mechanical properties of forsterite.

3.3.1 Two-step sintering

Two-step sintering was introduced on forsterite mainly to solve the grain growth issue experienced during sintering at high temperature (Kharaziha & Fathi, 2010). It was also suggested by Wang et al. (2006) that two-step sintering could achieved densification without grain growth by maintaining grain boundary diffusion and negating grain boundary migration. Generally, two-step sintering involved two stages of holding at the desired temperature. Usually the first stage of sintering is the highest temperature that will trigger the intermediate densification of forsterite under very short holding time. Second stage of sintering involved a very long holding at a lower sintering

temperature to allow the densification to continue and complete. It was explained that subduing the grain growth are related to the kinetics. The second stage of sintering would 'freeze' the microstructure hence slowing the kinetics and yet still suffices to continue the densification process (Chen & Wang, 2000; Feng et al., 2014). Figure 3.13 showed a typical two-step sintering profile commonly used in sintering forsterite ceramic. T_1 and T_2 signify the first and second stage of two-step sintering.

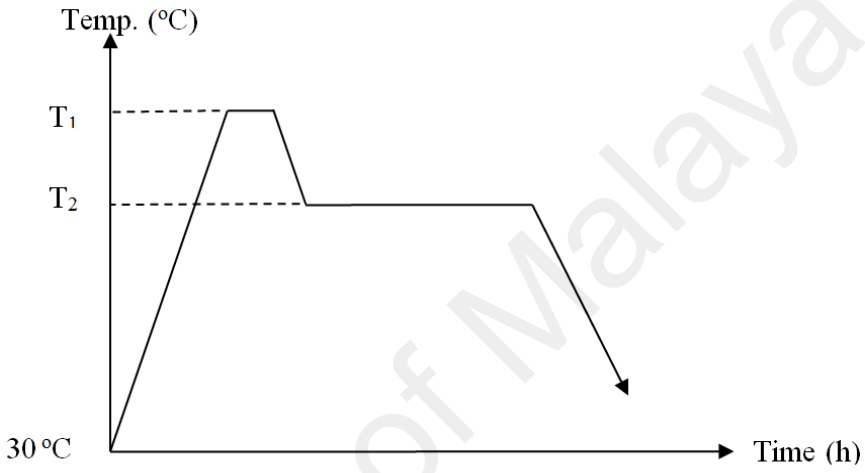

Figure 3.13: Example of a typical two-step sintering profile.

Fathi & Kharaziha (2009) had tried to implement two-step sintering method on forsterite that were synthesized via sol-gel route discussed in the Chapter 2.3.2. The first stage sintering temperature used was 1100 ^{o}C to 1300 ^{o}C and held for 30 min followed by the second stage at 750 ^{o}C and 850 ^{o}C and subsequently held for 2-15 hours. During the first stage of sintering, most of the samples had obtained relatively high densification. In comparison with the control (0 hour-curve), the relative density of two-step sintered samples were significantly higher as shown in Figure 3.14. The prolonged holding hours for 15 hours showed no noteworthy difference when sintered at 1150 ^{o}C as compared to the other lower holding hour samples. The densification of forsterite at low sintering temperature (T1 < 1150 ^{o}C) was incomplete due to the inactive grain boundary and volume diffusion which then halting the densification (Fathi & Kharaziha,

2009). According to Mazaheri et al. (2009), there was a critical second stage sintering temperature which would produce a fully densify structure without grain growth. However, upon sintering above 1200 ^{o}C, significant difference in relative density was observed for samples under different holding hours. Referring to Figure 3.15, the grain size drastically increased for sample with second step sintering temperature of 850 ^{o}C due to the inability to immobilize the grain boundary. Therefore, the author successfully obtained the best densification of forsterite without grain growth via two-step sintering with second stage sintering temperature of 750 ^{o}C for 15 hours.

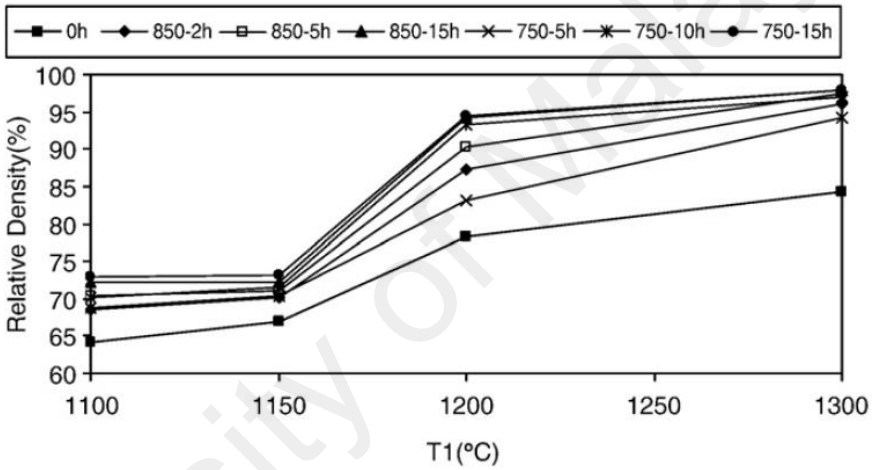

Figure 3.14: Relative density of forsterite bulk in a function of the first stage (T1) of two-step sintering temperature (Fathi & Kharaziha, 2009).

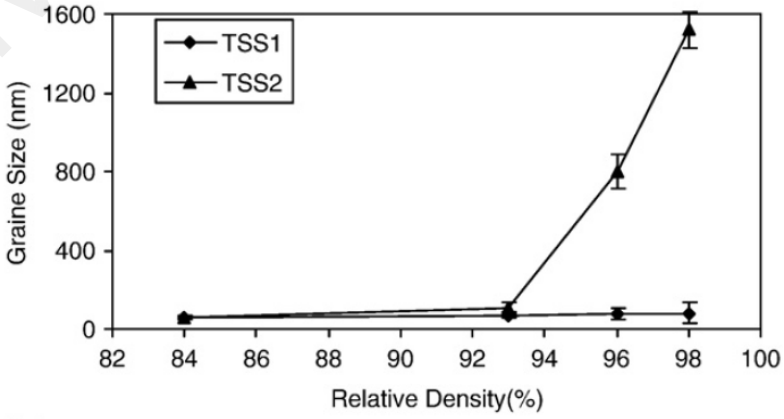

Figure 3.15: Average grain size versus relative density of forsterite bulk under TSS1 (T1 = 1300 ^{o}C and T2 = 750 ^{o}C) and TSS2 (T1 = 1300 ^{o}C and T2 = 850 ^{o}C) profiles with 15 hours holding for second step sintering (Fathi & Kharaziha, 2009).

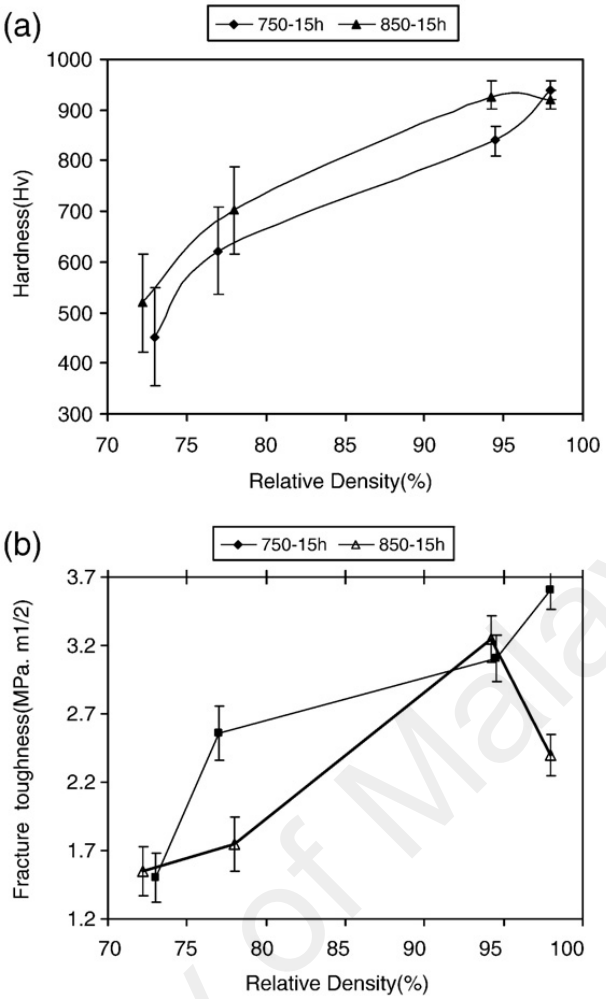

Figure 3.16: (a) Vickers hardness and (b) fracture toughness of forsterite as a function of relative density sintered at 1300 ^{o}C for first step sintering (Fathi & Kharaziha, 2009).

Further investigation was performed to relate the densification of forsterite under two-step sintering with the hardness and fracture toughness of forsterite (Figure 3.16). The hardness and fracture toughness of forsterite under two-step sintering regime (T2 = 750 ^{o}C for 15 hours) showed an increasing trend with a maximum value of 940 Hv and 3.61 MPa $m^{1/2}$, respectively. High second step sintering temperature (850 ^{o}C) showed declination in the mechanical properties upon obtaining high densification due to the grain coarsening phenomena. Hence, it was deduced that proper control of the second step sintering is very crucial to promote the advantage of two-step sintering method which is ensuring densification without grain growth (Fathi & Kharaziha, 2009).

3.3.2 Microwave sintering

3.3.2.1 Introduction

In the past years, microwave has been used extensively as an essential appliance in kitchens. However, the usage of microwave in material processing is still a new advancement. Microwave is widely used in the field of telecommunication via microwave frequencies, food processing, printing materials and biomedical fields but restricted to temperature below 500 ^{o}C. Utilizing microwave at high temperature has yet to mature when scaling-up for industries usage. Mostly, high temperature application uses conventional heating as it is well-established long before microwave was first introduced (Agrawal, 2006; Thostenson and Chou, 1999). Conventional thermal sintering involved heat transfer via conduction, convection and radiation to the surface of material whereas microwave heating involved the change of electromagnetic to thermal energy. With the introduction of microwave, volumetric heating and high heating rates was found to be beneficial as it eliminates the need for a slow heating rates to avoid thermal shock (reduce in production time) from conventional heating thus enhancing the overall quality of material (Agrawal, 2006; Thostenson & Chou, 1999; Yadoji et al., 2003; Zuo et al., 2013; Zuo et al., 2014). Also, selective sintering can be accomplished using microwave by taking into account the different dielectric properties of material. When materials in contact possess various dielectric properties, microwave will selectively choose the higher loss material and this phenomena can be widely used in joining of ceramics or polymer (Siores and DoRego, 1995). The notable advantage of microwave makes it an interesting method for new discoveries in the field of ceramic especially in sintering regime.

Microwave sintering for ceramics is a rather new to industry as it can hardly accommodate large amount of production. However, researchers have begun venturing into this field in hope to produce nanostructured ceramic which is known to exhibit

superior mechanical properties compared to standard materials (Agrawal, 2006; Bian et al., 2013). As discussed in the previous sections, many researchers had experienced grain coarsening and grain growth due to elevated sintering temperature above certain limit. Hence, Fathi & Kharaziha (2009) had introduced two-step sintering onto forsterite to solve the issue. However, the drawback of two-step sintering is the lengthy duration required to complete the sintering (> 15 hours). Thus, microwave is the alternate option used to produce nanostructured forsterite with minimal grain growth. Owing to the high heating rates as well as volumetric heating of microwave sintering, dense ceramics can be produced while maintaining its nanostructured morphology (Thuault et al., 2014). Further, the innovation of sintering method are focused on the improvement of mechanical properties of ceramic via modification of densification as well as reduction of fabrication time of materials (Presenda et al., 2015; Clark et al., 2004; Rybakov et al, 2013; Oghbaei & Mirzaee, 2010; Das et al., 2009).

Several important parameters are of concern during microwave sintering process. One of the parameters is the ability for the material to couple with microwave which is controlled by its dielectric properties. For example, zirconia has a very poor coupling with microwave below 400 ^{o}C and moderate coupling ability above the temperature. Hence, an early heating up to 400 ^{o}C is needed to allow the zirconia to couple with the microwave and it was suggested that a hybrid microwave sintering is required (Monaco et al., 2015). Silicon carbide susceptors was introduced into the hybrid microwave sintering to provide the initial heating via conduction until the material reached its critical temperature and began absorbing the microwave more effectively. Silicon carbide is well-known to absorb microwave easily at room temperature thus making it a suitable material for such purposes (Wang et al., 2006; Thostenson & Chou, 1999; Monaco et al., 2015).

The next important parameter is the methods to control the temperature. Two common methods used for controlling the temperature in the microwave furnace are pulsating powering of the magnetron at a fixed output power (operates under time controlled manner) and continuous powering of the magnetron under varying power output (power-control method) (Monaco et al., 2015). First method is usually used in the domestic oven in which a high output power was programmed on the magnetron prematurely whereas second method is commonly found for industrial usage whereby continuous adjustment on the output power was done to ensure the temperature maintained, increased or decreased according to the profile. Generally, both methods did not affect the grain growth or the densification of sample. The only difference is second method has higher accuracy in controlling the temperature than the first method (Yasuoka et al., 2006).

3.3.2.2 Microwave sintering on bioceramics

Recently, microwave sintering was introduced on forsterite by Bafrooei et al. (2014) using solid-state reaction method. The initial mixtures were prepared by mixing both silica gel and magnesium hydroxide ($Mg(OH)_2$) using planetary milling for 40 hours. Upon heating the mixtures under microwave irradiation, the phase purity of the powders were examined under various temperatures. Based on Figure 3.17, the lowest tested temperature (500 ^oC) showed signs of formation of forsterite peak and upon heating at 900 ^oC, pure phase forsterite was obtained. Any further heating of the powder would lead to peak the increase in peak intensity as well as enhancement of crystallite size. The surface area and particle size were measured accordingly and tabulated in Table 3.3. The increased in surface area until 900 ^oC was due to rapid decomposition and appearance of stresses which then led to particle decomposition. Nonetheless, further heating after 900 ^oC showed the decrease in surface area which can be simply due to grain growth (Bafrooei et al., 2014).

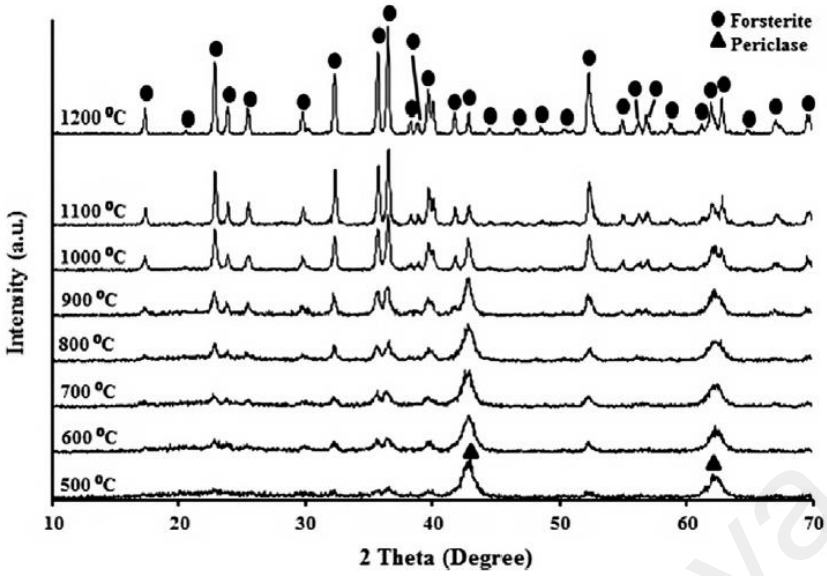

Figure 3.17: Phase purity of mixtures of initial precursors milled for 40 hours and heated at different temperatures via microwave heating (Bafrooei et al., 2014).

Table 3.3: Surface area and particle size of forsterite nanopowder at different temperature upon milled for 40 hours (Bafrooei et al., 2014).

Sample	Surface area (m^2 g^{-1})	Particle size (nm)
Ball milled for 40 h	30.7	-
Calcined at 900 ^oC	40.1	45
Calcined at 1000 ^oC	38.8	47
Calcined at 1100 ^oC	34.3	53
Calcined at 1200 ^oC	27.5	64.5

Sintering was conducted upon obtaining pure forsterite powder at 900 ^oC. The author had investigated on the relative density of forsterite upon sintering under various sintering temperatures. It was found that both conventional and microwave sintering methods showed a drastic increase on the densification initially and began to decrease at 1300 ^oC and 1250 ^oC, respectively, as shown in Figure 3.18. However, conventional sintering method used 2 hours long of holding time when heated to its corresponding temperature whereas microwave sintering did not have holding time. It was concluded by the author that microwave sintering provides better densification of forsterite at lower temperature and lesser time (Bafrooei et al., 2014). Based on the initial findings

of microwave sintering, the future of forsterite synthesized and sintered via microwave heating is very bright as promising results was obtained. Hence, further studies should be done on the forsterite since Bafrooei et al. (2014) only did a study on the densification without any further characterization on other mechanical properties such as hardness and fracture toughness.

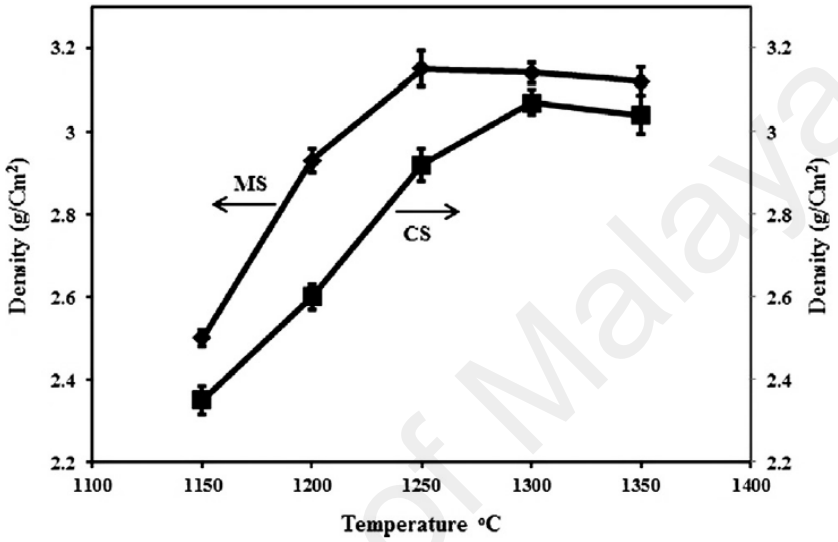

Figure 3.18: Relative density of forsterite ceramic sintered using conventional and microwave sintering (Bafrooei et al., 2014).

Aside from forsterite, microwave sintering has been widely used on other bioceramics such as HA, alumina and zirconia. Veljovic et al. (2010) had produced both HA and calcium deficient HA (HA/TCP), and microwave sintered it at 900, 1000, 1100 and 1200 ^{o}C for 15 min with heating rate of 20 ^{o}C/min. The XRD results (Figure 3.19 and 3.20) prevailed that no phase changes were observed for HA sample upon sintering using microwave irradiation whereas HA/TCP sample showed a change from β-TCP into α-TCP when sintering temperature reached 1200 ^{o}C.

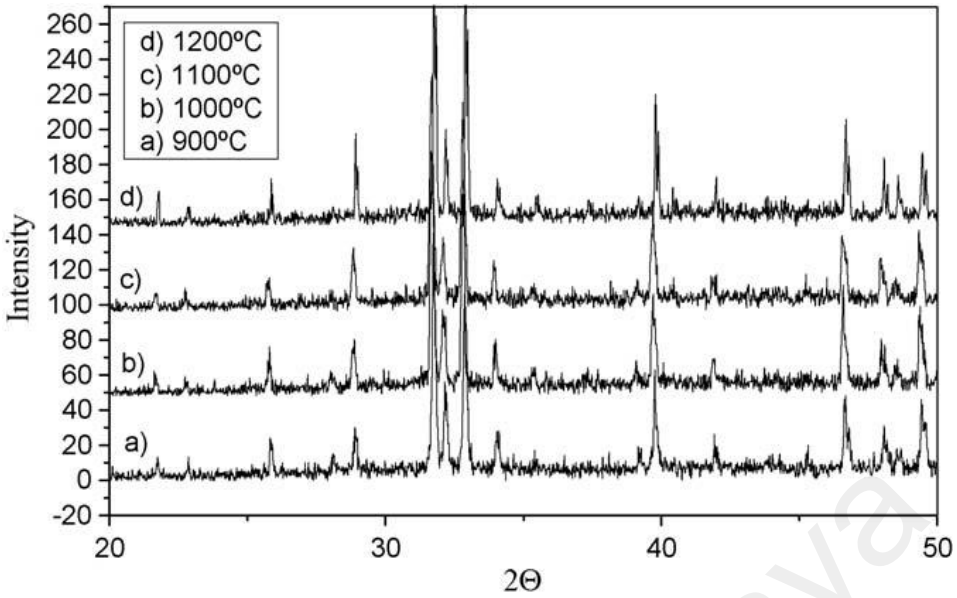

Figure 3.19: XRD traces of pure HA microwave sintered at 900, 1000, 1100 and 1200 ^{o}C (Veljovic et al., 2010).

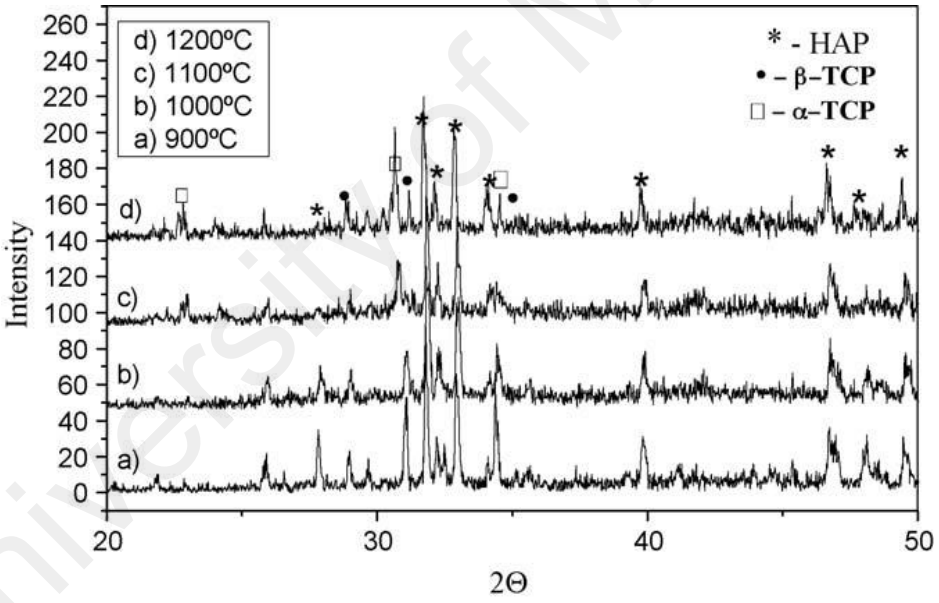

Figure 3.20: XRD traces of pure HA microwave sintered at 900, 1000, 1100 and 1200 ^{o}C (Veljovic et al., 2010).

It was reported that the microstructure showed uniform and fully dense HA sample at all sintering regime. The mean grain size of HA samples increased with sintering temperature with a minimum of 139 nm and maximum of 1.59 µm. HA/TCP samples also showed similar trends between grain size and sintering temperature with the

smallest and highest grain size of 100 nm and 4.70 µm, respectively. The relationship between grain size and sintering temperature is tabulated in Figure 3.21.

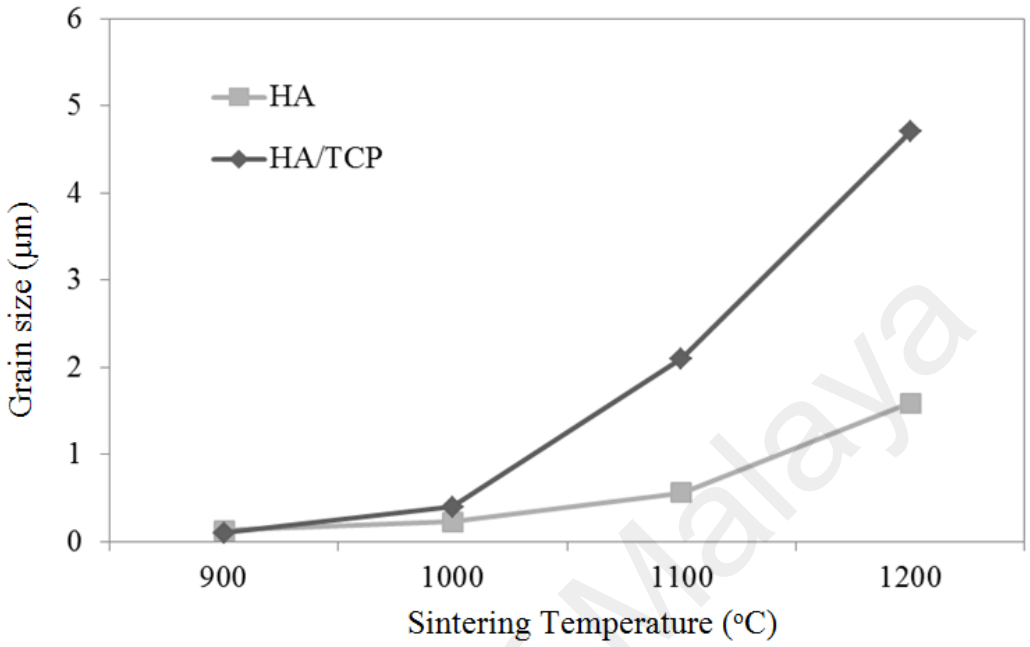

Figure 3.21: The relationship between grain size and sintering temperature of HA and HA/TCP

Based on the results obtained from microwave sintering, the author added a comparison between conventional and microwave sintered HA as shown in Table 3.4. It was demonstrated that microwave sintered samples possessed better overall mechanical properties than conventional sintered HA owing to the smaller grain size of microwave sintered samples and shorter heating duration.

Table 3.4: Processing conditions and mechanical properties of HA sintered via conventional and microwave sintering (Veljovic et al., 2010).

Temperature of sintering (^{o}C)	900		1000	
Type of sintering	Conventional	Microwave	Conventional	Microwave
Holding time (min)	120	15	120	15
Hardness (GPa)	2.75	3.45	3.95	4.19
Fracture toughness (MPa $m^{1/2}$)	0.77	1.30	0.89	1.04

In another work done by Bose et al. (2010), HA was synthesized and sintered in a microwave furnace with power ranging from 2000 – 2700 W. The samples were heated at 1000, 1100 and 1150 ^{o}C for 20 min. As observed, all mechanical properties that was characterized showed decreasing trend when the sintering temperature increases. This was due to the drastic increase in grain size of HA upon sintering at 1150 ^{o}C with an average grain size of 1.16 µm. A nano-grain size of 168 nm was successfully obtained at the lowest sintering regime which consequently produced excellent mechanical properties compared to other sintered samples (Bose et al., 2010). The mechanical properties of HA under various sintering cycles was tabulated in Table 3.5. Having grain size in nanometer scale has increased the overall volume of grain boundaries thus increasing the resistance towards indentation as well as crack propagation. Grain boundaries act as energy barrier that negate the propagation of cracks by either deflecting the cracks or immediately halting the crack propagation.

Table 3.5: Mechanical properties of HA with different sintering cycles (Bose et al., 2010).

Sintering cycle (^{o}C min^{-1})	Grain size (µm)	Microhardness (GPa)	Fracture toughness (MPa m$^{1/2}$)
1000/20	0.168	8.4	1.9
1100/20	0.52	7.3	1.5
1150/20	1.16	6.3	1.2

Borrell et al. (2012) proved that drastic improvement in the mechanical properties of zirconia was obtained using microwave sintering. Figure 3.22 showed the relation between relative density and sintering temperature using conventional and microwave sintering. Fully dense zirconia was successfully obtained for microwave sintered samples at 1400 ^{o}C as compared to conventional sintering method under shorter operating time. Regardless of holding time for microwave sintering, all samples showed similar final density at 1400 ^{o}C.

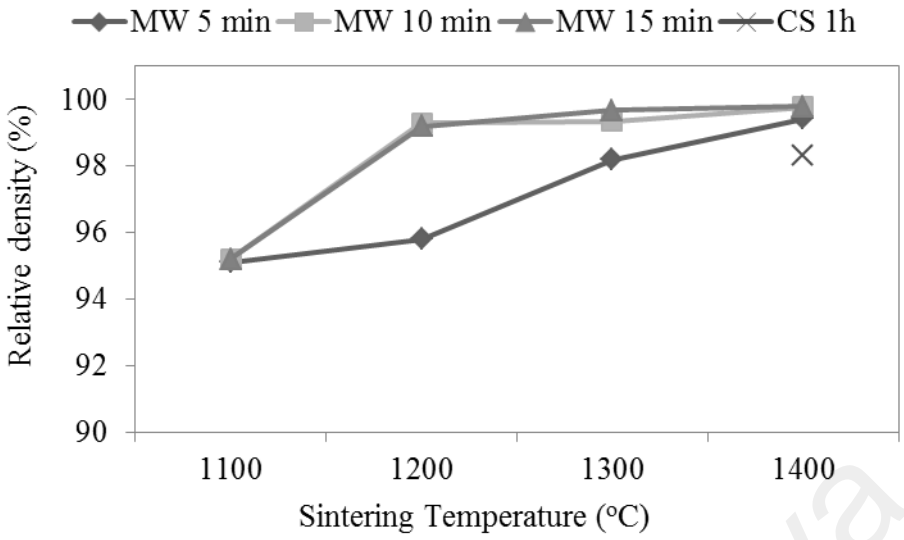

Figure 3.22: Effect of conventional and microwave sintering temperature on the relative density of zirconia (Borrell et al., 2012).

The grain size of zirconia increased with sintering temperature with the biggest grain size obtained for conventional sintered samples (as shown in Figure 3.23). No significant difference was observed between the microwave sintered samples implying that the main parameter that governed the grain growth phenomena is the sintering temperature. Higher heating rate in microwave resulted in grain refinement which allows the energy consumed was used for densification instead of coarsening of grains.

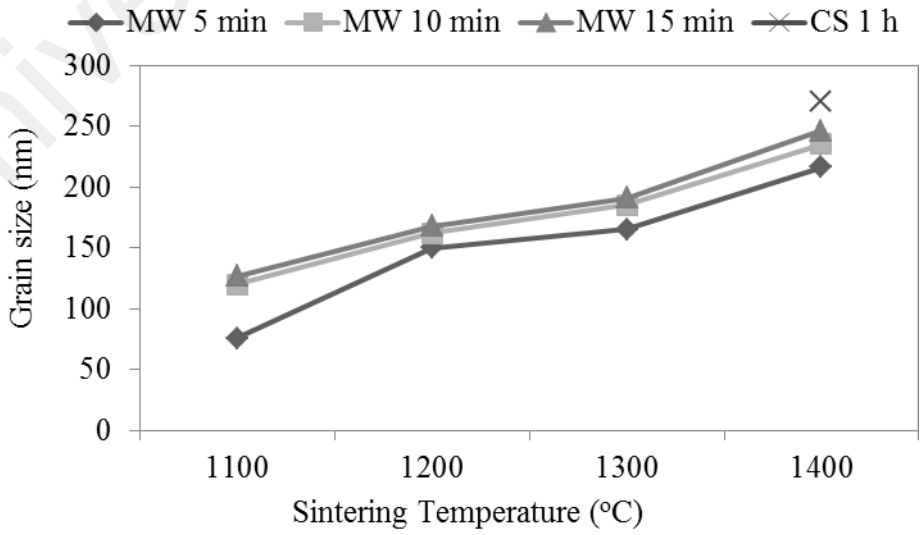

Figure 3.23: Effect of conventional and microwave sintering temperature on the grain size of zirconia (Borrell et al., 2012).

The fracture toughness result obtained was not dependent on the grain size of zirconia. Both conventional and microwave for 5 min samples showed same highest value of fracture toughness (4.48 MPa $m^{1/2}$) at 1400 ^{o}C as seen in Figure 3.24. It was claimed by the author that it is possible to have similar fracture toughness values although the grain sizes of conventional and microwave sintered samples were the same (Borrell et al., 2012).

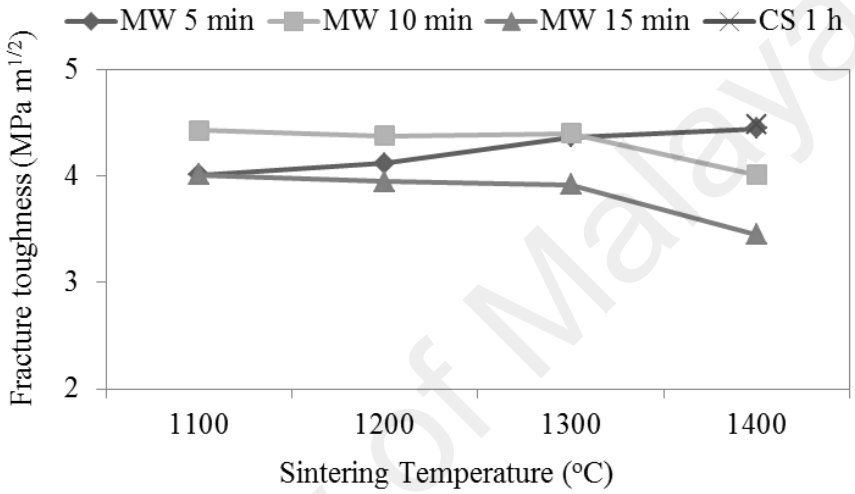

Figure 3.24: Effect of conventional and microwave sintering temperature on the fracture toughness of zirconia (Borrell et al., 2012).

3.4 Sintering additives on bioceramics

3.4.1 Introduction

Aside from sintering method, another technique that could contribute in improving the mechanical properties of ceramic is by addition of sintering additives. Doping additional chemical substance into bioceramic was widely used to improve chemical and mechanical properties. It was found that dopant could restrict grain growth up to an extent that nanocrystalline grains are obtained (Mukhopadhyay & Basu, 2007). Further, it is a cost-efficient method unlike other expensive and sophisticated routes such as hot isostatic pressing. It is important to optimize the profiling during the addition of additives which can be divided into two major parameters i.e. types and amounts of

sintering additives. Nevertheless, owing that forsterite is a new emerging bioceramic, the study on adding sintering additives to forsterite is very scarce.

3.4.2 Types of sintering additives

From literature, there are several choices of additives that were tested to further improve sinterability without decomposition or/and decreasing bioactivity (Suchanek et al., 1997). Each of these sintering additives will bring different effects towards the overall properties of bioceramic. An extensive research on these additives is necessary to optimize the profile as reported by Suchanek et al. (1997). According to the research, K_2CO_3, Na_2CO_3, H_3BO_3, KF, $CaCl_2$, KCl, KH_2PO_4, $(KPO_3)_n$, $Na_2Si_2O_5$, $Na_4P_2O_7$, Na_3PO_4, $(NaPO_3)_n$, $Na_5P_3O_{10}$ and β-$NaCaPO_4$ were selected as the sintering additives for HA and based on the results, it was justified that H_3BO_3, $CaCl_2$, KCl, KH_2PO_4, $(KPO_3)_n$, and $Na_2Si_2O_5$ did not enhance the densification of HA which implied that not every sintering additives produce positive effects (Suchanek et al., 1997).

Another research was done regarding the effect of dopant towards bioceramic by Bose et al. (2011). An evaluation was done on the influence of MgO, SrO and SiO_2 to the bioactivity and mechanical properties of β-tricalcium phosphate (β-TCP). During the phase analysis of these samples, a very weak sign of α-TCP was observed for samples containing SrO/SiO_2 whereas samples containing MgO showed only β-TCP (Bose et al., 2011). It was claimed by Bose et al. (2011) that the major phases of TCP remains unchanged although there was addition of sintering additives. Also, the combinations of various dopants were done and the densification of TCP showed significant different between samples which are tabulated in Table 3.6.

Table 3.6: Relative density and grain size of doped and undoped TCP sintered at 1250 ^{o}C for 2 hours (Bose et al., 2011).

Composition	Relative density (%)	Grain size (μm)
Undoped TCP	96.2	2.62
1 wt% Sr + 1wt% Mg doped TCP	97.7	2.33
1 wt% Sr + 0.5 wt% Si doped TCP	95.5	3.35
1 wt% Sr + 1 wt% Mg + 0.5 wt% Si doped TCP	95.9	5.43

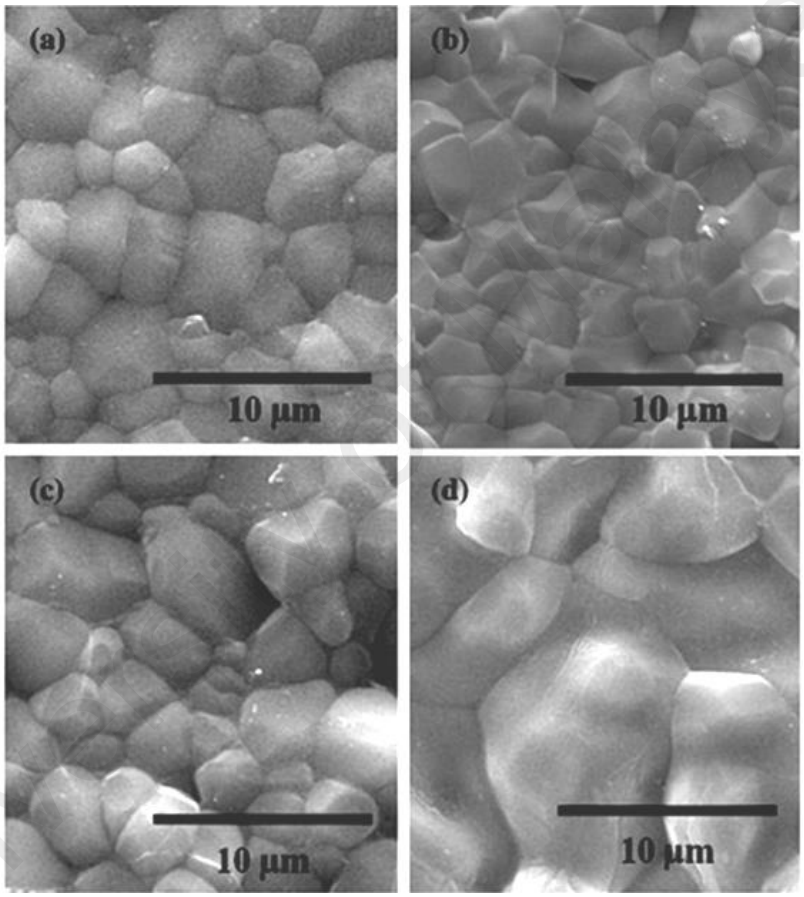

Figure 3.25: SEM micrograph of the grain size of (a) undoped TCP, (b) TCP-MgO/SrO, (c) TCP-SrO/SiO_2 and (d) TCP-MgO/SrO/SiO_2 sintered at 1250 ^{o}C for 2 hours (Bose et al., 2011).

According to Table 3.6, it is clear that Bose et al. (2011) discovered the effect of different combinations of dopant in enhancing the densification of TCP. The combination of 1 wt% Sr + 1 wt% Mg doped TCP produced the best densification compared to other samples and in fact, some combinations of dopant deteriorates the

density as compared to the undoped TCP. The justification of such result was hypothesized that the absence of α-TCP would increase the densification. Based on the SEM image shown in Figure 3.25, the grain size of TCP doped with 1 wt% Sr and 1 wt% Mg possessed the smallest grain size among other samples (Bose et al., 2011).

3.4.3 Amount of sintering additives

In a study done by Ramesh et al. (2007), investigation was conducted on the addition of manganese on HA. A range of 0.05 wt% until 1 wt% of manganese (Mn) was selected with sintering profile of 950 – 1450 ^{o}C for 2 hours at a ramping rate of 10 ^{o}C/min. The densification for all samples showed similar trends as sintering temperature increases (Figure 3.26). Upon sintering above 1000 ^{o}C, all samples showed very high relative density (~98%). Nonetheless, all doped samples showed 99% densification when sintered at 1100-1250 ^{o}C whereas pure HA samples only achieved a maximum of 98.9% at 1150 ^{o}C. No further densification was inspected as intergranular pores were observed upon further sintering as shown in Figure 3.27. In regards to hardness, it was found that 0.05 wt% of Mn possessed the highest hardness at 1000 ^{o}C as compared to the pure and other compositions HA. All doped HA showed reduction in hardness (Figure 3.28) as sintering temperature increases whereas pure HA showed drastic increase in hardness to a maximum of 7.21 GPa at 1050 ^{o}C and thereafter decreased with increasing temperature (Ramesh et al., 2007). Based on this findings, it can be concluded that the addition of Mn indeed enhanced the mechanical properties of HA but only at certain compositions.

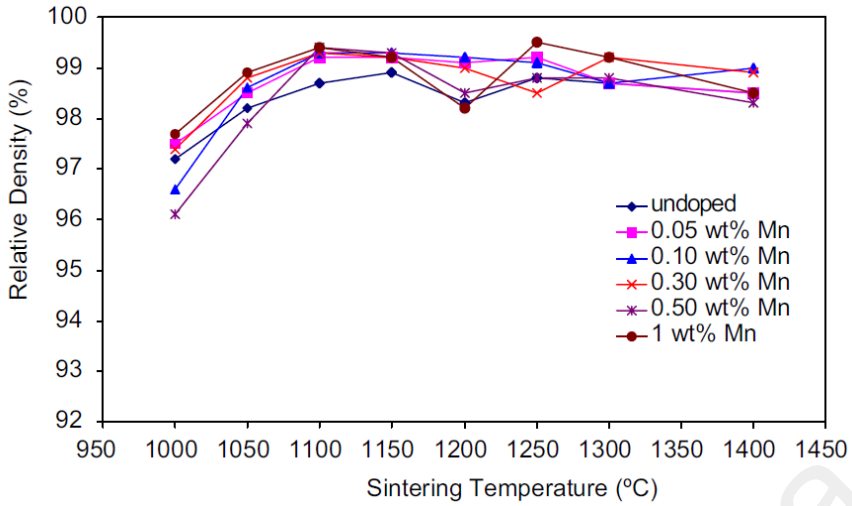

Figure 3.26: Relative density variation sintered at different sintering temperature (Ramesh et al., 2007).

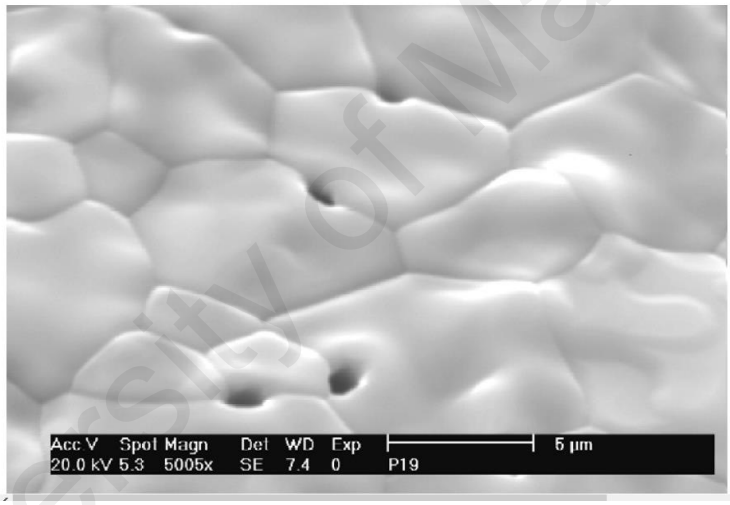

Figure 3.27: SEM micrograph of HA sintered at 1300 ^{o}C (Ramesh et al., 2007).

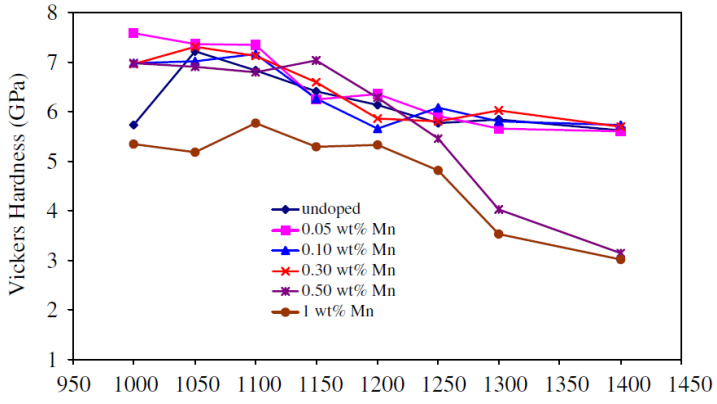

Figure 3.28: Effect of sintering temperature and Mn addition on the Vickers hardness of HA (Ramesh et al., 2007).

Alumina is a well-known candidate for bone implant owing to its wear resistance and high rigidity. Nonetheless, due to its limitation in fracture toughness, alumina was quickly substituted by zirconia as the potential candidate for load bearing applications. Hence, many researchers have conducted studies in the toughening of alumina via transformation toughening, second-phase addition, bridging of grains and others. In the work of Hassan et al., the author had added with niobium oxide (Nb_2O_5) in hope to enhance the mechanical properties of alumina. By controlling the sintering temperature to 1650 ^oC, the author varies the amount of Nb_2O_5 content to 0.25, 0.5 and 0.75 wt%. Promising results were shown in terms of its Vickers hardness and fracture toughness with a maximum of 34.4% and 35.5% higher than the undoped alumina, respectively (Figure 3.29 and 3.30) as compared to 0.75 wt% samples. Intergranular cracks were observed for 0.75 wt% samples and the author was convinced that the presence of liquid-phase Nb_2O_5 on the triple junctions of grains had reduced the energy thus allowing cracks to propagate along the grain boundaries instead of transgranular cracking (Hassan et al., 2014). From this study, it was found that adding more Nb_2O_5 to alumina provides better enhancement on the mechanical properties. However, the author did not pursue in adding higher content of Nb_2O_5 to obtain the optimum amount of the dopant. Nevertheless, it can be claimed that the amount of dopant used varies greatly between types of host as well as sintering additives itself.

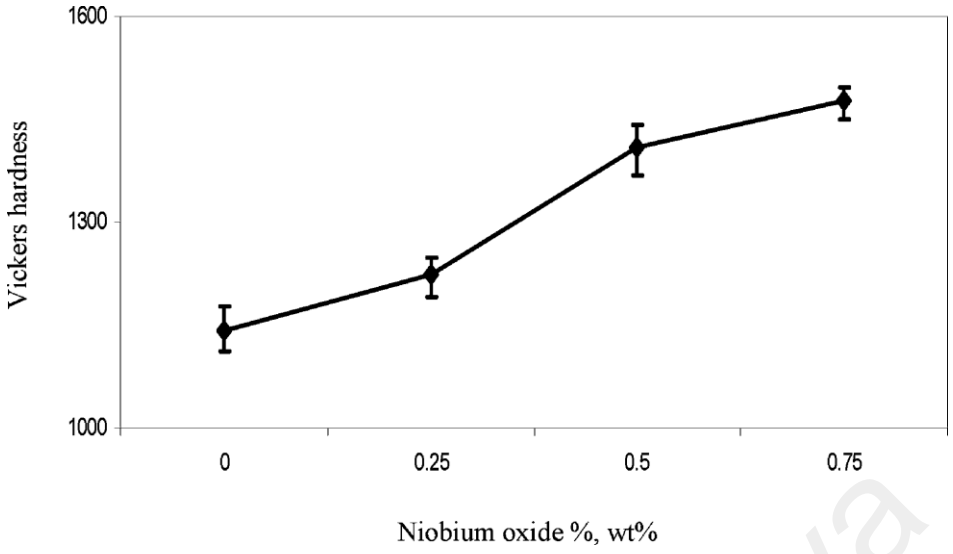

Figure 3.29: Effect of Nb_2O_5 content on the Vickers hardness of alumina composites sintered at 1650 ^oC (Hassan et al., 2014).

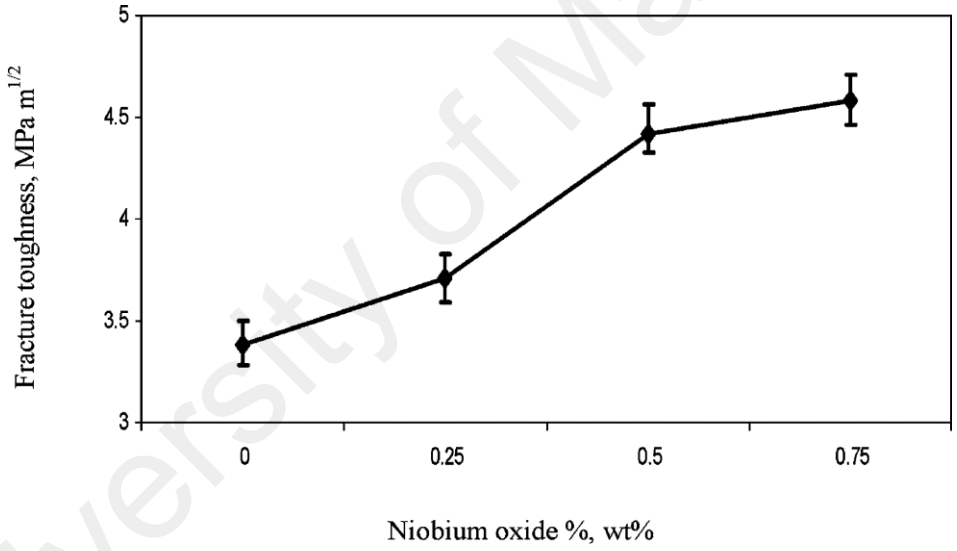

Figure 3.30: Effect of Nb_2O_5 content on the fracture toughness of alumina composites sintered at 1650 ^oC (Hassan et al., 2014).

3.4.4 Zinc oxide as sintering additive

The existence of ZnO has been known for thousands of years and now it has become a common engineering material in many industries. ZnO was considered as the forth (4th) most widely used metal after iron, aluminium and copper (Amir et al., 2012). Owing to its diverse application in industries, the production of ZnO has gone as high as one and a half million tons yearly and up until now, there are still researchers that tried

to uncover new interest of ZnO in other fields such as semiconductor industry. Also, ZnO was used as an ingredient for medicinal ointment in order to treat boils and carbuncles. Aside from that, Amir et al. (2012) also state that ZnO was applied in skin lotion as well in medical stream. Another major breakthrough of ZnO is the usage in rubber technology whereby it is used to reduce vulcanization process time (Amir et al., 2012). According to literatures, zinc was found to be beneficial in providing positive stimulatory effect on the bone construction. During skeletal breakdown, zinc was released and subdued osteoclastic bone resorption by preventing osteoclast-like cell from forming at the bone marrow cells (Yamaguchi, 2010; Miao et al., 2005; Ito et al., 2002; Murray & Messer, 1981).

Thus, a study was done on HA by introducing ZnO as the sintering additives. Further, during the addition of sintering additives into bioceramic, researchers have tried to obtain a suitable amount of additives used to avoid excessive doping that may lead to negative outcome towards the mechanical and bioactivity properties. Bandyopadhyay et al. (2007) obtained a fine result on the doping of ZnO in HA and tricalcium phosphate (TCP). Based on the study, it showed that upon adding 3.5 wt% of ZnO, some cells died during *in vitro* study thus concluding that the level of toxicity caused by excessive amount of ZnO leads to health hazard in human body. Nonetheless, an improved densification, microstructure, microhardness and cell material interaction of HA and TCP was observed for samples doped below 3.5 wt% (Bandyopadhyay et al., 2007). Furthermore, Bandyopadhyay et al. (2007) also discovered that for different bioceramic such as HA and TCP, the effect differs as well because TCP showed better microstructure formation (grain size of 1.9 μm) compared to HA (grain size of 5-6 μm) although the same amount of ZnO was added. All in all, it is essential to know and understand on the amount of dopant to be added into bioceramic because excessive additives could lead to negative effect whereas insufficient additives may lead to

redundancy on the bioceramic. Figure 3.31 showed that the densification of HAp is more prominent compared to TCP upon adding ZnO due to the drastic increment in density of HA.

The amount of ZnO doped will also effect on the densification. Another example of doping of ZnO and MgO on nano-HA was done by Kalita & Bhatt (2007). From the study, the maximum densification was obtained at both 1.0 wt% of ZnO and MgO. However, continue increasing the dopant concentration caused a gradual reduction on the density as shown in Figure 3.32. Also, the purity of nano-HA was observed and no alteration occurred thus proving that metal ions can improve mechanical properties of conventional HA ceramic even in nano-size (Kalita & Bhatt, 2007). In conclusion, the applicability of ZnO as a sintering additive is promising yet requires a proper optimization on the amount used to ensure positive outcome on the mechanical properties of the material.

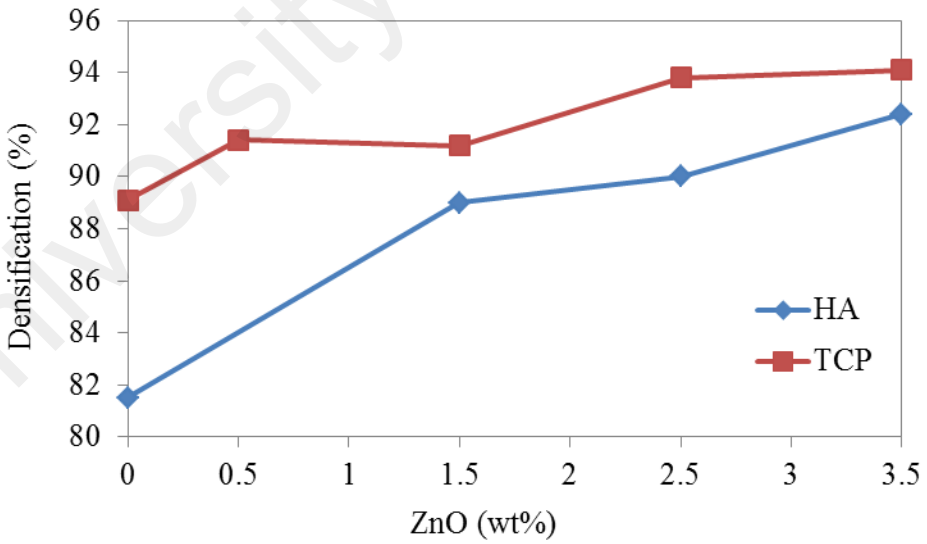

Figure 3.31: Densification of TCP and HA sintered at 1250 ^{o}C under different composition of ZnO addition (Bandhopadhyay et al., 2007).

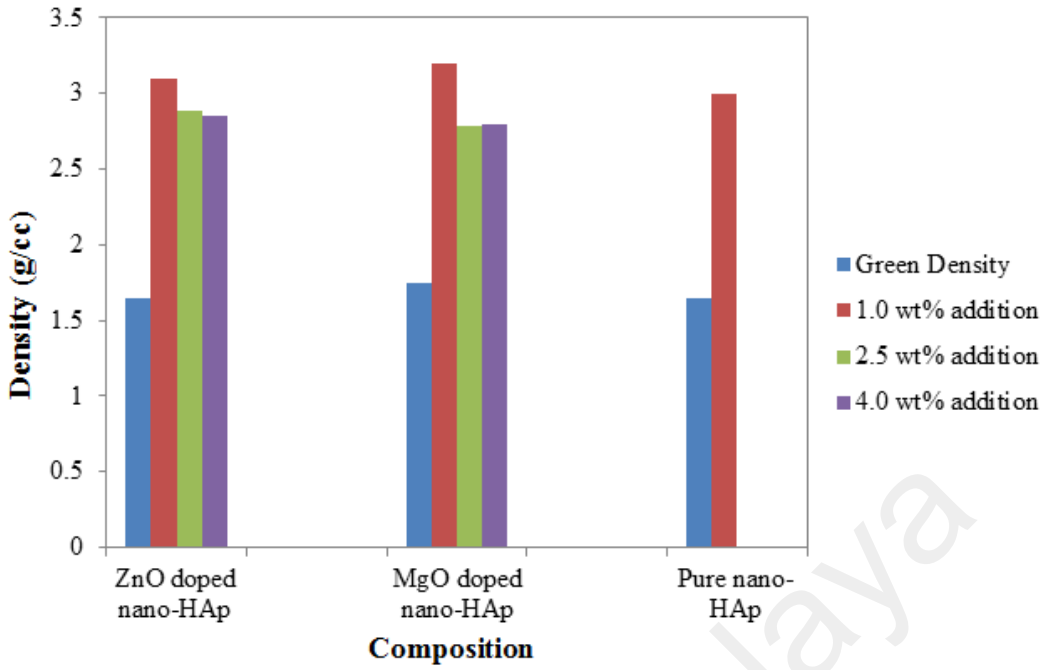

Figure 3.32: Density for green and sintered of pure and doped nano-HAp sintered at 1250 ^{o}C for 6 hours (Kalita & Bhatt, 2007)

Addition of ZnO into PMNT was established by Promsawat et al. (2012) and the densification, grain size, hardness and fracture toughness were characterized. The density of PMNT was not significantly affected by the addition of ZnO although the highest densification was obtained for 0.05 wt% ZnO as tabulated in Table 3.7 below. The author claimed that not only small amount of ZnO produced better densification but also reduce the influence of grain growth caused by ZnO (Figure 3.33). The enhancement in the mass transportation caused by ZnO addition from 0.05 to 0.1 wt% led to a sharp increase in grain size of PMNT/ZnO ceramics. Further increase in ZnO content (0.5 to 1.0 wt %) showed no significant changes in the grain size. Intergranular fracture was observed for PMNT ceramic whereas PMNT/ZnO showed a mixed-mode fracture consisting of both inter- and transgranular fractures. Transgranular fracture commonly occurs on large grains and hence causing cracks to propagate further and reducing the fracture toughness of material. Also, as the content of ZnO increases, it was believe that the pinning at grain boundary with added ZnO had created crack deflection towards the grain bulk causing high percentage occurrence of transgranular

fracture. Nevertheless, the fracture toughness value increases as the ZnO increases from 0.1 wt% onwards owing to the presence of micropores which act as obstruction to crack propagation. The hardness of 0.05 wt% of ZnO on PMNT showed the highest value of 5.3 GPa but further increasing the content showed slight decreased in hardness. The reduction in hardness could be associated by the grain size increase because grain boundaries in smaller grains matrix acts as stress concentration sites thus effectively blocking the dislocation pile-up from adjacent grains (Promsawat et al., 2012).

Table 3.7: Relative density, and grain size of PMNT/ZnO ceramics (Promsawat et al., 2012).

ZnO content (wt%)	Relative density (%)	Grain size (μm)
0	96.62	1.88
0.05	96.87	2.15
0.1	96.66	2.61
0.5	96.78	2.71
1.0	96.67	3.07

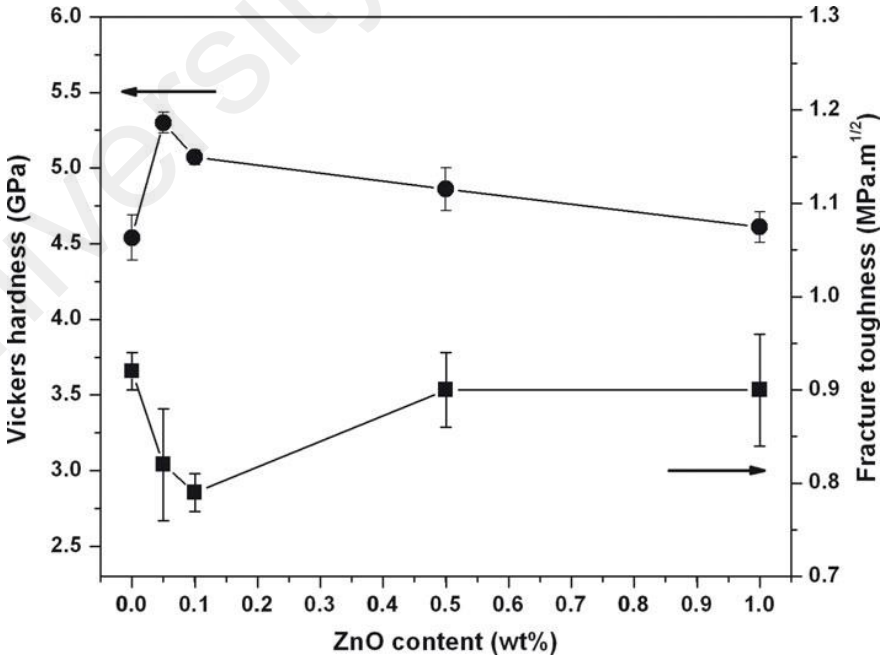

Figure 3.33: Vickers hardness and fracture toughness of PMNT/ZnO ceramics (Promsawat et al., 2012).

3.4.5 Application of sintering additives on forsterite

Up to date, forsterite was commonly doped with chromium especially in the field of optical. The development of laser materials for tunable near-IR fiber lasers and ultrabroadband fiber-optic amplifier has gained much interest from many researchers. As early as 1988, Petricevic et al. (1988) had explored into this field and incorporate chromium into forsterite resulting in the success of producing one of the most widely tunable solid-state lasers in the spectral region. However, insufficient study was conducted to investigate on the effect of different dopant concentration to fully optimize this groundbreaking result. Thus, Aseev et al. (2015) had continued the study by varying the chromium concentration as well as heat treatment temperature to investigate on how it affects the spectral luminescence properties and concluding that addition of chromium provides small difference in terms of quantum luminescence yield.

In summary, this chapter has presented the importance of heat treatment in the formation of phase pure forsterite. Sufficient temperature needs to be applied on forsterite to allow a complete reaction between the precursors. The mechanical properties of forsterite is highly dependent on the profiling and types of sintering methods used. Many studies have been conducted on the sinterability of forsterite using conventional method which includes regular sintering under atmospheric air with a simple heating to the desired temperature and cooling it back to room temperature. Two-step sintering was introduced on forsterite to elucidate the grain growth phenomena that was experienced in all conventional sintering but undesirable in industry due to long processing duration. Hence, microwave sintering was suggested as the next potential sintering method that could significantly reduce the sintering hours. Sintering additive was also introduced to forsterite as it allows enhancement in mechanical properties of forsterite with low cost and simplicity. Attrition milling was introduced as a new milling method to produce forsterite (solid state reaction)

CHAPTER 4: METHODOLOGY

4.1 Introduction

This chapter provides information on the methods employed and materials used to produce phase pure forsterite (Mg_2SiO_4). In addition, the technique used to add dopant into forsterite will be explained as well as the introduction to microwave sintering on forsterite. All characterization methods which include phase purity, mechanical properties analysis and morphology examination are also discussed in this chapter.

4.2 Powder synthesis

4.2.1 Starting powder preparation

For this research, forsterite powder was prepared via solid-state method. Two precursors, magnesium hydroxide carbonate or also known as magnesium carbonate basic (MHC), ($4MgCO_3*Mg(OH)_2*5H_2O$; Merck, 98%) and talc ($Mg_3Si_4O_{10}(OH)_2$); Sigma-Aldrich, 99%), were weighed (Mettler Toledo, Switzerland) as tabulated in Table 4.1 according to the chemical stoichiometry (Equation 4.1 and 4.2).

Table 4.1: Weight of precursors for a 50 g batch of forsterite

Chemical Precursor	Weight (g)
Magnesium Hydroxide Carbonate (MHC), $4MgCO_3*Mg(OH)_2*5H_2O$	43.068
Talc, $Mg_3Si_4O_{10}(OH)_2$	33.682
Ammonium Chloride, NH_4Cl	4.751

$$4MgCO_3*Mg(OH)_2*5H_2O + Mg_3Si_4O_{10}(OH)_2 + NH_4Cl \rightarrow 4MgSiO_3 + 4MgO + 4CO_2 + 7H_2O + HCl + NH_3 \quad (4.1)$$

$$MgO + MgSiO_3 \rightarrow Mg_2SiO_4 \quad (4.2)$$

A 500 ml beaker filled with 150 ml of 95% denatured, ethanol (Hamburg, Germany) was prepared and the as-weighed MHC powder was added into the beaker before subjecting ultrasonic pulse with 70 amps for 5 min (10s on, 1s off) with ultrasonic vibrator (Sonics & Materials, USA). This step was taken to ensure homogeneous mixing between the precursors by eliminating agglomeration of powder particle. Subsequently, talc was added into the same beaker (containing ultrasonicated-MHC + ethanol) to form mixtures of both precursors and underwent high frequency pulse again using similar parameters for 30 min.

4.2.2 Forsterite preparation with different milling durations

The effect of milling duration on the formation of forsterite was investigated. A conventional ball mill was used to blend the ultrasonicated powder at 350 rpm for 3 and 5 hours. The mixture was transferred into a 500 ml polypropylene bottle that served as milling jar. Upon filling up the milling jar with the mixture, zirconia ball (Retsch) with 3 mm diameter was added into the jar as the milling media. A ball to powder weigh ratio of 30:1 was used throughout the milling process. Ammonium chloride (NH_4Cl, Merck) was added into the milling jar at the final 10 min of the milling acting as a catalyst. Upon completion of milling process, the mixture in the milling jar was emptied by transferring it into a drying bowl through a sieve to separate the slurry (milled powder) from the zirconia balls. Lab wash bottle filled with ethanol was used to flush the residues in the milling jar and clean the zirconia balls from the slurry upon sieving to reduce wastage of precursors. The slurry was dried in a standard box oven under atmospheric air (Memmert, Germany) at 60 ^{o}C for 24 hours. The dried slurry was then grounded using mortar and pestle and sieved using a metal mesh with aperture size of 212 μm to obtain it in powder form.

4.2.3 Forsterite preparation with attrition milling

Attritor mill (Union Process, USA) was used to grind and mix the precursors under high grinding energy. 500 rpm was used during the milling process with 5 hours duration. The ultrasonicated mixture was transferred into the milling jar of the attritor mill with the aid of a funnel to ease the transferring process. Zirconia balls of 3 mm were used as milling media with ball to powder ratio of 30:1. Similarly, at the final 10 min of milling, NH_4Cl was added into the milling jar. The mixture was then dried, grounded and sieved using a metal mesh with aperture size of 212 µm.

4.2.4 Zinc oxide (ZnO) – doped forsterite powder preparation

Upon comparing the difference between ball and attritor mill in phase stability and mechanical properties under various sintering temperature, attritor mill was selected.

For the doping process, the powder obtained after sieving was heat treated in powder form using a box furnace (LT Furnace, Malaysia) to form pure forsterite powder. Firing temperature of 900 and 1000 ^{o}C with heating and cooling ramp rate of 10 ^{o}C/min and held for 2 hours was investigated. The chemical change upon heat treatment process was presented in equation 3.2 above. With the forsterite powder obtained through heat treatment, ZnO powder (Systerm, Malaysia) was mixed with forsterite powder via milling process. Three powder compositions, i.e. 0.5, 1.0 and 3.0 wt% ZnO-doped forsterite were prepared and Table 4.2 shows the weight percentage of ZnO added to forsterite.

For each different batches, both forsterite and ZnO powders were mixed in a 500 ml beaker filled with 150 ml of ethanol and undergone ultrasonic pulse for 30 min (10 s pulse on, 1 s pulse off) to ensure homogeneous mixing between the powders prior to milling. The mixture was transferred into the milling jar containing zirconia balls of 3 mm as the milling media (ball to powder ratio of 30:1). The attritor mill was set to 500

rpm with milling duration of 1 hour. The same procedure was carried out as previously done in the production of forsterite powder via attritor milling in section 4.2.3 (dry, ground and sieve).

Table 4.2: Table of ZnO weight percentage in forsterite and mass needed for a 50 g batch

ZnO weight percentage in forsterite (%)	Mass needed (g)	
	ZnO	Forsterite
0.0	0.00	50.00
0.5	0.25	49.75
1.0	0.50	49.50
3.0	1.50	48.50

4.3 Consolidation of green body

The powder was uniaxially pressed to produce the green bodies. A cylinder die with an internal diameter of 20 mm was used as the mold to compact the powders into pellet shape (20 mm dia. x 5 mm thickness). Oil-based lubricant such as, WD-40, was applied on the die as cleaning agent as well as to avoid the powder from sticking on the die during the removal of pellet upon compaction or also known as powder lamination. For every pellet, 1.5 g of powder was used and 2.5 MPa of pressure load was applied and held for 5 s before releasing the load.

4.3.1 Conventional sintering

Subsequently, pressureless sintering was carried out to consolidate the green samples using box furnace (LT furnace, Malaysia; Appendix A) under atmospheric air. The entire sintering process was estimated to complete within 10 to 20 hours with a typical sintering profile shown in Figure 4.1.

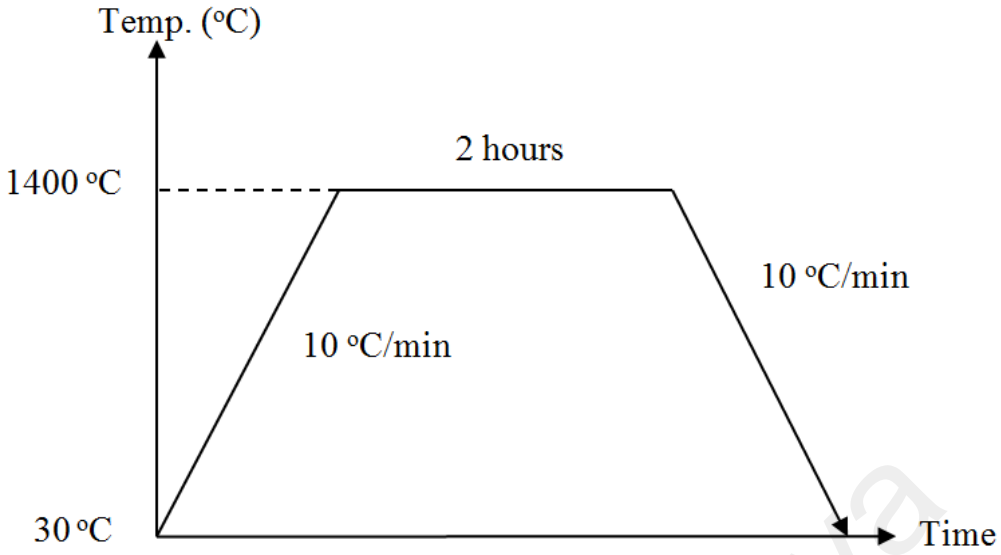

Figure 4.1: Sintering profile for the firing of green bulk samples via conventional sintering.

i. Heating from room temperature (30 ^{o}C) to the desired sintering temperature (1200 – 1500 ^{o}C with 50 ^{o}C interval) at a heating rate of 10 ^{o}C/min.

ii. Holding of 2 hours at the desired sintering temperature, and

iii. Cooling down to room temperature at 10 ^{o}C/min

4.3.2 Microwave sintering

Apart of using conventional sintering, microwave sintering was investigated to understand the mechanism behind the effect of microwave heating on the mechanical properties and morphology of forsterite. Forsterite bulk was prepared according to section 4.2.3 via attritor mill and consolidated using uniaxial press. The furnace model used is HAMiLab-C1500 (SYNOTHERM, China) operating at varying power up to 6 kW to ensure the heating rate to be constant at 50 ^{o}C/min. The input power used is 220 V and 50 Hz. The pyrometer used is 5R-1810 (IRCON, USA) as the temperature sensor with a dimension of the microwave multimode-cavity of 340 x 340 x 340 mm^{3}. The samples were sintered using similar profile pattern as conventional sintering with the following sintering parameters:

i. Heating from room temperature (30 ^{o}C) to the desired sintering temperature (1100 – 1250 ^{o}C with 50 ^{o}C interval) at a heating rate of 50 ^{o}C/min.

ii. Holding of 30 min at the desired sintering temperature, and

iii. Cooling down to room temperature at 50 ^{o}C/min

Phase stability, relative density, Vickers hardness, fracture toughness and morphology of microwave sintered samples were investigated.

4.4 Sample characterization

The characterizations of powder sample include the phase stability analysis (including crystallite size) with X-ray Diffraction, Brunaeur-Emmett-Teller surface area measurement, differential thermal and thermogravimetric analysis, powder morphology using scanning electron microscopy (SEM) and particle shape and size calculation via transmission electron microscopy (TEM).

The phase analysis and mechanical properties characterization were conducted on forsterite bulk samples which include X-ray Diffraction, relative density, Vickers hardness, fracture toughness and morphology examination via SEM and field-emission scanning electron microscope (FESEM) to observe the grain patterns.

4.4.1 Phase composition analysis

Phase analysis was performed through X-ray Diffraction (XRD) analysis (Empyrean, PANalytical, Netherlands) with parameters of 45 kV and 40 mA using Cu-K_{α} radiation source. The scanning speed and step size used was 0.5 ^{o}/min and 0.02^{o}, respectively. By referring to Joint Committee on Powder Diffraction Standards – International Center for Diffraction Data (JCPDS-ICCD) reference card, each XRD traces obtained was compared to the respective cards listed in Table 4.3 below.

Table 4.3: JCPDS reference cards to analyze the phases in forsterite powder

Chemical compositions	JCPDS reference no.
Forsterite	34-0189
Enstatite	11-0273
Magnesium Oxide (Periclase)	43-1022
Talc	13-0558
Magnesium Carbonate Hydroxide Hydrate	01-070-1177
Zinc Oxide	36-1451

The diffraction peak at ~ 35.6^{o} (2Θ) corresponding to (211) miller plane family of forsterite were chosen to calculate the crystallite size since it had sharper, highest and isolated peak from other peaks. The Scherrer equation (Equation 4.3) used is as follow (Cullity and Stock, 2001):

$$\boldsymbol{d} = \boldsymbol{0.9\lambda/(B\,cos\,\theta)} \quad (4.3)$$

Whereby,

d = crystallite size (Å)

λ = wavelength of Cu Kα radiation equal to 1.5406 Å

B = Full width half maximum (FWHM) of the selected peak (rad)

Θ = half of the diffraction angle (deg)

4.4.2 Brunaeur-Emmett-Teller (BET) surface area

Brunaeur-Emmett-Teller surface area analyzer (Micromeritics ASAP2020, TRISTAR II 3020 Kr) was used to measure the specific surface area of the powders obtained upon milling via nitrogen adsorption method. Specific surface areas of these powders will directly affect the formation of pure forsterite whereby with higher specific surface area,

a lower sintering temperature is required to obtain pure forsterite. The powders were degassed at 90 ^{o}C for 1 hour followed by 300 ^{o}C for 4 hours prior to analysis.

4.4.3 Differential thermal (DT) and thermogravimetric (TG) analysis

Differential thermal and thermogravimetric (Perkin Elmer, Pyris Diamond) analysis were conducted to provide information on the weight reduction of samples upon heating as well as to evaluate on the possible crystallization process of forsterite in obtaining a phase-pure powder. The process was conducted under air atmosphere beginning from 70 ^{o}C until 1000 ^{o}C with heating rate of 10 ^{o}C/min. The data obtained will be plotted into graph form to examine for any peaks that corresponded to weight lost and change of energy occurring throughout the firing process.

4.4.4 Bulk density measurement

The methods implemented to determine the bulk density is highly accurate, non-destructive and easy to perform. For the measurement of bulk density, Archimedes principle was applied into the water immersion technique by using a Mettler Toledo Balance AG204 Densi-meter (Appendix A). According to the principle, a body that is completely submerged or partially submerged in a fluid has a buoyancy force or resultant force acting upward with magnitude equal to the weight of water displaced by the body. Thus, weight of sample was measured in air and when submerged in water as well as after submerging into the water to calculate the density of sample. For non-porous samples, the density can be measured using Equation 4.4. For porous samples (density less than 80%) another additional equation will be used, which is shown in Equation 4.5 and 4.6. Based on Equation 4.5 and 4.6, the inclusion on actual weight of sample in water is due to the existence of porosity in the sample which will be consumed by the water upon soaking it thus increasing the total weigh of sample. Regardless of porosity, these two equations (Equation 4.5 and 4.6) can be applied for

non-porous samples since the values obtained differ only by a very small percentage (~0.1%). In this research, distilled water was used as the immersion medium.

For non-porous sample,

Bulk Density, $\rho_a = \rho_w * W_a / (W_a - W_w)$ (3.4)

Whereby,

ρ_a = bulk density of sample

ρ_w = density of distilled water used with respect to temperature (refer to appendix A)

W_a = weight of sample in air

W_w = weight of sample in water

For porous sample,

Bulk Density, $\rho_a = \rho_w * W_a / (W_a - W_{w,actual})$ (3.5)

$W_{w,\,actual} = W_w - (W_{a+w} - W_a)$ (3.6)

Whereby,

W_{a+w} = weight of sample in air after soaking in water

4.4.5 Vickers hardness and fracture toughness

Prior to Vickers hardness test, both grinding and polishing of the samples were done by using a grinder (Imtech Grinder-Polisher, Germany ; Appendix A) with silicon carbide (SiC) paper (600, 800 and 1200 grit) as a ground to remove the roughness and flatten the surface of the sintered sample thus refining the entire surface prior to

characterization. Polishing was done using a polishing cloth and diamond paste with 3 µ to 1 µ in order to obtain a reflective surface.

Hardness can be defined as a property of a material that measures the resistance of it towards permanent surface indentation or penetration (Albakry et al., 2003). This test will determine the ability of samples to withstand various forces. Vickers micro-hardness tester (Wolpert Wilson Instruments, USA – Germany) was used to analyze the hardness and fracture toughness of samples via indentation. An inverted pyramidal shape was used as the indenter and the schematic of the indentation can be represented in Figure 4.2. The loading force used varies between 100 g to 200 g and applied gently and held for 10 seconds.

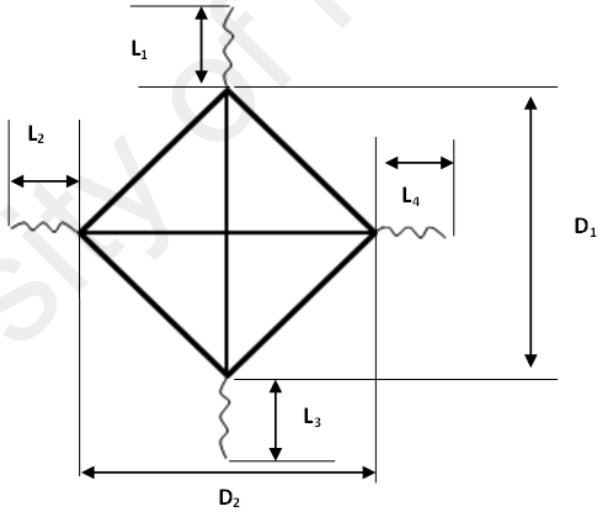

Figure 4.2: Schematic diagram of a pyramidal indenter used in Vickers hardness test (D1, D2 = diagonal length of indentation; L1, L2, L3, L4 = length of fracture).

By analyzing the crack or impression formed on the surface of the sample, the hardness of the sample can be obtained through the following equation:

$$H_v = 1.854P \,/\, ((2a)\text{^}2\,) \qquad (4.7)$$

Whereby,

H_v = Vickers hardness value

P = applied load

2a = average diagonal lengths = $\frac{D_1+D_2}{2}$

Vickers hardness value (H_v) can be obtained through the physical size of the indentation and based on the following ASTM E384-10e2 standard test method for Knoop and Vickers hardness of materials. In order to increase the accuracy of the measurement, three different points of indentations were made and the mean value was calculated.

Fracture toughness (K_{Ic}) of forsterite samples were measured using an equation formulated by Niihara (1985) (Equation 4.8). It is favorable to select Niihara's method because it is a non-destructive test which allowed the same sample to be used in obtaining three different locations for indentations. It has been verified in the literature that forsterite experienced Median or half-penny cracks instead of Palmqvist cracks (Kharaziha and Fathi, 2010).

$$\boldsymbol{K_{Ic} = 0.203 \times (\frac{c}{a})^{-1.5} \times H_v \times a^{0.5}} \quad (4.8)$$

Whereby,

K_{Ic} = fracture toughness

c = characteristic crack length (i.e. L + a, whereby L = average of L_1, L_2, L_3, and L_4 as depicted in Figure 4.2)

H_v = Vickers hardness value

a = half of the average diagonal length ($\frac{D1+D2}{2}$)

4.4.6 Grain size measurement

The grain size of forsterite bulk was measured on thermally etched samples via line intercept method on the SEM images. Polished surface was required for the measurement. In general, a test line was drawn on an A4 size SEM micrograph and the interception of the line and grain boundaries are calculated. At least 50 grains need to be covered by the test line and several lines are drawn before taking the average value. The average grain size was measured based on the equation suggested by Mendelson (1969) shown in Equation 4.9 and 4.10:

$$\bar{D} = 1.56\bar{L} \tag{4.9}$$

Whereby,

$\bar{D}$ = average grain size

$\bar{L}$ = measured average interception length over grains which was intercepted by the line drawn (equation 3.11)

$$\bar{L} = C/MN \tag{4.10}$$

Whereby,

C = total length of the test line

M = magnification of the SEM micrograph

N = number of intercepts

The method used to calculate the number of intersections was according to the Standard Test Method for Determining Average Grain Size (ASTM E112 – 10). The calculation of the number of intercept can be interpreted as follow:

- At the end point, if the line intercept with the grain boundary, it will be considered as 0.5 intersection. If the line does not intersect with grain boundary, no point will be given.
- Any tangential intersection with a grain boundary is considered as 1 intersection.
- Any line intersecting with triple-junction grain boundary is considered as 1.5 intersection.

This technique is restricted to certain limitations such as (Wurst and Nelson, 1972):

1. It can only be used on polycrystalline ceramics that formed a fully dense single-phase ceramic.
2. It requires a correction factor during the grain size calculation if two-phase microstructures were employed.
3. Huge amount of porosity and/or second phase (> 10 vol%) will greatly affect the accuracy of the measurement.

4.4.7 Morphology and Elemental Examination

4.4.7.1 Scanning Electron Microscope (SEM)

Scanning electron microscope (ProX, Phenom) and energy dispersive x-ray spectroscopy (EDX) were used to investigate on the morphology and elemental composition of bulk samples. It is important to analyze the grain structure as most mechanical behavior of ceramics is dependent to the grains. Elemental analysis was conducted to investigate the elements found on the selected spots on the grain structures.

Prior to SEM and EDX, the samples were grinded and polished to a mirror like surface finished. Upon polishing, samples were thermally etched at temperature 50 ^{o}C lower than its respective sintering temperature with holding time of 30 min and ramp rate of 10 ^{o}C/min for heating and cooling to delineate the grain boundaries.

4.4.7.2 Field-emission Scanning Electron Microscope (FESEM)

Similarly to SEM, field-emission scanning electron microscope was also used to investigate on the morphology of the bulk samples. The difference between SEM and FESEM is FESEM produced higher resolution images for a more detailed observation.

Prior to FESEM observation, the sample was etched (according to 3.3.8) and coated with platinum (~5 nm thickness) using JFC-1600 Auto Fine Coater, JEOL, to avoid from charging effect by increasing the conduction on sample during FESEM operation.

4.4.7.3 Transmission Electron Microscopy (TEM)

Transmission electron microscopy (TEM, JEOL, JEM-2100F, Japan) is another method to observe the morphology of samples with significantly higher resolution than SEM. This method was used to examine forsterite powder's size and shape. TEM operates similarly as a standard microscope but operating using electrons instead of light. With electrons acting as the source, it will travel through vacuum, concentrated into a thin beam using electromagnetic lenses, directed to the specimen (very thin and small area) and displayed at the viewing screen. The information of the imaging can be extracted by understanding that darker regions in the image imply more absorption of electrons by specimen and vice versa (Williams and Carter, 1996).

Prior to examination, the powder was suspended in ethanol and placed in an ultrasonic bath for 30 min to disperse the powder. The suspension was dripped on a copper grid which contained a holey carbon film and left to dry for 5 days in a dry cabinet. The flow chart of the project is shown in Figure 4.3.

4.4.7.4 Cell morphology

In this study, MC3T3-E1 osteoblast-like cell was used for cell morphology study. The cell attachment ability and morphology on the samples were evaluated by loading

the cells on the sample and incubated for 4 hours, 1 day and 3 days. The samples were rinsed gently under phosphate buffer saline and fixed with glutaraldehyde (Sigma-Aldrich, 3%) in sodium phosphate buffer at 4 ^{o}C for 2 hours. Then, graded series of ethanol solutions (50%, 60%, 70%, 80%, 90% and 100%) were used to dehydrate the samples with cell for 30 min at 4 ^{o}C. The samples were then dried in hexamethyldisilazane (HDMS, Wako, Japan). Fixation for 30 min was done on the cell area after adding 500 µl of HDMS. This step was repeated for three times in order to flush away the ethanol content completely. Upon evaporation of HDMS, the samples were gold-sputtered prior to SEM.

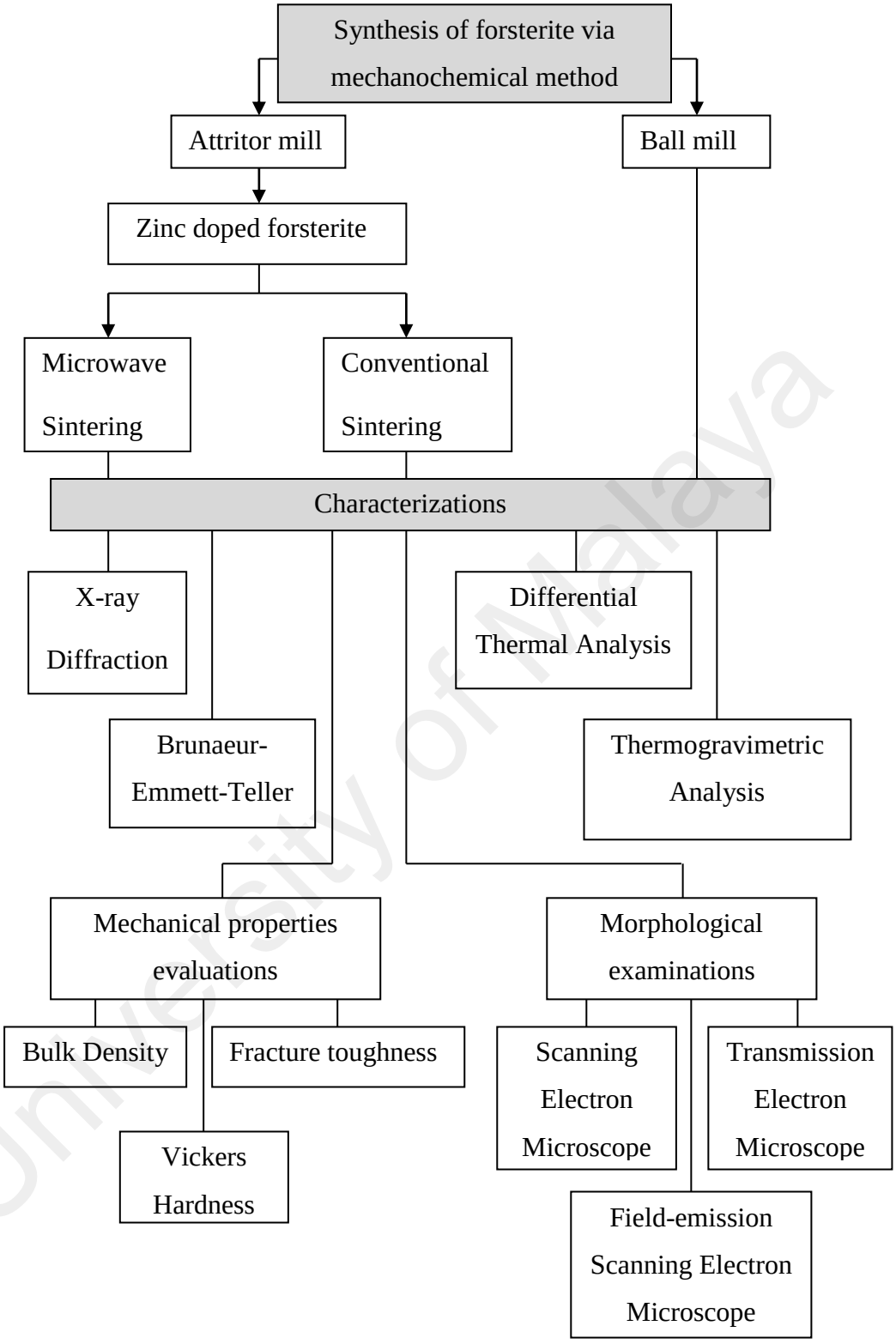

Figure 4.3: Flow chart of project research

CHAPTER 5: RESULTS AND DISCUSSION

The result and discussion will be divided into three major parts which include Part 1: Comparison in phase stability and mechanical properties between ball and attrition milling in synthesizing forsterite powder. Based on the outcome of this study, one of the milling methods will be selected based on the results obtained to undergo for Part 2: Sinterability of forsterite incorporated with zinc oxide (ZnO) as sintering additives. Prior to the investigation of ZnO addition on forsterite, a short cell morphology study was conducted using MC3T3-E1 osteoblast-like cell for 4 h, 1 day and 3 days to investigate on the cell attachment and cell spreading. In Part 2, mechanical properties of pure and doped-forsterite bulk will be compared upon conventional sintering in air atmosphere. Various ZnO content will be studied to obtain for the best profile for doped- forsterite. The beneficial effect of ZnO will be discussed in this Part by considering the grain size point of view. Lastly, comparison between microwave and conventional sintering will be deliberated in Part 3. Upon obtaining the results from Part 2, microwave sintering will be conducted on the samples with comprehensive examination of the "microwave effect" on doped and pure forsterite in terms of mechanical properties.

5.1 Part 1: Comparison between types of milling and milling duration in synthesizing forsterite ceramic

In this part, solid-state reaction method was chosen as the synthesizing method of forsterite but with different milling methods being employed. Prior to the comparison between the milling methods, initial study was conducted with 3 and 5 hours of milling duration for the ball milling in order to obtain the minimum milling duration required to obtain pure forsterite powder at 1300 ^{o}C.

5.1.1 Phase analysis of starting powder

Mixing of two precursors in solid-state reaction method was conducted via milling process. Prior to the synthesis, the precursors were verified using XRD and the traces were shown in Figure 5.1 and 5.2. It was found that the powders were pure with peaks of high intensities as each of the peaks corresponded with their respective chemical. The reference cards for all chemicals can be found in Appendix B. Any impurities/secondary phases will be indicated in symbols.

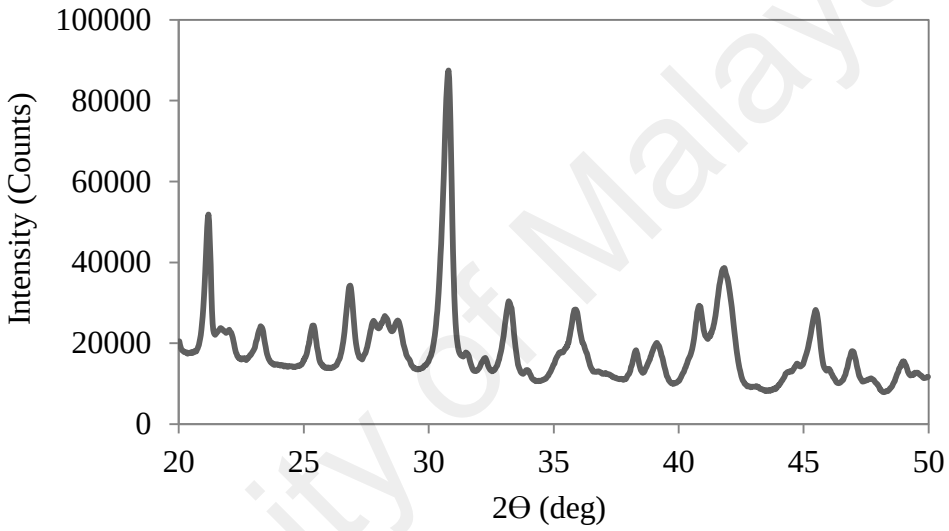

Figure 5.1: XRD traces of magnesium carbonate powder.

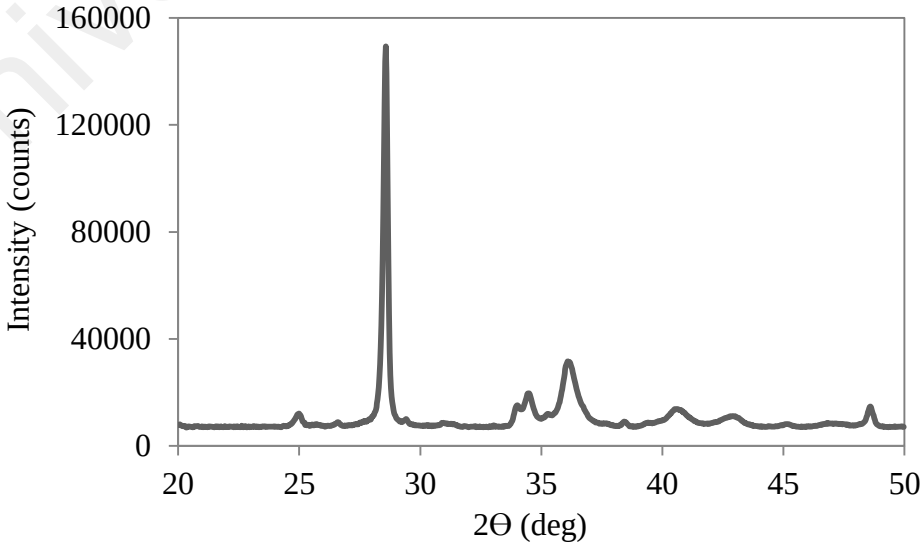

Figure 5.2: XRD traces of talc powder.

Prior to sintering, XRD was done on the milled mixture (proto forsterite) powder obtained after ball and attrition milling for 5 hours. Based on the XRD result (Figure 5.3), it was found that only two compositions were observed showing the presence of both magnesium carbonate and talc which were the two main precursors used. Both milling methods produced the same XRD traces of proto forsterite powder. Ammonium chloride (NH_4Cl) was not observed in the traces due to the very small amount added during the milling process. NH_4Cl was added into the mixture to act as a catalyst to form forsterite. It was insufficient to produce forsterite powder based only on milling process and this finding was in line with the result reported by Tavangarian & Emadi (2009). Thus, sintering was carried out to produce phase-pure forsterite powder.

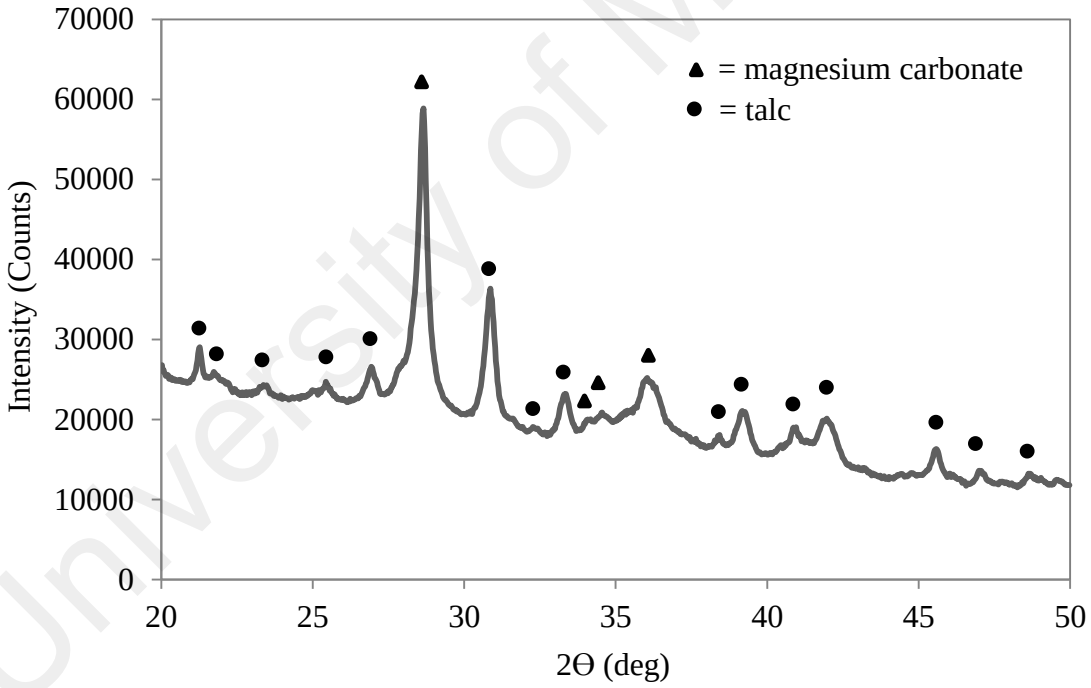

Figure 5.3: XRD traces of proto forsterite powder upon attrition milling for 5 hours.

5.1.2 Phase and particle size analysis of forsterite powder and bulk

Phase analysis was conducted on the samples with 3 and 5 hours of ball milling at temperature ranging from 1200 – 1500 ^{o}C. Based on Figure 5.4 and 5.5, both samples showed sign of secondary phase, particularly periclase (MgO), when sintered at 1200

^{o}C. It was found that sample with 5 hours milling had slightly higher degree of crystallinity as compared to 3 hours milling sample. For the XRD analysis, all the peaks show forsterite peaks (reference card: JCPDS 00-034-0189 found in Appendix B) unless stated.

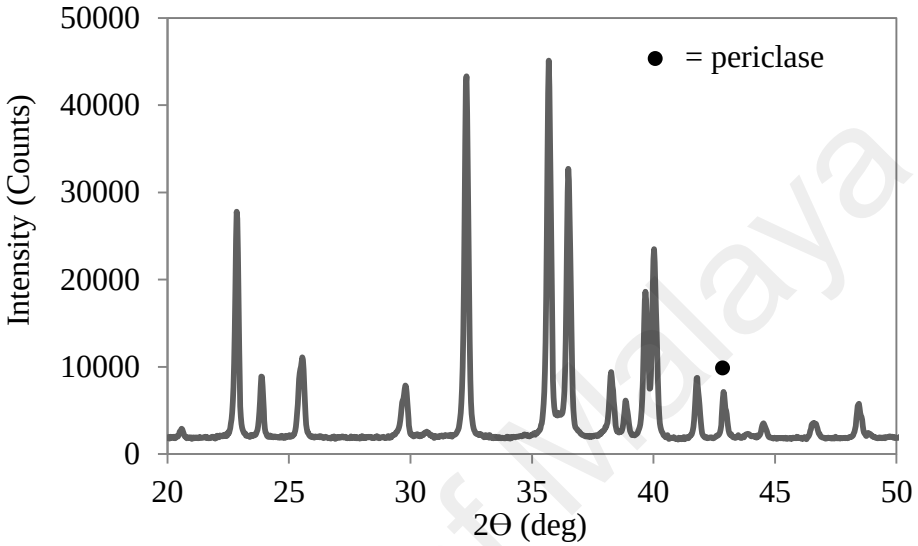

Figure 5.4: XRD of conventional milled forsterite bulk for 3 hours and sintered at 1200 ^{o}C for 2 hours at ramp rate of 10 ^{o}C/min.

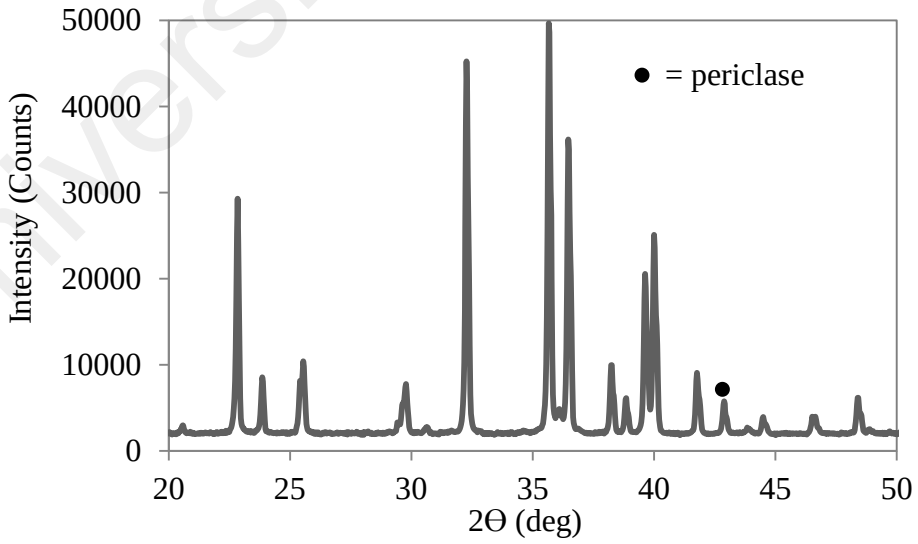

Figure 5.5: XRD of conventional milled forsterite bulk for 5 hours and sintered at 1200 ^{o}C for 2 hours at ramp rate of 10 ^{o}C/min.

Further increasing the sintering temperature to 1300 ^{o}C had successfully produce pure forsterite for samples with 5 hours milling. However, samples with 3 hours milling still showed sign of MgO but with lower intensity as compared when sintered at 1200 ^{o}C. This finding is in agreement with other researchers whereby the minimum required temperature to obtain pure forsterite powder without heat treatment is at 1300 ^{o}C. Figure 5.6 and 5.7 show the phase purity of both samples milled at 3 hours and 5 hours, respectively, sintered at 1300 ^{o}C. Subsequently, as the sintering temperature increases from 1200 to 1300 ^{o}C, the sample with 3 hours milling showed marginal decrease in the intensity of the MgO. It was suggested that the reaction rate during the intermediate stage had increased and gradually forming pure forsterite phase. In this preliminary study, only the appearance of MgO was observed and no enstatite ($MgSiO_3$) was found. From the work done by Tavangarian and Emadi (2010), the author found both secondary phases in the forsterite sample upon heating unlike the result found in this study.

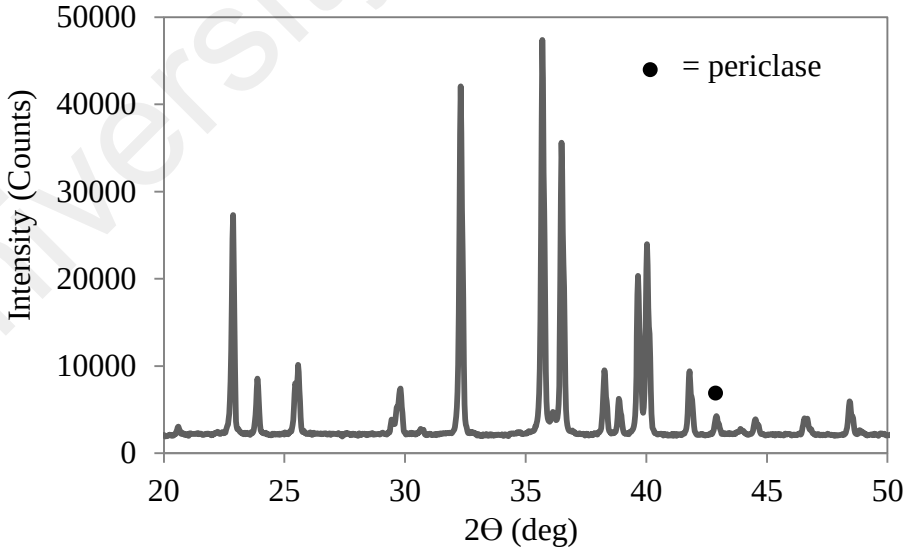

Figure 5.6: XRD of conventional milled forsterite bulk for 3 hours and sintered at 1300 ^{o}C for 2 hours at ramp rate of 10 ^{o}C/min.

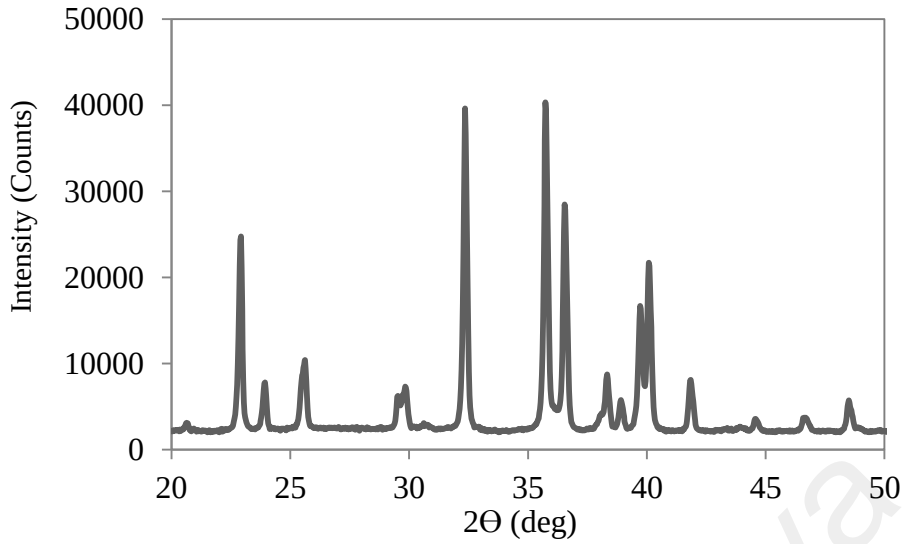

Figure 5.7: XRD of conventional milled forsterite bulk for 5 hours and sintered at 1300 ^{o}C for 2 hours at ramp rate of 10 ^{o}C/min.

Prolonging the milling duration has proven to be beneficial in forming pure forsterite powder at lower sintering temperature. This can be attributed by a more homogeneous mixing between the precursors (MHC and talc) and higher grinding energy thus reducing the required sintering temperature (energy) to obtain pure phase forsterite powder. The effect of higher grinding energy on the precursors could be observed through the particle size of the powders upon milling shown in Table 5.1. A slight decrease in the particle size (from 97.42 to 90.85 nm) and increase in specific surface area (from 18.83 to 20.19 m^2/g) had contributed towards the refinement of particles thus accelerating the process in forming pure forsterite powder when the milling duration increases. The relationship between particle size and the formation of pure forsterite can be explained via Herring's scaling law of sintering whereby the rate of sintering is inversely proportional to the square of the powder particle size. Fathi and Kharaziha (2009) also reported similar findings on the need for a longer milling duration to form pure forsterite at lower sintering temperature. Nonetheless, no further characterization was carried out by the researcher to provide sufficient understanding on the effect of milling duration on the particle and specific surface area of forsterite (Fathi &

Kharaziha, 2009). In this work, further sintering was carried out until 1500 ^{o}C and no decomposition or reappearance of secondary phases were observed for both samples as shown in Figure 5.8 and 5.9.

Table 5.1: Particle size and specific surface area of proto forsterite powder milled using conventional ball mill.

Samples	Specific Surface Area (m^2/g)	Particle Size (nm) via BET	Particle Size (nm) via TEM
Ball Mill (3 hr)	18.83	97.42	87-117
Ball Mill (5 hr)	20.19	90.85	60-73

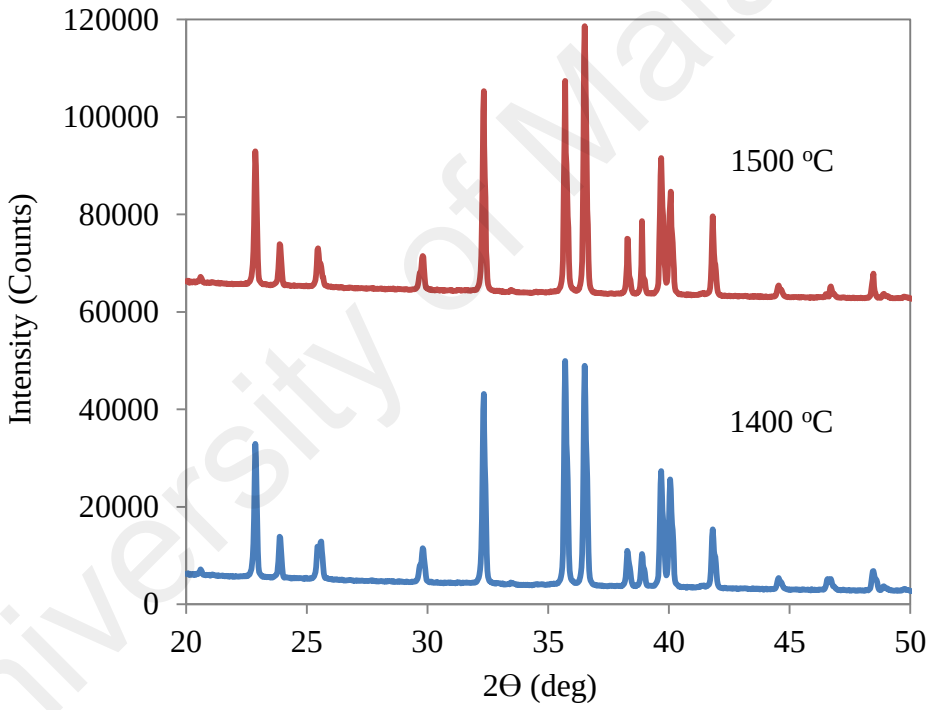

Figure 5.8: XRD of conventional ball milled forsterite bulk for 3 hours and sintered at 1400 and 1500 ^{o}C for 2 hours at ramp rate of 10 ^{o}C/min.

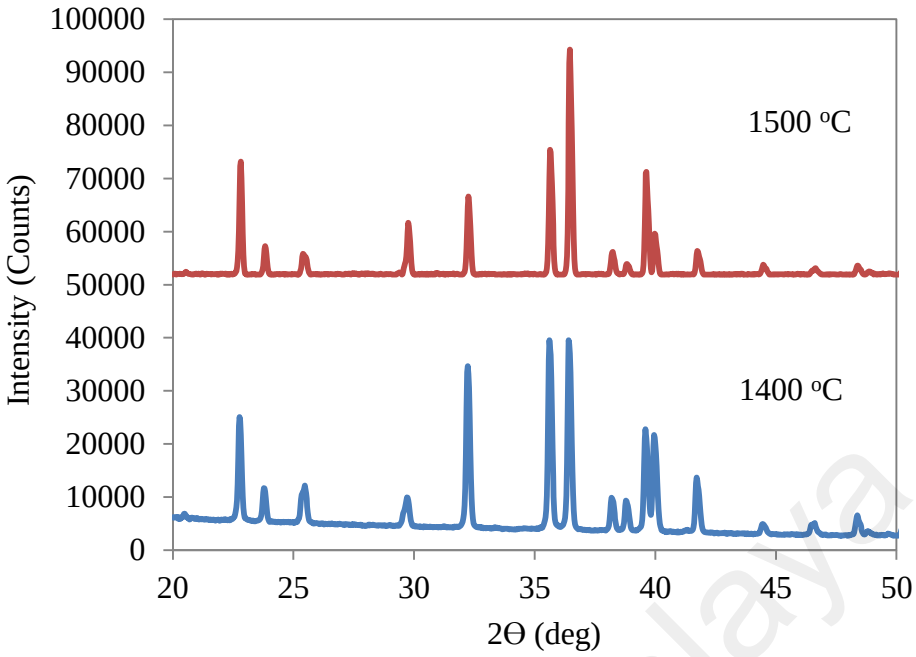

Figure 5.9: XRD of conventional ball milled forsterite bulk for 5 hours and sintered at 1400 and 1500 °C for 2 hours at ramp rate of 10 °C/min.

Upon XRD analysis on the samples, 5 hours of milling was selected as a fixed milling duration in order to ease the comparison between ball and attrition milling. Similarly, phase analysis was carried out on attritor milled samples sintered at 1200 to 1500 °C and the results were presented in Figure 5.10. It was found that at all sintering regime, only phase pure forsterite samples were observed implying that attritor milling produced significantly better result than ball milling.

Hence, by comparing the particle size and specific surface area, attritor milled powder showed significantly smaller particle size ranging from 23-28 nm with 4 times higher specific surface area value compared to ball milled powder (Table 5.2). It is agreeable that smaller particle size is correlated to the required sintering temperature to produce pure forsterite powder. This finding has contributed significantly towards the production of forsterite via solid-state method as pure forsterite can be obtain at lower sintering temperature without the need for heat treatment.

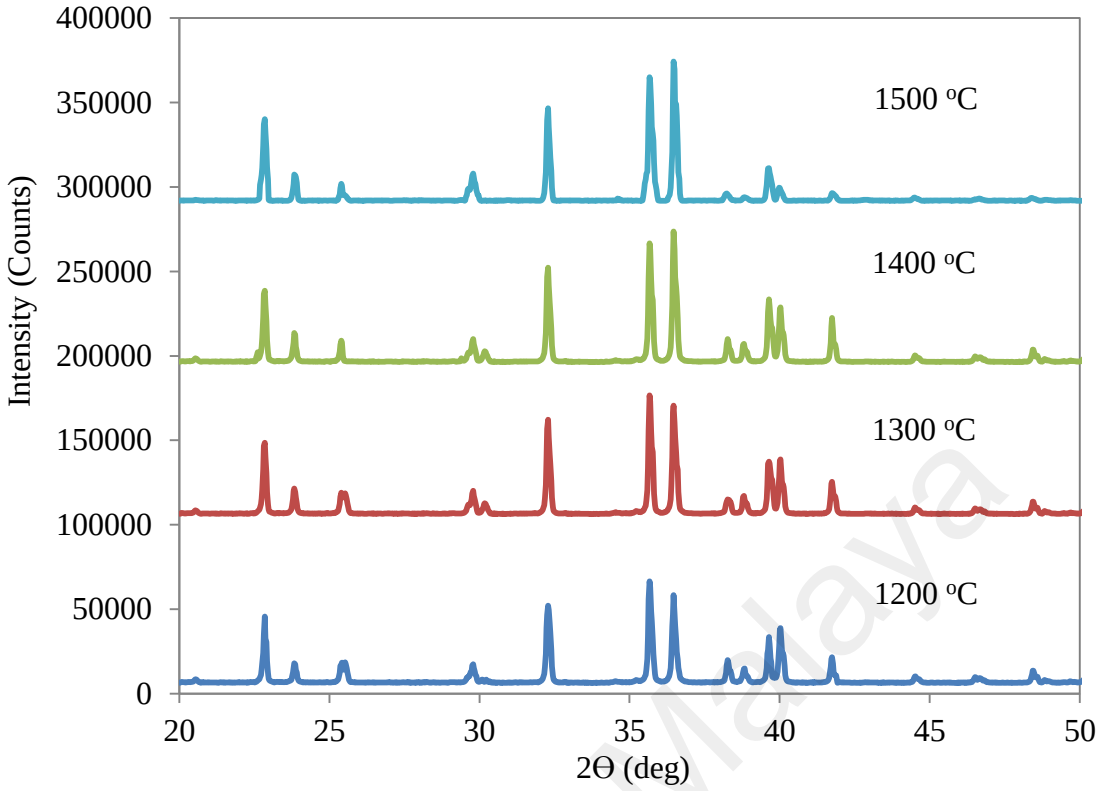

Figure 5.10: XRD of attritor milled forsterite bulk for 5 hours and sintered at 1200, 1300, 1400 and 1500 ^{o}C for 2 hours at ramp rate of 10 ^{o}C/min.

The particle size obtained in this present work is also comparable to that reported from sol-gel method by other researcher although sol-gel method is well-known to produce very small particle size powder (Sanosh et al., 2010). Further, in another work done by Mirhadi et al. (2015), two-step sintering was implemented in hope to control the growth of the particles. However, this method requires very long sintering duration (~ 22 hours) to obtain particle size of 33 nm which is almost similar to that obtained by using attrition milling with conventional sintering as found in the present research.

Table 5.2: Particle size and specific surface area of proto forsterite powder milled using conventional ball mill and attritor mill.

Samples	Specific Surface Area (m^2/g)	Particle Size (nm) via BET	Particle Size (nm) via TEM
Ball Mill (5 hr)	20.19	90.85	60-73
Attritor Mill (5 hr)	87.08	21.06	23-28

SEM image of the forsterite powder obtained via attrition milling showed a loosely packed fine powder with combination of both small and large particles (Figure 5.11).The TEM images of the powders were presented in Figure 5.12. Based on the images, all the powders were agglomerated due to the molecular attractions and the particle size of attritor milled powders showed significantly finer particles as compared to the ball milled powders, regardless of milling duration.

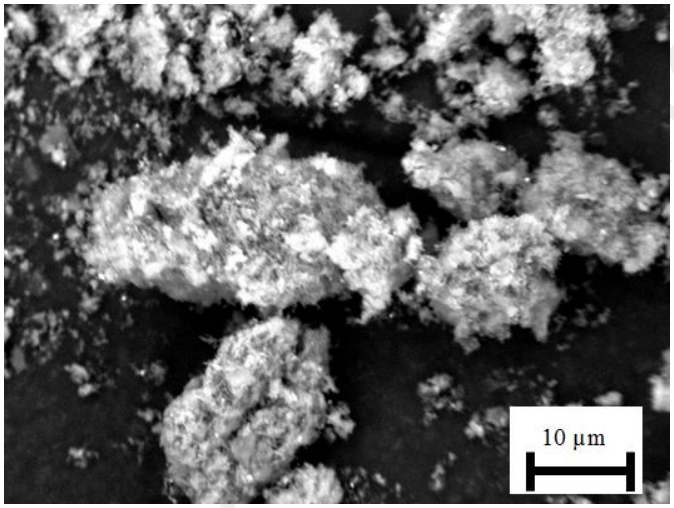

Figure 5.11: SEM image of forsterite powder upon attrition milling revealing the presence of loosely packed powders with both small and large size particles.

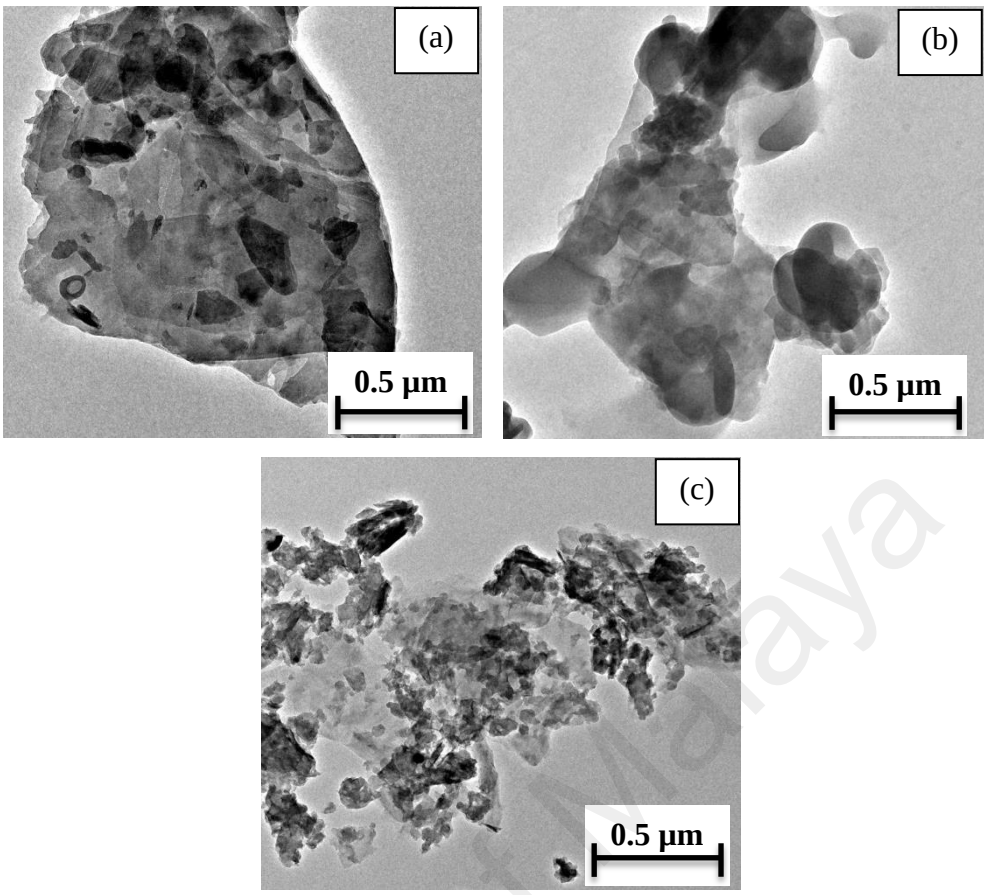

Figure 5.12: TEM images of powders upon (a) ball milled for 3 hours, (b) ball milled for 5 hours and (c) attritor milled for 5 hours.

5.1.3 Mechanical properties and cell morphology of forsterite

Based on the phase stability results obtained, it was found that attrition milling produced significantly better result than ball milling when milled (5 hours) and sintered (1200 – 1500 ^{o}C for 2 hours with ramp rate of 10 ^{o}C/min) at similar profile. Further investigation was carried out on the mechanical properties of both of these samples in terms of bulk density, Vickers hardness and fracture toughness followed with morphological testing to investigate the underlying mechanism for any mechanical enhancement found.

The effect of sintering temperature on the densification of both ball milled (BM) and attritor milled (AM) samples is shown in Figure 5.13. Samples were heated to the desired temperature at 10 ^{o}C/min, held for 2 hours and cooled to room temperature at 10

^{o}C/min. The theoretical density of forsterite was taken as 3.221 g/cm^{3} (Ghomi et al, 2011).

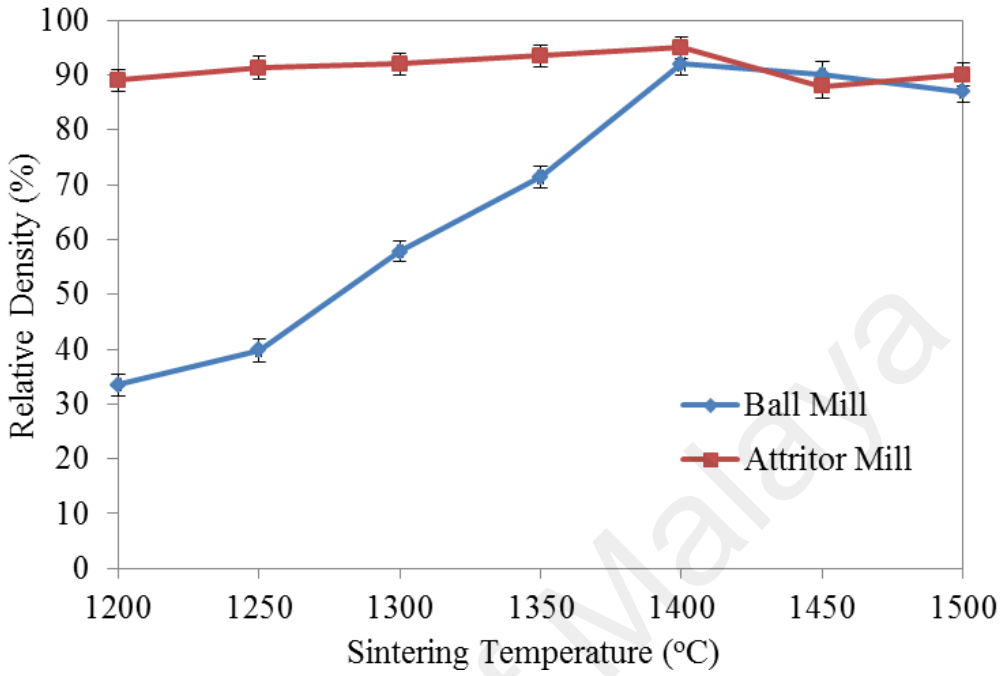

Figure 5.13: Relative density comparison between conventional ball mill (BM) and attritor mill (AM) for 5 hours of forsterite bulk as a function of sintering temperature.

Both samples showed similar trend of increasing in density with sintering temperature until 1400 ^{o}C. Beyond 1400 ^{o}C, a marginal decrease in the density for both samples was observed. At the lowest sintering temperature, AM sample had 89.0% relative density whereas BM sample was only at 37.8%. This can be attributed by the incomplete reaction between the precursors upon sintering. Presence of MgO in the sample had caused the density to be very low as compared to AM samples. MHC will breakdown into magnesium oxide and carbon dioxide during the initial reaction before combining with talc to form forsterite. Upon breaking down, MgO will react with talc to form forsterite when sufficient energy was provided. However, sintering temperature of 1200 ^{o}C was insufficient for the reaction to complete thus causing small traces of MgO in the BM sample.

At 1250 ^{o}C, AM sample had reached > 90.0% relative density and gradually increase from 91.3% at 1250 ^{o}C to 92.0% and 93.5% at 1300 ^{o}C and 1350 ^{o}C, respectively. On the other hand, BM sample showed tremendous increase from 1250 ^{o}C onwards with 39.8% relative density to 58.7% and 72.5% at 1300 ^{o}C and 1350 ^{o}C, respectively. A maximum relative density of 95.0% and 94.2% was obtained by AM and BM sample at 1400 ^{o}C, respectively. The difference in the relative density of both AM and BM was significant at the low sintering temperature. However, as sintering temperature increases to 1400 ^{o}C, only marginal difference in density was observed. This implied that the used of attrition milling had aided in the early formation of forsterite but did not improved the overall final densification of forsterite as BM sample also reached similar maximum density with AM sample at 1400 ^{o}C. At this point, both samples have reached the plateau in densification as the increased was not apparent.

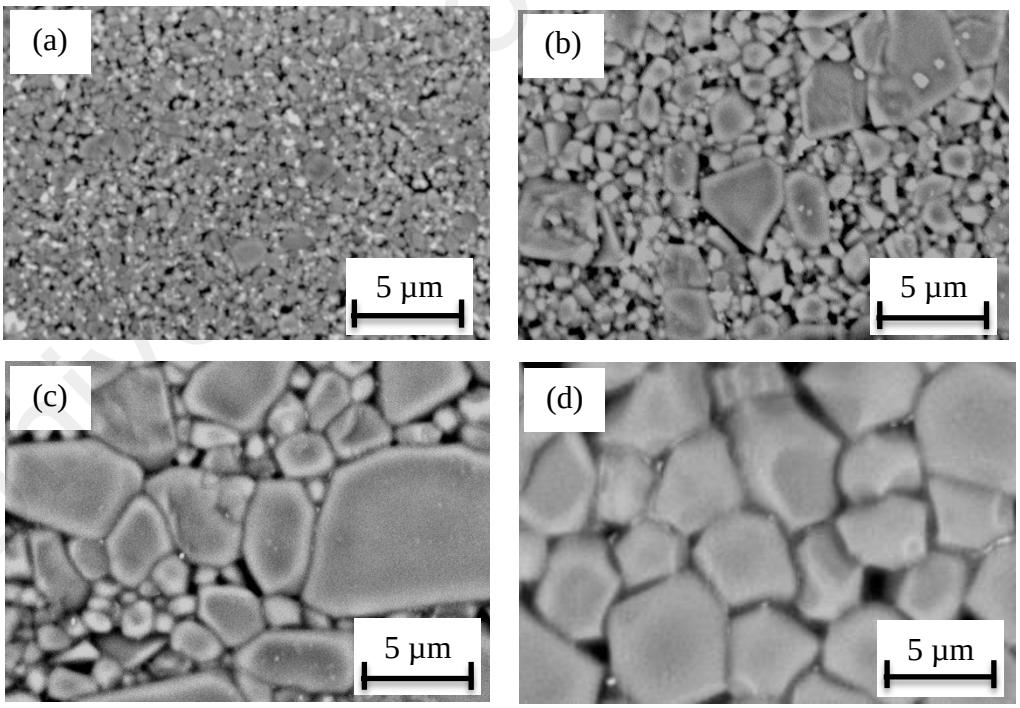

Figure 5.14: Morphology of AM sample sintered at (a) 1200 ^{o}C, (b) 1300 ^{o}C, (c) 1400 ^{o}C and (d) 1500 ^{o}C for 2 hours at 10 ^{o}C/min. Large pores were entrapped between small and large grains when sintered at 1500 ^{o}C.

Due to the inconsistent grain size and grain growth of forsterite as shown in Figure 5.14, pores were entrapped in between the grains and limit the densification up to 95.0% only. The reduction in densification of forsterite after sintered above 1400 ^{o}C was attributed by the grain growth of forsterite. At this point, the grains had grown excessively large leading to the inability for the pores to be removed from the grains completely. Nevertheless, the densification of AM samples is presently higher than Ni et al. (2007) and Sara et al. (2011) that obtained 92.5% using sol-gel route and 90.7% using solid-state method, respectively.

The effect of sintering temperature on the hardness of forsterite is shown in Figure 5.15. In general, AM samples showed a more superior hardness than BM samples at all sintering regime. A maximum of 9.8 GPa was successfully obtained by the AM sample at a low sintering temperature of 1250 ^{o}C. A mild fluctuation within the range of 9.4 GPa to 9.8 GPa was observed throughout the sintering range from 1250 ^{o}C to 1400 ^{o}C.

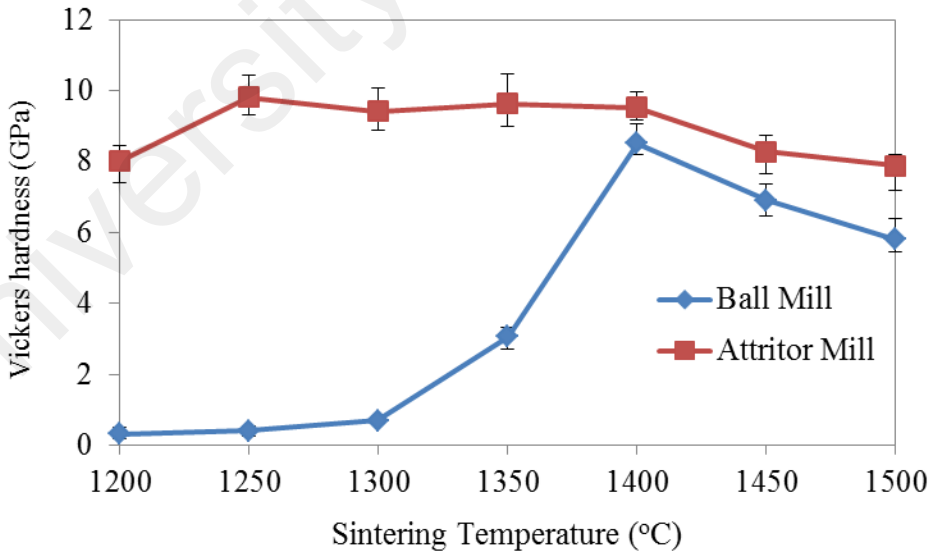

Figure 5.15: Vickers hardness of ball and attritor milled forsterite as a function of sintering temperature.

On the other hand, BM samples showed similar trend to the densification with a maximum hardness of 8.52 GPa obtained at 1400 ^{o}C. Beyond 1400 ^{o}C the hardness

started to decrease. The very low hardness (< 1 GPa) of BM samples at 1200 ^{o}C was due to the presence of secondary phase, MgO, and also the slow densification. Also, the increase in density of BM samples can be reflected with the improved of hardness with increasing sintering temperature until 1400 ^{o}C as plotted in Figure 5.16. A slow increase in hardness from 1200 ^{o}C to 1300 ^{o}C signified that early grain formation was still taking place which is illustrated in Figure 5.17. Thereafter, formation of grains began at 1350 ^{o}C in which a drastic increase in hardness was observed. Nevertheless, a decrease in hardness was observed for both AM and BM samples when sintered above 1400 ^{o}C owing to the rapid diffusion process.

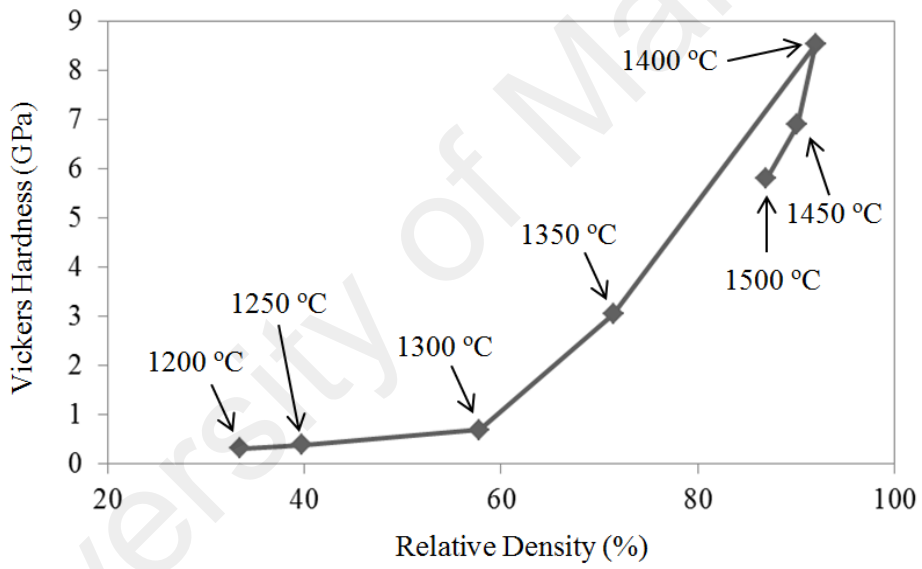

Figure 5.16: Variation of hardness with density of sintered BM samples

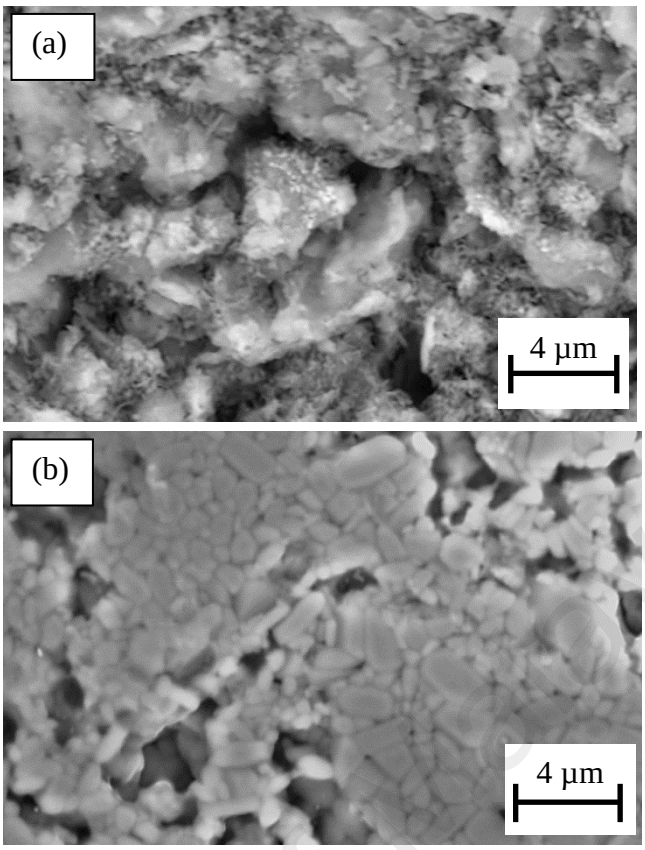

Figure 5.17: Morphology of BM sample sintered at a) 1200 ^{o}C and b) 1300 ^{o}C for 2 hours at 10 ^{o}C/min.

According to Ramesh et al. (2013), the hardness of forsterite continued to increase with sintering temperature from 1200 to 1500 ^{o}C. This finding was not reflected with the result obtained using attrition milling due to the difference in the particle size. Finer particles obtained from high grinding energy using attritor mill has led to the early formation of grains at low sintering temperature (1200 ^{o}C) as shown in Figure 5.14a. Further, BM samples showed almost similar trend as Ramesh et al. (2013) work but due to excessive grain growth of BM samples, the hardness began to deteriorate above 1450 ^{o}C unlike the other author's work. Grain growth at high sintering temperature is unavoidable due to the acceleration of diffusion process.

The fracture toughness of both samples sintered at various temperatures was plotted in Figure 5.18. The BM sample showed an increase in fracture toughness during the initial stage of sintering until 1400 ^{o}C. Beyond this temperature, the value of fracture toughness began to drop and this trend was seen to be similar to that of density and hardness. At 1200 ^{o}C, the fracture toughness of BM sample had less than 0.8 MPa $m^{1/2}$ and the increase in sintering temperature to 1300 ^{o}C showed a very slow increment of fracture toughness for BM sample. Nonetheless, a drastic increase in fracture toughness was observed when sintering temperature reached 1350 ^{o}C whereby the value had increased from 0.8 MPa $m^{1/2}$ to 3.22 MPa $m^{1/2}$ and continued increasing to a maximum of 3.52 MPa $m^{1/2}$ at 1400 ^{o}C. Beyond this temperature, the fracture toughness had deteriorated.

On the other hand, for AM samples, the fracture toughness values showed a fluctuating trend initially but reside with a maximum fracture toughness of 4.3 MPa $m^{1/2}$ at 1400 ^{o}C, and deteriorate as the sintering temperature continued to increase, similar to BM sample's trend. The fracture toughness value of AM sample was significantly higher than the BM sample at almost all sintering regime. In comparison with the results obtained via two step sintering conducted by Fathi and Kharaziha (2009), they had obtained only 3.61 MPa $m^{1/2}$ for fracture toughness. The effect of high grinding energy using attrition milling had significantly enhanced the fracture toughness of forsterite as compared to conventional milling and two-step sintering method.

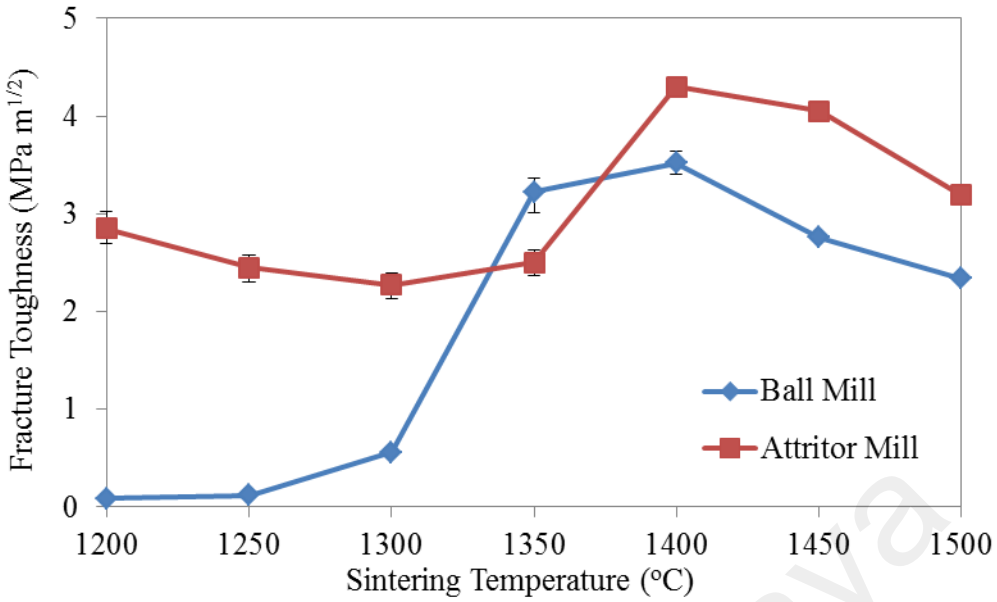

Figure 5.18: Fracture toughness of ball and attritor milled of forsterite as a function of sintering temperature.

In regards to the drastic increase of fracture toughness value for BM sample at sintering temperature of 1350 ^{o}C, it can attributed by not only the grain formation but also the shape of the grains. Elongated grain structures were observed throughout the forsterite sample as shown in Figure 5.19. It was believed that such grain structure could contribute to the enhancement of fracture toughness especially when they were dispersed evenly around the grain matrix. Becher et al. (2005) also found that large fraction of elongated grains enhanced crack deflection and subsequently increase the fracture toughness of the material. Nonetheless, although BM samples had elongated grains, AM samples still showed significantly better fracture toughness properties due to the initial powders obtained. The particle size obtained played a more prominent role in enhancing the mechanical properties of forsterite instead of the grain shape. Both samples showed a decrease in fracture toughness beyond 1400 ^{o}C due to the excessive grain growth phenomena as observed in Figure 5.14 and 5.20.

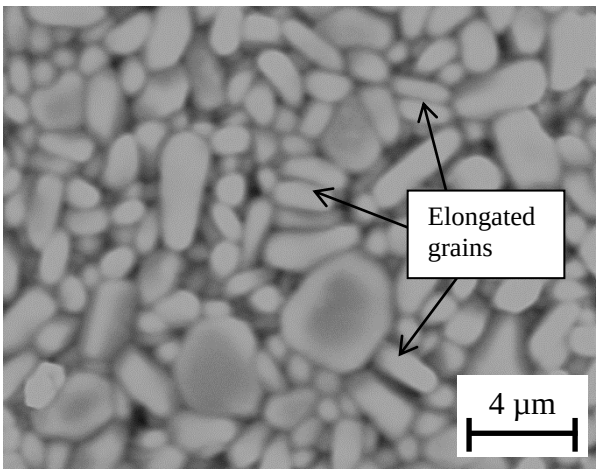

Figure 5.19: Morphology of BM sample sintered at 1400 ^{o}C. Arrows showed the formation of elongated grain structure in forsterite.

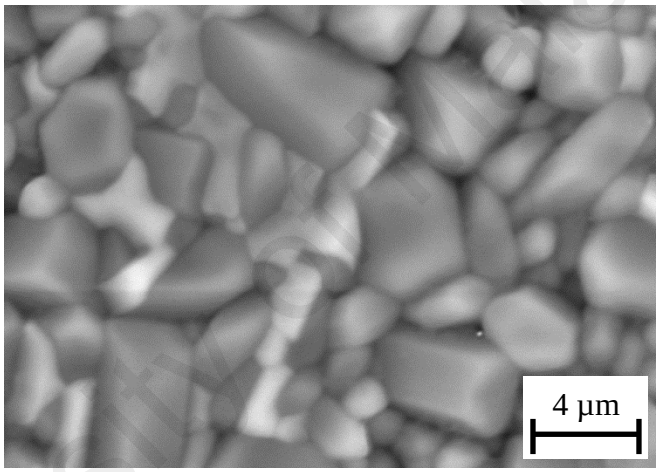

Figure 5.20: Morphology of BM sample sintered at 1500 ^{o}C. High ratio of large to small grain was observed and pores were still detected.

Figure 5.21 and 5.22 represent the morphologies feature of osteoblast-like cells cultured on AM sample (sintered at 1400 ^{o}C) for 4 h, 1 day and 3 days of culture. Based on observation on 4 h cultured sample, the attached cell showed sign of filopodial extensions (white arrow) conforming to the AM sample. It was observed that the cells adhere and spread well throughout the sample surface with bridges formed across the undulations while spreading over them.

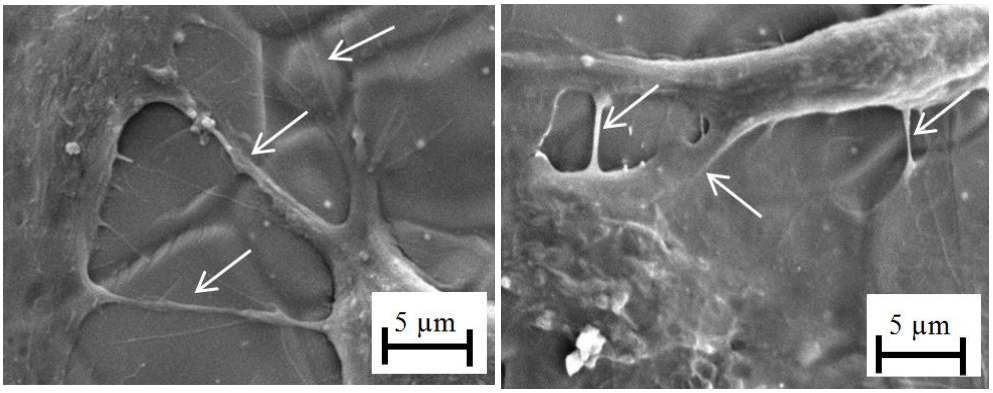

Figure 5.21: Cell morphology upon culturing for 4 hours on AM sample (sintered at 1400 ^{o}C). The white arrows indicate the adhered cell with filopodial extensions.

As the incubation time prolonged to 1 day and 3 days, the cells continue to proliferate on the surface of AM sample as shown in Figure 5.22. Small cells are growing on the surface of AM sample seen on day 1 culture with whisker-like filopodial. The cells were still growing continuously and on day 3 of culture, dense layer of cells were observed covering the surface of sample to induce extracellular matrix development. This promising result showed that AM sample has the potential to be used in clinical application.

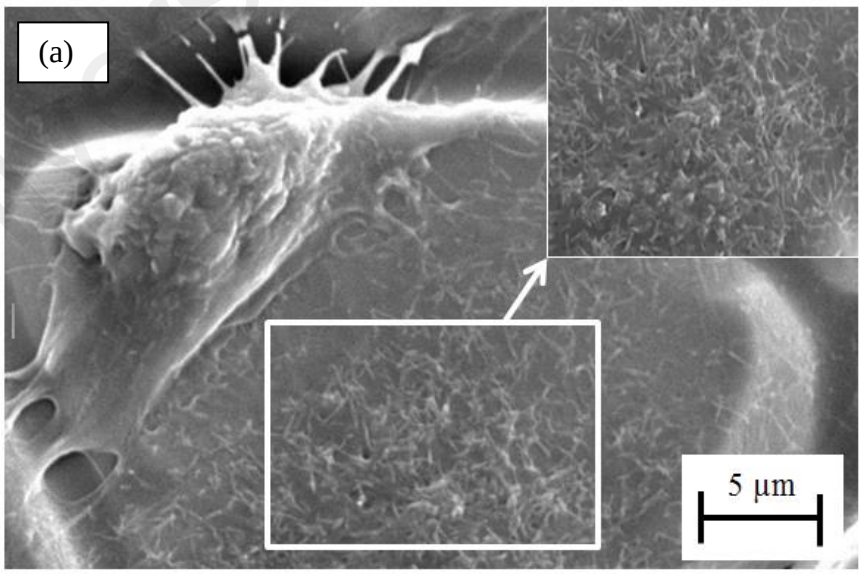

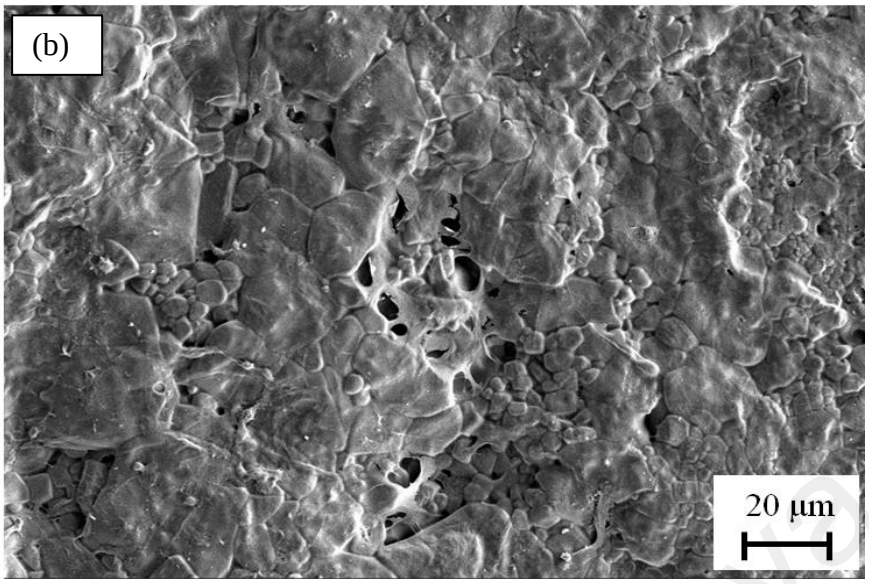

Figure 5.22: SEM image of cells proliferation of MC3T3-E1 on AM sample: (a) 1 day culture and (b) 3 days culture.

5.2 Part 2: Comparison between ZnO doped forsterite and pure forsterite

This section will discuss on the effect of doping forsterite with small amount of zinc oxide (ZnO). Forsterite powder was prepared prior to the doping process. Unlike the previous work discussed in Section 5.1, whereby forsterite bulk was immediately synthesized without heat treatment process during the powder stage, this study requires forsterite powder prior to the doping process. According to literatures, directly heating the mixture containing the precursors (MHC and talc) with the sintering additives would result in the substitution instead of doping of forsterite (Andrew, 2007; Song, 2010). Thus, heat treatment was conducted on the attritor milled powder upon sieving at 1000 ^{o}C for 2 hours with a ramping rate of 10 ^{o}C/min using a box furnace.

Thermal analysis was conducted on the powder to observe for any exothermic peaks which will indicate the crystallization temperatures of forsterite. The weight losses during the heating process was also observed to rectify the thermal analysis obtained and justify the probable processes that could occur during the entire heat treatment stage. The differential thermal analysis (DTA) was carried out from 100 to 1000 ^{o}C. Based on Figure 5.23, two endothermic peaks (at 200 ^{o}C and 450 ^{o}C) and two exothermic peaks (815 ^{o}C and 940 ^{o}C) were observed. Two stages of weight loss were observed at below 200 ^{o}C and 450 ^{o}C. The first stage of weight loss could be attributed by the removal of water content within the powder. Second stage showed a more significant reduction in the weight owing to the decomposition of magnesium carbonate and chlorine ion as well as the crystallization of MgO. This occurrence was also supported by Fathi and Kharaziha (2008) in which similar phenomena was observed in the author's work. Upon crystallization of MgO, the weight continued to decrease marginally until 1000 ^{o}C. Further, the two exothermic peaks were observed in the DTA analysis which defined the beginning of the formation of forsterite. According to Fathi and Kharaziha (2009), the decomposition of MHC into MgO and CO_2 is a positive free

energy change indicating that the reaction is endothermic whereas the formation of forsterite occurred due to the negative free energy change which indicates an exothermic reaction. Thus, heat treatment temperature of above 940 ^{o}C was used in order to form pure forsterite powder.

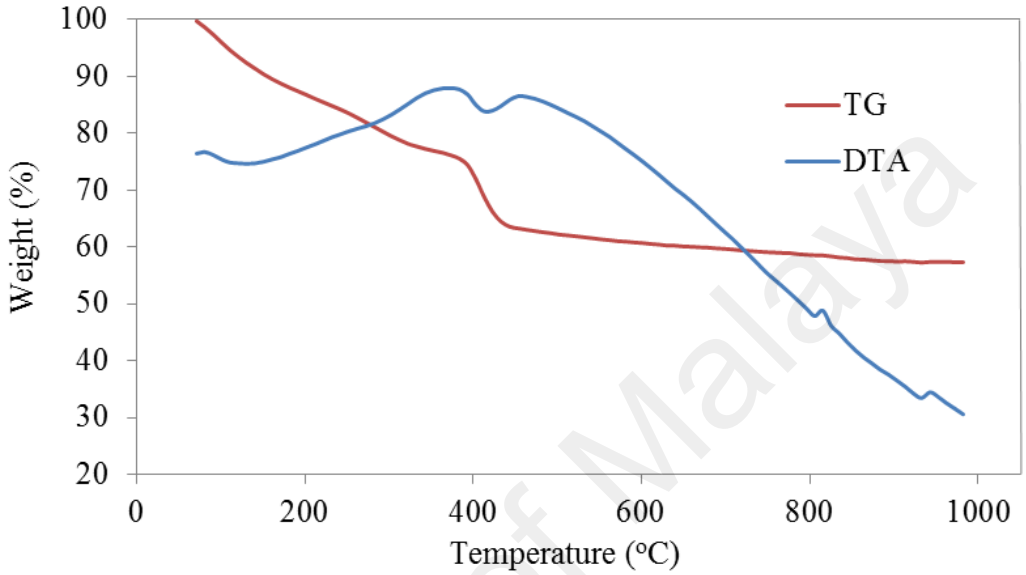

Figure 5.23: TG and DTA curves of attritor-milled powder heat treated up to 1000 ^{o}C.

The phase analysis of the heat treated powder is shown in Figure 5.24. Only pure forsterite peaks were observed in the XRD result. Phase pure forsterite powder was successfully obtained prior to the doping process. Upon doping via attrition milling, the green samples were obtained using uniaxial pressing followed by pressureless sintering at predefined temperatures.

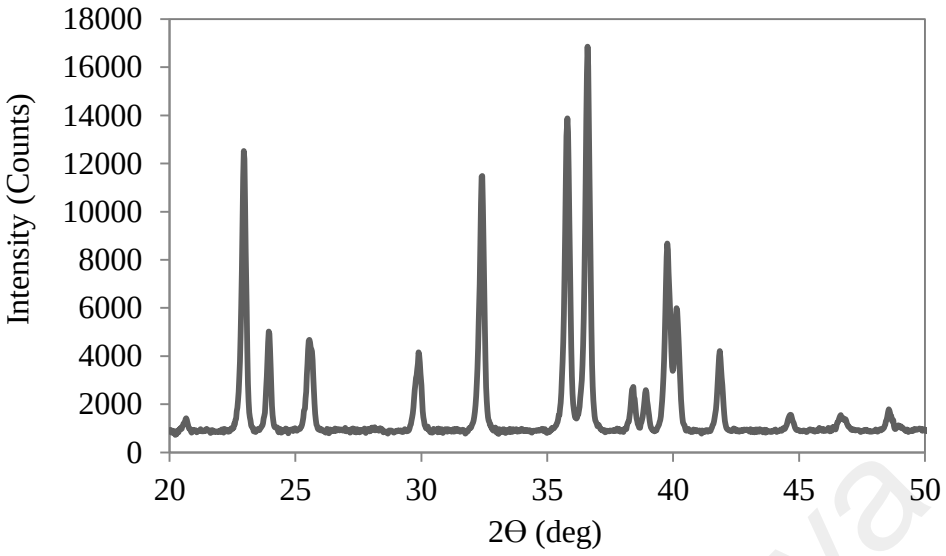

Figure 5.24: XRD of heat treated forsterite powder at 1000 ^{o}C for 2 hours with ramping rate of 10 ^{o}C/min.

5.2.1 Phase and elemental analysis of forsterite bulk

The XRD signatures of all the samples (pure and doped) showed no presence of secondary phases as shown in Figure 5.25, 5.26, 5.27 and 5.28. All XRD figures are accompanied with the JCPDS reference number 34-0189 for forsterite. These results showed that the addition of ZnO did not cause any decomposition on forsterite at all sintering regime. XRD analysis was unable to trace the presence of ZnO due to the very small content added into forsterite. Hence, it can be assumed that sintering temperature and dopant content did not affect the phase stability of forsterite.

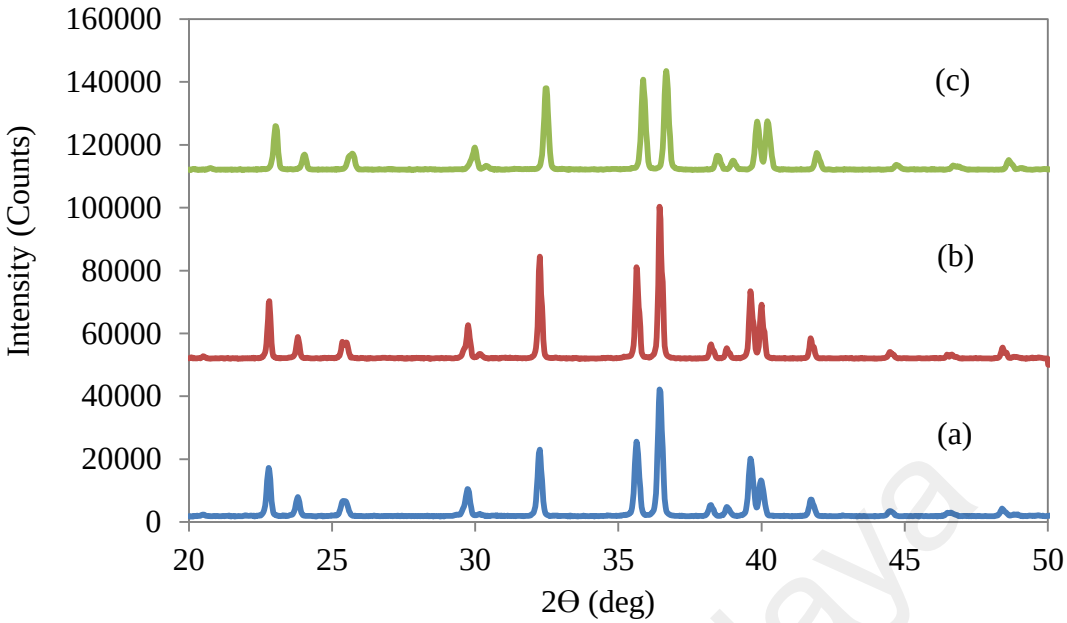

Figure 5.25: XRD traces of pure (undoped) forsterite sintered at (a) 1200 ^{o}C, (b) 1250 ^{o}C and (c) 1500 ^{o}C.

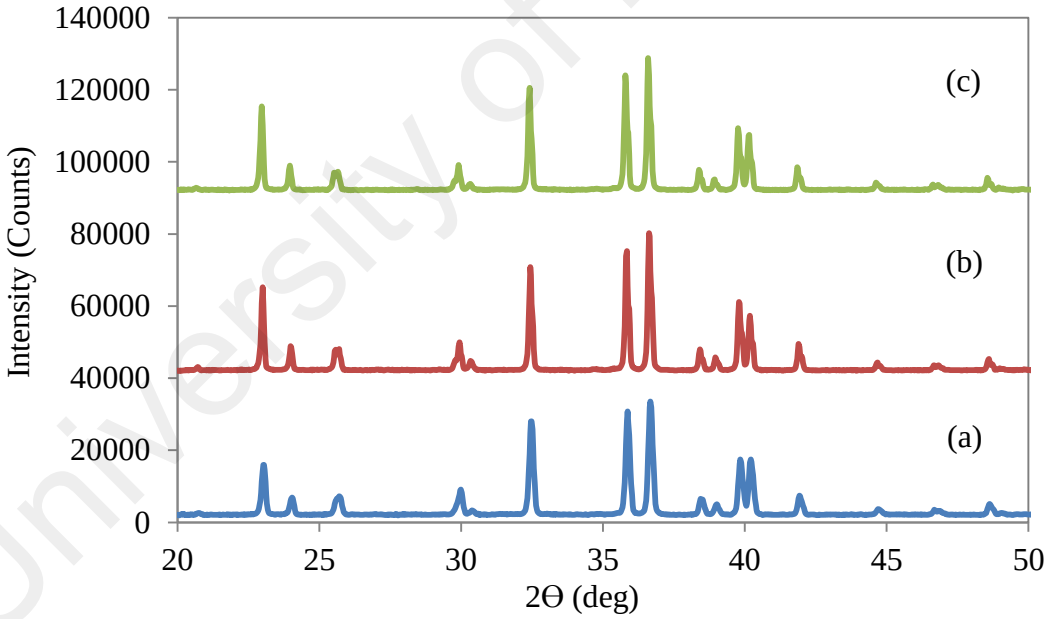

Figure 5.26: XRD traces of 0.5 wt% ZnO doped forsterite sintered at (a) 1200 ^{o}C, (b) 1250 ^{o}C and (c) 1500 ^{o}C.

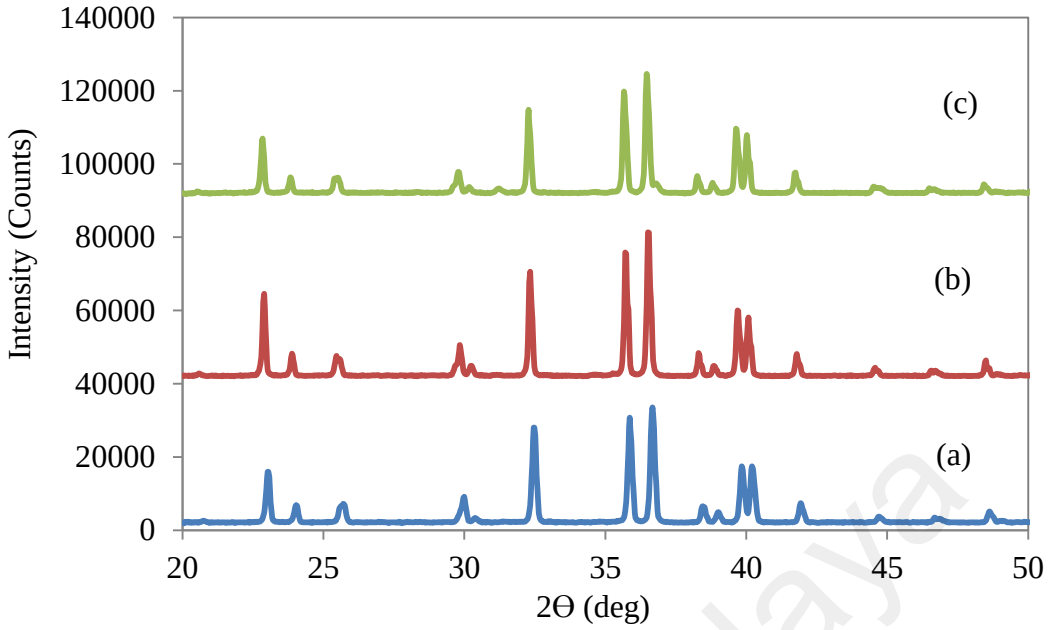

Figure 5.27: XRD traces of 1.0 wt% ZnO doped forsterite sintered at (a) 1200 ^{o}C, (b) 1250 ^{o}C and (c) 1500 ^{o}C.

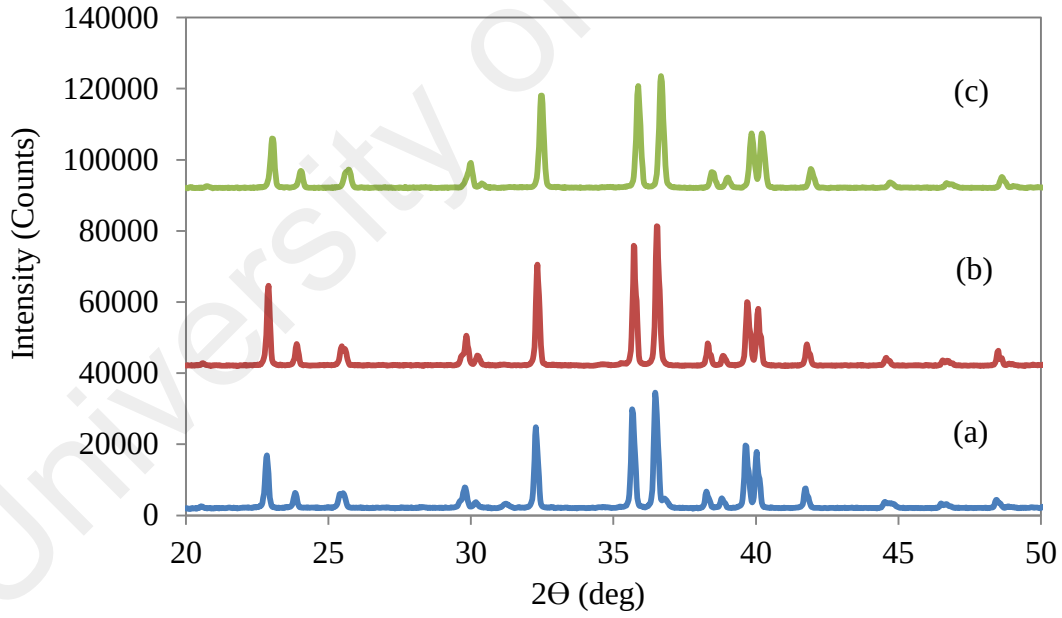

Figure 5.28: XRD traces of 3.0 wt% ZnO doped forsterite sintered at (a) 1200 ^{o}C, (b) 1250 ^{o}C and (c) 1500 ^{o}C.

Only 3.0 wt% ZnO doped forsterite samples showed the ZnO peak during the elemental analysis at all sintering regime as shown in Figure 5.29. The small amount of ZnO (< 3.0 wt%) added was undetected in both phase and elemental analysis.

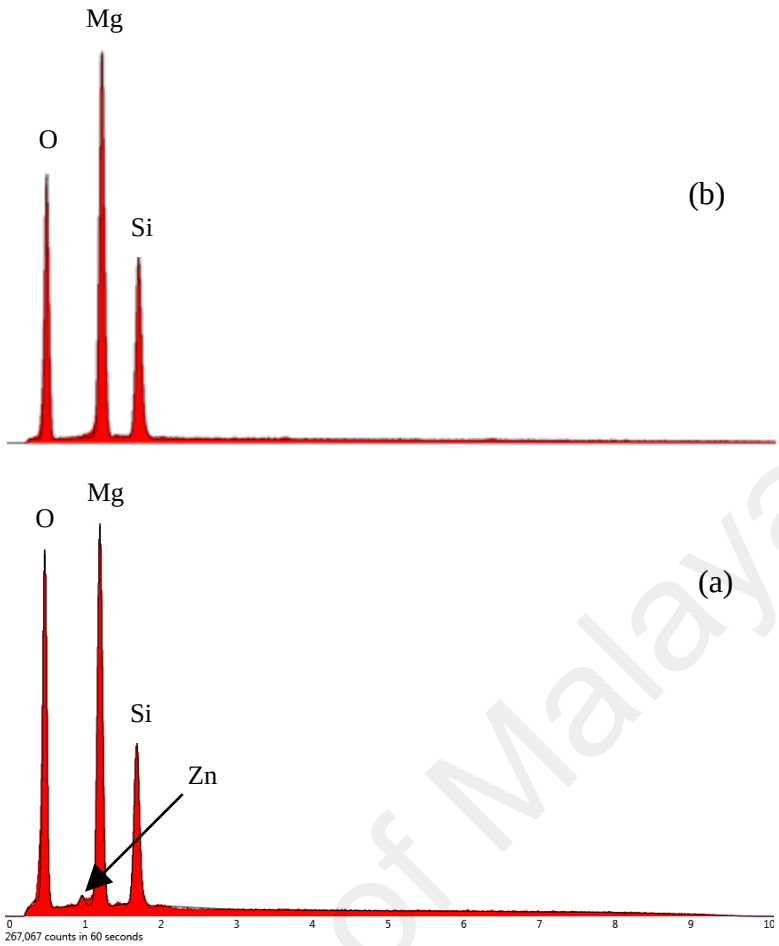

Figure 5.29: Elemental analysis of (a) 3.0 wt% and (b) 1.0 wt% of ZnO content sintered at 1500 ^{o}C

5.2.2 Sinterability of forsterite bulk

All samples sintered at 1500 ^{o}C showed sign of possible melting because of the difficulty in removing the samples from the crucible. Upon removal, the side that is in contact with the crucible showed slight distortion on the surface. Hence, no further sintering was carried out above 1500 ^{o}C. The effect of ZnO doping on the relative density of forsterite is shown in Figure 5.30.

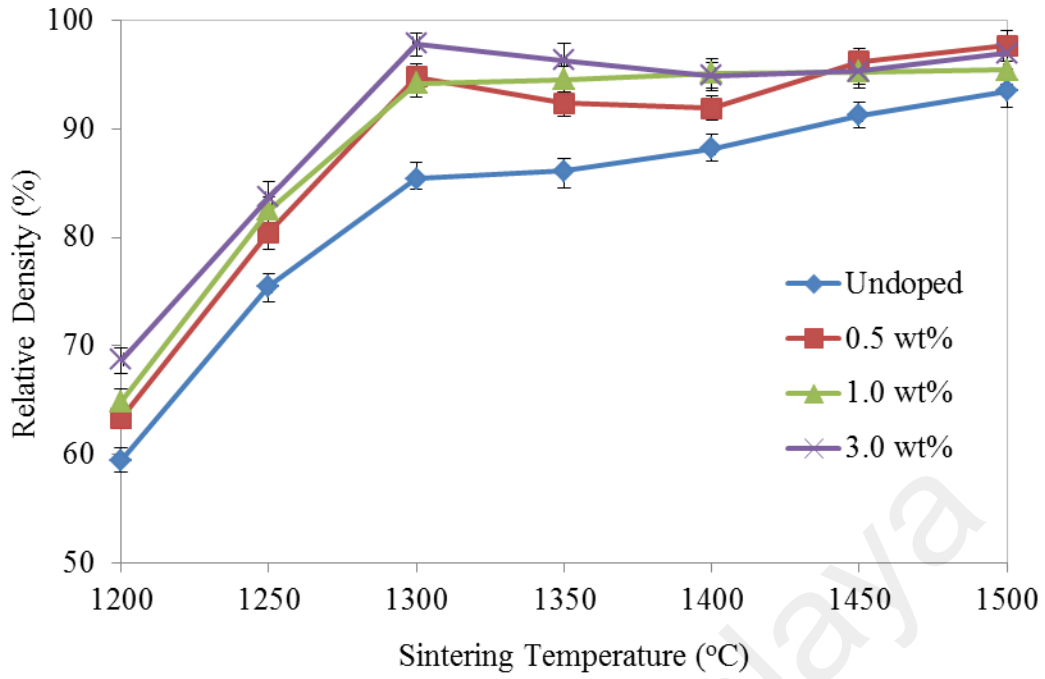

Figure 5.30: Relative density variation as a function of sintering temperatures for forsterite.

Generally, the bulk density of all samples increases with sintering temperature. Pure forsterite samples showed continuous increase in bulk density up to 1500 ^{o}C with a maximum value of 93.5%. A drastic rate of increase in density was observed when sintered from 1200 ^{o}C to 1300 ^{o}C. On the other hand, the inclusion of ZnO in forsterite possessed significantly higher bulk density at all sintering regime and reached a maximum of 97.8 % relative density at 1300 ^{o}C for 3.0 wt% doped samples followed by 0.5 wt% and 1.0 wt% ZnO doped samples with value of 97.7% and 95.5%, respectively, sintered at 1500 ^{o}C. Among all compositions, 3.0 wt% doped samples reached its densification plateau at 1300 ^{o}C whereas other compositions at 1400 ^{o}C. Based on this early investigation, it can be implied that ZnO addition is beneficial to the densification of forsterite.

The effect of ZnO inclusion on the average Vickers hardness sintered at various temperatures is shown in Figure 5.31. All sintered samples showed similar trend with an early increase in hardness to a maximum value and gradually decrease with increasing

sintering temperatures. As seen on the pure forsterite samples, the hardness continue to increase from 1200 ^{o}C to a maximum of 8.5 GPa at 1400 ^{o}C and eventually decrease beyond this temperature. Based on observation, it was found that all doped samples possessed similar maximum hardness value of 9.7-9.9 GPa and the highest hardness obtained by 1.0 wt% sample at 1400 ^{o}C.

However, when the samples were sintered at the lowest sintering regime (1200 ^{o}C), most of the samples showed < 1 GPa and this could be correlated with the low bulk density (Figure 5.31) obtained. Morphology examination in Figure 5.32 had justified that all samples had yet to densify to fully form grains. Huge pores were observed particularly on pure forsterite sample which contributed in the very low density and hardness. Also, owing to the porosity, fracture toughness measurement was unable to be conducted on 1200 ^{o}C sintered samples as no cracks could propagate through the large pores.

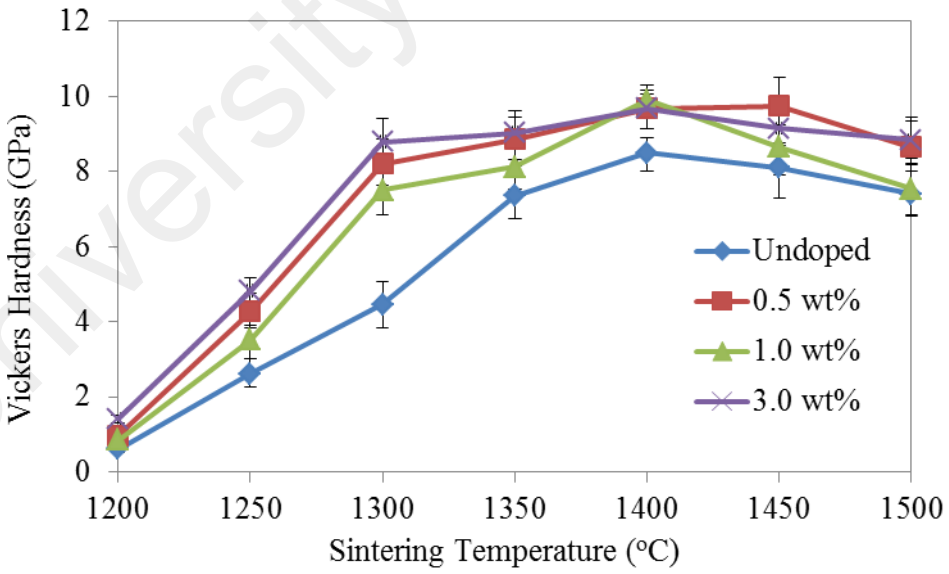

Figure 5.31: Vickers hardness variation as a function of sintering temperature for forsterite.

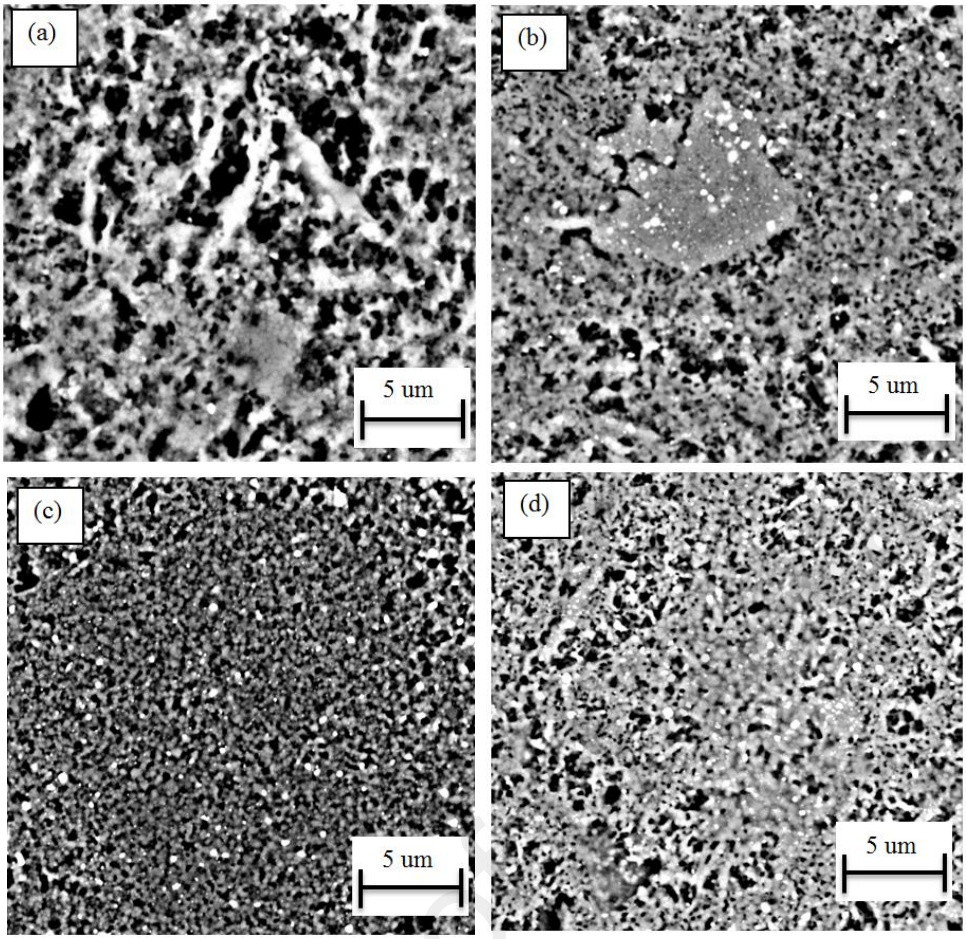

Figure 5.32: Morphology of (a) undoped, (b) 0.5 wt%, (c) 1.0 wt% and (d) 3.0 wt% ZnO-doped forsterite sintered at 1200 ^{o}C.

The inclusion of ZnO also enhanced the fracture toughness of forsterite as shown in Figure 5.33. As the sintering temperature increases, all ZnO composition except 3.0 wt% samples showed similar trend with the pure forsterite. In fact, the fracture toughness trends of these samples are the same with trend of Vickers hardness as well. The variation of Vickers hardness with fracture toughness for pure forsterite sample was shown in Figure 5.34. This trend is similar to that of 0.5 wt% and 1.0 wt% ZnO samples whereby the decrease in hardness beyond sintering temperature of 1400 ^{o}C has deteriorated the fracture toughness as well.

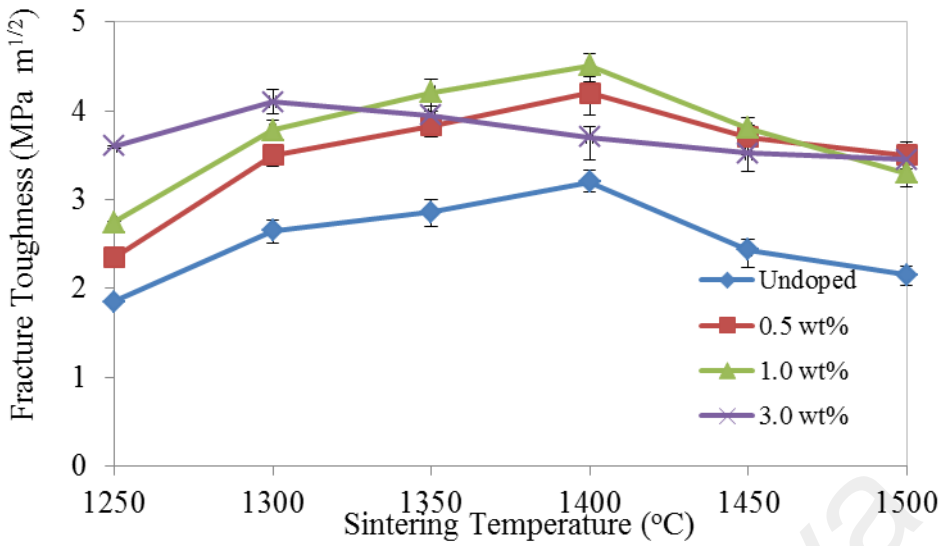

Figure 5.33: Fracture toughness variation as a function of sintering temperature for forsterite.

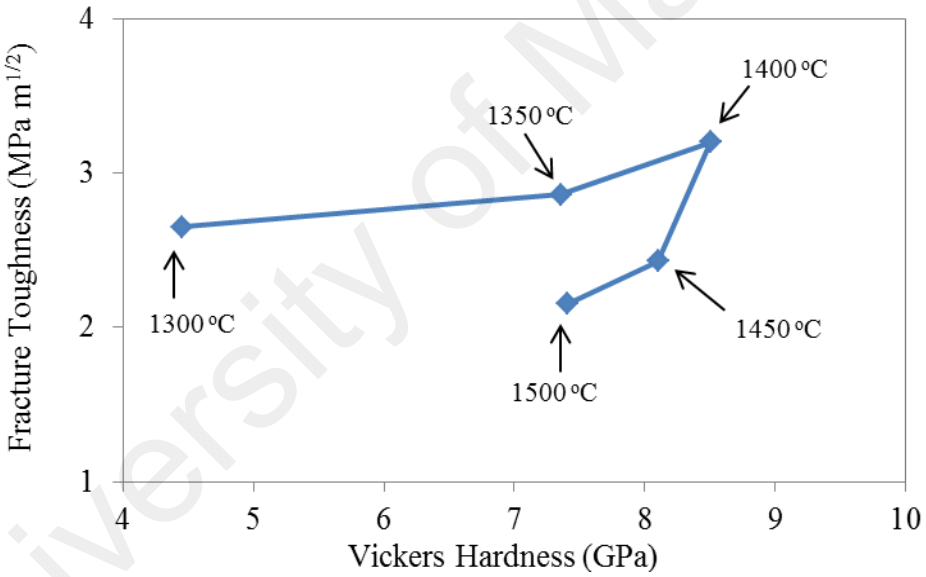

Figure 5.34: Fracture toughness variation in terms of Vickers hardness for pure forsterite samples.

In the case of 3.0 wt% ZnO sample, the fracture toughness value increases to a maximum of 4.1 MPa $m^{1/2}$ at 1300 ^{o}C before deteriorating. The highest fracture toughness was obtained by 1.0 wt% ZnO at 1400 ^{o}C with a value of 4.51 MPa $m^{1/2}$. This value is very encouraging as it possessed higher fracture toughness value than the pure forsterite sample as well as the non-heat treated forsterite obtained earlier in Section 5.1.3. The toughening of 3.0 wt% ZnO samples can be attributed by the grain size as

shown in Figure 5.35. The grain size obtained for 3.0 wt% ZnO sample at 1300 ^{o}C was below 1 µm unlike the other samples. Owing to the very small grain size, cracks will require higher energy to propagate across the grains. The smaller grain size has higher grain boundaries over grains ratio and thus more effectively hindering the propagation of cracks. Further, as the sintering temperature increases, 3.0 wt% ZnO samples showed a more radical increase in the grain size relative to the other samples. The grain size result showed that increasing the composition of ZnO added to forsterite beyond 1.0 wt% could benefit in suppressing grain growth below 1300 ^{o}C sintering temperature. Nevertheless, all doped samples showed reduction in grain size compared to the pure samples. The difference in grain size of pure and doped samples can be observed in Figure 5.36. In general, the superiority in fracture toughness of 1.0 wt% ZnO doped sample could be attributed by the influence of relative density and grain size.

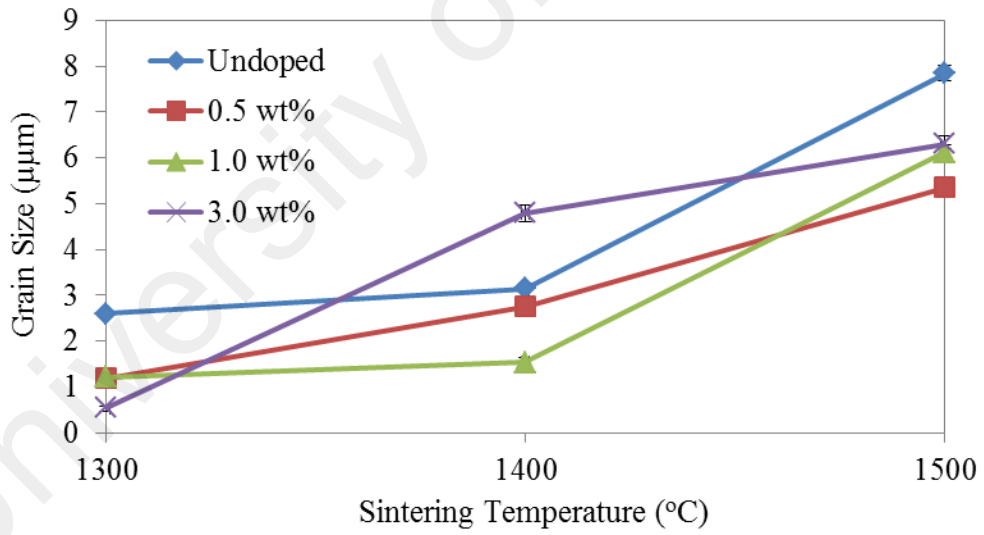

Figure 5.35: Grain size of pure and doped forsterite bulk under various sintering temperatures.

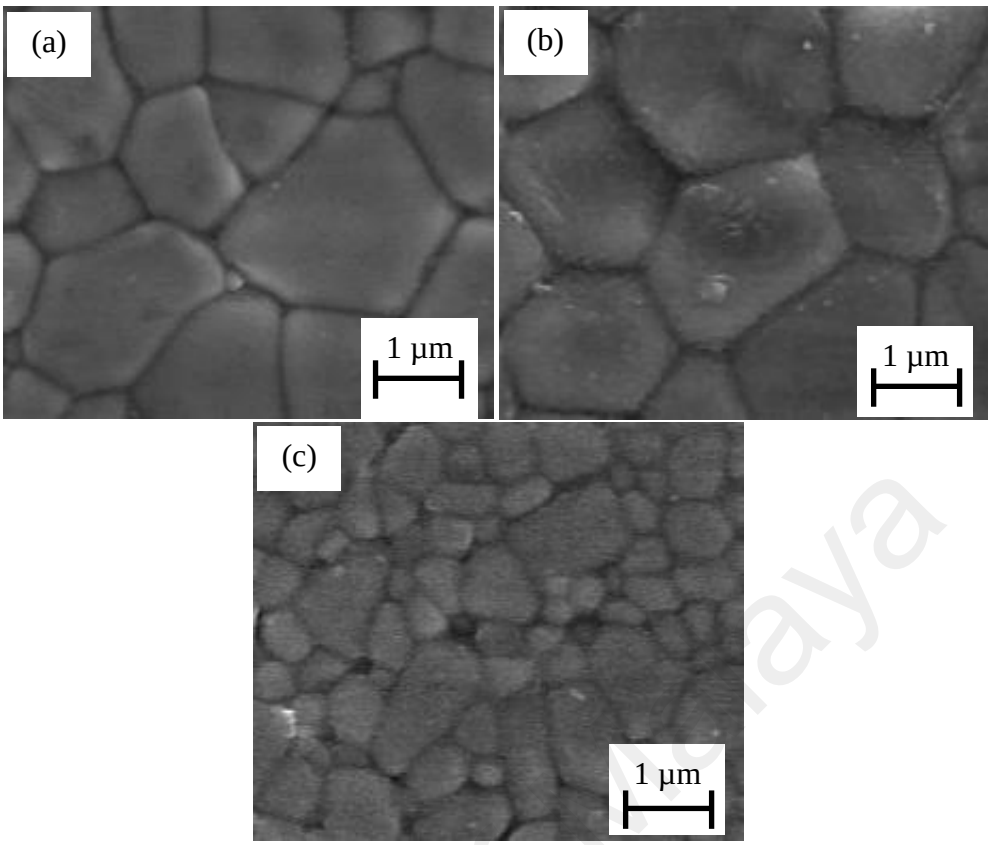

Figure 5.36: Morphology of (a) undoped, (b) 0.5 wt% and (c) 1.0 wt% ZnO doped forsterite bulk sintered at 1400 ^{o}C.

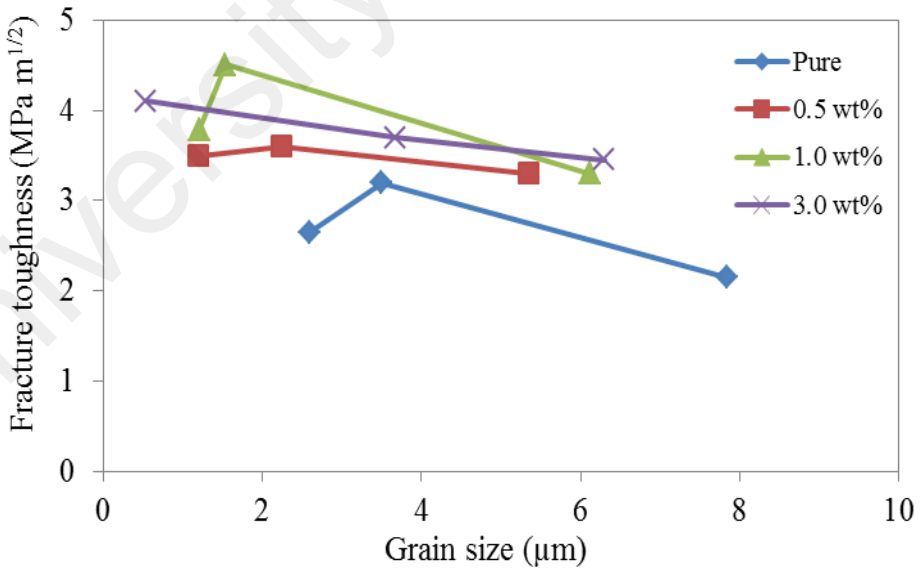

Figure 5.37: Fracture toughness dependence on the grain size of forsterite.

Based on literatures and observation made, it was known that below certain critical grain size (d_c), the hardness and fracture toughness of forsterite are controlled by the bulk density. Beyond d_c the bulk density will not be the controlling variable but instead the grain growth. This is proven from Figure 5.37 in which d_c for pure forsterite was estimated to be about 3.2 μm. For the doped samples, increasing the composition of ZnO had evidently decreases the d_c of forsterite.

In summary, the results presented in this section (Part 2) showed that 1.0 wt% doped forsterite samples possessed the highest fracture toughness and hardness properties. ZnO was proven to be a good grain size inhibitor for forsterite at composition below 1.0 wt% and further increasing the content led to higher rate of increase in grain size upon sintering at 1300 ^{o}C. Nevertheless, all doped samples are more superior that the undoped samples.

5.3 Part 3: Effect of microwave sintering on the sinterability of forsterite

Upon understanding the beneficial effect of ZnO addition on forsterite, further study was conducted to investigate the effect of microwave sintering on both pure and doped samples. As mentioned earlier in Chapter 3, microwave sintering was reported to have successfully reduced the activation temperature of HA. Hence, in this work the sintering range studied will be lowered to 1100-1250 ^{o}C and investigation was done on the phase stability and mechanical properties of the samples.

5.3.1 Phase analysis of forsterite bulk

The application of microwave sintering did not affect the phase stability of pure and doped forsterite bulk. In fact, even at lower sintering temperature (1100 ^{o}C), microwave sintering successfully produced phase-pure forsterite as shown in Figure 5.38. No phase changes were also observed upon sintering at 1250 ^{o}C (Figure 5.39).

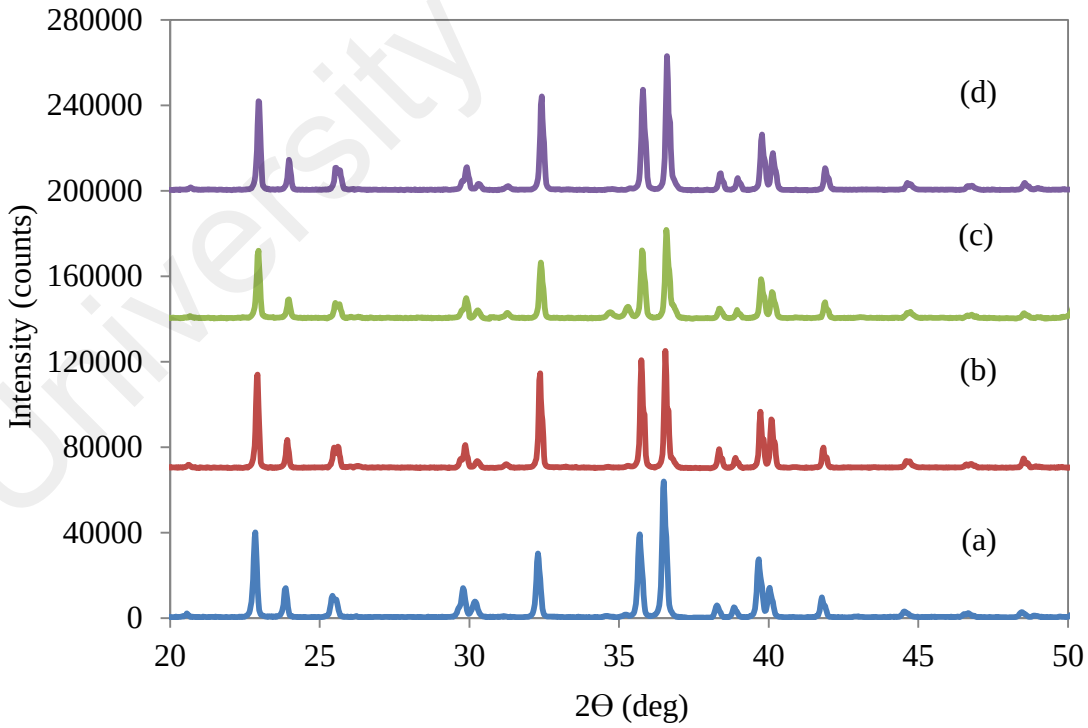

Figure 5.38: XRD traces of (a) undoped, (b) 0.5 wt%, (c) 1.0 wt% and (d) 3.0 wt% doped ZnO forsterite microwave sintered at 1100 ^{o}C.

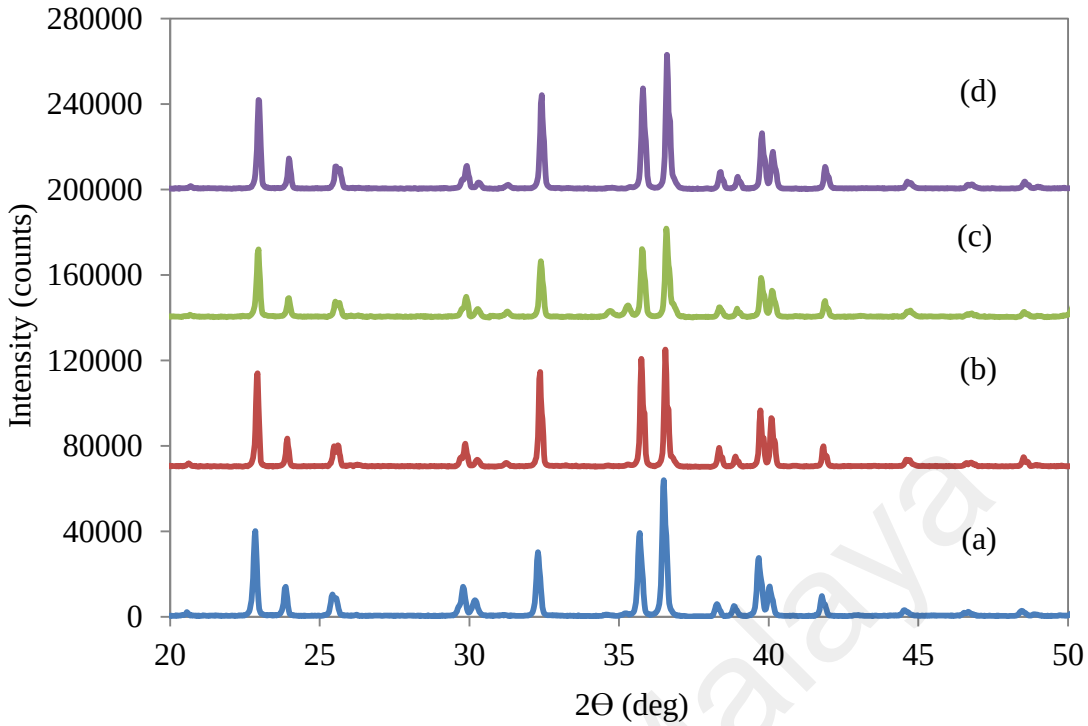

Figure 5.39: XRD traces of (a) undoped, (b) 0.5 wt%, (c) 1.0 wt% and (d) 3.0 wt% doped ZnO forsterite microwave sintered at 1250 ^{o}C.

5.3.2 Mechanical properties evaluation of forsterite bulk

The variation of the relative density of samples sintered at various temperatures is shown in Figure 5.40. In general, all samples showed a similar trend with increasing sintering temperature, i.e. relative density increases with increasing sintering temperature.

The relative density of pure forsterite sample possessed the lowest maximum relative density (87.9%) as compared to the doped samples. The highest relative density was obtained by all three different compositions of ZnO samples ranging from 98-99% relative density. Further, 0.5 wt% ZnO sample showed superiority in relative density compared to other samples for all sintering regime with 57.4% at sintering temperature of 1100 ^{o}C to a maximum of 98% at 1250 ^{o}C. Nonetheless, as the ZnO composition increases to 1.0 wt% and 3.0 wt%, the relative density significantly dropped to 48.7% and 42.6% when sintered at 1100 ^{o}C, respectively. Also, 3.0 wt% ZnO showed poorer

densification than pure forsterite sample at 1100 ^{o}C to 1200 ^{o}C. High amount of ZnO added into forsterite had inhibited the densification of forsterite. Figure 5.41 shows the morphology of 3.0 wt% ZnO sample sintered at 1200 ^{o}C. It was observed that the grains were yet to densify.

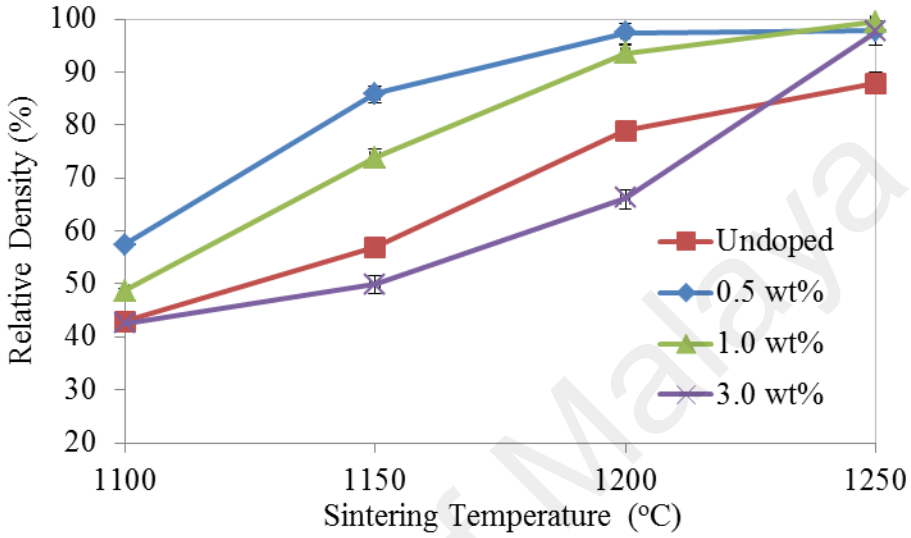

Figure 5.40: Relative density variation of forsterite with different ZnO composition as a function of sintering temperature.

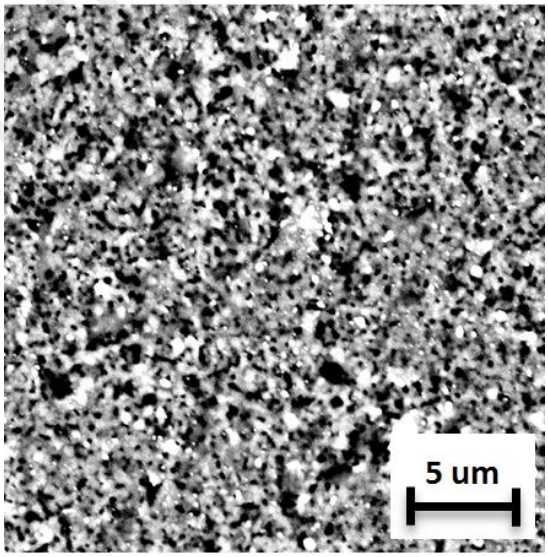

Figure 5.41: SEM morphology of 3.0 wt% ZnO sample sintered at 1200 ^{o}C.

In the early stage of sintering at 1100 ^{o}C, all samples showed poor densification value and the morphology of the samples were presented in Figure 5.42. All ZnO doped

samples showed similar morphological structure interpreting that higher temperature is required to allow the formation of grains leading to densification. The porosities observed in the SEM images directly reflect the outcome of the densification value obtained for all samples.

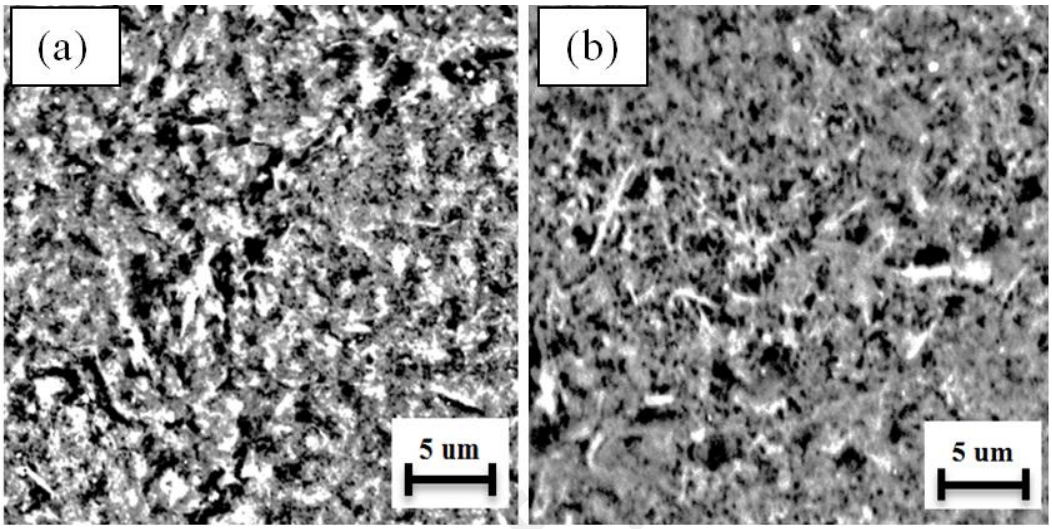

Figure 5.42: Morphology of (a) pure (undoped) and (b) 0.5 wt% ZnO doped forsterite samples microwave-sintered at 1100 ^{o}C.

The relationship between Vickers hardness and sintering temperature for all ZnO compositions are shown in Figure 5.43.

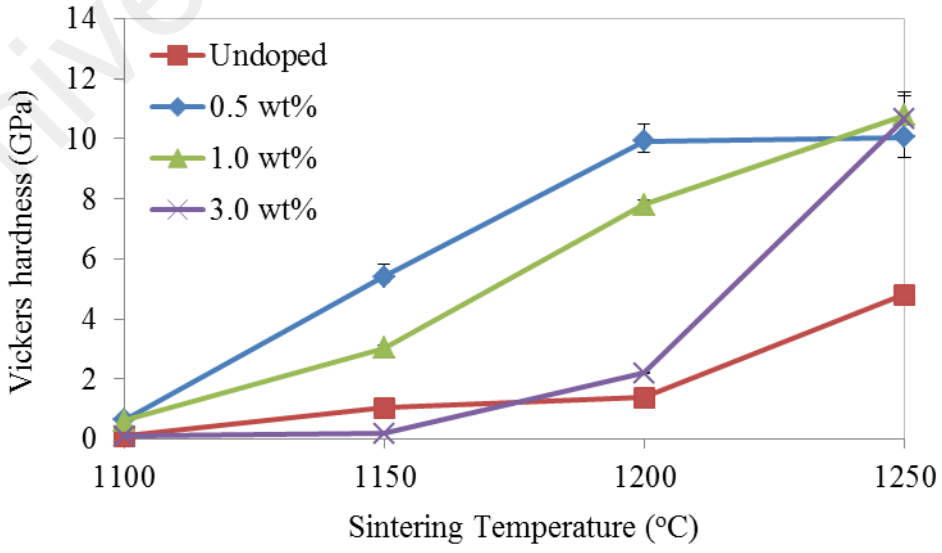

Figure 5.43: Vickers hardness variation as a function of sintering temperature of forsterite bulk.

Generally, all samples showed enhancement in hardness as sintering temperature increases. Pure and 3.0 wt% doped ZnO sample was found to have a minimal enhancement in hardness at low sintering temperature (1100 ^{o}C to 1200 ^{o}C) and began to only show drastic increase at 1250 ^{o}C. Nonetheless, the overall performance of 0.5 wt% and 1.0 wt% doped ZnO samples showed a more superior hardness than pure and 3.0 wt% doped ZnO samples until 1200 ^{o}C. Although all samples showed similar hardness value (~0.5 GPa) at sintering temperature of 1100 ^{o}C, 1.0 wt% ZnO sample showed a significant increase in hardness to a maximum of 10.79 GPa at 1250 ^{o}C. Although 3.0 wt% ZnO sample showed a less promising result during sintering process, a drastic increase in hardness was observed at 1250 ^{o}C with value of 10.65 GPa which is higher than both undoped and 0.5 wt% ZnO samples.

The increasing trend for all samples is relatively similar with the densification trend. It was attributed that the hardness of all samples is directly affected by their densification performance. Figure 5.44 shows the variation of hardness in terms of relative density. It was found that pure forsterite samples require higher densification values in order to have an apparent effect on the hardness properties.

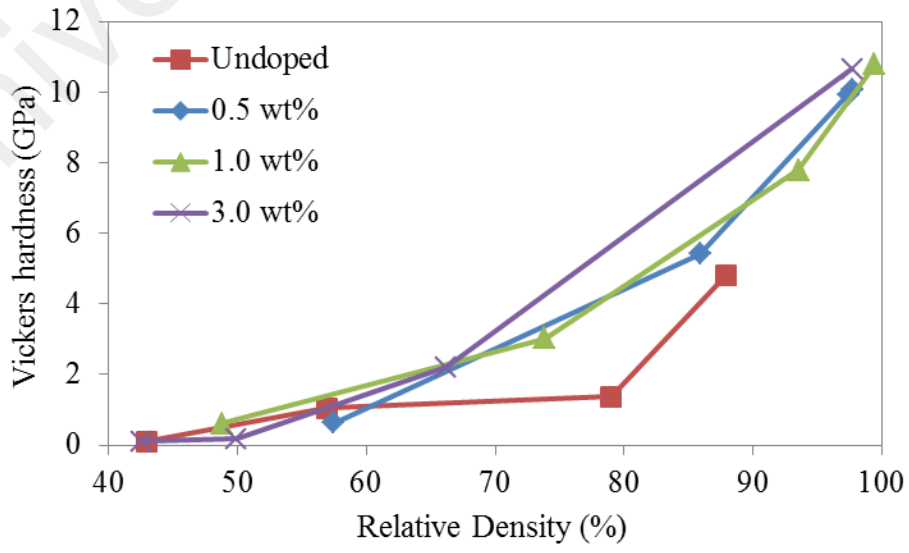

Figure 5.44: Vickers hardness variation in terms of relative density.

Figure 5.45 showed the fracture toughness variation with respect to sintering temperature. In general, all samples exhibited an increasing trend throughout the sintering regime. Overall, 1.0 wt% ZnO doped sample possessed the highest fracture toughness value of 4.25 MPa $m^{1/2}$ followed by 3.0 wt% ZnO, 0.5 wt% ZnO and undoped samples with a value of 3.84 MPa $m^{1/2}$, 3.72 MPa $m^{1/2}$ and 3.65 MPa $m^{1/2}$, respectively at sintering temperature of 1250 ^{o}C. The results obtained for fracture toughness complied well with the hardness results.

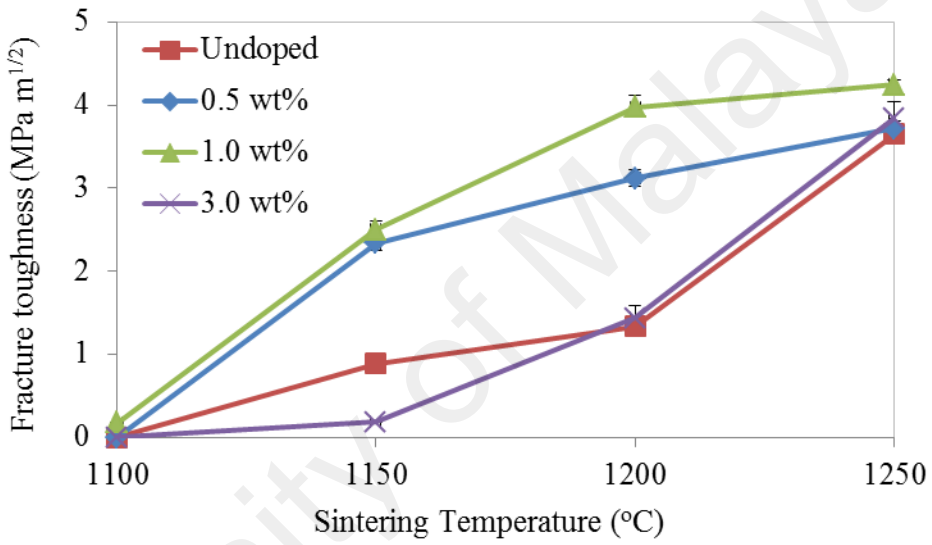

Figure 5.45: Fracture toughness variation as a function of sintering temperature of forsterite bulk.

The overall mechanical properties improvement of 3.0 wt% ZnO samples under sintering range from 1100 ^{o}C to 1200 ^{o}C was found to be rather sluggish as compared to other doped samples. This was attributed by the slow densification of forsterite as discussed earlier and shown in Figure 5.39. The grain size of 3.0 wt% ZnO sample was found to be marginally larger with a value of 1 µm as compared to undoped, 0.5 wt% and 1.0 wt% ZnO samples (0.8 µm, 0.85 µm and 0.9 µm, respectively) when microwave-sintered at 1250 ^{o}C. Nevertheless, the small difference in grain size between the samples may not be the contributing factor to the enhanced fracture toughness of 0.5 wt% and 1.0 wt% ZnO doped samples. Further investigation was conducted on the

morphology of doped sample and presented in Figure 5.46. Cluster-like particles were observed between grains as seen in Figure 5.46b. These particles were found to be ZnO (based on EDX result) clustering and segregating around the grains which could be the contributing factor to the slightly higher grain size of doped sample.

Figure 5.47 showed the correlation between Vickers hardness and fracture toughness relation. The increase in fracture toughness was directly related to the increase of hardness. Although the grain size of undoped sample sintered at 1250 ^{o}C was smaller than the 1.0 wt% ZnO doped sample, it was found that the fracture toughness of the latter was higher. The dominant factor that contributed to the high fracture toughness value of 1.0 wt% ZnO doped sample is believed to be the density and hardness.

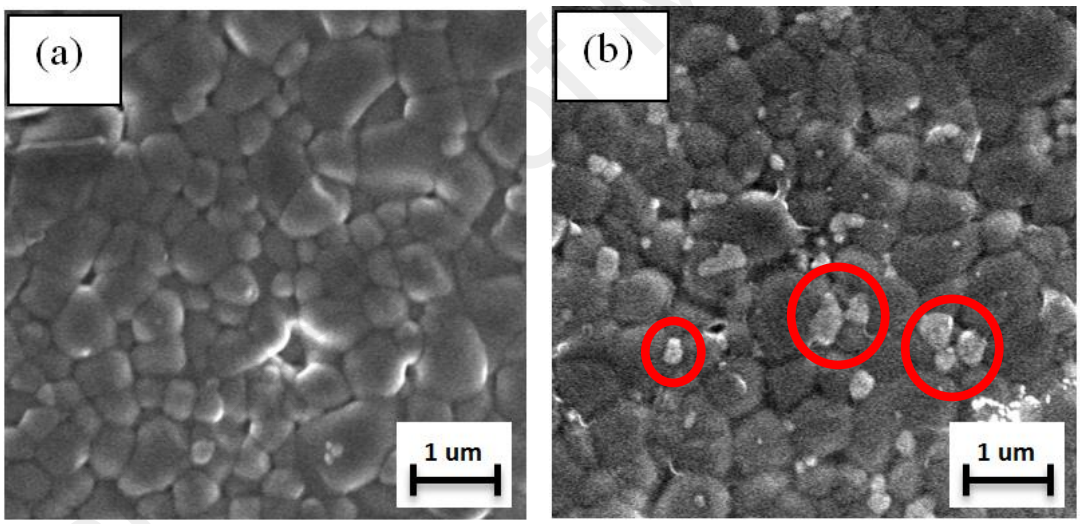

Figure 5.46: SEM morphology of a) undoped and b) 1.0 wt% ZnO doped samples microwave sintered at 1250 ^{o}C. Red circles indicating the clustering of ZnO particles.

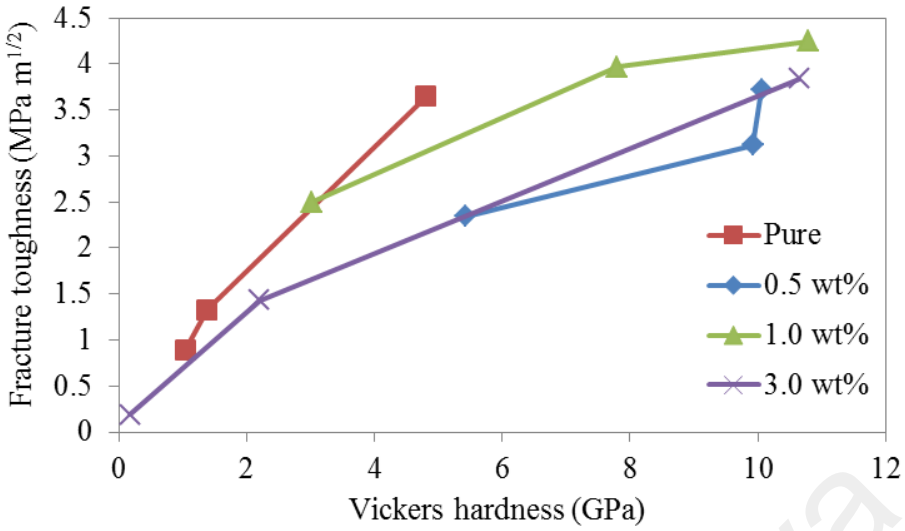

Figure 5.47: Fracture toughness variation as a function of Vickers hardness.

Upon concluding that the densification of 0.5 wt% and 1.0 wt% ZnO doped samples was the reason behind the high fracture toughness, further observation was done on the morphology of doped samples. Aside from the segregation of ZnO particles around the surface, the remnants of liquid phase were observed on the grain structure upon higher magnification near the vicinity of the clustering particles as shown in Figure 5.48 (doped samples).

The distortion on the grain shape was observed with formation of rounded edge grain instead of an equiaxed grains proving the presence of liquid phase (shape distortion). The grain shape of forsterite was altered due to the diffusion process allowing for tighter and denser packing of grains as seen in Figure 5.46.

The rapid initial densification of 0.5 wt% and 1.0 wt% doped samples was due to the presence of capillary force exerted by the wetting liquid on the solid grains thus accelerating the particle rearrangement process to reach its equilibrium state. Further evidence on the presence of liquid phase can be observed on the 3.0 wt% doped sample as shown in Figure 5.49. Large amount of liquid phase was observed located specifically at the pores of 3.0 wt% doped sample when sintered at 1150 ^{o}C. As

proposed by Law (1968), the grain growth rate was expressed in Equation 5.1 (Law, 1968).

$$\frac{dG}{dt} = \frac{2DSM\sigma}{\mathrm{KTd}\delta}\left(\frac{G}{G_o} - 1\right) \qquad \text{Equation 5.1}$$

whereby, D is the diffusion constant of solid in liquid, S is the solubility of a flat surface, M is the mol mass, σ is the solid-liquid surface energy. D is the density of the sample, δ is the thickness of the liquid phase area and G_o is the critical grain radius. The increase in the thickness of the liquid phase is indirectly proportional to the grain growth rate thus slowing the densification rate of 3.0 wt% ZnO doped samples at low sintering temperature. EDX was done on the white circle shown in Figure 5.49 and the result was illustrated in Table 5.3. High content of ZnO was detected at the liquid phase area as compared to the grain proving that the liquid phase formation was due to the presence of ZnO. Nevertheless, at higher sintering temperature (1250 ^{o}C), the grain began to grow larger thus significantly improving the density of 3.0 wt% doped sample having similar density with other doped samples as the pores were removed by the growing grains and filled by the liquid phase (Figure 5.50).

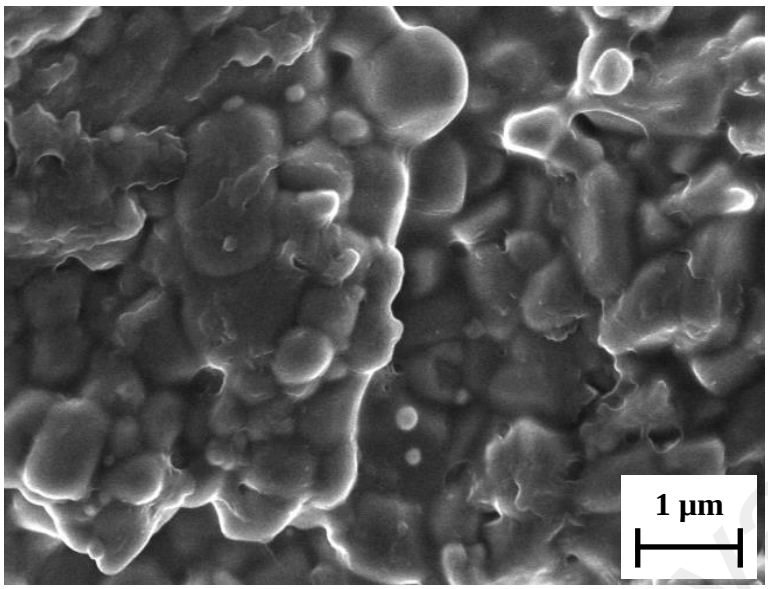

Figure 5.48: Morphology of 1.0 wt% ZnO doped sample microwave sintered at 1250 ^{o}C.

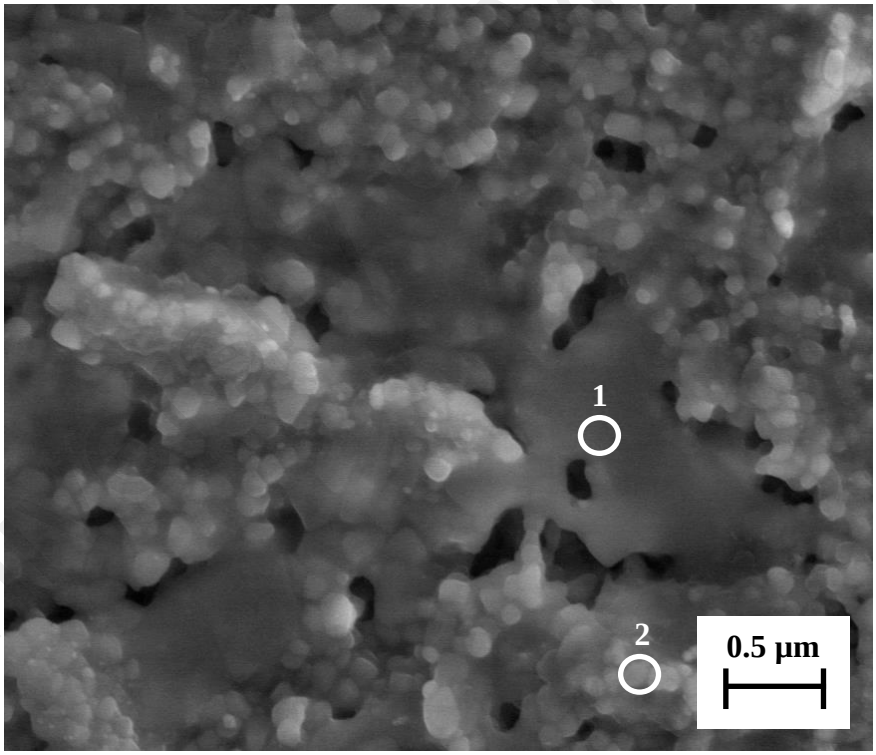

Figure 5.49: Morphology of 3.0 wt% ZnO doped forsterite sample microwave sintered at 1150 ^{o}C. White circle signify the spot for EDX.

Table 5.3: EDX result on 3.0 wt% ZnO doped forsterite sample microwave sintered at 1150 ^{o}C.

Spot	Element	Atomic %	Wt%
1	O	57.06	44.34
	Mg	26.29	31.05
	Si	15.61	21.29
	Zn	1.05	3.32
2	O	56.30	44.25
	Mg	28.47	34.01
	Si	14.82	20.45
	Zn	0.40	1.29

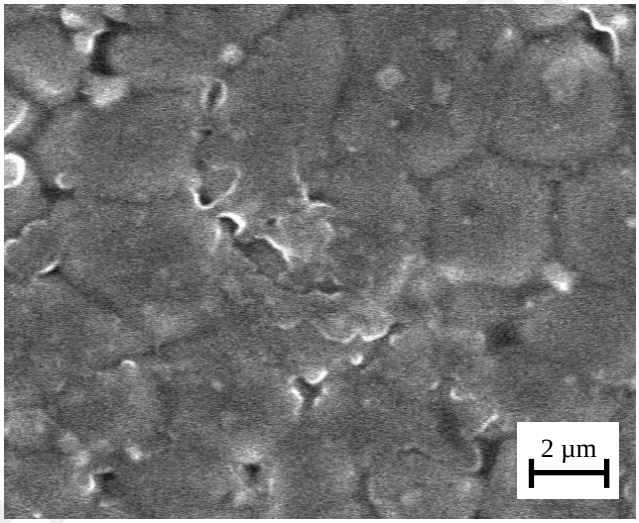

Figure 5.50: Morphology of 3.0 wt% ZnO doped forsterite sample microwave sintered at 1250 ^{o}C

The present result indicated that 1.0 wt% ZnO doped samples possessed the highest mechanical properties with a maximum of 99.43%, 10.79 GPa and 4.25 MPa $m^{1/2}$ for relative density, Vickers hardness and fracture toughness, respectively. Clusters of ZnO particle were observed throughout the morphology of the doped samples which may cause the slightly larger grains of doped samples. Nevertheless, the controlling factor for its high fracture toughness lies on the high densification and hardness instead of grain size and this relatively high densification rate of 0.5 wt% and 1.0 wt% ZnO doped

samples was due to the presence of liquid phase that provides capillary actions in grains accelerating its particle rearrangement towards equilibrium. Slow densification process was observed on the highest ZnO composition (3.0 wt%) at low sintering temperature but upon grain coarsening, the grain size began to increase quicker and finally reaching similar density with other doped samples at 1250 ^{o}C.

5.3.3 Comparison between conventional sintering (CS) and microwave sintering (MS)

5.3.3.1 Pure (undoped) forsterite

As discussed in the earlier section, microwave sintering is a newly introduced sintering technique for forsterite. Nonetheless it was fully understood that microwave sintering is term as volumetric heating unlike conventional sintering (Borrell et al., 2014). Hence, it is expected that forsterite should possessed enhanced mechanical properties when sintered using microwave furnace.

Looking at Figure 5.25, 5.38 and 5.39, it was found that conventional and microwave sintering did not show any difference in terms of phase purity. Both methods of sintering showed only forsterite phase although the sintering regime studied for microwave sintering was lower (1100 ^{o}C to 1250 ^{o}C) than conventional sintering (1200 ^{o}C to 1500 ^{o}C).

In order for a fair comparison between both of these sintering methods, similar sintering temperature was selected for comparison purposes and both samples were heat treated into forsterite powder prior to pressing and sintering. Only sintering temperatures of 1200 ^{o}C and 1250 ^{o}C were chosen for this comparative analysis.

In terms of relative density, MS samples possessed significantly higher density than CS samples when sintered at 1200 ^{o}C and 1250 ^{o}C. MS sample achieved a maximum of

87.88% relative density as compared to CS sample having 75.48% when sintered at 1250 ^{o}C. Based on the morphologies of both samples shown in Figure 5.51, two major differences between both sintering methods were observed. First is the grain size of MS sample is significantly smaller than CS sample. Also, the level of porosities observed for CS sample is higher than MS sample. The SEM image of MS sample showed a very dense and compact grain structures unlike CS sample that already undergoes grain growth with grain size larger than MS sample and have yet to fully densify. Microwave sintering was known to promote forward diffusion of ions which then accelerates the densification process of forsterite. CS sample requires sintering temperature of up to 1400 ^{o}C in order to achieve similar densification as MS sample at 1250 ^{o}C. The significant reduction in sintering temperature and mode of heating has contributed in restraining the grain growth while enhancing the densification process of forsterite.

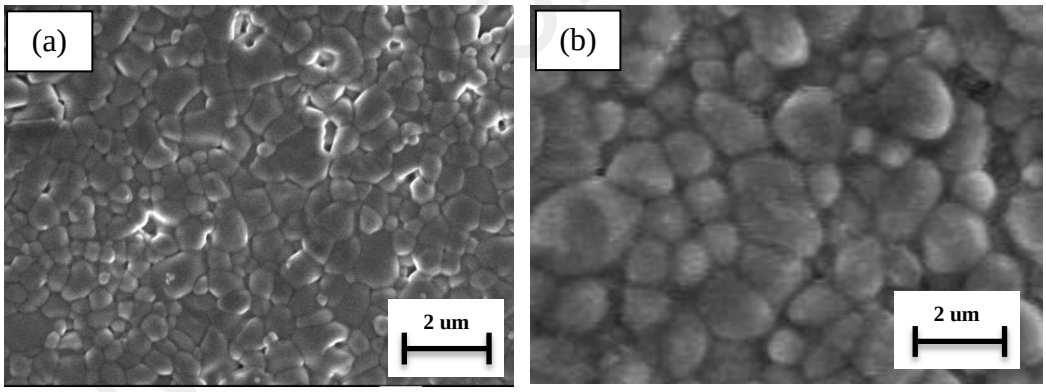

Figure 5.51: SEM image of pure forsterite sintered at 1250 ^{o}C via a) microwave sintering and b) conventional sintering

Similarly, the hardness and fracture toughness value of MS sample is higher than CS sample at both sintering regime (1200 ^{o}C and 1250 ^{o}C). Both of hardness and toughness values of MS samples obtained were almost two times larger than CS samples. Due to the low density of CS sample at 1200 ^{o}C, no cracks were observed after indentation making it impossible to determine the fracture toughness. The fracture toughness of MS sample was higher than the maximum fracture toughness (K_{Ic} = 3.2 MPa $m^{1/2}$) of heat-

treated CS sample obtained when sintered at 1400 ^{o}C. This finding proved that microwave sintering had successfully enhance the overall mechanical properties (as shown in Table 5.4) of forsterite ceramic at a lower sintering temperature.

Table 5.4: Mechanical properties of pure forsterite sintered via conventional and microwave sintering

Sintering temp. (^{o}C)	Relative density (%)		Vickers hardness (GPa)		Fracture toughness (MPa m$^{1/2}$)	
	CS	MS	CS	MS	CS	MS
1200	59.45	79.00	0.62	1.38	-	1.33
1250	75.48	87.88	2.61	4.80	1.85	3.65

5.3.3.2 ZnO doped forsterite

Since both sintering modes showed that 1.0 wt% ZnO doped forsterite possessed the highest mechanical properties, comparative discussion will be done on both of these samples under same sintering temperature.

Both of these samples showed no sign of secondary phases upon sintering. No ZnO content was found for both samples as well as shown in Figure 5.27 and 5.39. Thus, the mechanical properties of both samples were not affected by the phase purity.

CS sample sintered at 1200 ^{o}C possessed very low mechanical properties as compared to MS sample under equal sintering temperature. Slow densification was observed for CS sample, similar to the undoped samples discussed in section 5.3.3.1. The MS sample sintered at 1250 ^{o}C was almost fully dense having relative density of 99.44% as compared to CS sample having 82.53%. It can be claimed that MS sample had reached its densification plateau at this point. The grain structures for both samples were shown in Figure 5.52. No pores were observed for MS sample whereas CS sample showed otherwise.

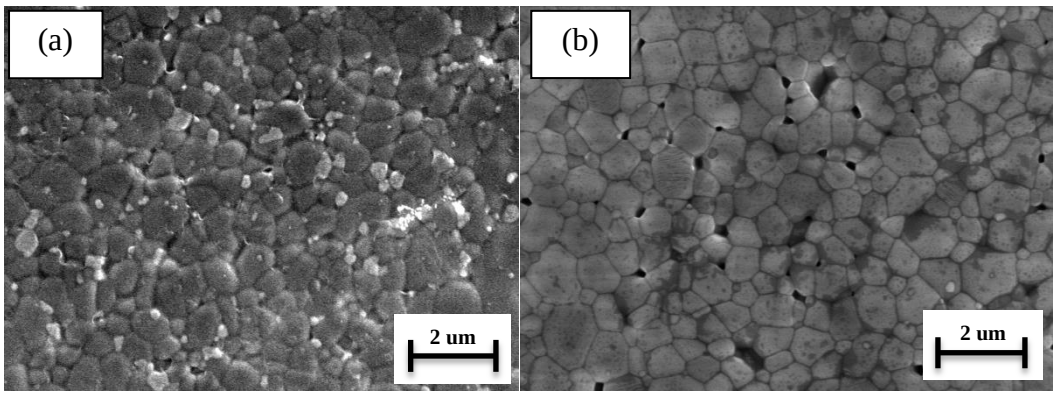

Figure 5.52: SEM images of 1.0 wt% ZnO doped forsterite sintered at 1250 ^{o}C via a) microwave sintering and b) conventional sintering

Hence, the hardness and fracture toughness of MS samples were far more superior to CS samples having 3 times higher in hardness and almost 2 times the toughness of CS sample when sintered at 1250 ^{o}C. Nevertheless, as the sintering temperature of CS increases to 1400 ^{o}C, the most optimum temperature for CS samples, the fracture toughness of CS sample is comparable to the MS sample sintered at 1250 ^{o}C. The overall mechanical properties of 1.0 wt% ZnO doped forsterite for both sintering modes were tabulated in Table 5.5.

Another observation made was the presence of cluster-like ZnO particle observed in MS samples as discussed earlier (Figure 5.46). It was found that CS sample did not possess such morphology. This indicated that microwave sintering produced an adverse effect on ZnO dopant. Unlike CS sample, whereby the grain size was inhibited by the presence of ZnO, MS sample showed an opposite effect with grain size marginally larger than the undoped sample under equal sintering condition. It was noted that the clustering and segregation of dopants could lead to the deterioration of mechanical properties as reported by Charkravarty et al (2007). Nonetheless, in this study the mechanical properties of doped samples still show superiority in mechanical properties due to the densification and hardness being the contributing factors toward the enhancement of fracture toughness instead of grain size.

Table 5.5: Mechanical properties of 1.0 wt% ZnO doped forsterite sintered via conventional and microwave sintering

Sintering temp. (^{o}C)	Relative density (%)		Vickers Hardness (GPa)		Fracture toughness (MPa m$^{1/2}$)	
	CS	MS	CS	MS	CS	MS
1200	64.87	93.55	0.851	7.8	0.67	3.97
1250	82.53	99.44	3.517	10.79	2.74	4.245

In this study, comparison between the conventional and microwave sintering was discussed. Generally microwave sintering retains the phase purity of the forsterite bulk and no decompositions of secondary phases were observed, similarly to the conventional sintering as discussed earlier. Nonetheless, MS samples successfully enhance the overall mechanical properties of forsterite with reduced required sintering temperature. However, the ability of ZnO to inhibit grain growth was restrained in microwave sintering. Although grain growth was unable to be inhibited, the overall mechanical property of forsterite was still enhanced owing to the high densification at low sintering temperature of doped sample. This was attributed by the liquid phase presence that accelerates the densification of forsterite during particle rearrangement stage.

CHAPTER 6: CONCLUSIONS

6.1 Conclusions

In this study, attrition milling was introduced into the mechanochemical method or also known as solid-state reaction method to synthesize forsterite powder. The sinterability of forsterite produced by using attrition milling was compared with the commonly used ball milling in terms of its mechanical properties. The effect of adding ZnO on the sinterability of forsterite, especially fracture toughness, was investigated. A thorough comparison was also conducted between conventional sintering and microwave sintering to investigate the beneficial effect of microwave sintering on the sinterability of forsterite ceramic.

The following conclusions were successfully drawn from this research:

1. The application of heat treatment and/or sintering is necessary in producing forsterite powder/bulk as milling alone showed the presence of incomplete reaction between talc and magnesium carbonate.
2. Longer milling duration (3 hours vs 5 hours) was found to reduce the required sintering temperature to produce phase-pure forsterite bulk.
3. High purity single-phase forsterite bulk was successfully synthesized using attrition milling upon sintering from 1200 ^{o}C to 1500 ^{o}C. Ball milling requires higher sintering temperature (1300 ^{o}C) in order to obtain phase-pure forsterite bulk.
4. Smaller powder particle size (23-28 nm) of attrition-milled (AM) powder was obtained as compared to ball-milled (BM) powder (60-73 nm) upon milling for 5 hours in both cases. Owing to the smaller particle size and high specific surface area of the former, pure forsterite was successfully obtained at a low sintering temperature followed by an early densification of forsterite.

5. The synthesized forsterite via attrition milling achieved a high relative density of 89-95% when sintered at 1200 ^{o}C – 1500 ^{o}C whereas ball milled samples require sintering temperature of at least 1400 ^{o}C to produce similar density.
6. AM samples were unable to further increase its density due to the presence of both large and small grains that causes micropores to be entrapped between them as the grain grows.
7. The hardness of AM samples exhibited higher hardness value than BM samples regardless of sintering temperature. A maximum of 9.8 GPa was successfully obtained at sintering temperature of 1250 ^{o}C for AM sample.
8. The slow increase in hardness of BM samples was due to the late densification of the sample and only began to densify after sintering above 1300 ^{o}C. 'Necking' process was observed on the morphology of BM sample when sintered at 1300 ^{o}C. The difference between both AM and BM samples in terms of hardness and density was attributed by the particle size of the powder prior to sintering process.
9. Fracture toughness of BM sample showed similar trend with its density and hardness. The optimum temperature having the highest fracture toughness of BM sample was at 1400 ^{o}C, similar to that of density and hardness. AM sample obtained the highest fracture toughness of 4.3 MPa $m^{1/2}$ at 1400 ^{o}C. The drastic increase in fracture toughness of BM sample at sintering temperature above 1300 ^{o}C was due to the formation of elongated grains which was found to be beneficial in enhancing fracture toughness.
10. Cell morphology studies using MC3T3-E1 osteoblast-like cell have shown promising result on AM sample for clinical application. Day 1 observation showed continuous growth of the cell by forming small whisker-like filopodial

on the surface of sample and a very dense cell forming a thin layer on the surface of the sample on the third day.

11. According to the thermal analysis, the endothermic peaks observed were related to the removal of water content from the powder and the decomposition of magnesium carbonate to recrystallize MgO. The exothermic peaks were indicating the beginning of the formation of forsterite and it was concluded that 940 ^{o}C is the required heat treatment temperature to form forsterite powder.
12. Phase-pure forsterite powder was successfully obtained upon heat treatment at 1000 ^{o}C.
13. Both undoped and ZnO doped forsterite at all compositions showed only forsterite peak in the XRD analysis. The highest amount of ZnO composition (3.0 wt%) did not show signs of ZnO peak. Nevertheless, elemental analysis using EDX was able to detect the presence of ZnO for only 3.0 wt% ZnO doped samples.
14. All samples showed an increase in relative density with increasing sintering temperature. Doped samples possessed a more superior density than undoped samples at all sintering regime. The highest relative density was 97.8% obtained by 3.0 wt% ZnO doped sample sintered at 1300 ^{o}C followed by 97.7% and 95.5% from 0.5 wt% and 1.0 wt% ZnO doped samples, respectively, when sintered at 1500 ^{o}C.
15. 3.0 wt% ZnO doped samples had reached its densification plateau earlier at 1300 ^{o}C sintering temperature than other samples (1400 ^{o}C). This could be attributed by the beneficial effect of ZnO on the densification rate of forsterite ceramic.
16. The undoped sample achieved a maximum of 8.5 GPa when sintered at 1400 ^{o}C whereas all doped samples possessed similar maximum hardness within the range of 9.7-9.9 GPa. The low hardness value obtained at 1200 ^{o}C was attributed

by the low densification of the respective samples. The morphology of the samples showed that grains were yet to form at this stage.

17. ZnO inclusion in forsterite was found to enhance the fracture toughness of forsterite. The highest fracture toughness obtained was 4.51 MPa $m^{1/2}$ by 1.0 wt% ZnO doped sample sintered at 1400 ^{o}C.
18. In terms of grain size, the fracture toughness of 3.0 wt% ZnO doped sample showed a more superior value at 1300 ^{o}C but began to show deterioration in fracture toughness as sintering continues to a higher temperature. This was attributed by the smaller grain size of the sample as compared to other samples but due to the drastic increase in the grain size, the fracture toughness was also affected.
19. Further increasing the amount of ZnO in forsterite has led to the inability of ZnO to inhibit grain growth as sintering temperature increases. The increase of ZnO had also significantly reduces the d_c of forsterite thus causing deterioration of fracture toughness at smaller grain size.
20. 1.0 wt% ZnO doped sample showed the best mechanical properties compared to other samples and ZnO was proven to serve as a good grain size inhibitor at composition of 1.0 wt% and below.
21. Microwave sintering was found to not cause any disruption on the phase purity of forsterite bulk, similar to conventional sintering.
22. Undoped forsterite sample obtained 87.9% relative density when sintered at 1250 ^{o}C. Doped samples were found to possess a more superior relative density with value ranging from 98-99% for all three compositions when sintered at the same temperature.

23. The highest amount of ZnO composition (3.0 wt%) did not possessed similar trend as the other compositions when sintered from 1100 ^{o}C to 1200 ^{o}C as the density of this sample began to densify beyond 1200 ^{o}C.
24. Highest hardness was obtained by 1.0 wt% ZnO doped sample with value of 10.65 GPa via microwave sintering at temperature of 1250 ^{o}C. The increase in hardness of all samples was attributed by its respective densification. Nonetheless, the doped samples showed a more superior densification and hardness than the undoped sample.
25. The fracture toughness of microwave-sintered 1.0 wt% ZnO doped sample was found to the best with a value of 4.25 MPa $m^{1/2}$ followed by 3.0 wt% ZnO, 0.5 wt% ZnO and undoped samples ranging from 3.65 MPa $m^{1/2}$ to 3.85 MPa $m^{1/2}$. The trend of fracture toughness complied well with the hardness and relative density result.
26. The increase amount of ZnO composition was found to marginally increase the grain size of forsterite. Conducting microwave sintering on ZnO doped forsterite has shown an adverse effect on the grain size of forsterite with 1 µm grain size from 0.85 µm and 0.9 µm for 0.5 wt% ZnO and 1.0 wt% ZnO doped samples, respectively.
27. Cluster-like particles were observed throughout the grain morphology of doped samples which reduces the effectiveness of ZnO as grain growth inhibitor. Nonetheless, the dominant factor that affects the overall mechanical properties of forsterite is density and hardness instead of grain size.
28. Microwave of ZnO doped samples clearly showed the presence of liquid phase due to the ZnO addition which increases the rate of densification of forsterite thus improving the mechanical properties of forsterite, particularly fracture toughness, even at low sintering temperature (1150 ^{o}C).

29. Doping of ZnO up to 3.0 wt% resulted in an opposite side-effect as compared to 0.5 wt% and 1.0 wt% ZnO doped samples. Instead of increasing the densification rate at low sintering temperature (1150 ^{o}C), 3.0 wt% doped sample showed a very slow densification rate owing to the high thickness of liquid phase found in the grain vicinity. It was found that high thickness of liquid phase slowed the grain growth rate of sample thus inhibiting the densification of forsterite at low sintering temperature (<1200 ^{o}C).
30. Microwave sintering had significantly reduced the required sintering temperature to achieve similar densification of forsterite. 87.88% relative density was successfully obtained using microwave sintering at temperature of 1250 ^{o}C whereas conventional sintering requires 1400 ^{o}C to obtain similar densification.
31. In regards to fracture toughness, microwave sintering allowed forsterite to obtain fracture toughness of 3.65 MPa $m^{1/2}$ at temperature of 1250 ^{o}C unlike conventional sintering that only obtained 1.85 MPa $m^{1/2}$ and 3.2 MPa $m^{1/2}$ at temperature of 1250 ^{o}C and 1400 ^{o}C, respectively, on heat-treated forsterite.
32. In comparison between 1.0 wt% ZnO doped samples sintered via microwave and conventional method, MS samples had reached its densification plateau at 1250 ^{o}C with value of 99.44% whereas CS sample still showed many porosities throughout the grain structures.
33. Comparable fracture toughness was obtained between MS and CS when sintered at 1250 ^{o}C and 1400 ^{o}C, respectively. With reduction in the required sintering temperature for the optimum mechanical properties, microwave sintering had proven to be beneficial in reducing the temperature needed as well as improving the mechanical properties while retaining the phase purity of forsterite.

6.2 Future directions

Based on current study, many findings were made and there are many other possible improvements that can be taken. There are uncertainties occurring throughout the research which requires further investigation that could enhance the sinterability of forsterite especially the fracture toughness.

As discussed earlier in this work, ZnO was found to be beneficial to forsterite in inhibiting the grain growth phenomena. Reduction in grain size has indeed enhances the fracture toughness of forsterite but it would be clearer to go further in detail on the function of ZnO towards the grain boundaries and its distribution throughout the grain morphology. Microwave sintering is a new field to venture for forsterite. A more detailed study can be conducted to obtain the optimum profile with the best mechanical properties for forsterite and probing the underlying mechanism. Also, it was found that conventional and microwave sintering produce some exciting results on ZnO doped samples as CS samples showed inhibition on grain growth whereas MS samples showed otherwise. With the following suggestions for future directions, it will be great to clarify these phenomena.

1. The composition and distribution upon sintering process of grain boundaries phases can be enlighten, particularly on doped samples, by running an in depth investigation using X-ray Photoelectron Spectroscopy (XPS) analysis.
2. Although literatures have shown that ZnO addition on HA was found to be non-toxic but biocompatibility test should be conducted in depth with studies on the cell attachment, adhesion, proliferation and cytotoxicity test as well as simulated bodily fluid (SBF) study on the ZnO doped forsterite to ensure that it is viable for clinical usage.

3. A more detail profiling of microwave sintering on forsterite can be conducted to fully understand the mechanical properties trend with varying sintering temperature, sintering ramp rate and sintering time. Knowing that the grain size obtained was still 1.0 μm and below when sintered at 1250 ^{o}C, further sintering can be conducted to observe on the grain growth of forsterite under microwave sintering and probably improvement on mechanical properties.
4. Addition of other sintering additives (manganese oxide, zirconia) can be conducted on forsterite to investigate the probable beneficial effect. Microwave sintering can be cooperated with these sintering additives to venture on other interesting possibilities of microwave effect on doped forsterite.
5. Cold isostatic pressing (CIP) was known to provide additional reinforcement towards the enhancement in mechanical properties of other ceramic such as hydroxyapatite. This reinforcement could further increase the mechanical properties of forsterite.

REFERENCES

Aboushelib, M. N., Kleverlaan, C. J., & Feilzer, A. J. (2008). Evaluation of a high fracture toughness composite ceramic for dental application. *Journal of Prosthodontics, 17*(7), 538-544.

Afonina, G. A., Leonov, V. G., & Popova, O. N. (2005). Production of forsterite powder using sol gel technology. *Glass and Ceramics, 62,* 248-252.

Agrawal, D. (2006). Microwave sintering of ceramics, composites and metallic materials and meting of glasses. *Transactions of the Indian Ceramic Society, 65*(3), 129-144.

Althoff, J., Quint, P., Krefting, E. R., & Hohling, H. J. (1982). Morphological studies on the epiphyseal growth plate combined with biochemical and X-ray microprobe analyses. *Histochemistry, 74*(4), 541-552.

Amir, M., McDonagh, A. M. & Cortie, M. B. (2012). Zinc oxide particles: Synthesis, properties and applications. *Chemical Engineering Journal, 185-186,* 1-22.

Amogh, T., Mangesh, G., & Anna, P. N. (2010). A Brief Review: Biomaterials and Their Application. *International Journal of Pharmacy and Pharmaceutical Sciences, 2*(4), 19-23.

Andrew J. Berry, Andrew M. Walker, Jorg Hermann, Hugh St. C. O'Neill, Garry J. Foran, & Gale, J. D. (2007). Titanium substitution mechanisms in forsterite. *Chemical Geology, 242,* 176-186.

Aseev, V. A., Zhukov, S. N., Kuleshsov, N. V., Kuril'chik, S. V., Mudryi, A. V., Nikonorov, N. V., Rokhmin, A. S., & Yasyukevich, A. S. (2015). Spectral luminescence characteristics of forsterite nano glass ceramics doped with chromium ions. *Optics and Spectroscopy, 118*(1), 146-150.

Baláž, P. (2008). High-Energy Milling *Mechanochemistry in Nanoscience and Minerals Engineering* (pp. 103-132): Springer Berlin Heidelberg.

Bandyopadhyay, A., Withey, E.A., Moore, J. & Bose, S. (2007). Influence of ZnO doping in calcium phosphate ceramics. *Materials Science and Engineering, 27,* 14-17.

Becher, P. F., Sun, E. Y., Plucknett, K. P., Alexander, K. B., Hsueh, C.-H., Lin, H.-T., Waters, S. B., Westmoreland, C. G., Kang, E.-S., Hirao, K., & Brito, M. E. (2005). Microstructural Design of Silicon Nitride with Improved Fracture Toughness: I, Effects of Grain Shape and Size. *Journal of the American Ceramic Society, 81*(11), 2821-2830.

Bernotat, S. & Schonert, K. (1998). Size reduction. In*: Ullmann's Encyclopedia of Industrial Chemistry*. VCH Verlagsgesellschaft, Weinheim, B2, 5.1–5.39.

Best, S. M., Porter, A. E., Thian, E. S., & Huang, J. (2008). Bioceramics: Past, present and for the future. *Journal of the European Ceramic Society, 28*(7), 1319-1327.

Bian, H.-m., Yang, Y., Wang, Y., Tian, W., Jiang, H.-f., Hu, Z.-j., & Yu, W.-m. (2012). Alumina–titania ceramics prepared by microwave sintering and conventional pressure-less sintering. *Journal of Alloys and Compounds, 525*, 63-67.

Binyamin, G., Shafi, B.M. & Mery, C.M. (2006). Biomaterials: A primer for surgeons. *Seminars in Pediatric Surgery*, **15**, 276-283.

Bizot P. & Sedel L. (2001). Alumina bearings in hip replacement: theoretical and practical aspects. *Operative Techniques in Orthopaedics., 4*, 263-269.

Borrell, A., Salvador, M. D., Peñaranda-Foix, F. L., & Cátala-Civera, J. M. (2013). Microwave Sintering of Zirconia Materials: Mechanical and Microstructural Properties. *International Journal of Applied Ceramic Technology, 10*(2), 313-320.

Borrell, A., Salvador, M. D., Miranda, M., Penaranda-Foix, F. L., & Catala-Civera, J. M. (2014). Microwave technique: A powerful tool for sintering ceramic materials. *Current Nanoscience, 10*, 32-35.

Bose, S., Dasgupta, S., Tarafder, S., & Bandyopadhyay, A. (2010). Microwave-processed nanocrystalline hydroxyapatite: simultaneous enhancement of mechanical and biological properties. *Acta Biomater, 6*(9), 3782-3790.

Bose, S., Tarafder, S., Baneree, S. S., Davies, N. M., & Bandyopadhyay, A. (2011). Understanding in vivo response and mechanical property variation in MgO, SrO and SiO2 doped b-tTCP. *Bone, 48*(6), 1282-1290.

Briend, F.J. (2011). Biomaterials & scaffolds for tissue engineering. *Materials Today, 14*(3), 88-95.

Brindley, G. W., & Hayami, R. (1965). Mechanism of formation of forsterite and enstatite from serpentine. *Materials Research Laboratory, 12*, 505.

Cao, W. & Hench, L. L. (1996). Bioactive materials. *Ceramics International, 22*, 493-507.

Carlisle, E. M. (1988). Silicon as a trace nutrient. *The Science of the Total Environment, 73*, 95-106.

Castro, C. L. D., & Mitchell, B. S. (2002). Nanoparticles for mechanical attrition. In M. I. Baraton (Ed.), *Synthesis, Functionalization and Surface Treatment of Nanoparticles* (pp. 1-15): American Scientific Publishers.

Catledge, S. A., Fries, M. D., Vohra, Y. K., Lacefield, W. R., Lemons, J. E., Woodard, S., & Venugopalan, R. (2002). Nanostructured ceramcs for biomedical implants. *Journal of nanoscience and nanotechnoogy, 2*(3-4), 293-312.

Chakravarty, D., Bysakh, S., Muraleedharan, K., Rao, T. N., & Sundaresan, R. (2007). Spark Plasma Sintering of Magnesia-Doped Alumina with High Hardness and Fracture Toughness. Journal of the American Ceramic Society, 91(1), 203-208.

Chen, I. W., & Wang, X. H. (2000). Sintering dense nanocrystalline ceramics without final-stage grain growth. *Nature, 404*, 168-171.

Cheng, L., Liu, P., Chen, X., Niu, W., Yao, G., Liu, C., . . . Zhang, H. (2012). Fabrication of nanopowders by high energy ball milling and low temperature sintering of Mg2SiO4 microwave dielectrics. *Journal of Alloys and Compounds, 513*, 373-377.

Chesters, J. H. (1983). *Refractories: Production and properties*. London: IOM Communications Ltd.

Chevalier, J., & Gremillard, L. (2009). Ceramics for the medical applications: a picture for the next 20 years. *Journal of European Ceramic Society, 29*, 1245-1255.

Chou, J., Valenzuela, S. M., Santos, J., Bishop, D., Milthorpe, B., Green, D. W., Ben-Nissan, B. (2014). Strontium- and magnesium-enriched biomimetic beta-TCP macrospheres with potential for bone tissue morphogenesis. *J Tissue Eng Regen Med, 8*(10), 771-778

Clark, D. E., Folz, D. C. & Mahmoud, M. M. (Eds.). (2004). *Microwave solution for ceramic engineers*. Westerville: American Ceramic Society.

Clarke, I. C., Manaka, M., Green, D. D., Williams, P., Pezzotti, G., Kim, Y. H., . . . Gustafson, G. A. (2003). Current status of zirconia used in total hip implants. *Journal of Bone and Joint Surgery, 85*(4), 73-84.

Coadou, C. L., Karst, N., Emieux, F., Sicardy, O., Montani, A., Bernard-Granger, G., . . . Simonato, P. (2015). Assessment of ultrathin yttria-stabilized zirconia foils for biomedical applications. *Journal of Materials Science, 50*, 6197-6207.

Cottom, B. A., & Mayo, M. J. (1996). Fracture toughness of nanocrystalline ZrO2-3mol-percent Y2O3 determined by vickers indentation. *Scripta materialia, 34*(5), 809-814.

Cullity, B. D. & Stock, S. R. (2001) Elements of X-Ray Diffraction. 3rd Edition, Prentice-Hall, Inc., New York.

Das, S., Mukhopadhyay, A. K., Datta, S., & Basu, D. (2009). Prospects of microwave processing: an overview. *Bulletin of Materials Science, 32*, 1-13.

Dee, K. C., Puleo, D. A. & Bizios, R. (2003). An introduction to tissue biomaterial interactions. Wiley-Liss, Inc.

Deville S., Chevalier, J. and Gremillard, L. (2006). Influence of surface finish and residual stresses on the ageing sensitivity of biomedical grade zirconia. *Biomaterials, 27*, 2186-92.

Dorozhkin, S.V. (2009). Calcium orthophosphate-based biocomposites and hybrid biomaterials. *Journal of Materials Science, 44(9)*, 2343-2387.

Dorozhkin, S. V. (2010). Bioceramics of calcium orthophosphates. *Biomaterials, 31*(7), 1465-1485.

Dorozhkin, S.V. & Best, S. (2002). Biological and Medical Significance of Calcium Phosphates, *Angewandte Chemie International Edition, 41(17)*, 3130-3146.

Douy, A. (2002). Aqueous Syntheses of Forsterite (Mg2SiO4) and Enstatite (MgSiO3). *Journal of Sol-Gel Science and Technology, 24*(3), 221-228

Fathi. M.H. & Kharaziha, M. (2008). Mechanically activated crystallization of phase pure nanocrystalline forsterite powders. *Materials Letters, 62(27),* 4306-4309.

Fathi, M. H., & Kharaziha, M. (2009). Two-step sintering of dense, nanostructural forsterite. *Materials Letters, 63*(17), 1455-1458

Feng, P., Niu, M., Gao, C., Peng, S., & Shuai, C. (2014). A novel two-step sintering for nano-hydroxyapatite scaffolds for bone tissue engineering. *Scientific Reports, 4*, 5599.

Geetha M., Singh, A. K., Asokamani, R. & Gogia, A. K. (2009). Ti based biomaterials, the ultimate choice for orthopaedic implants – A review. *Progress in Materials Science, 54*, 397-425.

Ghomi, H., Jaberzadeh, M. & Fathi, M.H. (2011). Novel fabrication of forsterite scaffold with improved mechanical properties. *Journal of Alloys and Compounds, 509,* 63-68.

Gutwein, L. G., & Webster, T. J. (2002). Osteoblast and chrondrocyte proliferation in the presence of alumina and titania nanoparticles. *Journal of Nanoparticle Research, 4*, 231-238.

Hassan, A. M., Awaad, M., Bondioli, F., & Naga, S. M. (2014). Densification Behavior and Mechanical Properties of Niobium-Oxide-Doped Alumina Ceramics. *Journal of Ceramic Science and Technology, 5*(1), 51-56.

Hassanzadeh-Tabrizi, S. A., Bigham, A., & Rafienia, M. (2016). Surfactant-assisted sol-gel synthesis of forsterite nanoparticles as a novel drug delivery system. *Mater Sci Eng C Mater Biol Appl, 58,* 737-741.

Hench, L. L. (1998). Bioceramics. *Journal of American Ceramic Society, 81*(7), 1705-1728.

Hench, L.L. (2000). The challenge of orthopaedic materials. *Current Orthopaedics, 14*, 7-15.

Hiraga, T., Tachibana, C., Ohashi, N., & Sano, S. (2010). Grain growth systematics for forsterite enstatite aggregrates: Effect of lithology on grain size in the upper mantle. *Earth and Planetary Science Letters, 291*(1-4), 10-20.

Ito, A., Kawamura, H., Otsuka, M., Ikeuchi, M., Ohgushi, H., Ishikawa, K., . . . Ichinose, N. (2002). Zinc-releasing calcium phosphate for stimulating bone formation. *Materials Science and Engineering: C, 22*(1), 21-25.

Jayaswal, G. P., Dange, S. P., & Khalikar, A. N. (2010). Bioceramic in dental implants: A review. *Journal of Indian Prosthodontic Society, 10*(1), 8-12.

Jing, L. I., Qi, W., Jihui, L., & Peng, L. (2009). Synthesis process of forsterite refractory by iron ore tailings. *Journal of Environmental Sciences Supplement*, 92-95.

Juhasz, J. & Best, S. (2012). Bioactive ceramics: processing, structures and properties. *Journal of Materials Science*, *47(2)*, 610-624.

Katti, K.S. (2004). Biomaterials in total joint replacement. *Colloids and Surfaces B: Biointerfaces*, *39*, 133-142.

Kazakos, A., Komarneni, S., & Roy, R. (1990). Preparation and densification of forsterite (Mg2SiO4) by nanocomposite sol-gel processing. *Materials Letters*, *9*(10), 405-409.

Khanal, S. P., Mahfuz, H., Rondinone, A. J., & Leventouri, T. (2016). Improvement of the fracture toughness of hydroxyapatite by incorporation of carboxyl functionalized single walled nanotubes (CfSWCNTs) and nylon. *Materials Science and Engineering: C, 60*, 204-210.

Kharaziha, M., & Fathi, M. H. (2010). Improvement of mechanical properties and biocompatibility of forsterite bioceramic addressed to bone tissue engineering materials. *J Mech Behav Biomed Mater, 3*(7), 530-537.

Kosanović, C., Stubičar, N., Tomašić, N., Bermanec, V., & Stubičar, M. (2005). Synthesis of a forsterite powder by combined ball milling and thermal treatment. *Journal of Alloys and Compounds, 389*(1-2), 306-309.

Kiss, S.J., Kostic, E., Djurovic, D. & Boskovic, S. (2001). Influence of mechanical activation and fluorine ion on forsterite formation. *Powder Technology*, *114*, 84-88.

Kloss, F.R. & Gassner, R. (2006). Bone and aging: Effects on the maxillofacial skeleton. *Experimental Gerontology*, *41*, 123-129.

Kokubo, T., Kim, H.M. & Kawashita, M. (2003). Novel bioactive materials with different mechanical properties. *Biomaterials*, *24*, 2161-2175.

Kosanovic, C., Stubicar, N., Tomasic, N., Bermanec, V. & Stubicar, M. (2005), Synthesis of a forsterite powder by combined ball milling and thermal treatment. *Journal of Alloys and Compounds, 389(1)*, 306-309.

Kostic, E., Kiss, S., & Boskovic, S. (1997). Decrease of the MgAl2O4 formation temperature. *Powder Technology, 92*, 271-274.

Law, K.W. (1968). Grain growth in UO_2-Al_2O_3 in the presence of a liquid phase. *General Electric Research and Development Center, Schenectady, New York*, 12301.

Lawson, S. (1995). Environmental degradation of zirconia ceramics. *Journal of the European Ceramic Society, 15*, 485-502.

Lee, S. K. Y., Tan, C. Y., Lai, S. K. L., Tolouei, R., Amiriyan, M., Yap, B. K., & Ramesh, S. (2011). *Sintering behaviour of forsterite bioceramics*. Paper presented at the 2011 Natl. Postgrad. Conf.

LeGeros, R. Z. (1991). Calcium phosphate in oral biology and medicine. *Monographs in Oral Science, 15*, 1-201.

LeGeros, R. Z. and LeGeros, J. P. (1993). Dense hydroxyapatite. *In An Introduction to Bioceramics*. Ed. by Hench, L. L. and Wilson, J. (World Scientific, Singapore) Chapter 9, 139.

Liu, C. C., Yeh, J. K., & Aloia, J. F. (1988). Magnesium directly stimulates osteoblast proliferation. *Journal of Bone and Mineral Research, 3*, 104.

Livage, J., Babonneau, F., Chatry, M., & Coury, L. (1997). Sol-gel synthesis and NMR characterization of ceramics. *Ceramics International, 23*, 13-18.

Llyod, S.N. & Cross, W. (2002). The current use of biomaterials in urology. *European Urology Supplements*, *1*, 2-6.

Maliavski, N. I., Dushkin, O. V., Tchekounova, E. V., Markina, J. V., & Scarinci, G. (1997). An organic-inorganic silica precursor suitable for the sol-gel synthesis in aqueous media. *Journal of Sol-Gel Science and Technology, 8*, 571-575.

McCormick, P. G. (1995). Application of mechanical alloying to chemical refining (overview). *Materials Transactions, 36*(2), 161-169.

Mendelson, M. I. (1969). Average Grain Size in Polycrystalline Ceramics. *Journal of American Ceramic Society*, 52, 443-446.

Miao, S., Weng, W., Cheng, K., Du, P., Shen, G., Han, G., & Zhang, S. (2005). Sol-gel preparation of Zn-doped fluoridated hydroxyapatite films. *Surface & Coatings Technology, 198*, 223-226.

Mitchell, M. B. D., Jackson, D., & James, P. F. (1998). Preparation and characterization of forsterite (Mg2SiO4) aerogels. *Journal of Non-Crystalline Solids, 225*, 359-364.

Mohamed, N.R. (2007). *Sintering of Ceramics*. CRC Press.

Monaco, C., Tucci, A., Esposito, L., & Scotti, R. (2013). Microstructural changes produced by abrading Y-TZP in presintered and sintered conditions. *Journal of Dentistry*, *41*(2), 121-126.

Monaco, C., Prete, F., Leonelli, C., Esposito, L., & Tucci, A. (2015). Microstructural study of microwave sintered zirconia for dental applications. *Ceramics International, 41*(1), 1255-1261.

Mukhopadhyay, A., & Basu, B. (2007). Consolidation-microstructure-property relationships in bulk nanoceramics and ceramic nanocomposites: a review. *Structural ceramic nanomaterials, 52*(5), 257-288.

Murray, E. J., & Messer, H. H. (1981). Turnover of bone zinc during normal and accelerated bone loss in rats. *Journal of Nutrition, 111*, 1641-1647.

Mustafa, E., Khalil, N., & Gamal, A. (2002). Sintering and microstructure of spinel–forsterite bodies. *Ceramic International, 28*, 663-667.

Naderi, H., Matin, M. M., & Barhrami, A. R. (2011). Critical issues in tissue engineering: biomaterials, cell sources, angiogenesis and drug delivery systems. *Journal of biomaterials applications*, 1-17.

Naghiu, M. A., Gorea, M., Mutch, E., Kristaly, F., & Tomoaia-Cotisel, M. (2013). Forsterite Nanopowder: Structural Characterization and Biocompatibility Evaluation. *Journal of Materials Science & Technology, 29*(7), 628-632.

National Institutes of Health (NIH). (1982). Clinical applications of biomaterials. *NIH Consensus Statement, 4*(5), 1-19.

Ni, S., Chou, L., & Chang, J. (2007). Preparation and characterization of forsterite (Mg2SiO4) bioceramics. *Ceramics International, 33*(1), 83-88.

O'Brien, F. J. Biomaterials & scaffolds for tissue engineering. *Materials Today, 14*(3), 88-95.

Ohsato, H., Tsunooka, T., Sugiyama, T., Kakimoto, K.-i., & Ogawa, H. (2006). Forsterite ceramics for millimeterwave dielectrics. *Journal of Electroceramics, 17*(2-4), 445-450.

Oghbaei, M., & Mirzaee, O. (2010). Microwave versus conventional sintering: a review of fundamentals, advantages and applications. *Journal of Alloys and Compounds, 494*, 175-189.

Park J. B. & Bronzino, J. D. (Eds.). (2003). *Biomaterials: principles and applications.* Boca Rator: CRC Press.

Petricevic, V., Gayen, S. K., Alfano, R. R., Yamagishi, K., Anzai, H., & Yamaguchi, Y. (1988). Laser action in chromium-doped forsterite. *Applied Physics Letters, 52*(13), 1040-1042.

Piconi, C., & Maccauro, G. (1999). Zirconia as a ceramic biomaterials. *Biomaterials, 20*(1), 1-25.

Pietak, A. M., Reid, J. W., Stott, M. J., & Sayer, M. (2007). Silicon substitution in the calcium phosphate bioceramics. *Biomaterials, 28*, 4023-4032.

Popov, O. N., Frolova, V. P., Orlova, V. N., Shatova, N. P., & Izosenkova, A. V. (1988). Contact interaction of aluminosilicate and basic refractories. *Refractories For The Consumer, 29*(3), 259-262.

Presenda, A., Salvador, M. D., Penaranda-Foix, F. L., Moreno, R., & Borrell, A. (2015). Effect of microwave sintering on microstructure and mechanical properties in Y-TZP materials used for dental applications. *Ceramic International, 41*, 7125-7132.

Promsawat, M., Watcharapasom, A., & Jiansirisomboon, S. (2012). Effects of ZnO nanoparticulate addition on the properties of PMNT ceramics. *Nanoscale Research Letters, 7*(1), 65.

Ramakrishna, S., Mayer, J., Wintermantel, E. & Leong, K.W. (2001). Biomedical applications of polymer-composite materials: A review. *Composites Science and Technology, 61*(9), 1189-1224.

Ramesh, S., Yaghoubi, A., Lee, K. Y., Chin, K. M., Purbolaksono, J., Hamdi, M., & Hassan, M. A. (2013). Nanocrystalline forsterite for biomedical applications: synthesis, microstructure and mechanical properties. *Journal of Mechanical Behavior of Biomedical Materials, 25*, 63-69.

Ramesh, S., Tan, C. Y., Peralta, C. L., & Teng, W. D. (2007). The effect of manganese oxide on the sinterability of hydroxyapatite. *Science and Technology of Advanced Materials, 8*(4), 257-263.

Rybakov, K. I., Olevsky, E. A., & Krikun, E. V. (2013). Microwave sintering: fundamentals and modeling. *Journal of American Ceramic Society, 96*, 1003-1020.

Saberi, A., Alinejad, B., Negahdari, Z., Kazemi, F., & Almasi, A. (2007). A novel method to low temperature synthesis of nanocrystalline forsterite. *Materials Research Bulletin, 42*(4), 666-673.

Saberi, A., Negahdari, Z., Alinejad, B., & Golestani-Fard, F. (2009). Synthesis and characterization of nanocrystalline forsterite through citrate–nitrate route. *Ceramics International, 35*(4), 1705-1708.

Sanosh, K.P., Balakrishnan, A., Francis, L. & Kim, T.N. (2010). Sol–gel synthesis of forsterite nanopowders with narrow particle size distribution. *Journal of Alloys and Compounds, 495(1)*, 113-115.

Schoppka, S., Schmid, T., Schmid, C., & Lehle, K. (2010). Curent strategies in cardiovascular biomaterial functionalization. *Materials, 3*(1), 638-655.

Shi, F., Du, P. C., Liu, J. X., Wu, J. W., & Luo, C. Y. (2012). Preparation of Forsterite by Solid State Synthesis Process and its Dielectric Properties. *Advanced Materials Research, 534*, 110-113.

Sionkowska, A. (2011). Current research on the blends of natural and synthetic polymers as new biomaterials: Review. *Progress in Polymer Science, 36*(9), 1254-1276.

Siores, E. and DoRego, D. (1995). Microwave applications in materials joining. *Journal of Materials Processing Technology. 48(12*), 619-625.

Song Kai Xin, Xu Jun Ming, Hu Xiao Ping, Zheng Liang, Ying Zhi Hua, & Bin, Q. H. (2010). *Microwave dielectric properties of Al-substituted forsterite ceramics*. Paper presented at the International Conference on Electrical and Control Engineering.

Straley, K. S., Foo, C. W. P., & Heilshorn, S. C. (2010). Biomaterial design strategies for the treatment of spinal cord injuries. *Journal of Neurotrauma, 27*, 1-19.

Suchanek, W., Yashima, M., Kakihana, M., & Yoshimura, M. (1997). Hydroxyapatite ceramics with selected sintering additives. *Biomaterials, 80*, 2805-2813.

Suchanek, W. & Yoshimura, M. (1998). Processing and properties of hydroxyapatite ceramics with selected sintering additives. *Biomaterials, 13*, 94-117.

Sun, H.-T., Fujii, M., Nitta, N., Mizuhata, M., Yasuda, H., Deki, S., & Hayashi, S. (2009). Molten-Salt Synthesis and Characterization of Nickel-Doped Forsterite Nanocrystals. *Journal of the American Ceramic Society, 92*(4), 962-966.

Suryanarayana, C. (2001). Mechanical alloying and milling. *Progress in Materials Science, 46*, 1-184.

Tavangarian, F., & Emadi, R. (2009). Mechanical activation assisted synthesis of pure nanocrystalline forsterite powder. *Journal of Alloys and Compounds, 485*(1-2), 648-652.

Tavangarian, F., Emadi, R., & Shafyei, A. (2010). Influence of mechanical activation and thermal treatment time on nanoparticle forsterite formation mechanism. *Powder Technology, 198*(3), 412-416.

Tavangarian, F., & Emadi, R. (2010a). Synthesis of nanocrystalline forsterite (Mg2SiO4) powder by combined mechanical activation and thermal treatment. *Materials Research Bulletin, 45*(4), 388-391.

Tavangarian, F., & Emadi, R. (2010b). Synthesis of pure nanocrystalline magnesium silicate powder. *Ceramics Silikaty, 54*(2), 122-127.

Tavangarian, F., & Emadi, R. (2011). Improving degradation rate and apatite formation ability of nanostructure forsterite. *Ceramics International, 37*(7), 2275-2280.

Thostenson, E.T. & Chou, T.W. (1999). Microwave processing: fundamentals and applications. *Composite: Part A, 30*, 1055-1071.

Thuault, A., Savary, E., Hornez, J. C., Moreau, G., Descamps, M., Marinel, S., & Leriche, A. (2014). Improvement of the hydroxyapatite mechanical properties by direct microwave sintering in single mode cavity. *Journal of European Ceramic Society, 34*, 1865-1871.

Tomoaia, G.H., Soritau, O., Cotisel, M.T., Pop, L.B., Pop, Mocanu, A., Horovitz, O. & Bobos, L.D. (2013). Scaffolds made of nanostructured phosphates, collagen and chitosan for cell culture, *Powder Technology*, *238*, 99-107.

Vallepu, R., Nakamura, Y., Komatsu, R., & Ikeda, K. (2995). Preparation of forsterite by the geopolymer technique-gel compositions as a function of pH and crystalline phases. *Journal of Sol-Gel Science and Technology, 35*, 107-114.

Veljović, D., Zalite, I., Palcevskis, E., Smiciklas, I., Petrović, R., & Janaćković, D. (2010). Microwave sintering of fine grained HAP and HAP/TCP bioceramics. *Ceramics International, 36*(2), 595-603.

Verdun, H. R., Thomas, L. M., Andrauskas, D. M., McCollum, T., & Pinto, A. (1988). Chromium-doped forsterite laser pumped with 1.06 μm radiation. *Applied Physics Letters, 53*(26), 2593.

Vorman, J. (2003). Magnesium: Nutrition and metabolism. *Mol Aspects Med., 24*, 27-37.

Wang, J., Binner, J., & Vaidhyanathan, N. (2006). Evidence for the microwave effect during hybrid sintering. *Journal of American Ceramic Society, 89*(6), 1977-1984.

Wang, M. (2003). Developing bioactive composite materials for tissue replacement. *Biomaterials, 24*, 2133-2151.

Wang, X. H., Chen, P. L., & Chen, I. W. (2006). Two-step sintering of ceramics with constant grain-size I. Y2O3. *Journal of American Ceramic Society, 89*, 431-437.

Wang, W., Ouyang, Y., & Poh, C. K. (2011). Orthopaedic implant technology: Biomaterials from past to future. *Biomaterials in Orthopaedic Implant Technology, 40*(5), 237-244.

Webster, T. J., Ergun, C., Doremus, R. H., Siegel, R. W., & Bizios, R. (2001). Enhanced osteoclast-like cell functions on nanophase ceramics. *Biomaterials, 22*(11), 1327-1333.

Williams, D. B. & Carter, C. B. (1996). The transmission electron microscope. *Springer US.*

Williams, D. F. (2009). On the nature of biomaterials. *Biomaterials, 30*(30), 5897-5909.

Wise, D. L. (2000). Biomaterials Engineering and Devices. *Humana Press; Berlín, Germany*, 205-319.

Wolf, F. I. and Cittadini, A. (2003). Chemistry and biochemistry of magnesium. *Mol Aspects Med., 24*, 3-9.

Wurst, J. C. & Nelson, J. A. (1972). Lineal Intercept Technique for Measuring Grain Size in Two-phase Polycrystalline Ceramics. *Journal of American Ceramic Society, 5*, 109.

Yadoji, P., Peelamedu, R., Agrawal, D. & Roy, R. (2003). Microwave sintering of Ni-Zn ferrites: comparison with conventional sintering. *Materials Science and Engineering: Part B, 98*, 269-278.

Yamaguchi, M. (2010). Role of nutritional zinc in the prevention of osteoporosis. *Molecular and Cellular Biochemistry, 338*, 241-254.

Yasuoka, M., Nishimura, Y., Nagaoka, T., & Watari, K. (2006). Influence of different methods of controlling microwave sintering. *Journal of Thermal Analysis and Calorimetry, 83*(2), 407-410.

Yoldas, B. E. (1982). Introduction and effect of structural variations in inorganic polymers and glass networks. *Journal of Non-Crystalline Solids, 51*, 105-121.

Zuo, F., Carry, C., Saunier, S., Marinel, S., & Goeuriot, D. (2013). Comparison of the microwave and conventional sintering of alumina: effect of MgO doping and particle size. *Journal of American Ceramic Society, 96*, 1732-1737.

Zuo, F., Badev, A., Saunier, S., Goeuriot, D., Heuguet, R., & Marinel, S. (2014). Microwave versus conventional sintering: Estimate of the appraten activation energy for densification of alpha-alumina and zinc oxide. *Journal of the European Ceramic Society, 34*, 3103-3110.

LIST OF PUBLICATIONS AND PAPERS PRESENTED

Published works as well as papers presented at conferences, seminars, symposiums etc pertaining to the research topic of the research report/ dissertation/ thesis are suggested be included in this section. The first page of the article may also be appended as reference.

Publications

1. **Sinterability of forsterite prepared via solid-state reaction,** (2015) *International Journal of Applied Ceramic Technology*, Vol. 12, 437-442.
2. **Study on the effects of milling time and sintering temperature on the sinterability of forsterite (Mg_2SiO_4),** (2015) *Journal of the Ceramic Society of Japan*, Vol. 123, 1032-1037.
3. **Effect of Attritor Milling on Synthesis and Sintering of Forsterite Ceramics,** (2016) *International Journal of Applied Ceramic Technology*, Vol. 13, 726-735.
4. **The effects of calcium-to-phosphorus ratio on the densification and mechanical properties of hydroxyapatite ceramic,** (2015) *International Journal of Applied Ceramic Technology*, Vol. 12, 223-227.
5. **The effect of sintering ramp rate on the sinterability of forsterite ceramics** (2014) *Materials Research Innovations*, Vol. 18, 61-64.
6. **Effect of calcination on the sintering behavior of hydroxyapatite,** (2014) Ceramics Silikaty, Vol. 58, 320-325.

Conferences

1. **Effect of ball milling in synthesizing pure forsterite**, (2014) *AUN/SEED-NET Regional Conference on Materials Engineering (RCME).*

2. **The effect of heat treatment time on the formation of forsterite (Mg_2SiO_4),** (2015) *International Journal of Life Sciences Biotechnology and Pharma Research (ICBBT).*
3. **Rapid Densification of Forsterite Ceramic via Microwave Sintering,** (2016) *the First International Conference on Civil Engineering and Materials Science (ICCEM2016).*

APPENDIX A

Calculation of raw materials preparation

The reaction between the precursors occurred in two stages. First and second stages were governed by the following equation:

$$4MgCO_3*Mg(OH)_2*5H_2O + Mg_3Si_4O_{10}(OH)_2 + NH_4Cl \rightarrow 4MgSiO_3 + 4MgO + 4CO_2 + 7H_2O + HCl + NH_3 \quad \text{A-1}$$

$$MgO + MgSiO_3 \rightarrow Mg_2SiO_4 \quad \text{A-2}$$

The reaction to produce forsterite based on equation A-2 was based on MgO and $MgSiO_3$ knowing the $4MgCO_3*Mg(OH)_2*5H_2O$ will decompose into MgO and CO_2 gas. Ammonium chloride (NH_4Cl) was not directly involved in the reaction and acted only as a catalyst. Table A-1 showed the molecular weight of the precursors and forsterite.

Table A-1: Molecular weight of various compositions

Compositions	Molecular weight (g/mol)
$4MgCO_3*Mg(OH)_2*5H_2O$	485
$Mg_3Si_4O_{10}(OH)_2$	379.3
Mg_2SiO_4	140.7
NH_4Cl	53.5

50 g of $4Mg_2SiO_4$ $= \frac{50\ g}{4(140.7)\ g/mol}$

= **0.0888 mol**

Based on the equation, 1 mol of MgO with 1 mol of talc will produce 1 mol of forsterite. Hence, 0.0888 mol of forsterite can be produced by using 0.0888 mol for both $MgCO_3$ and talc.

Amount of $4MgCO_3*Mg(OH)_2*5H_2O$ = (0.0888 mol) x (485 g/mol)

= **43.068 g**

Amount of talc = (0.0888 mol) x (379.3 g/mol)

= **33.682 g**

Amount of NH_4Cl = (0.0888 mol) x (53.5 g/mol)

= **4.751 g**

APPENDIX B

JCPDS information

Name and formula

Reference code:	00-034-0189
Mineral name:	Forsterite, syn
Compound name:	Magnesium Silicate
PDF index name:	Magnesium Silicate
Empirical formula:	Mg_2O_4Si
Chemical formula:	Mg_2SiO_4

Crystallographic parameters

Crystal system:	Orthorhombic
Space group:	Pmnb
Space group number:	62
a (Å):	5.9817
b (Å):	10.1978
c (Å):	4.7553
Alpha (°):	90.0000
Beta (°):	90.0000
Gamma (°):	90.0000
Calculated density (g/cm^3):	3.22
Measured density (g/cm^3):	3.28
Volume of cell (10^6 pm^3):	290.07
Z:	4.00
RIR:	-

Subfiles and quality

Subfiles:	Common Phase Educational pattern Inorganic Mineral NBS pattern
Quality:	Star (S)

Comments

Color:	Colorless
Creation Date:	1/1/1970
Modification Date:	1/1/1970
Sample Preparation:	$MgCO_3$ and SiO_2 were mixed in a 2:1 molar ratio and heated at 800 C overnight, 1300 C for 21 hours, 1500 C for 25 hours, and 1525 C for 24 hours with intermittent grinding
Color:	Colorless

Temperature of Data Collection:	Pattern taken at 26(2) C
Optical Data:	A=1.645, B=1.660, Q=1.679, Sign=+, 2V=92°
Additional Patterns:	To replace 7-74 and validated by calculated pattern 21-1260
Additional Patterns:	See ICSD 26374 (PDF 74-714); See ICSD 27529 (PDF 74-1678); See ICSD 34112 (PDF 76-513); See ICSD 9334 (PDF 71-792); See ICSD 9685 (PDF 71-1080); See ICSD 12124 (PDF 71-1792); See ICSD 62524 (PDF 78-1369); See ICSD 62525 (PDF 78-1370); See ICSD 62526 (PDF 78-1371); See ICSD 62527 (PDF 78-1372); See ICSD 68588 (PDF 80-783).

References

Primary reference:	*Natl. Bur. Stand. (U.S.) Monogr. 25*, **20**, 71, (1984)
Optical data:	Sahama., *Bur. Mines Rep. Invest.*

Peak list

No.	h	k	l	d [A]	2Theta[deg]	I [%]
1	0	2	0	5.10212	17.367	22.0
2	0	1	1	4.30749	20.603	4.0
3	1	2	0	3.88119	22.895	76.0
4	1	0	1	3.72220	23.887	25.0
5	1	1	1	3.49596	25.458	26.0
6	0	2	1	3.47675	25.601	22.0
7	1	2	1	3.00647	29.691	14.0
8	2	0	0	2.99062	29.852	18.0
9	0	3	1	2.76534	32.348	66.0
10	1	3	1	2.50973	35.748	83.0
11	2	1	1	2.45668	36.547	100.0
12	1	4	0	2.34558	38.344	13.0
13	0	1	2	2.31504	38.870	13.0
14	2	2	1	2.26732	39.722	57.0
15	0	4	1	2.24703	40.096	37.0
16	1	1	2	2.15894	41.807	23.0
17	2	3	1	2.03031	44.593	7.0
18	0	3	2	1.94787	46.589	6.0
19	2	4	0	1.94067	46.772	5.0
20	0	5	1	1.87436	48.531	8.0
21	2	0	2	1.86079	48.908	3.0
22	3	2	0	1.85688	49.018	2.0
23	3	0	1	1.83877	49.533	1.0
24	2	1	2	1.82991	49.789	1.0
25	3	1	1	1.80898	50.405	4.0
26	1	5	1	1.78861	51.020	5.0
27	2	2	2	1.74828	52.285	73.0
28	0	4	2	1.73861	52.598	24.0
29	3	2	1	1.72942	52.899	6.0
30	1	4	2	1.66979	54.944	16.0
31	1	6	0	1.63472	56.226	15.0
32	3	3	1	1.61731	56.886	17.0
33	0	6	1	1.60080	57.527	2.0
34	2	5	1	1.58837	58.020	4.0
35	3	4	0	1.57077	58.733	11.0
36	0	1	3	1.56657	58.906	8.0
37	1	0	3	1.53234	60.357	2.0
38	1	1	3	1.51444	61.146	10.0
39	3	1	2	1.51112	61.295	9.0
40	2	4	2	1.50324	61.651	11.0
41	1	5	2	1.49899	61.845	20.0
42	4	0	0	1.49544	62.008	30.0

43	2	6	0	1.47795	62.825	33.0
44	1	2	3	1.46741	63.328	3.0
45	3	2	2	1.46375	63.505	3.0
46	0	3	3	1.43654	64.853	4.0
47	2	6	1	1.41107	66.172	2.0
48	1	3	3	1.39684	66.934	13.0
49	3	3	2	1.39300	67.143	14.0
50	2	1	3	1.38744	67.448	9.0
51	2	5	2	1.37476	68.155	2.0
52	3	5	1	1.36574	68.668	1.0
53	2	2	3	1.35051	69.553	22.0
54	0	4	3	1.34645	69.793	15.0
55	4	3	1	1.31549	71.685	11.0
56	1	4	3	1.31307	71.838	9.0
57	3	6	0	1.29371	73.085	5.0
58	4	0	2	1.26607	74.950	2.0
59	2	7	1	1.26270	75.185	1.0
60	4	1	2	1.25608	75.651	3.0
61	0	5	3	1.25152	75.975	1.0
62	3	6	1	1.24775	76.246	3.0
63	4	4	1	1.24484	76.456	3.0
64	3	0	3	1.24113	76.726	3.0
65	3	1	3	1.23173	77.420	1.0
66	2	4	3	1.22757	77.732	2.0
67	3	5	2	1.22284	78.089	2.0
68	1	7	2	1.21598	78.615	1.0
69	1	8	1	1.20603	79.391	1.0

Stick Pattern

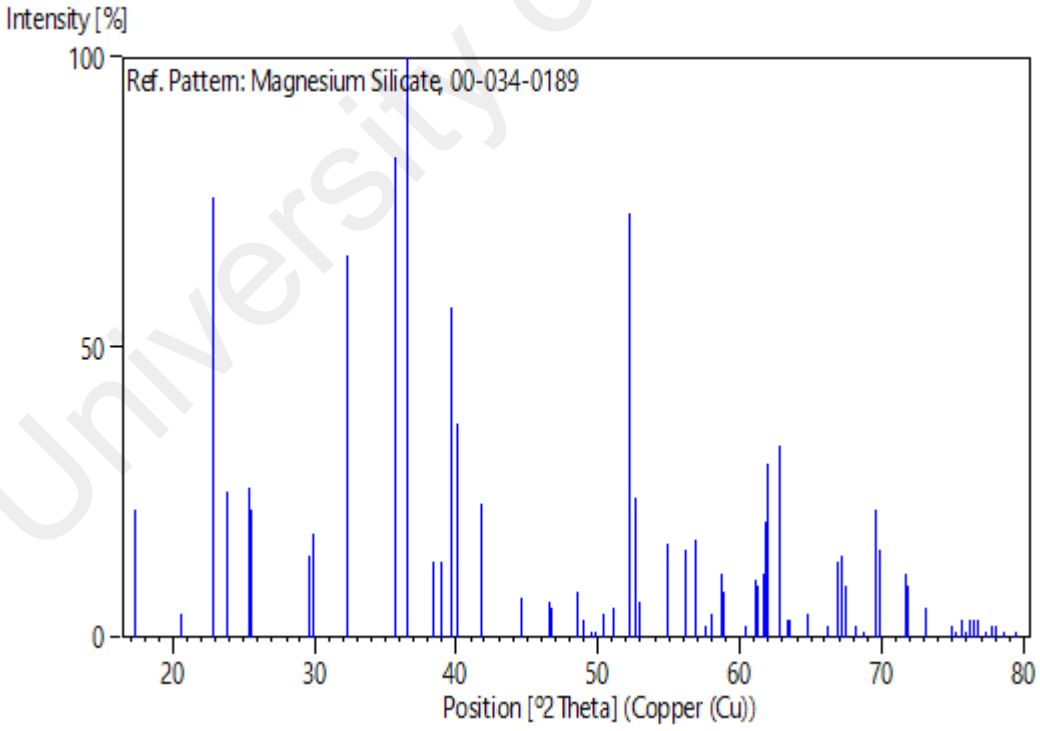

Figure B-1: JCPDS reference of forsterite (Mg_2SiO_4)

Name and formula

Reference code:	00-013-0558
Mineral name:	Talc-2*M*
Compound name:	Magnesium Silicate Hydroxide
PDF index name:	Magnesium Silicate Hydroxide
Empirical formula:	$H_2Mg_3O_{12}Si_4$
Chemical formula:	$Mg_3Si_4O_{10}(OH)_2$

Crystallographic parameters

Crystal system:	Monoclinic
Space group:	C2/c
Space group number:	15
a (Å):	5.2870
b (Å):	9.1580
c (Å):	18.9500
Alpha (°):	90.0000
Beta (°):	99.5000
Gamma (°):	90.0000
Calculated density (g/cm^3):	2.78
Measured density (g/cm^3):	2.58
Volume of cell (10^6 pm^3):	904.94
Z:	4.00
RIR:	-

Subfiles and quality

Subfiles:	Corrosion Forensic Inorganic Mineral Pigment/Dye
Quality:	Indexed (I)

Comments

Color:	Colorless, white, green, brown
Creation Date:	1/1/1970
Modification Date:	1/1/1970
Optical Data:	A=1.5445(5), B=1.5915(2), Q=1.5945(5), Sign=-, 2V=0-30°
Color:	Colorless, white, green, brown
Sample Source or Locality:	Specimen from Manchuria, China. Magnesite removed on purification
Additional Patterns:	To replace 3-881. 1 Enhanced by orientation.

References

Primary reference:	Stemple, Brindley., *J. Am. Ceram. Soc.*, **43**, 34, (1960)

Optical data: Deer, W., Howie, R., Zussman, J., *Rock Forming Minerals*, **3**, 121, (1962)

Peak list

No.	h	k	l	d [A]	2Theta[deg]	I [%]
1	0	0	2	9.34000	9.461	100.0
2	0	0	4	4.66000	19.029	90.0
3	-1	1	1	4.55000	19.494	30.0
4	-1	1	4	3.51000	25.354	4.0
5	1	1	3	3.43000	25.956	1.0
6	0	0	6	3.11600	28.625	100.0
7	0	2	5	2.89200	30.895	1.0
8	-2	0	2	2.62900	34.075	12.0
9	-1	3	2	2.59500	34.536	30.0
10	1	3	2	2.47600	36.252	65.0
11	0	0	8	2.33500	38.525	16.0
12	2	2	1	2.21200	40.759	20.0
13	-2	0	6	2.19600	41.069	10.0
14	2	0	4	2.12200	42.570	8.0
15	-1	3	6	2.10300	42.974	20.0
16	2	2	4	1.93000	47.046	6.0
17	0	0	10	1.87000	48.652	40.0
18	-2	4	2	1.72500	53.045	2.0
19	1	5	2	1.68200	54.512	20.0
20	0	0	12	1.55700	59.304	20.0
21	0	6	0	1.52700	60.590	40.0
22	3	3	0	1.50900	61.390	10.0
23	3	3	2	1.46000	63.687	8.0
24	3	1	6	1.40600	66.442	16.0
25	-1	3	12	1.39400	67.089	20.0
26	3	3	5	1.33600	70.420	16.0
27	2	4	8	1.31800	71.528	10.0
28	-2	6	4	1.29700	72.870	10.0
29	1	7	0	1.26900	74.748	10.0
30	-3	5	8	1.16900	82.438	6.0

Stick Pattern

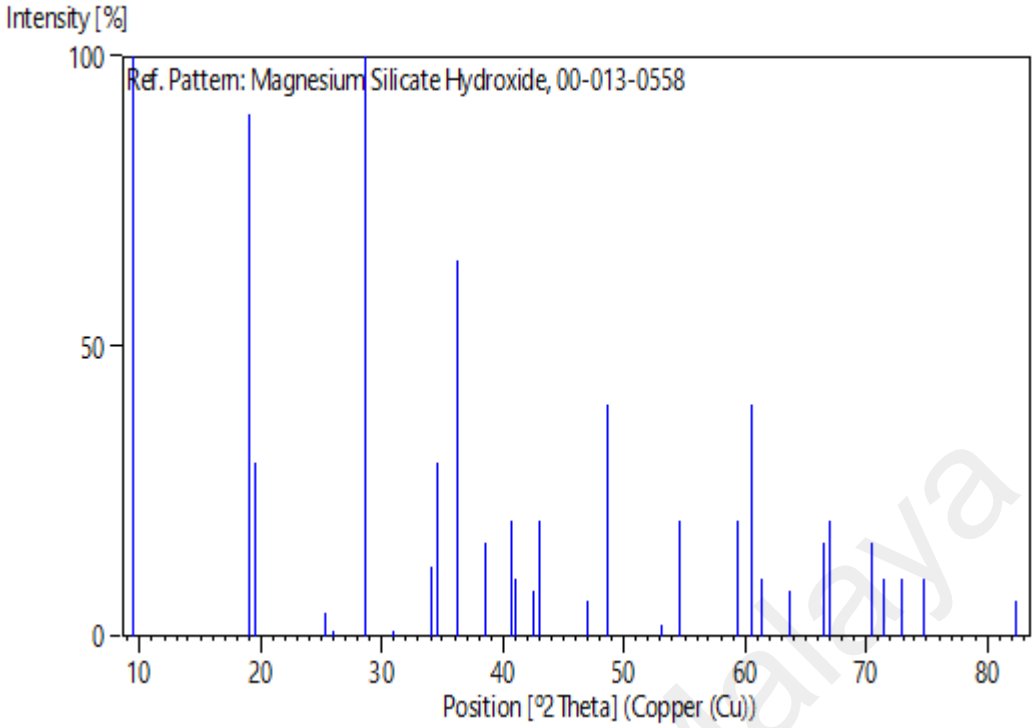

Figure B-2: JCPDS reference of talc

Name and formula

Reference code:	01-070-1177
Mineral name:	Hydromagnesite
Compound name:	Magnesium Carbonate Hydroxide Hydrate
ICSD name:	Magnesium Carbonate Hydroxide Hydrate
Empirical formula:	$C_4H_{10}Mg_5O_{18}$
Chemical formula:	$Mg_5 (CO_3)_4 (OH)_2 (H_2O)_4$

Crystallographic parameters

Crystal system:	Orthorhombic
Space group:	Bbam
Space group number:	64
a (Å):	18.3710
b (Å):	8.9610
c (Å):	8.3840
Alpha (°):	90.0000
Beta (°):	90.0000
Gamma (°):	90.0000
Calculated density (g/cm^3):	2.25
Measured density (g/cm^3):	2.24
Volume of cell (10^6 pm^3):	1380.20
Z:	4.00
RIR:	0.88

Subfiles and quality

Subfiles:	Corrosion ICSD Pattern Inorganic Mineral
Quality:	Calculated (C)

Comments

ICSD collection code:	002341
Creation Date:	1/1/1970
Modification Date:	1/1/1970
ICSD Collection Code:	002341
Calculated Pattern Original Remarks:	ATOM H 1 +1 40.00 Atoms not located in unit cell
Temperature Factor:	ITF
Sample Source or Locality:	Specimen from Fort Point, San Francisco, CA, USA. The crystal structure of hydromagnesite.

References

Primary reference:	*Calculated from ICSD using POWD-12++*, (1997)
Structure:	Akao, M., Marumo, F., Iwai, S.I., *Acta Crystallogr., Sec. B*, **30**, 2670, (1974)

Peak list

No.	h	k	l	d [A]	2Theta[deg]	I [%]
1	2	0	0	9.18544	9.621	45.7
2	2	1	0	6.41426	13.795	49.0
3	1	1	1	5.80816	15.242	100.0
4	4	0	0	4.59272	19.311	6.4
5	0	2	0	4.48050	19.799	5.8
6	0	0	2	4.19197	21.177	18.4
7	4	1	0	4.08718	21.727	6.5
8	2	2	0	4.02697	22.056	5.0
9	2	0	2	3.81361	23.306	7.0
10	2	1	2	3.50905	25.361	7.1
11	3	2	1	3.32031	26.829	15.3
12	4	2	0	3.20713	27.795	7.8
13	5	1	1	3.15038	28.306	13.0
14	4	0	2	3.09618	28.812	8.1
15	6	0	0	3.06181	29.142	3.4
16	4	1	2	2.92642	30.523	5.7
17	2	2	2	2.90408	30.763	50.7
18	6	1	0	2.89735	30.837	42.9
19	2	3	0	2.84058	31.469	2.6
20	1	3	1	2.78132	32.157	2.5
21	5	2	1	2.69077	33.270	15.1
22	1	1	3	2.64022	33.926	0.5
23	3	3	1	2.55676	35.069	1.0
24	4	2	2	2.54717	35.205	0.9
25	6	2	0	2.52793	35.482	5.0
26	4	3	0	2.50400	35.833	12.5
27	6	0	2	2.47252	36.305	6.2
28	3	1	3	2.44587	36.714	1.4

29	7	1	1	2.41213	37.247	3.1
30	6	1	2	2.38345	37.712	0.6
31	1	2	3	2.35170	38.240	4.7
32	8	0	0	2.29636	39.199	9.8
33	0	4	0	2.24025	40.223	1.1
34	5	3	1	2.23393	40.341	2.1
35	3	2	3	2.21122	40.774	10.5
36	7	2	1	2.18619	41.262	6.7
37	2	4	0	2.17645	41.455	3.5
38	5	1	3	2.15882	41.809	16.3
39	4	3	2	2.14969	41.995	12.4
40	6	3	0	2.13809	42.234	4.4
41	0	0	4	2.09599	43.124	0.6
42	8	2	0	2.04346	44.291	1.6
43	1	3	3	2.02825	44.641	3.8
44	8	0	2	2.01348	44.986	2.5
45	5	2	3	1.99233	45.490	14.8
46	0	4	2	1.97580	45.892	1.9
47	8	1	2	1.96496	46.160	3.0
48	9	1	1	1.93605	46.890	8.6
49	2	4	2	1.93162	47.004	5.2
50	7	3	1	1.91919	47.327	0.9
51	4	0	4	1.90465	47.711	2.1
52	0	2	4	1.89852	47.875	1.7
53	4	1	4	1.86482	48.796	2.0
54	2	2	4	1.85922	48.952	3.3
55	10	0	0	1.83693	49.586	4.9
56	8	3	0	1.82054	50.063	3.1
57	4	4	2	1.81498	50.227	2.2
58	9	2	1	1.81355	50.269	2.0
59	6	4	0	1.80798	50.435	1.0
60	5	3	3	1.78402	51.161	0.2
61	7	2	3	1.75942	51.929	3.8
62	4	2	4	1.75452	52.085	2.2
63	1	5	1	1.74468	52.401	1.9
64	1	4	3	1.74010	52.549	6.0
65	10	2	0	1.69821	53.949	0.1
66	2	3	4	1.68656	54.352	0.9
67	10	0	2	1.68082	54.553	1.0
68	7	4	1	1.66975	54.945	2.2
69	6	4	2	1.66015	55.290	1.2
70	10	1	2	1.65370	55.525	0.9
71	1	1	5	1.64159	55.970	3.1
72	2	5	2	1.62115	56.739	11.4
73	11	1	1	1.61121	57.121	4.5
74	4	3	4	1.60724	57.275	2.4
75	8	4	0	1.60357	57.419	0.8
76	3	1	5	1.59154	57.894	0.7
77	5	4	3	1.57844	58.420	5.3
78	10	2	2	1.57519	58.552	3.7
79	10	3	0	1.56482	58.979	7.4
80	4	5	2	1.55109	59.553	0.5
81	9	2	3	1.54698	59.727	0.4
82	11	2	1	1.53833	60.098	0.9
83	12	0	0	1.53055	60.435	4.2
84	8	1	4	1.52549	60.656	2.4
85	3	2	5	1.52119	60.846	0.4
86	5	1	5	1.50381	61.625	2.6
87	8	4	2	1.49772	61.903	1.4
88	0	6	0	1.49350	62.098	1.1
89	9	4	1	1.48497	62.494	0.1
90	2	6	0	1.47414	63.006	1.2
91	10	3	2	1.46601	63.396	2.1
92	8	2	4	1.46321	63.531	1.2

93	1	3	5	1.45755	63.807	0.5
94	7	4	3	1.45481	63.941	1.9
95	4	4	4	1.45204	64.078	1.2
96	12	2	0	1.44868	64.244	1.3
97	5	2	5	1.44318	64.519	2.2
98	3	6	1	1.42972	65.201	1.0
99	4	6	0	1.42029	65.688	2.2
100	11	1	3	1.41560	65.933	2.0
101	8	5	0	1.41284	66.079	1.2
102	0	6	2	1.40688	66.395	2.9
103	0	0	6	1.39732	66.908	3.0
104	7	1	5	1.39557	67.003	2.5
105	10	0	4	1.38154	67.775	1.1
106	13	1	1	1.37694	68.033	0.6
107	8	3	4	1.37446	68.172	0.1
108	12	2	2	1.36922	68.469	0.4
109	10	1	4	1.36540	68.688	0.9
110	12	3	0	1.36239	68.861	0.4
111	5	3	5	1.35854	69.083	0.1
112	7	2	5	1.34758	69.726	0.5
113	10	4	2	1.34539	69.856	0.8
114	6	6	0	1.34232	70.039	0.5
115	8	5	2	1.33884	70.248	1.1
116	0	2	6	1.33396	70.543	1.3
117	13	2	1	1.32971	70.803	1.9
118	9	4	3	1.32768	70.927	1.1
119	11	4	1	1.32219	71.266	1.3
120	10	2	4	1.32020	71.390	0.7
121	1	6	3	1.31383	71.790	0.6
122	14	0	0	1.31221	71.892	0.8
123	7	5	3	1.30793	72.164	0.4
124	4	5	4	1.30591	72.294	0.2
125	14	1	0	1.29836	72.781	0.2
126	12	3	2	1.29568	72.956	0.1
127	11	3	3	1.29245	73.168	0.2
128	3	6	3	1.28775	73.479	0.1
129	10	5	0	1.28285	73.806	1.0
130	4	2	6	1.28102	73.929	0.8
131	6	6	2	1.27730	74.180	0.5
132	8	4	4	1.27358	74.433	1.4
133	6	0	6	1.27120	74.596	0.9
134	2	7	0	1.26789	74.824	0.3
135	12	4	0	1.26397	75.096	0.4
136	5	4	5	1.26089	75.312	0.6
137	14	2	0	1.25860	75.473	0.8
138	10	3	4	1.25383	75.811	0.4
139	14	0	2	1.25229	75.920	1.0
140	13	1	3	1.24878	76.172	0.7
141	5	6	3	1.23929	76.861	0.7
142	12	0	4	1.23626	77.084	0.7
143	4	7	0	1.23314	77.315	0.4
144	10	5	2	1.22670	77.797	0.1
145	6	2	6	1.22293	78.083	0.4
146	1	5	5	1.22173	78.174	0.3
147	4	3	6	1.22019	78.291	0.5
148	0	6	4	1.21631	78.589	0.5
149	13	2	3	1.21392	78.774	0.5
150	12	4	2	1.21015	79.068	0.3
151	2	6	4	1.20578	79.411	0.4

Stick Pattern

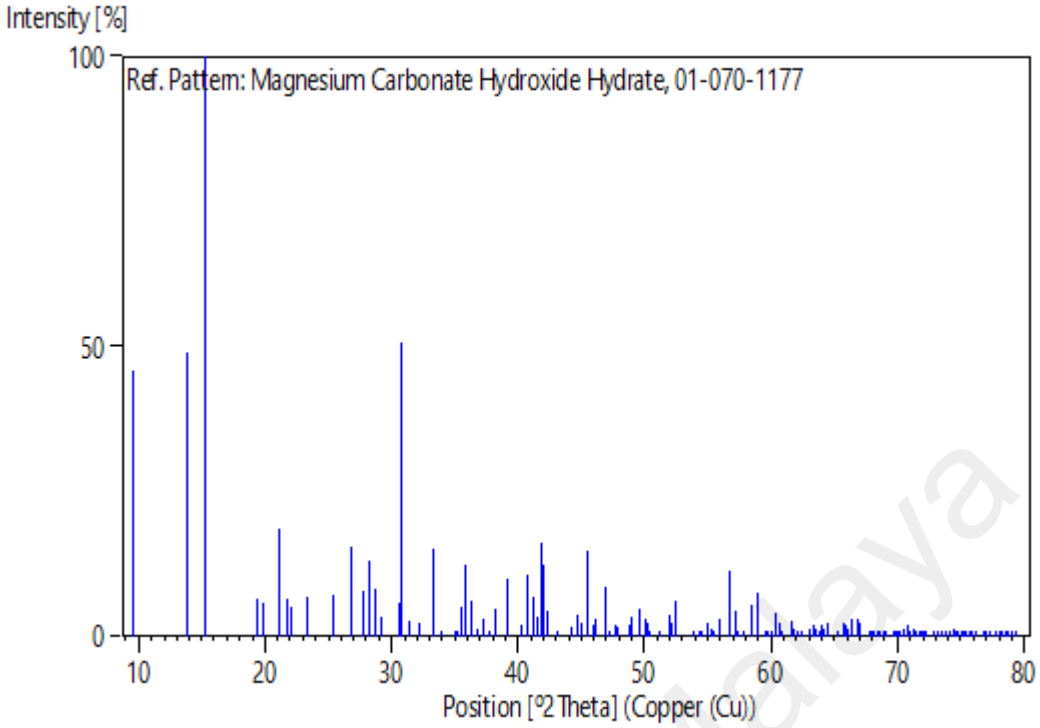

Figure B-3: JCPDS reference of magnesium carbonate hydroxide hydrate

Name and formula

Reference code:	00-043-1022
Mineral name:	Periclase, syn
Compound name:	Magnesium Oxide
PDF index name:	Magnesium Oxide
Empirical formula:	MgO
Chemical formula:	MgO

Crystallographic parameters

Crystal system:	Cubic
Space group:	Fm-3m
Space group number:	225
a (Å):	4.2130
b (Å):	4.2130
c (Å):	4.2130
Alpha (°):	90.0000
Beta (°):	90.0000
Gamma (°):	90.0000
Calculated density (g/cm^3):	3.59
Volume of cell (10^6 pm^3):	74.78
Z:	4.00
RIR:	3.03

Status, subfiles and quality

Status:	Marked as deleted by ICDD
Subfiles:	Alloy, metal or intermetalic Corrosion Inorganic Mineral Pharmaceutical
Quality:	Calculated (C)

Comments

Creation Date:	1/1/1970
Modification Date:	1/1/1970

Calculation of diffractometer peak intensities done with MICRO-POWD v. 2.2 (D. Smith and K. Smith) using default instrument broadening function (NBS Table), diffracted beam monochromator polarization correction, and atomic scattering factors corrected for anomalous dispersion. Cell parameters from Sasaki, S. et al., \ITProc. Jpn. Acad.\RG, \BF55\RG 43-48 (1979). Atomic positions from same source: Mg in 2a, O in 1b

Isotropic thermal parameters also from same source: Mg, B=.312; O, B=.362

Deleted Or Rejected By:	Deleted by 45-946, experimental pattern; minerals subcommittee 6/94.

References

Primary reference:	Grier, D., McCarthy, G., North Dakota State University, Fargo, North Dakota, USA., *ICDD Grant-in-Aid*, (1991)

Peak list

No.	h	k	l	d [A]	2Theta[deg]	I [%]
1	1	1	1	2.43200	36.931	11.0
2	2	0	0	2.10600	42.909	100.0
3	2	2	0	1.48950	62.283	51.0
4	3	1	1	1.27030	74.658	6.0
5	2	2	2	1.21620	78.598	15.0
6	4	0	0	1.05320	94.006	6.0
7	3	3	1	0.96650	105.689	3.0
8	4	2	0	0.94210	109.699	18.0

Stick Pattern

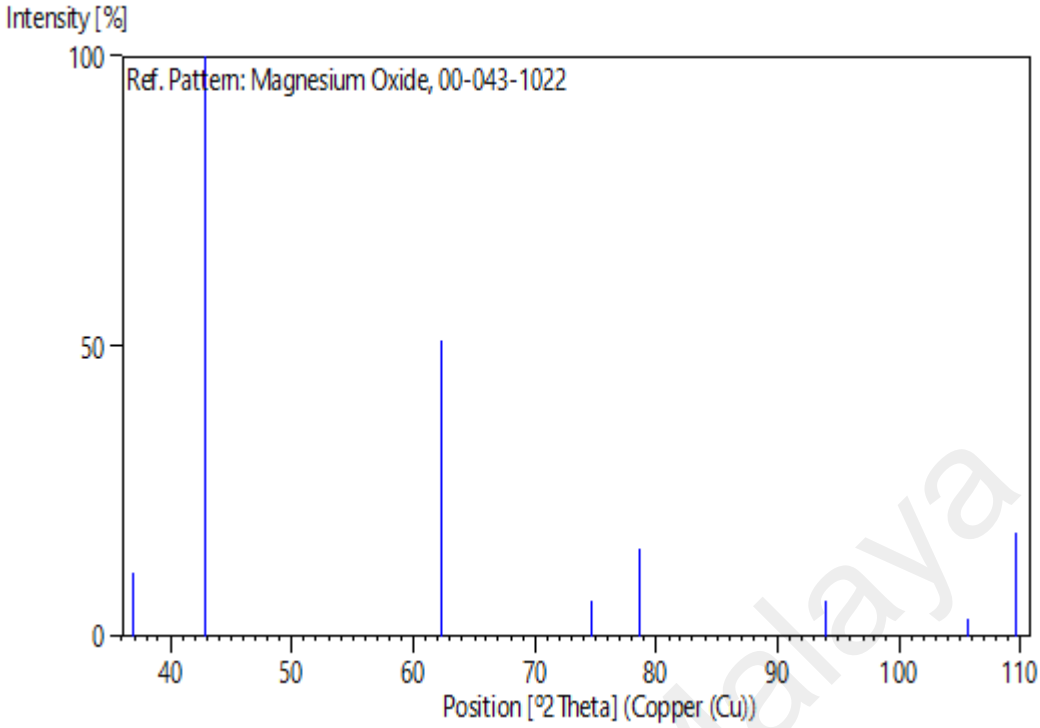

Figure B-4: JCPDS reference of periclase (MgO)

Name and formula

Reference code:	00-011-0273
Compound name:	Magnesium Silicate
Common name:	proto-enstatite
PDF index name:	Magnesium Silicate
Empirical formula:	MgO_3Si
Chemical formula:	$MgSiO_3$

Crystallographic parameters

Crystal system:	Orthorhombic
Space group:	Pbcn
Space group number:	60
a (Å):	9.2500
b (Å):	8.7400
c (Å):	5.3200
Alpha (°):	90.0000
Beta (°):	90.0000
Gamma (°):	90.0000
Calculated density (g/cm^3):	3.10
Volume of cell (10^6 pm^3):	430.10
Z:	8.00
RIR:	-

Subfiles and quality

Subfiles:	Inorganic
Quality:	Indexed (I)

Comments

Color:	Colorless
Creation Date:	1/1/1970
Modification Date:	1/1/1970
Optical Data:	A=1.65, B=1.65, Q=1.66, Sign=+, 2V=70°
Color:	Colorless
Sample Preparation:	Pattern made at 27 C of the quenched high temperature form that is stable above 1050 C
Additional Patterns:	See ICSD 2-6489 (PDF 74-816).

References

Primary reference:	Smith., *Acta Crystallogr.*, **12**, 515, (1959)
Optical data:	Atlas., *J. Geol.*, **60**, 127, (1952)

Peak list

No.	h	k	l	d [A]	2Theta[deg]	I [%]
1	1	1	0	6.35000	13.935	3.0
2	2	0	0	4.62000	19.196	1.0
3	0	2	0	4.37000	20.305	3.0
4	1	1	1	4.09000	21.712	1.0
5	2	1	1	3.24000	27.507	20.0
6	1	2	1	3.17000	28.127	100.0
7	3	1	0	2.90800	30.721	40.0
8	1	3	0	2.77900	32.185	3.0
9	2	2	1	2.72600	32.828	20.0
10	3	1	1	2.55100	35.151	30.0
11	1	3	1	2.46200	36.465	7.0
12	2	0	2	2.30500	39.046	20.0
13	2	3	1	2.23600	40.302	5.0
14	2	1	2	2.22900	40.435	3.0
15	3	3	0	2.11700	42.675	5.0
16	4	1	1	2.06100	43.894	3.0
17	1	4	1	1.97500	45.912	20.0
18	3	3	1	1.96800	46.085	20.0
19	4	2	1	1.90800	47.622	1.0
20	2	4	1	1.85000	49.212	1.0
21	3	2	2	1.82900	49.816	1.0
22	5	1	0	1.81000	50.375	5.0
23	4	0	2	1.74500	52.391	1.0
24	4	3	1	1.71600	53.345	13.0
25	4	1	2	1.71100	53.514	3.0
26	1	4	2	1.66100	55.260	5.0
27	0	2	3	1.64200	55.955	20.0
28	4	2	2	1.62100	56.745	5.0
29	4	4	0	1.58800	58.035	1.0
30	2	5	1	1.56400	59.013	1.0
31	6	0	0	1.54300	59.897	1.0
32	3	5	0	1.52100	60.854	1.0
33	5	3	1	1.49900	61.845	15.0
34	1	3	3	1.49500	62.028	15.0

35	0	6	0	1.45700	63.834	7.0
36	6	2	1	1.40300	66.602	1.0
37	0	4	3	1.37600	68.085	7.0
38	3	3	3	1.35900	69.057	5.0

Stick Pattern

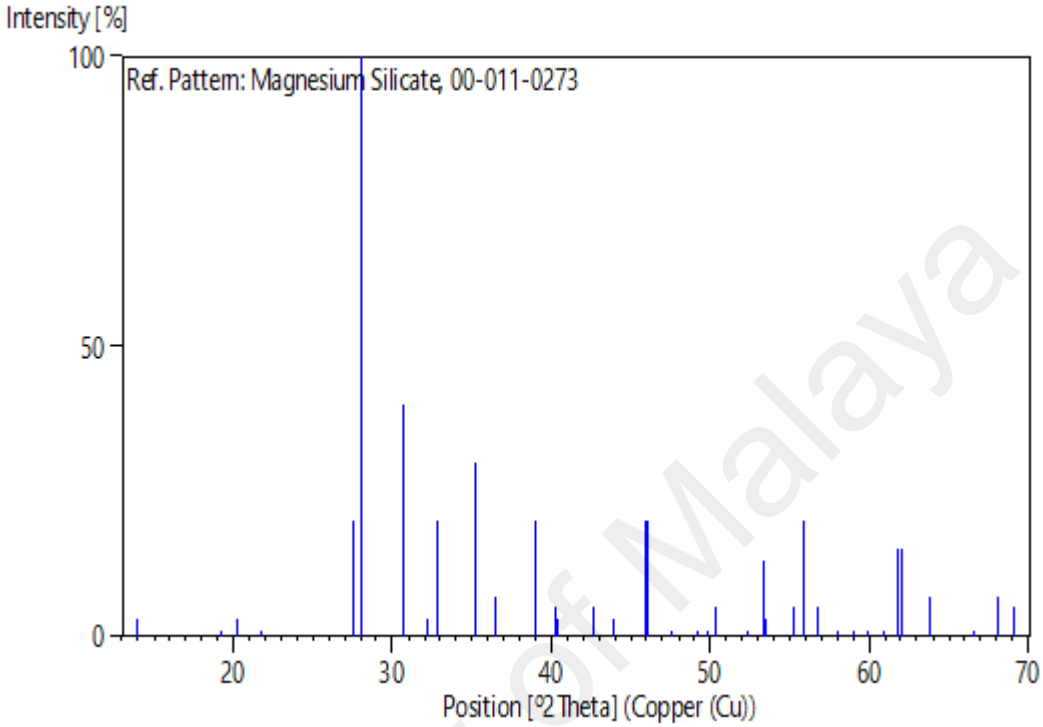

Figure B-5: JCPDS reference of enstatite ($MgSiO_3$)

Name and formula

Reference code:	00-036-1451
Mineral name:	Zincite, syn
Compound name:	Zinc Oxide
Common name:	zinc white
PDF index name:	Zinc Oxide
Empirical formula:	OZn
Chemical formula:	ZnO

Crystallographic parameters

Crystal system:	Hexagonal
Space group:	P63mc
Space group number:	186
a (Å):	3.2498
b (Å):	3.2498
c (Å):	5.2066
Alpha (°):	90.0000
Beta (°):	90.0000
Gamma (°):	120.0000

Volume of cell (10^6 pm^3):	47.62
Z:	2.00
RIR:	-

Subfiles and quality

Subfiles:	Alloy, metal or intermetalic Common Phase Corrosion Educational pattern Forensic Inorganic Mineral NBS pattern Pharmaceutical Pigment/Dye
Quality:	Star (S)

Comments

Color:	Colorless
Creation Date:	1/1/1970
Modification Date:	1/1/1970
Sample Source or Locality:	The sample was obtained from the New Jersey Zinc Co., Bethlehem, Pennsylvania, USA
Color:	Colorless. The structure was determined by Bragg (1) and refined by Abrahams, Bernstein (2). A high pressure cubic NaCl-type of ZnO is reported by Bates et al. (3) and a cubic, sphalerite type is reported by Radczewski, Schicht (4)
Temperature of Data Collection:	The approximate temperature of data collection was 26 C
Additional Patterns:	To replace 5-664 (5)
Powder Data:	References to other early patterns may be found in reference (5)
Optical Data:	B=2.013, Q=2.029, Sign=+.

References

Primary reference:	McMurdie, H., Morris, M., Evans, E., Paretzkin, B., Wong-Ng, W., Ettlinger, L., Hubbard, C., *Powder Diffraction*, **1**, 76, (1986)
Structure:	2. Abrahams, S., Bernstein, J., *Acta Crystallogr., Sec. B*, **25**, 1233, (1969)
Optical data:	*Dana's System of Mineralogy, 7th Ed.*, **I**, 504
Other:	5. Swanson, H., Fuyat, R., *Natl. Bur. Stand. (U.S.), Circ. 539*, **2**, 25, (1953)

Peak list

No.	h	k	l	d [A]	2Theta[deg]	I [%]
1	1	0	0	2.81430	31.770	57.0
2	0	0	2	2.60332	34.422	44.0
3	1	0	1	2.47592	36.253	100.0
4	1	0	2	1.91114	47.539	23.0
5	1	1	0	1.62472	56.603	32.0

6	1	0	3	1.47712	62.864	29.0
7	2	0	0	1.40715	66.380	4.0
8	1	1	2	1.37818	67.963	23.0
9	2	0	1	1.35825	69.100	11.0
10	0	0	4	1.30174	72.562	2.0
11	2	0	2	1.23801	76.955	4.0
12	1	0	4	1.18162	81.370	1.0
13	2	0	3	1.09312	89.607	7.0
14	2	1	0	1.06384	92.784	3.0
15	2	1	1	1.04226	95.304	6.0
16	1	1	4	1.01595	98.613	4.0
17	2	1	2	0.98464	102.946	2.0
18	1	0	5	0.97663	104.134	5.0
19	2	0	4	0.95561	107.430	1.0
20	3	0	0	0.93812	110.392	3.0
21	2	1	3	0.90694	116.279	8.0
22	3	0	2	0.88256	121.572	4.0
23	0	0	6	0.86768	125.188	1.0
24	2	0	5	0.83703	133.932	3.0
25	1	0	6	0.82928	136.521	1.0
26	2	1	4	0.82370	138.513	2.0
27	2	2	0	0.81247	142.918	3.0

Stick Pattern

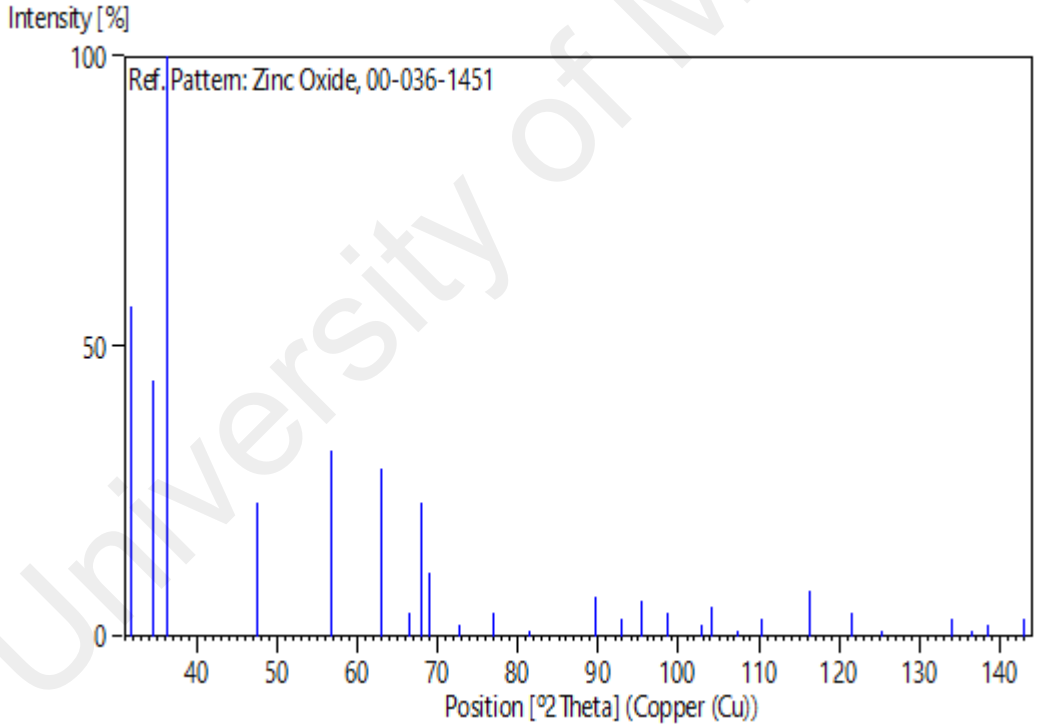

Figure B-6: JCPDS reference of zinc oxide (ZnO)

APPENDIX C

Materials and Equipments

Figure C-1: (a) Magnesium hydroxide carbonate (magnesium carbonate basic), (b) talc and (c) zinc oxide powder

Figure C-2: BEL Engineering Balance

Figure C-3: Shimadzu AY220 Densi-meter balance

Figure C-4: Sonics & Materials VX500 Ultrasonic pulser

Figure C-5: Union Press Attritor mill

Figure C-6: Endecotts stainless steel test sieve

Figure C-7: Bench press machine

Figure C-8: Memmert Oven

Figure C-9: LT Box furnace

Figure C-10: Grinding and polishing machine

Figure C-11: PANalytical Empyrean X-ray diffractometer

Figure C-12: Shimadzu HMV Microhardness tester

Figure C-13: Micromeritics ASAP 2020 Surface area analyzer

Figure C-14: Perkin Elmer Pyris Diamond Differential scanning calorimeter

Figure C-15: Phenom Pro-X Scanning electron microscope

Figure C-16: JEOL Field-emission Scanning electron microscope

Figure C-17: JEOL Transmission electron microscope

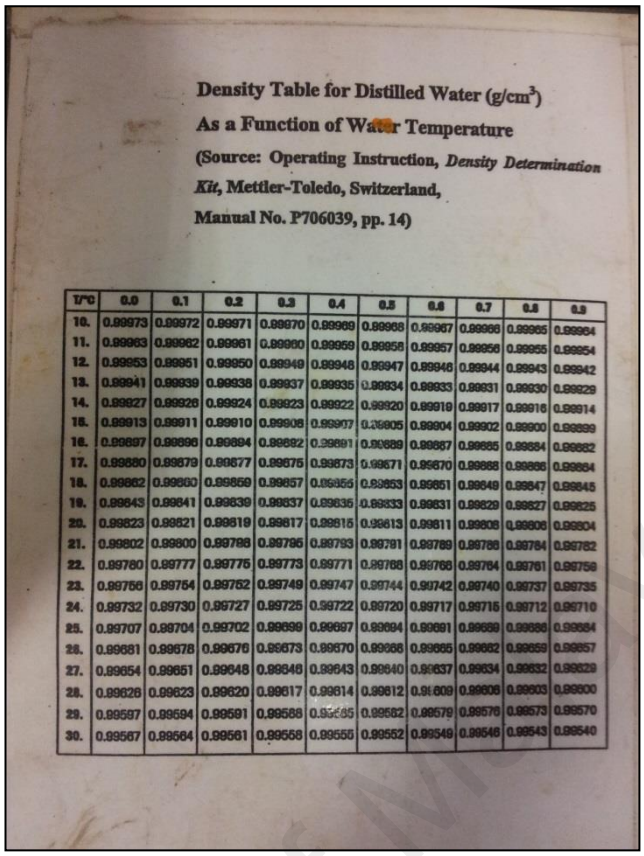

Density Table for Distilled Water (g/cm^3)
As a Function of Water Temperature
(Source: Operating Instruction, *Density Determination Kit*, Mettler-Toledo, Switzerland, Manual No. P706039, pp. 14)

T/°C	0.0	0.1	0.2	0.3	0.4	0.5	0.6	0.7	0.8	0.9
10.	0.99973	0.99972	0.99971	0.99970	0.99969	0.99968	0.99967	0.99966	0.99965	0.99964
11.	0.99963	0.99962	0.99961	0.99960	0.99959	0.99958	0.99957	0.99956	0.99955	0.99954
12.	0.99953	0.99951	0.99950	0.99949	0.99948	0.99947	0.99946	0.99944	0.99943	0.99942
13.	0.99941	0.99939	0.99938	0.99937	0.99935	0.99934	0.99933	0.99931	0.99930	0.99929
14.	0.99927	0.99926	0.99924	0.99923	0.99922	0.99920	0.99919	0.99917	0.99916	0.99914
15.	0.99913	0.99911	0.99910	0.99908	0.99907	0.99905	0.99904	0.99902	0.99900	0.99899
16.	0.99897	0.99896	0.99894	0.99892	0.99891	0.99889	0.99887	0.99885	0.99884	0.99882
17.	0.99880	0.99879	0.99877	0.99875	0.99873	0.99871	0.99870	0.99868	0.99866	0.99864
18.	0.99862	0.99860	0.99859	0.99857	0.99855	0.99853	0.99851	0.99849	0.99847	0.99845
19.	0.99843	0.99841	0.99839	0.99837	0.99835	0.99833	0.99831	0.99829	0.99827	0.99825
20.	0.99823	0.99821	0.99819	0.99817	0.99815	0.99813	0.99811	0.99809	0.99806	0.99804
21.	0.99802	0.99800	0.99798	0.99796	0.99793	0.99791	0.99789	0.99786	0.99784	0.99782
22.	0.99780	0.99777	0.99775	0.99773	0.99771	0.99768	0.99766	0.99764	0.99761	0.99758
23.	0.99756	0.99754	0.99752	0.99749	0.99747	0.99744	0.99742	0.99740	0.99737	0.99735
24.	0.99732	0.99730	0.99727	0.99725	0.99722	0.99720	0.99717	0.99715	0.99712	0.99710
25.	0.99707	0.99704	0.99702	0.99699	0.99697	0.99694	0.99691	0.99689	0.99686	0.99684
26.	0.99681	0.99678	0.99676	0.99673	0.99670	0.99668	0.99665	0.99662	0.99659	0.99657
27.	0.99654	0.99651	0.99648	0.99646	0.99643	0.99640	0.99637	0.99634	0.99632	0.99629
28.	0.99626	0.99623	0.99620	0.99617	0.99614	0.99612	0.99609	0.99606	0.99603	0.99600
29.	0.99597	0.99594	0.99591	0.99588	0.99585	0.99582	0.99579	0.99576	0.99573	0.99570
30.	0.99567	0.99564	0.99561	0.99558	0.99555	0.99552	0.99549	0.99546	0.99543	0.99540

Figure C-18: Density table for distilled water